

University of Nebraska - Lincoln

DigitalCommons@University of Nebraska - Lincoln

Student Research Projects, Dissertations, and
Theses - Chemistry Department

Chemistry, Department of

5-2013

The Electrochemical Analysis of Bovine Bone Derived Supercapacitors, Organic Peroxide Explosives, and Conducting Polymer Nanojunctions

Paul Goodman

University of Nebraska-Lincoln, pagoodman5@huskers.unl.edu

Follow this and additional works at: <http://digitalcommons.unl.edu/chemistrydiss>



Part of the [Chemistry Commons](#)

Goodman, Paul, "The Electrochemical Analysis of Bovine Bone Derived Supercapacitors, Organic Peroxide Explosives, and Conducting Polymer Nanojunctions" (2013). *Student Research Projects, Dissertations, and Theses - Chemistry Department*. 39. <http://digitalcommons.unl.edu/chemistrydiss/39>

This Article is brought to you for free and open access by the Chemistry, Department of at DigitalCommons@University of Nebraska - Lincoln. It has been accepted for inclusion in Student Research Projects, Dissertations, and Theses - Chemistry Department by an authorized administrator of DigitalCommons@University of Nebraska - Lincoln.

The Electrochemical Analysis of Bovine Bone Derived Supercapacitors, Organic
Peroxide Explosives, and Conducting Polymer Nanojunctions

by

Paul A. Goodman

A DISSERTATION

Presented to the Faculty of
The Graduate College at the University of Nebraska
In Partial Fulfillment of Requirements
For the Degree of Doctor of Philosophy

Major: Chemistry

Under the Supervision of Professor Jody G. Redepenning

Lincoln, Nebraska

May, 2013

The Electrochemical Analysis of Bovine Bone Derived Supercapacitors, Organic Peroxide Explosives, and Conducting Polymer Nanojunctions

Paul A. Goodman, Ph.D.

University of Nebraska, 2013

Adviser: Jody G. Redepenning

Electrochemical methods are an extremely diverse set of tools that can be applied to a large number of systems for quantitative, qualitative, and synthetic purposes. For the work described in this dissertation, electrochemical methods provided the basis for the analysis or fabrication of three unique systems.

Chapter 1 describes the analysis of carbon monoliths, produced by the pyrolysis of bovine bone, as electrodes in supercapacitor devices. After pyrolysis of the bone and subsequent removal of the hydroxyapatite support structure, via acid or ethylenediaminetetraacetic acid, a conductive carbon monolith that retains the macroscopic structure of the original bone remains. Analysis of the Raman spectra demonstrates that the carbon is similar to amorphous carbons. Electrochemical analysis shows that the monoliths have a specific capacitance of 134 ± 11 F/g in aqueous solutions of potassium nitrate and 108 ± 9 F/g in the ionic liquid 1-ethyl-3-methylimidazolium bis(trifluoromethylsulfonyl)imide.

Chapter 2 discusses the application of electrochemical methods to the analysis of the explosive triacetone triperoxide (TATP) in nonaqueous solutions. The $E_{1/2}$ for the reduction of TATP at a glassy carbon electrode surface is -2.25 V vs.

ferrocene/ferrocenium at a scan rate of 100 mV/s and is well described by a relatively slow two-electron reduction followed by a fast chemical transformation, as determined by bulk electrolysis and digital simulation experiments. It was found that the first reduction product of [tris(2-2'-bipyridine) ruthenium (III)]²⁺ reacts with TATP in solution and shifts the reduction of the peroxide by +550 mV to -1.70 V vs. ferrocene.

Chapter 3 describes the electrochemical polymerization of aniline and pyrrole to bridge gaps of 50-200 nm between micropatterned electrodes. It was determined that polyaniline deposited from aqueous solutions of aniline containing sulfuric acid resulted in relatively uniform and stable bridges. Polypyrrole deposited from dry acetonitrile solutions of pyrrole containing tetrabutylammonium hexafluorophosphate also produced relatively uniform and stable bridges. When the oxidation states of the polymer bridges were switched from neutral to oxidized the resistance of the junctions decreased by 40% and 50% for polyaniline and polypyrrole, respectively. Junctions of this type could be used as the basis for sensor devices in the future.

Acknowledgements

This dissertation would not have been possible without help and support from many people. First, I would like to thank my advisor, Professor Jody Redepenning. His guidance during my time at Nebraska has helped me develop as a critical thinker. I have learned a great deal about being a good scientist from Professor Redepenning, and I have also learned a lot about setting priorities and balancing life outside the lab. I would also like to thank the members of my supervisory committee, Professor David Hage, Professor Rebecca Lai, Professor Jian Zhang, Professor Wonyoung Choe, and Professor Stephen Ducharme. Thank you also to Dr. Andrei Sokolov for helping me set up the electronics for measurements, Dr. Yong Feng Lu for the use of his research group's Raman spectroscopy instrument and Drs. You (Joe) Zhou, and Han Chen for their help with scanning electron microscopy.

I would also like to thank my current and former lab members, Lukasz Gauza, Dr. Kristopher Hiebner, Dr. Troy Wiegand, and Dr. Chris Schwartz. I wish to extend a special thank you to Ben Wymore. Ben performed the Focused Ion Beam milling that was instrumental for my work with conducting polymer nanojunctions, and helped me with all other aspects of the microfabrication techniques that I used. Additionally, our discussions about research and coursework helped to guide my work, while our discussions about sports, movies, and many other topics continually delayed progress for both of us. Another special thank you goes to Haoming Li, who did a great deal of the sample preparation and recorded Raman spectra (with the assistance of Yang Gao) for my work with supercapacitors.

Defense Advanced Research Projects Agency (DARPA) provided the funding for my work related to triacetone triperoxide and conducting polymer nanojunctions. My work with supercapacitors was funded by the Nebraska Center for Energy Sciences Research. I would also like to thank the Department of Defense Science Research Mathematics and Research for Transformation (SMART) program for providing me with a scholarship that supported me, and my family.

Additionally, I would like to thank my family, without whom none of this would have been possible. My parents, Matt and Jill, have always been extremely supportive of everything that I have done, and my decision to go to graduate school was no exception. They are always available for help and support, and knowing that they are always behind me has helped get me to where I am today more than I can express in words. I only hope that I can be half as good at parenting as they are. Thank you to my sisters Jennifer Frett and Melissa Bowling who helped push me and have set great examples for me to mimic.

Finally, I would like to thank my beautiful wife Janet. Her ability to tolerate me, especially during the process of writing this dissertation, is nothing short of a miracle. I cannot express how grateful I am for everything she does to help me, particularly in stressful times. I am a very lucky man. I must also thank our daughter Elizabeth. A big smile from my baby girl at the end of the day has the ability to turn a bad day into a good one almost instantaneously.

Table of Contents

Chapter 1—The Preparation of Carbon Monoliths Derived from Bovine

Bone and Their Analysis as Supercapacitor Electrodes	1
Introduction.....	1
Experimental.....	5
Chemicals.....	5
Sample Preparation and Pyrolysis	7
Surface Area Measurements	8
Raman Spectral Analysis	8
Compressive testing	8
Electrode Preparation and Electrochemical Analysis.....	9
Calculation of Specific Capacitance	11
Results and Discussion	12
Scanning Electron Microscopy	12
Structural Analysis by Raman Spectroscopy	14
Electrochemical Characterization	18
Specific Surface Area and Its Relationship to Specific Capacitance.....	33
Influence of Pyrolysis Conditions.....	38
Mechanical Testing	41
Modification Attempts	42
Conclusions.....	49
References.....	52

Chapter 2—The Qualitative Electrochemical Analysis of Triacetone

Triperoxide.....	56
Introduction.....	56
Experimental.....	65
Chemicals.....	65
TATP Synthesis.....	67
Electrochemical Measurements.....	67
Bulk Electrolysis.....	68
Digital Simulations.....	68
Catalytic Reduction.....	68
Nafion Electrodes.....	69
Tris-(2-2' bipyridine) ruthenium (II) hexafluorophosphate preparation.....	69
Results and Discussion.....	70
TATP Electrochemistry.....	70
Position of the Reduction Wave.....	70
Voltammetric Differences at Various Electrode Surfaces.....	75
Cyclic Voltammetry.....	76
Bulk Electrolysis.....	83
Digital Simulation.....	85
Catalytic Reduction.....	91
Introduction.....	91
Porphyrins.....	91

Ferrous Ion	97
Miscellaneous Compounds	99
Nafion Film Electrodes	101
Ruthenium Tris Bipyridine	108
Conclusions	114
References	117
Chapter 3—Bridged Nanjunctions via the Electrochemical	
Polymerization of Aniline and Pyrrole	124
Introduction	124
Experimental	128
Preparation of the Substrate	128
Electrochemical Polymerization Cell	129
Electrochemical Polymerization Procedure	131
Characterization	134
Results and Discussion	135
Polyaniline	135
Polyaniline Nanjunction 1	137
Polyaniline Nanjunction 2	143
Polyaniline Nanjunction 3	146
Polyaniline Nanjunction 4	150
Polyaniline Nanjunction 5	154
Polyaniline Nanjunction 6	156
Polyaniline Nanjunction 7	162

Polypyrrole.....	166
Polypyrrole Nanojunction 1	169
Polypyrrole Nanojunction 2	172
Polypyrrole Nanojunction 3	177
Polypyrrole Nanojunction 4	181
Conclusions.....	187
References.....	190

Figures, Equations, and Tables

<u>Title</u>	<u>Page</u>
Equation 1.1- Capacitors in Series.....	2
Equation 1.2- Energy in a Capacitor.....	3
Figure 1.1- Photograph of HA Composites	6
Figure 1.2- Photograph of Capacitor Test Cell.....	10
Equation 1.3- Definition of Specific Capacitance	11
Equation 1.4- Capacitors in Series Using Specific Capacitance.....	11
Equation 1.5- Specific Capacitance of Monoliths Definition.....	12
Equation 1.6- Equation of Specific of Monoliths	12
Figure 1.3- SEM of Monoliths.....	13
Figure 1.4- TEM of Monoliths.....	15
Figure 1.5- SAED of Monoliths.....	16
Figure 1.6- Raman Spectra Comparison.....	17
Figure 1.7- Raman Fitting for Monoliths.....	19
Figure 1.8- Cyclic Voltammograms for Supercapacitor Device	21
Figure 1.9- Linear Dependence of Voltammetric Response.....	22
Figure 1.10- Chronocoulometric Response for Supercapacitor Device	23
Equation 1.7- Capacitor Charge with Time	24
Figure 1.11- Chronopotentiometric Response of Device	25
Equation 1.8- Current Response of a Capacitor to Voltage Step.....	27
Figure 1.12- Natural Log Current Plot for Capacitor Discharge	28
Figure 1.13- Scale-up Capacitor Response.....	32

Figure 1.14- Voltammetric Response of Device with HA.....	34
Figure 1.15- Nitrogen Adsorption Isotherm	35
Figure 1.16- DFT Surface Area Response	37
Table 1.1- Comparison of Preparation Conditions	40
Figure 1.17- Compressive Testing Response.....	43
Table 1.2- Compressive Testing Results	44
Figure 1.18- Pseudocapacitor Voltammetric Response 1	47
Figure 1.19- Pseudocapacitor Voltammetric Response 2.....	48
Figure 2.1- TATP Structure	58
Equation 2.1- Fluorine E^o	62
Equation 2.2- Lithium E^o	62
Equation 2.3- Iron EDTA Reduction	63
Equation 2.4- Iron EDTA Reaction with Hydrogen Peroxide.....	63
Equation 2.5- $\text{Ru}(\text{bpy})_3^{2+}$ Reduction.....	65
Equation 2.6- $\text{Ru}(\text{bpy})_3^{2+}$ Oxidation	65
Equation 2.7- $\text{Ru}(\text{bpy})_3^{2+*}$ Production	65
Equation 2.8- $\text{Ru}(\text{bpy})_3^{2+*}$ Relaxation.....	65
Equation 2.9- $\text{Ru}(\text{bpy})_3^{1+}$ Reaction with TATP	65
Figure 2.2- TATP Voltammetric Response at Au, Pt, and GC.....	71
Figure 2.3- TATP Voltammetric Response with Phenol	73
Figure 2.4- TATP Voltammetric Response at Various Scan Rates	77
Equation 2.10- Calculation of Alpha	78
Figure 2.5- Peak Potential Shift.....	79

Figure 2.6- TATP Voltammetric Response, Multiple Cycles.....	81
Figure 2.7- TATP Voltammetric Response Without Polishing.....	82
Figure 2.8- Bulk Electrolysis Result.....	84
Figure 2.9- Digital Simulation Result.....	88
Table 2.1- Digital Simulation Rate Constant Shift.....	89
Figure 2.10- F ₈ TPPCo Voltammetric Response.....	93
Figure 2.11- Iron Porphyrin Voltammetric Response.....	94
Figure 2.12- Rhodium Porphyrin Voltammetric Response.....	96
Figure 2.13- Ferric Chloride Voltammetric Response.....	98
Figure 2.14- Miscellaneous Compounds Voltammetric Response.....	100
Figure 2.15- Nafion Coated Electrode Voltammetric Response.....	102
Figure 2.16- Iron Loading Voltammetric Response.....	105
Figure 2.17- Nafion Electrode Wetting Voltammetric Response.....	107
Figure 2.18- Ru(bpy) ₃ ²⁺ with TATP Voltammetric Response.....	109
Equation 2.11- Catalytic Mediation Response.....	110
Equation 2.12- Lambda Definition.....	110
Table 2.2- Potential Shift Summary.....	111
Equation 2.13- Simplified Catalytic Mediation Response.....	112
Figure 2.19- Catalytic Mediated Electron Transfer Response.....	113
Figure 3.1- SEM of Nanojunctions.....	130
Figure 3.2- Photograph of Electrochemical Cell.....	132
Table 3.1- Polymerization Baths.....	133
Figure 3.3- Polyaniline Polymerization Voltammetric Response.....	136

Figure 3.4- Polyaniline Nanojunction 1 Polymerization	138
Figure 3.5- Polyaniline Nanojunction 1 Response	140
Equation 3.1- Resistivity.....	142
Figure 3.6- Polyaniline Nanojunction 2 Connection	144
Figure 3.7- Polyaniline Nanojunction 2 SEM.....	145
Figure 3.8- Polyaniline Nanojunction 3 Polymerization	147
Figure 3.9- Polyaniline Nanojunction 3 SEM.....	148
Figure 3.10- Polyaniline Nanojunction 3 Response	149
Figure 3.11- Polyaniline Nanojunction 4 Polymerization	151
Figure 3.12- Polyaniline Nanojunction 4 Response	152
Figure 3.13- Polyaniline Nanojunction 4 SEM.....	153
Figure 3.14- Polyaniline Nanojunction 5 SEM.....	155
Figure 3.15- Polyaniline Nanojunction 6 Response	157
Figure 3.16- Polyaniline Nanojunction 6 SEM.....	158
Figure 3.17- Polyaniline Nanojunction 6 Voltammogram in MeCN	160
Figure 3.18- Polyaniline Nanojunction 6 Impedance	161
Figure 3.19- Polyaniline Nanojunction 7 SEM.....	163
Figure 3.20- Polyaniline Nanojunction 7 Response	164
Figure 3.21- Polyaniline Nanojunction 7 Impedance	165
Figure 3.22- Polypyrrole Polymerization Voltammetric Response	168
Figure 3.23- Polypyrrole Nanojunction 1 Connection.....	170
Figure 3.24- Polypyrrole Nanojunction 1 Response.....	171
Figure 3.25- Polypyrrole Nanojunction 2 Polymerization.....	173

Figure 3.26- Polypyrrole Nanojunction 2 SEM.....	174
Figure 3.27- Polypyrrole Nanojunction 2 Response.....	176
Figure 3.28- Polypyrrole Nanojunction 3 Polymerization.....	179
Figure 3.29- Polypyrrole Nanojunction 3 SEM.....	180
Figure 3.30- Polypyrrole Nanojunction 4 Polymerization.....	182
Figure 3.31- Polypyrrole Nanojunction 4 SEM.....	183
Figure 3.32- Polypyrrole Nanojunction 4 Resistance 1	185
Figure 3.33- Polypyrrole Nanojunction 4 Resistance 2	186

Chapter 1

The Preparation of Carbon Monoliths Derived from Bovine Bone and Their Analysis as Supercapacitor Electrodes

Portions of this chapter are based on material previously presented in:
Paul A. Goodman, H. Li, Y. Gao , Y. F. Lu, J. D. Stenger-Smith, Jody Redepenning;
Preparation and characterization of high surface area, high porosity carbon monoliths
from pyrolyzed bovine bone and their performance as supercapacitor electrodes. Carbon
(2013), <http://dx.doi.org/10.1016/j.carbon.2012.12.066>

Introduction

The diminishing availability of fossil fuels, coupled with the increase in new primary energy sources, makes the development of new ways to store energy an increasingly important pursuit. The surge in popularity of hybrid electric vehicles and portable electronic devices has created a large potential market for these novel storage devices. Supercapacitors, or more accurately electrochemical double layer capacitors (EDLC), offer one option for meeting part of this rising demand. Supercapacitors make use of the inherently high capacitance of the electrochemical double layer at high-surface-area electrodes, which are usually some form of carbon [1]. One of the great benefits of supercapacitors is that, in addition to the relatively large amounts energy stored, charging and discharging the electrochemical double layer are highly reversible processes that can be cycled many tens of thousands of times with very little degradation [2-4]. The first patent for such a device was awarded to Becker in 1957 [5].

A commonly used description of the electrochemical double layer is known as the Gouy-Chapman-Stern model. This model describes the overall electrochemical double layer capacitance, C_{meas} , as a combination of two individual interfacial capacitances. The first is the capacitance of the diffuse layer, C_1 , as described by Gouy and Chapman. This

capacitance is a result of the ordering of ions, treated as point charges, in the diffuse region of the solution in response to an applied potential at an electrode surface. The so-called Helmholtz layer contributes the second capacitance, C_2 . The Helmholtz layer is the compact layer of ions, with a finite size, directly adjacent to the electrode surface. Stern proposed the addition of this compact layer to the Gouy-Chapman treatment to account for the unlimited rise in differential capacitance caused by the treatment of ions as point charges rather than species of finite size. Though this description ignores the effects of some additional phenomena such as specific adsorption, and differences in ion sizes, it generally provides a good agreement with the overall features of experimental data [1, 6].

Based on the reciprocal relationship between two capacitors connected in series,

$$\frac{1}{C_{meas}} = \frac{1}{C_1} + \frac{1}{C_2} \quad (1.1)$$

the smaller of these two capacitances (C_1 and C_2) will have a larger contribution to the overall value of C_{meas} . In a system with a high concentration of electrolyte, such as a supercapacitor, the value for C_1 is very large relative to C_2 [6]. Therefore, the capacitance of the Helmholtz layer dictates the value for C_{meas} in an EDLC system.

The distance of closest approach for charge compensating ions as defined by the original description of the Helmholtz layer, as well as the extended description published later by Grahame, implies that the effective “dielectric” thickness in the electrochemical double layer is on the order of 4 Å, or roughly the size of an ion or molecule [1, 7]. When one assumes an applied potential to the electrode surface of 1 V, the estimated magnitude of the electric field across this interface is on the order of 10^9 V/m.

It is this large field, made possible by the highly stable nature of the system, that gives rise to the naturally high capacitance of the double layer. Given the generally accepted generic value for the capacitance of the double layer of approximately $20 \mu\text{F}/\text{cm}^2$, one can estimate that an electrode with a surface area of $1000 \text{ m}^2/\text{g}$ would have a specific capacitance of $200 \text{ F}/\text{g}$. The energy stored in a capacitor is directly proportional to the capacitance, as shown in Equation 1.2:

$$E = \frac{1}{2} CV^2 \quad (1.2)$$

where E is energy, C is capacitance, and V is applied voltage. This relationship shows that maximizing the stored energy in EDLCs can be accomplished by increasing the electrode area, and also by increasing the applied voltage in the system. Equation 1.2 is an accurate approximation of the capacitance in the same limit as the Helmholtz model, the simple model of the electrochemical double layer capacitance that first appeared over one hundred years ago. The Helmholtz layer dominates the measured capacitance of an electrode when the concentration of ions in solution is high. In the time since the Helmholtz model was first introduced, a large number of refinements have been made to models that describe double layer thermodynamics and kinetics. A summary of these refinements, including historical treatments, appears as a full chapter in the advanced electrochemistry text, "Electrochemical Methods" [6]. One of the challenges of EDLCs is that the maximum applied voltage must be low enough to avoid electrolyte breakdown. Highly stable electrolyte systems, such as those based on non-aqueous solvents or ionic liquids, have allowed the operating potential of supercapacitor devices to be increased significantly, leading to higher energy densities compared to first generation, aqueous devices [4, 8-11].

In addition to advances in electrolyte stability, advances have also been made in the carbon materials used as the electrodes. Carbon fabrics produced by Hung et al. are reported to have a specific capacitance of 90 F/g at room temperature using propylene carbonate solutions of tetraethylammonium tetrafluoroborate as the electrolyte [12]. Lin et al. made porous activated carbon fibers via the pyrolysis of polyacrylonitrile which they reported to have specific capacitances of 180 F/g in aqueous sulfuric acid electrolyte [13]. Many groups have developed supercapacitors based on carbon nanotubes with results varying from 20 F/g up to 140 F/g depending on the modification techniques used [14-17]. Bushueva et al. and Gao et al. have both reported the use of carbon nano-onions as capacitor electrodes with specific capacitance values of around 100 F/g [18, 19]. Graphene is another form of carbon that has been explored by many researchers. Two specific examples are those by Vivekchand et al. and Stoller et al., who reported specific capacitances of 117 and 135 F/g, respectively, in aqueous electrolytes [4, 8].

One common method for producing carbon materials is the pyrolysis of carbon-containing polymers to leave behind a conductive carbon network [20-23]. Applying pyrolysis techniques to powdered animal bones can produce a bone char containing a high percentage of conductive carbon with specific surface areas of approximately 2100 m²/g [23, 24]. These materials have been demonstrated to work as cathodes in lithium-sulfur batteries [24].

The work presented in this chapter demonstrates that the pyrolysis of intact bovine cortical bone produces high-surface-area carbon monoliths, which can be used as electrode material for EDLCs. When pyrolysis of the organic components within the bone is performed under the conditions described, the resulting composites contain

conductive carbon interwoven with the structural hierarchy natural to the hydroxyapatite (HA). This natural inorganic “scaffold” prevents the collapse of the carbon structure during the pyrolysis and is largely conserved at the macroscopic, and to a lesser extent, microscopic scales. Photographs of some examples of these carbon/HA composites are shown in Figure 1.1.

Untreated plugs of cortical bone, such as the one shown in Figure 1.1, exhibit a density of approximately 2.0 g/cm^3 . In this starting material, approximately 75% of the mass is HA, and about 25% is water, collagen, and other organic materials. During the pyrolysis procedure described in the experimental section of this chapter, the organic constituents decompose to produce the black materials shown in Figure 1.1, which contain about 3% C by weight. Removing the HA by chemical means, such as dilute acid or chelating agents like ethylenediaminetetraacetic acid (EDTA), leaves behind monolithic conductive carbon networks with densities of approximately 0.05 g/cm^3 , from which EDLC prototypes have been constructed. These networks exhibit high specific surface areas and are self-supporting. This chapter describes the characterization of these monoliths and examines their performance as supercapacitors in both aqueous media and ionic liquids.

Experimental

Chemicals: EDTA (tetrasodium salt, Sigma Aldrich, premium grade, St. Louis, MO), potassium nitrate (KNO_3 , Sigma Aldrich, puriss grade, St. Louis, MO), acetonitrile (Burdick and Jackson, HPLC grade, Muskegon, MI), hydrochloric acid (Fluka, trace metal grade, St. Louis, MO), and activated carbon (Darco KB-G, Sigma Aldrich, St. Louis, MO) were used as purchased. 1-Ethyl-3-methylimidazolium bis(trifluoro-

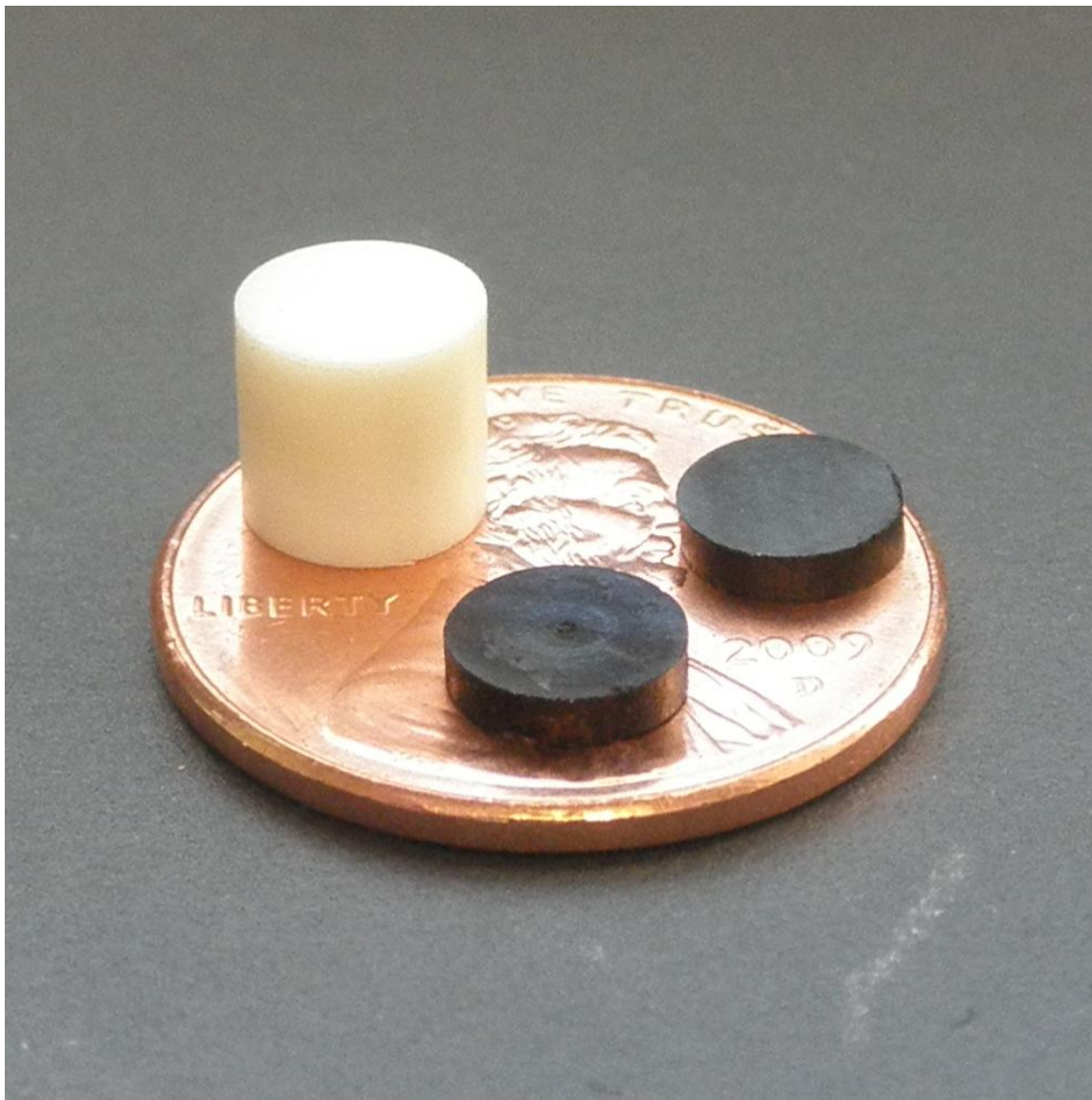


Figure 1.1. Photograph of a bovine bone plug (upper left), and two pyrolyzed disks (upper right and lower), all of which still contain their hydroxyapatite scaffold.

methylsulfonyl)imide (EMIBTI, Ionic Liquid Technologies, Tuscaloosa, AL) was filtered through silica gel activated at 400 °C for 24 h to remove impurities. A small section (2 mm) of glassy carbon rod (TCR-30, Electrosynthesis, Inc., Lancaster, NY) was pulverized in a mortar in pestle prior to being characterized by Raman spectroscopy.

Sample Preparation and Pyrolysis: Cylindrical bone plugs were machined in the longitudinal direction from the diaphyseal section of bovine femurs (Premium Protein Products, Lincoln, NE) with a 6 mm diameter dowel tool, as described previously by Wiegand et al. [25]. The plugs were sectioned on a lathe into cylindrical disks 6 mm in diameter and 1.5 mm thick. These disks were then stacked in an 8 mm inner diameter quartz tube and heated *in vacuo* (20 mTorr) using a Thermo Scientific (Waltham, MA) Model F46240CM-33 oven with a Eurotherm 2408 temperature controller. The pyrolysis was performed using an adaptation of the heating protocol by described by Tormala and Romppanen for the preparation of glassy carbon from lignins [26]. The temperature of the bone disks was initially raised rapidly from room temperature to 180 °C over approximately 4 min. The temperature was then increased from 180 to 750 °C at a ramping rate of 18 °C/h. Finally, over 5 min the temperature was ramped from 750 to 1000 °C, at which point the oven was switched off and allowed to cool passively for 16 h to room temperature. The preparation of the disks was largely performed by Haoming Li with my occasional assistance. Prior to surface area and electrochemical characterization, the HA was removed from pyrolyzed disks by immersing them for 120 h in 40 mL of a pH 7.5, 500 mM aqueous solution of EDTA. Finally, the samples were rinsed three times (over two hours for each rinsing) in 40 mL of deionized water to remove any remaining EDTA.

Surface Area Measurements: Specific surface areas were measured by nitrogen adsorption using the Brunauer, Emmett, Teller (BET) method [27]. All adsorption measurements were made using a Micromeritics (Norcross, GA) ASAP 2020 Surface Area and Porosity Analyzer.

Raman Spectral Analysis: Raman spectroscopy was performed using a Renishaw (Hoffman Estates, IL) inVia Dispersive Micro-Raman Spectrometer with an argon laser excitation source at a wavelength of 514.5 nm. Samples were prepared by pressing powdered carbon into a pellet prior to analysis. Fitting of the spectra was performed using OriginPro v 8.0 software (OriginLab, Northampton, MA) as reported by Sadezky et al. [28]. These authors reported that the Raman spectra of carbon materials are well fit by five Lorentzian peaks: G (attributed to an ideal graphitic lattice with E_{2g} symmetry), D1 (attributed to a disordered graphitic lattice with A_{1g} symmetry), D2 (disordered graphitic lattice with E_{2g} symmetry), D3 (amorphous carbon fragments that may include functionalized small molecules), and D4 (disordered graphitic lattice with A_{1g} symmetry, and ionic impurities). Haoming Li collected the Raman spectra with the assistance of Yang Gao. I performed the fitting analysis with the assistance of Mr. Li. All of the spectroscopy equipment needed to perform the Raman characterizations was maintained by Professor Yongfeng Lu and his research group in the Department of Electrical Engineering at the University of Nebraska (Lincoln, NE).

Compressive Testing: Compression testing experiments were performed using a single axis Instron 5967 electromechanical machine with a 30 kN load cell (Norwood, MA). For the monolith materials, the testing was performed by compressing 6 mm x 12 mm rods of the material at a rate of 0.1 mm/min to an extension of 0.6 mm. The

compression was then reversed and the load decreased at the same rate until the extension returned to 0 mm.

Electrode Preparation and Electrochemical Analysis: When the interstitial solvent was allowed to evaporate in air, the carbon monoliths progressively deformed if the hydroxyapatite support structure had been removed. For this reason, electrochemical characterizations required that the monoliths remain fully solvated once the HA scaffold was removed. After the HA were extracted from the carbon/HA composites, as described above, the monoliths (filled with deionized water) were placed in a 2 M solution of KNO_3 in water and allowed to equilibrate for 6 h. A glass microfiber prefilter (Millipore, Billerica, MA) was then placed between two discs to separate them, and the resulting sandwich was inserted near the center of a 3 cm long section of 0.65 cm ID \times 1.3 cm OD Tygon® tubing (Formulation R-3606) filled with 2 M $\text{KNO}_3(\text{aq})$. Modest pressure from two gold plated stainless steel rods provided electrical contact. A silver wire, inserted through the tubing wall into the electrolyte cavity, served as a pseudoreference electrode for all three-electrode electrochemical measurements. All openings were then sealed with epoxy (Hardman Double Bubble Extra Fast Setting, West End, NC) to prevent solvent evaporation and leakage. This configuration provides a convenient setup in which both two-electrode and three-electrode measurements can be made. Non-aqueous cells were prepared by equilibrating the disks in acetonitrile (three times for two hours each) to remove the water. The disks were then immersed in \sim 1 mL of EMIBTI and placed *in vacuo* for 16 h to remove the acetonitrile. Electrochemical cells were then assembled as described above, but with EMIBTI as the electrolyte/solvent. Images of the cell components and an intact cell are shown in Figure 1.2. The electrode materials were

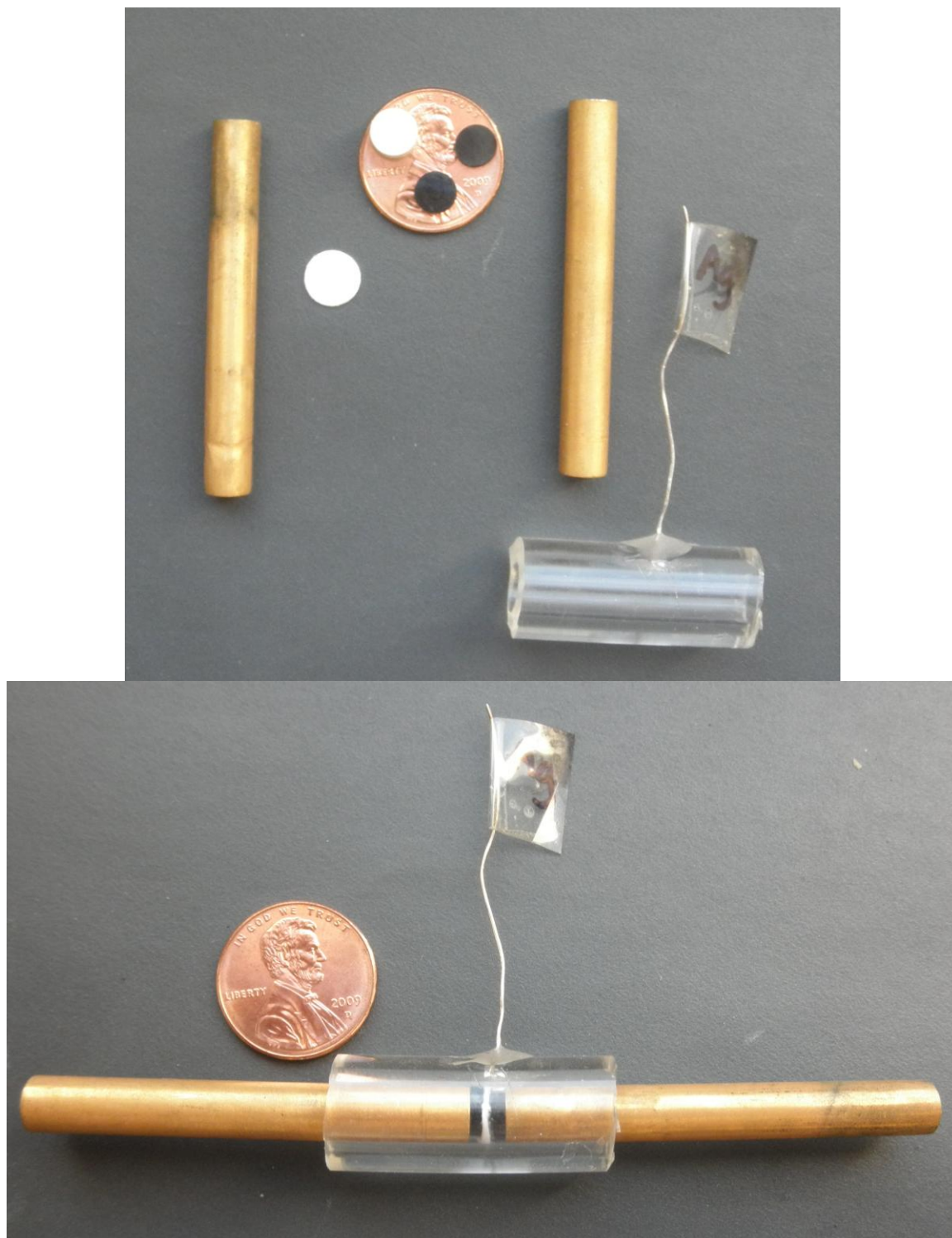


Figure 1.2. Photographs of the individual components of the supercapacitor device cell (top) and an image of the assembled cell (bottom).

characterized using cyclic voltammetry, chronoamperometry, chronocoulometry, and chronopotentiometry employing a CHI 760C potentiostat (Austin, TX). Electrode masses used to calculate specific capacitance for these electrodes were measured by washing the monoliths with water, or acetonitrile (three times over two hours each) to remove solvent and electrolyte, followed by drying at approximately 50 °C.

Calculation of Specific Capacitance: Many of the electrochemical measurements were made in two-electrode cells in which both electrodes were carbon monoliths. The masses of these electrodes were always similar but not the same, as were the single-electrode double layer capacitances. In order to determine the specific capacitance of the material itself I accounted for the differences in electrode mass as follows. In a two-electrode EDLC, each electrode functions as a capacitor and so, in the simplest approximation, the equivalent circuit is composed of two capacitors in series. The well-known reciprocal relationship shown in equation (1.1) can be used to relate the measured capacitance (C_{meas}) to the individual capacitances of this series (C_1 and C_2). Using the definition of specific capacitance shown in equation (1.3)

$$C_s = \frac{C}{m} \quad (1.3)$$

where C is the capacitance of the individual electrode, C_s is its specific capacitance, and m is its mass, one can rewrite equation (1.1) in terms of the specific capacitances and the electrode masses as shown in equation (1.4),

$$\frac{1}{C_{meas}} = \frac{1}{C_{s1}m_1} + \frac{1}{C_{s2}m_2} \quad (1.4)$$

where C_{s1} and C_{s2} are the specific capacitance of electrode 1 and electrode 2, respectively. The monoliths were prepared from the same starting material, under the same conditions,

and generally in the same batch process, therefore it is reasonable to assume that the specific capacitances of the electrodes were the same, i.e., C_s

$$C_{s1} = C_{s2} = C_s \quad (1.5)$$

Substituting the definition found in equation (1.5) into equation (1.4) gives a simple relationship, equation (1.6), which relates the measured capacitances in two-electrode devices to the specific capacitance of material used to fabricate it.

$$C_s = C_{meas} \left(\frac{m_1 + m_2}{m_1 m_2} \right) \quad (1.6)$$

Results and Discussion

Scanning Electron Microscopy: The scanning electron micrographs (SEM) shown in Figure 1.3 provide an intermediate perspective between the photograph in Figure 1.1 and the transmission electron microscopy (TEM) shown in Figure 1.4. The top image in Figure 1.3 shows a representative portion of the monolith after pyrolysis but before extraction of the HA. Note that under these pyrolysis conditions the macro-scale and meso-scale structures of the original cortical bone are largely preserved. This view of a polished transverse cross section plainly displays osteon bundles centered on Haversian canals that are approximately 30 μm in diameter. Closer examination also reveals an abundance of smaller lacuna, where osteocytes were previously located, between the lamellae.

Imaging following the removal of the HA and after supercritical CO_2 drying reveals the sheeted structure of the carbon in the monoliths. The fractured sample shown in the bottom image of Figure 1.3 is representative of all samples examined. Higher magnification using SEM did not provide additional information about the structure of

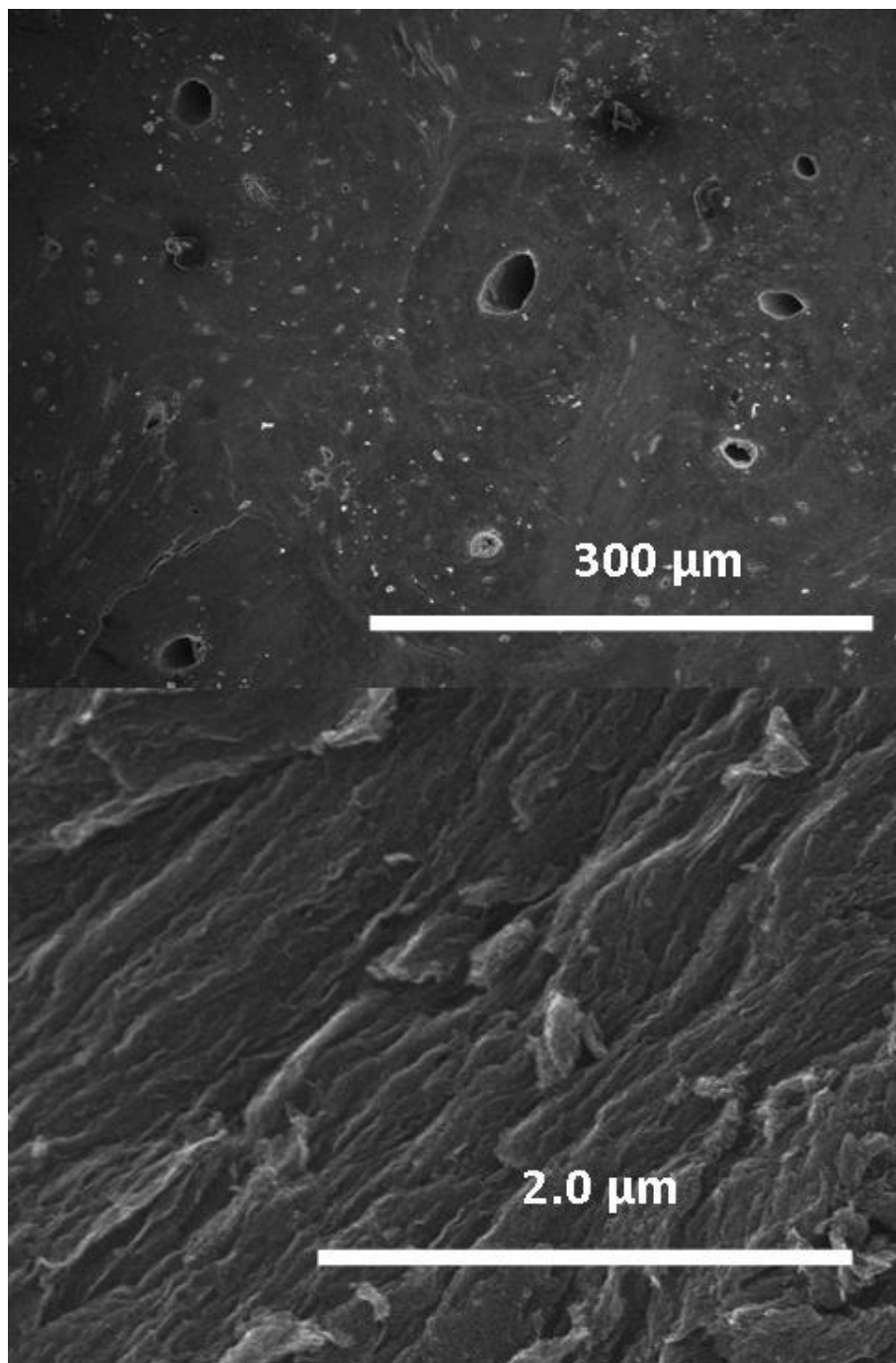


Figure 1.3. SEM micrographs of a pyrolyzed disk cut from a bovine femur displaying a polished surface which still displays the macroscopic structure of the hydroxyapatite scaffold (top) and the remaining carbon after the hydroxyapatite has been removed showing the loosely packed sheet-like structure of the carbon (bottom).

the sheets. It is clear that the sheets are not densely stacked, but the thickness of an individual sheet is too small to be determined by SEM. The natural conductivity of the monoliths was sufficient to eliminate the need for application of a conductive coating on the samples shown in Figure 1.3; therefore, some small artifactual charging effects may exist.

Figure 1.4 provides much more information about the structure of the carbon in the monoliths. It appears, based on these images, that the carbon is largely composed of dispersed, graphitic sheets and that individual sheets are accessible to the solvent and electrolyte. The TEM images of the carbon in the monoliths appear to be intermediate between that of graphene and the amorphous carbon allotropes examined by Czigány and Hultman [29]. Additional evidence for this similarity is seen in the selected area electron diffraction (SAED) patterns shown in Figure 1.5. The low intensity of the peaks in the pattern indicates that the ordering of the atoms in the monolith is relatively short range. Despite the ordering being only short range, the peak in the SAED intensity profile at 1.2 Å is associated with the C-C bond in graphene, and the peak at 2.3 Å suggests that there is only slight curvature of the carbon sheets in the material [29].

Structural Analysis by Raman Spectroscopy: Raman spectroscopy is a straightforward and information-rich means of characterizing the carbon in the monoliths and comparing it to other forms of carbon. Figure 1.6 shows a comparison of the Raman spectra of graphite, glassy carbon, activated carbon, and a representative sample of the carbon monoliths prepared for this study. It is apparent that the spectra of the monolith and that of the Darco KB-G activated carbon are quite similar.

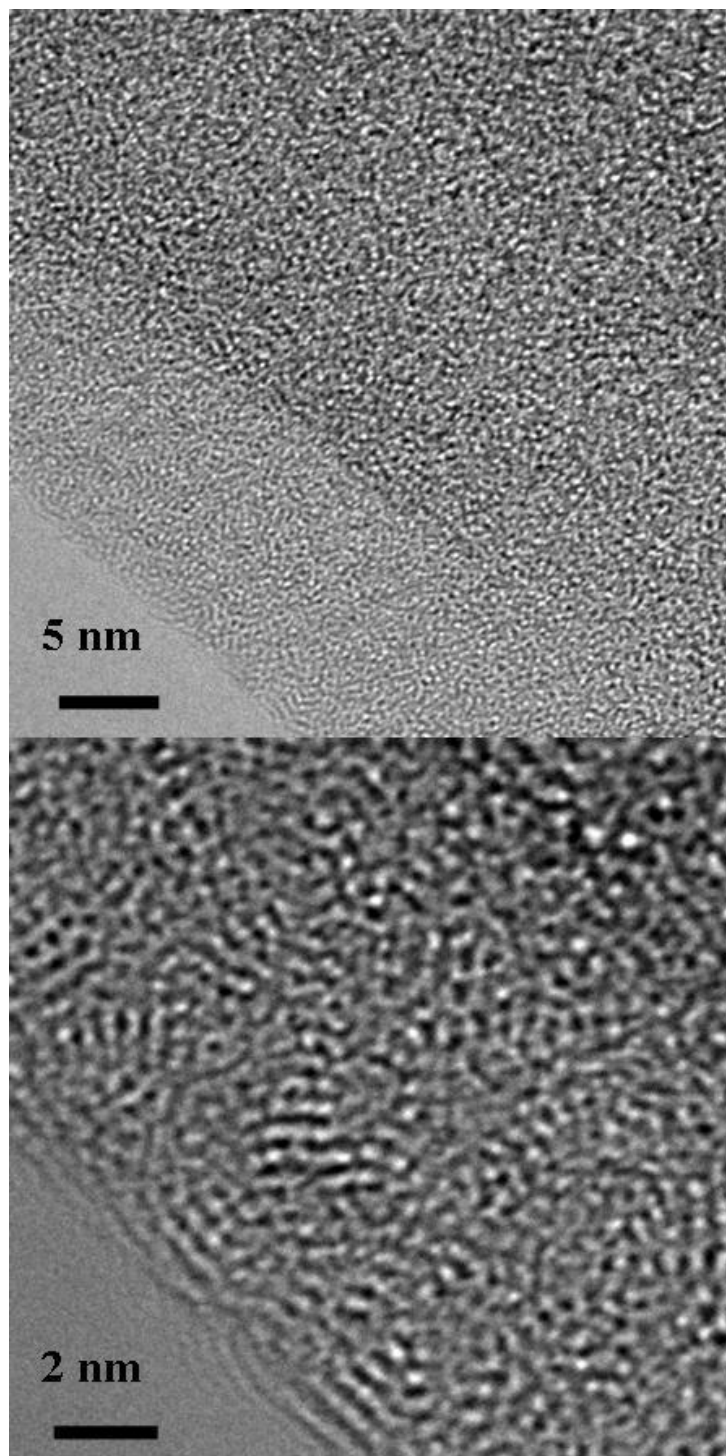


Figure 1.4. TEM micrograph displaying the layered structure of the carbon contained within the monoliths at two different magnification levels.

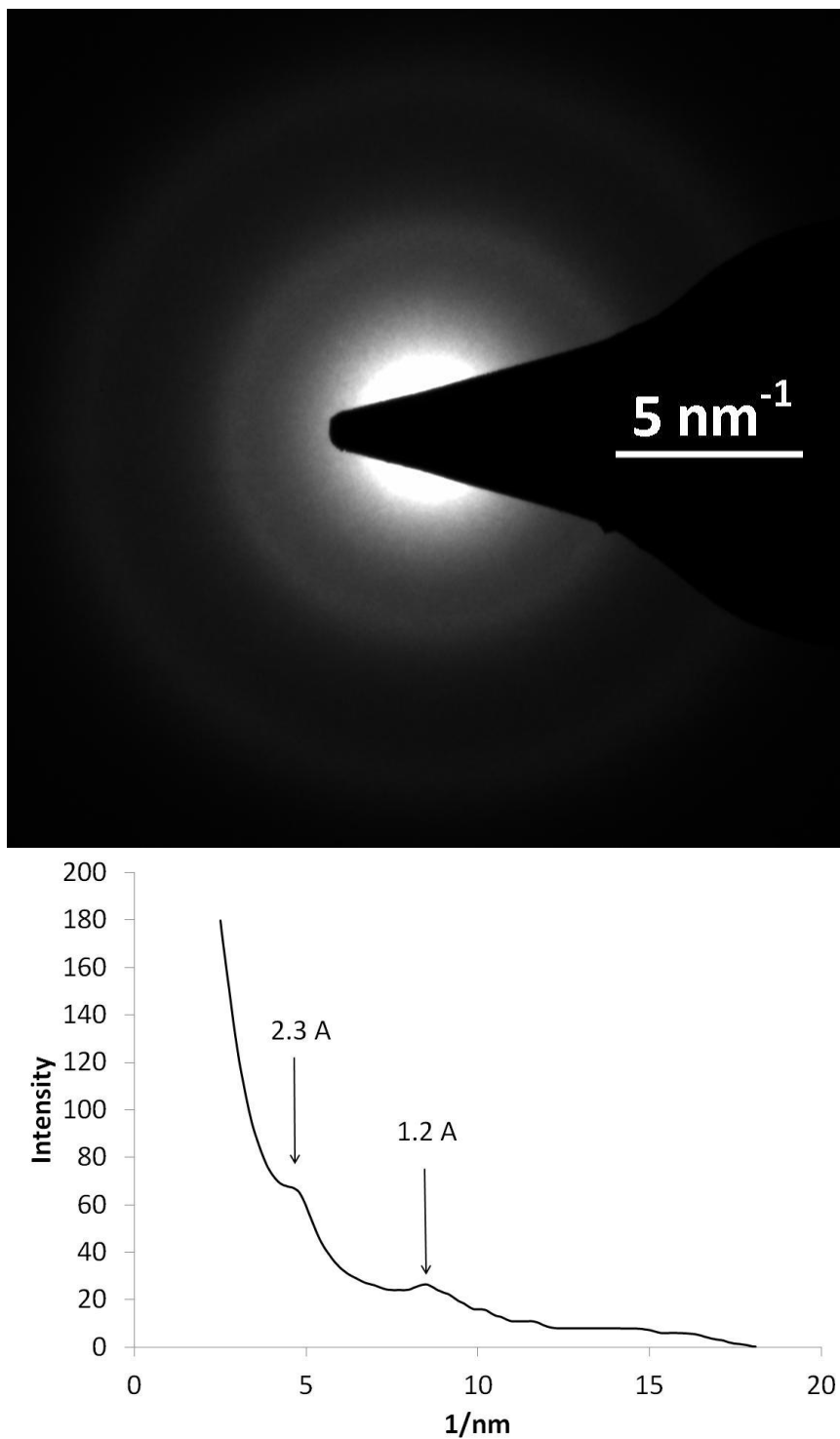


Figure 1.5. The selected area electron diffraction pattern for the carbon monolith material (top) accompanied by the associated intensity profile (bottom).

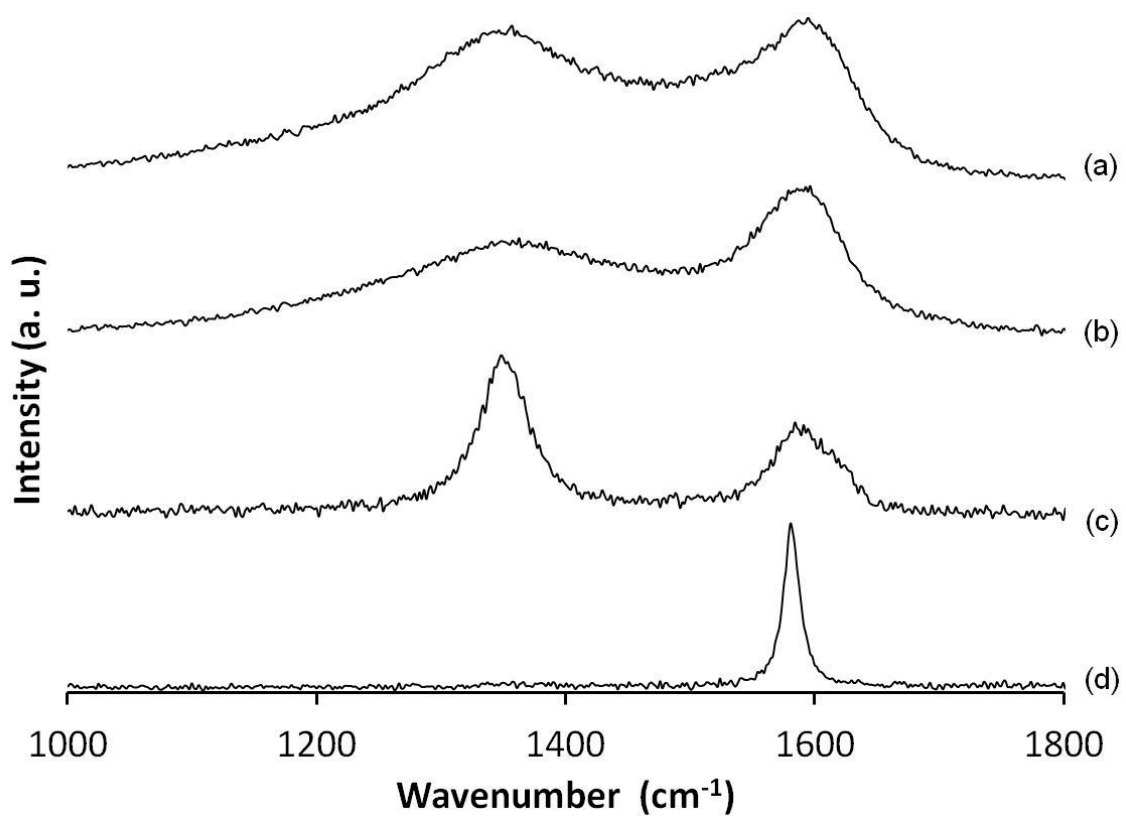


Figure 1.6. The Raman spectra for various types of carbon: (a) carbon derived from bovine bone described here, (b) commercial activated carbon, (c) glassy carbon, and (d) graphite.

To further analyze and compare the structure of the monoliths, as revealed through Raman spectroscopy, I applied a fitting technique to the Raman spectra that has become common for materials like these, as described in the experimental section. Figure 1.7 shows that fitting the Raman spectrum using the five Lorentzian peaks suggested by Sadezky et al. provides a close fit to the experimental data [28]. The fitted spectrum for carbon monoliths agrees with the qualitative assessment that the monoliths are similar to amorphous activated carbon. More detailed analysis of the fitting reveals that the D1 and D3 bands exhibit a proportionately larger contribution to the overall spectrum of the monolith than in other activated carbons [28]. An increase in the D1 band, which is assigned to the graphene-like edges in the disordered graphitic lattice, is desired since it would logically result in a high surface area material with high electrical conductivity. Upon comparison to activated carbon, the increase in the D3 band, which is assigned to organic fragments and surface functional groups, could pose a problem. The presence of these “contaminants” might be undesirable for EDLC applications if they proved to be electrochemically active. However, the electrochemical performance of the monoliths indicates that this is not the case.

Electrochemical Characterization: One might anticipate that electrochemical measurements would reveal high specific capacitances since TEM and Raman spectroscopy lead to the conclusion that the carbon monoliths appear to be composed of networks of graphene-like carbon in which the individual sheets are likely accessible to solvent and electrolyte,. Characterization of the material as electrodes in EDLC devices demonstrates that this is the case. Cyclic voltammograms of the bone-derived carbon monoliths in aqueous 2 M KNO_3 and EMIBTI in a two-electrode configuration are

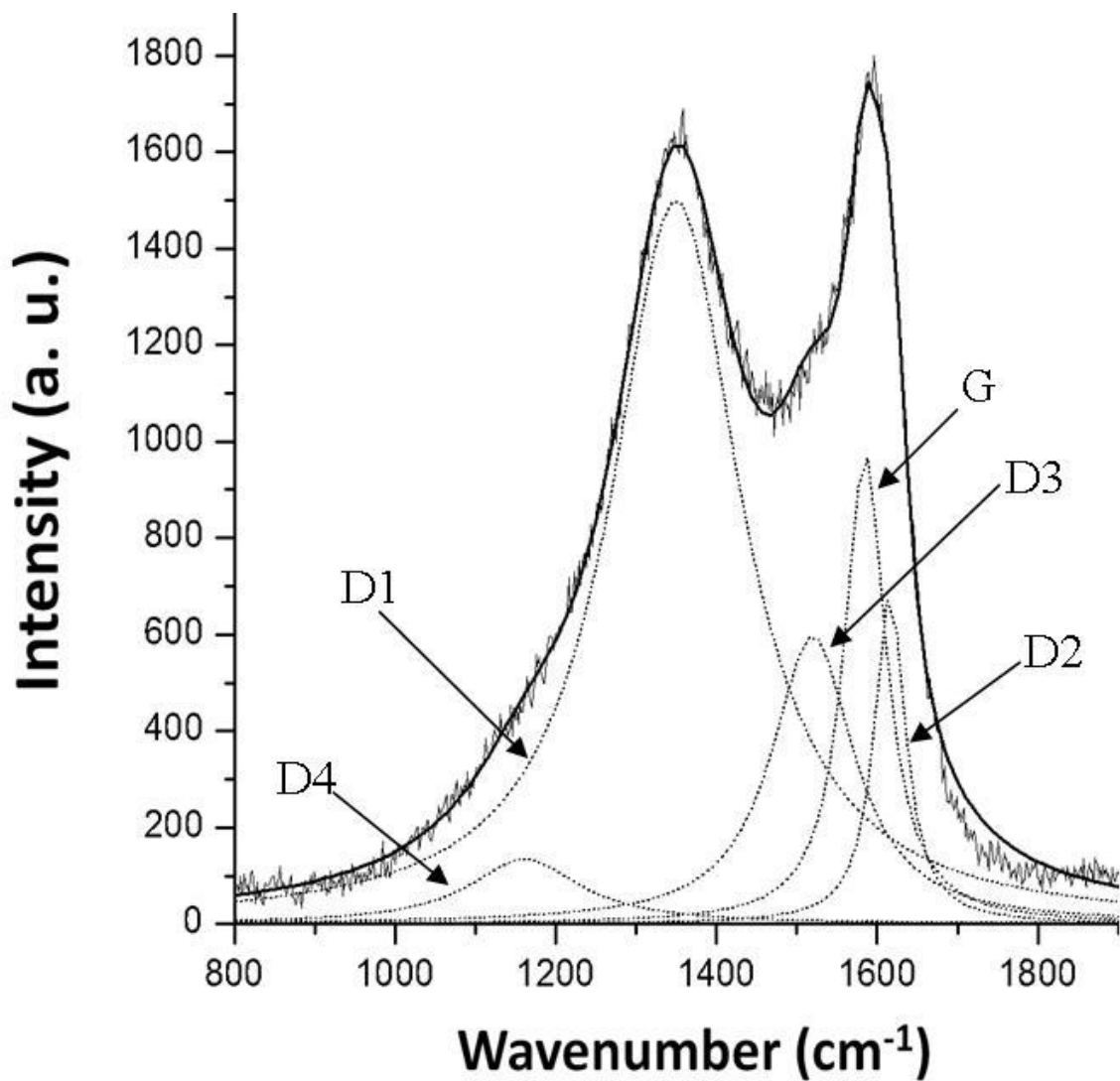


Figure 1.7. The results of the fitting of the Raman spectra of the carbon monolith material using five Lorentzian peaks, illustrating that the monolith is similar to other amorphous carbons with the exception that the D1 and D3 bands contributions are proportionally higher than in other amorphous carbon examples.

shown in Figure 1.8 (top and bottom, respectively). These voltammograms display a box-like shape that is characteristic of a series resistance-capacitor (RC) circuit. The fact that no obvious features are present in the voltammograms indicates that effectively no Faradaic processes are taking place within the potential range. The linear plots that result when the charging current for cyclic voltammograms is plotted versus the scan rate, as shown in Figure 1.9, reinforce this conclusion [6].

The chronocoulometric response to a potential step of representative samples of the carbon monolith materials in aqueous and EMIBTI systems are shown in Figure 1.10 top and bottom, respectively. The plateau-like shape of the charge response again reveals the capacitive nature of the system. The observation that the charge returns to effectively zero upon application of the reverse potential step ($\Delta V = 0$) indicates that the monoliths have a very high coulombic efficiency in this EDLC configuration. The specific capacitances of the carbon monoliths prepared under these conditions are 134 ± 11 F/g and 108 ± 9 F/g in aqueous KNO_3 and EMIBTI, respectively, at 95% confidence. The specific capacitance values of other recently reported monoliths such as those by Taer, et al. (138 F/g); Li, Xianyou, et al. (110 F/g); and Li, Pröbstle, and Fricke, are similar to those observed for the monoliths prepared in this work [30-32]. The low density of this material leads to a low volumetric capacitance of only 7 F/cm^3 , which is approximately 25% of the value reported recently for thick films of the carbide-derived carbon described recently by Chmiola, et al. [33]. The values of specific capacitance listed above are independent of the electrochemical experiment used to determine the capacitance: cyclic voltammetry, chronocoulometry, chronoamperometry, or galvanostatic charging.

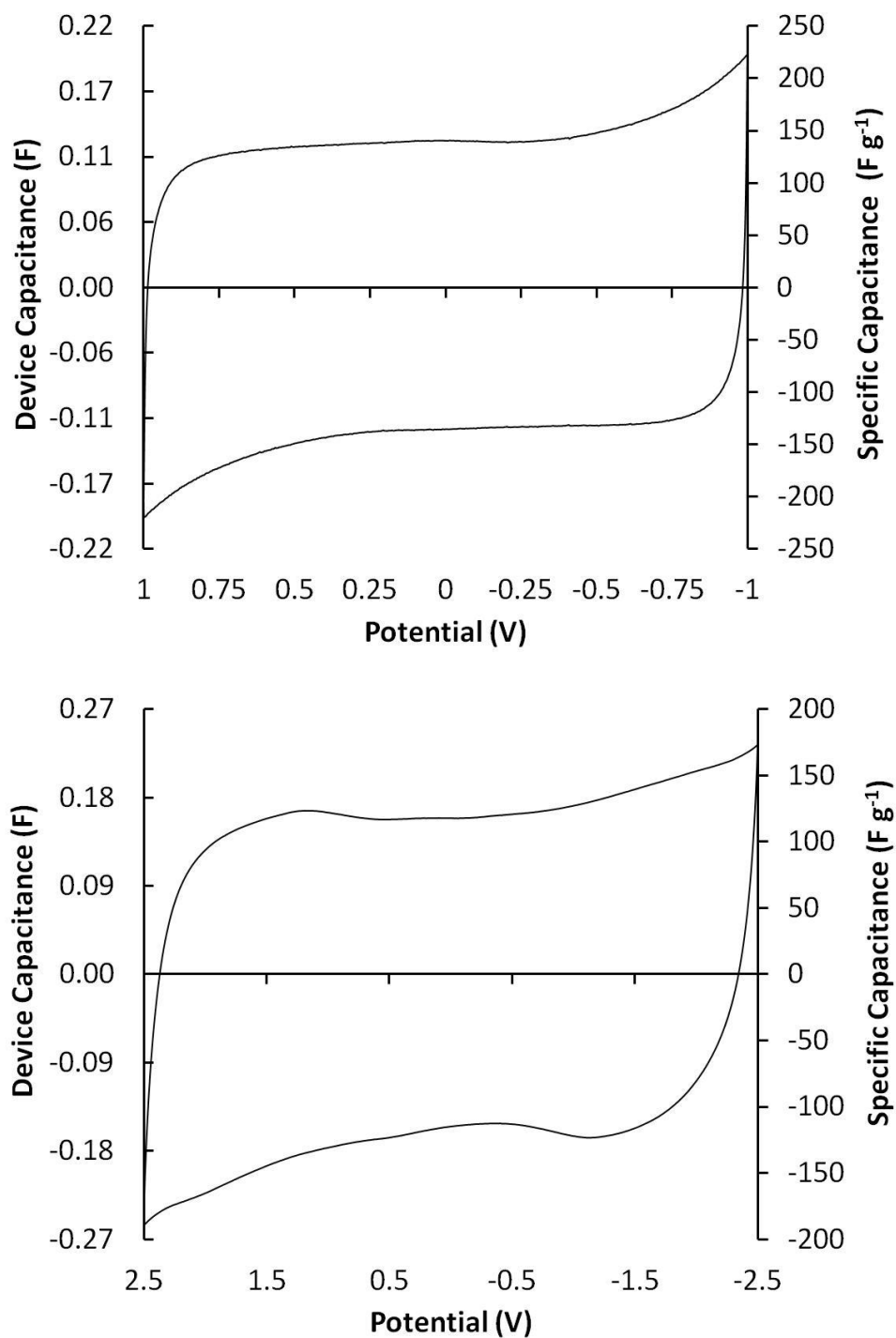


Figure 1.8. Typical examples of the cyclic voltammograms of two-electrode devices in aqueous KNO_3 solution (top) and EMIBTI (bottom) at 10 mV/s and 5 mV/s scan rates, respectively, displaying the characteristic box like shape of an RC circuit.

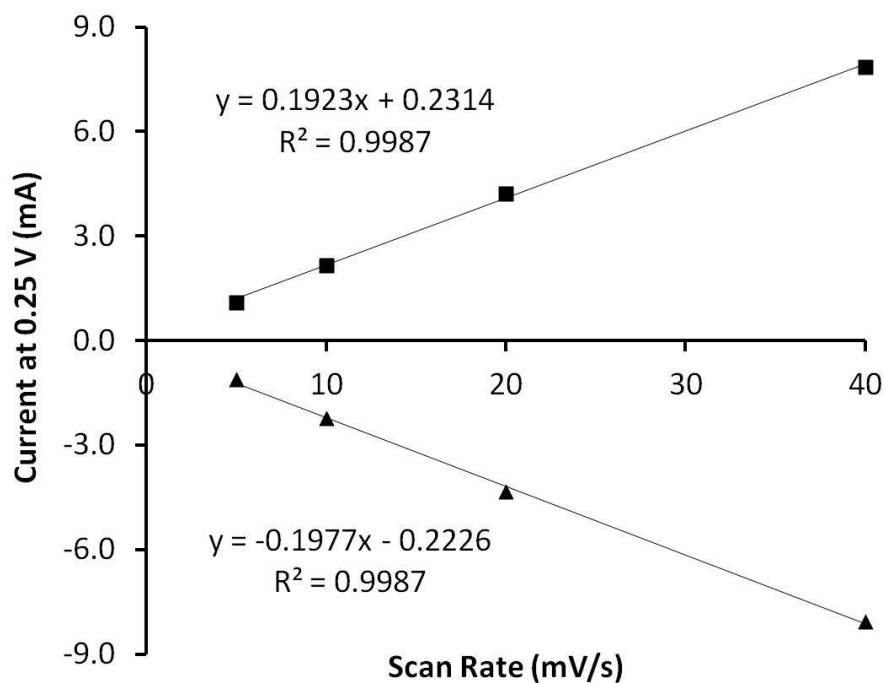
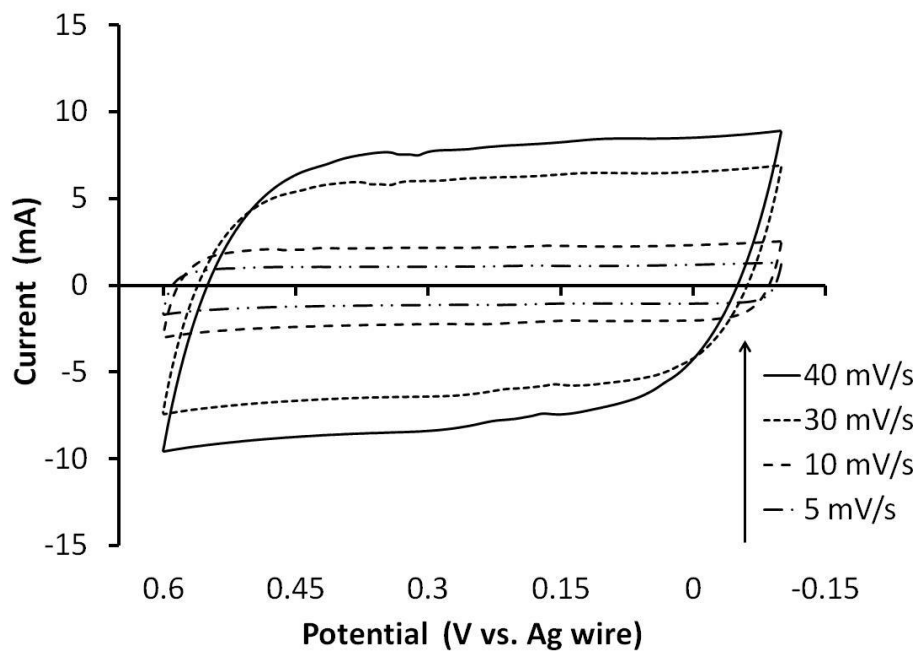


Figure 1.9. The voltammograms of a 3-electrode cell in 2 M aqueous KNO₃ electrolyte at various scan rates (top). The magnitude of the charging current varies linearly with the scan rate (bottom).

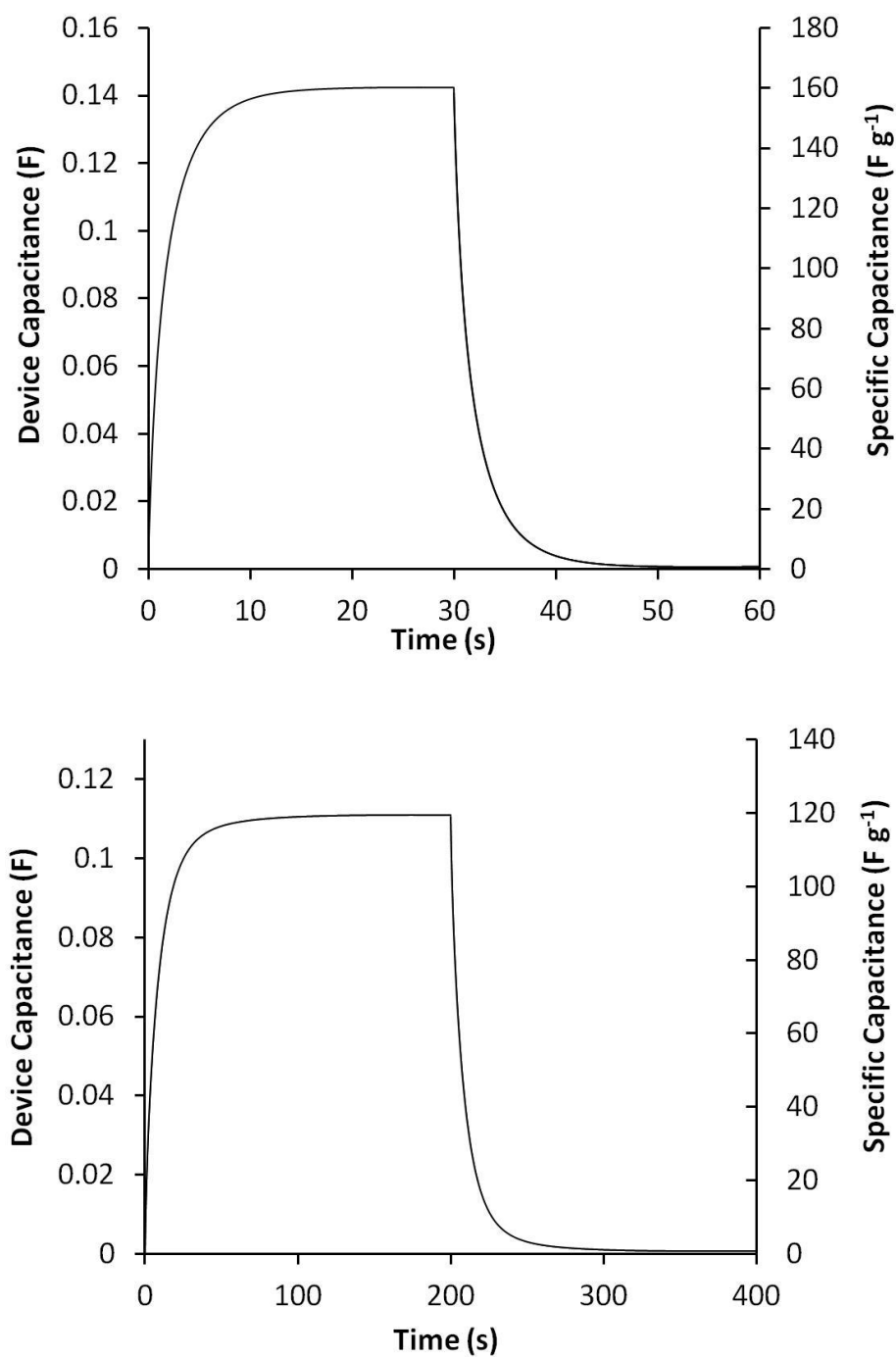


Figure 1.10. The chronocoulometric response of prototype EDLC devices composed of bone derived carbon monoliths in aqueous KNO_3 (top) and EMIBTI (bottom) to a 100 mV or 1 V potential step, respectively. The plateau-like shape demonstrates the capacitive nature of the system. The charge depletion in response to the returns step demonstrates the high coulombic efficiency of these devices.

The procedure for calculating specific capacitance from the cyclic voltammetry data is straightforward. By taking the derivative of the relationship $Q = CV$ with respect to time, where Q is charge, C is capacitance, and V is voltage, and assuming C is constant, one is left with the result:

$$\frac{dQ}{dt} = C \frac{dV}{dt} \quad (1.7)$$

Recognizing that $dQ/dt = i$ (current) and that $dV/dt = v$ (scan rate) one can see that dividing the constant charging current by the scan rate gives capacitance. For this work, the charging current was taken as the average value over the middle 50% of the potential window scanned. This averaging eliminated any errors associated with the current near the switching potentials, which is influenced by the RC time constant of the system.

Chronocoulometric data actually came from the integrated chronoamperometric response recorded by the potentiostat. The difference between a true chronocoulometry experiment and a chronoamperometry experiment is that in true chronocoulometry the charge passed in the system is measured by capacitors within the electronics of the potentiostat. For all of my measurements the current response was recorded and the signal was numerically integrated to get the charge response. By plotting the charge vs. time resulting from the applied potential step, one can obtain the total charge directly from the plateau, as demonstrated in Figure 1.10.

Calculation of the capacitance from the galvanostatic charge/discharge data was done following the technical note published by Maxwell Technologies [34]. Figure 1.11 shows an example of the galvanostatic charge/discharge response of a typical capacitor device in both aqueous (top) and ionic liquid (bottom) systems. The largely triangular shape of the response is again indicative of the capacitive nature of the system.

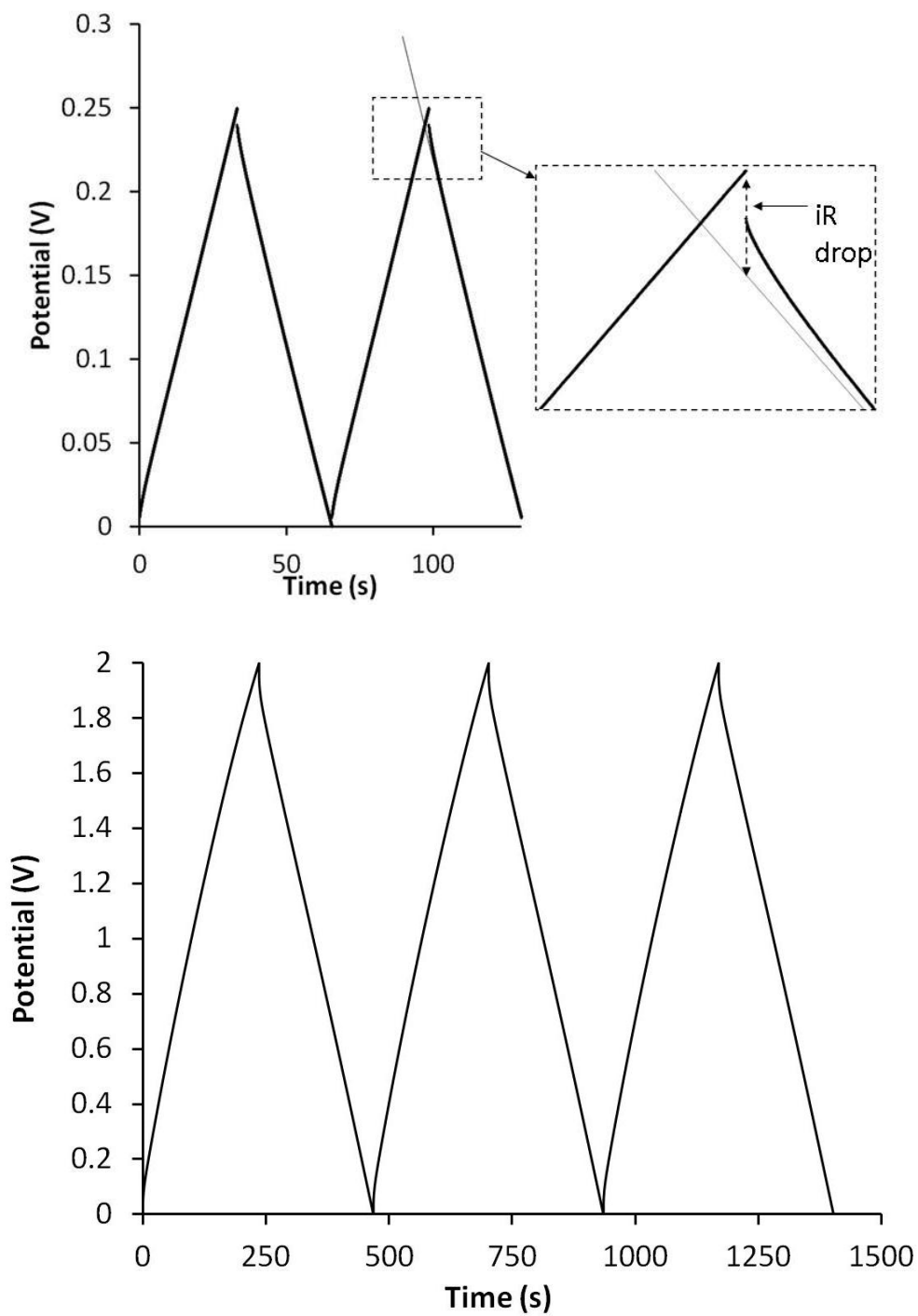


Figure 1.11. Galvanostatic charge/discharge response of two-electrode devices in aqueous KNO_3 (top left) and EMIBTI (bottom) in response to 1 mA of applied current. A close up of the peak potential (top right) demonstrates how IR is calculated from the discharge data.

Curvature is indicative of a Faradaic process or a potential dependant capacitance. At low electrolyte concentrations the capacitance of the double layer does show a potential dependence, but for the experiments reported here the electrolyte concentration is high enough that one would not expect to observe this behavior; therefore, curvature would strongly suggest the presence of Faradaically active contaminants [35]. For the devices used in my work the capacitance was calculated by finding a linear best fit of the response for the latter 75% of the discharge cycles. The slope of this line corresponds to dV/dt in Equation (1.7). Dividing the applied current by this number results in the value of C for the system.

The slight vertical drop in the voltage, observed upon commencement of the discharging process, corresponds to the potential drop caused by the resistance of the cell (iR). Therefore, one can calculate the equivalent series resistance of the system by dividing the potential drop at the onset of the discharge step by the applied current. The value for iR in my work was taken as the difference between the maximum potential and the potential calculated from the best fit equation employed above for the determination of the capacitance, as demonstrated by the inset in Figure 1.11. Burke and Miller reported that using this extrapolation method eliminates the underestimation of the resistance, which can happen when the potential drop is taken as the first point measured after switching from charging to discharging, as is commonly done in the literature [36]. The slight curvature between this initial drop and the eventual linear region is due to the time dependent resistance observed for porous electrodes. The time dependence disappears, and the response becomes linear, once the current is evenly distributed

throughout the electrode. Farahmandi, and the team of Srinivasan and Weidner independently reported mathematical models to describe this time dependence [37, 38].

The chronoamperometric response to a potential step offered another method to determine the resistance of the prototype devices used in this work. A simple series RC circuit, as described by the well-known equation (1.8), was used to model the current response.

$$i = \frac{E}{R} e^{-t/RC} \quad (1.8)$$

More specifically, the resistance was determined by applying a double potential step to a two-electrode device with monoliths serving as both electrodes. Taking the natural logarithm of equation (1.8) yields a linear transform in which the slope of a plot of $\ln(i)$ vs. $-t$ is $1/RC$. In practice, the plots of the actual current response data proved to be slightly non-linear and concave upward, indicating that the effective RC time constant was increasing slightly with time, as demonstrated in Figure 1.12. It was not surprising that the simple series RC model did not fit the data at short times. It has been reported in multiple sources that porous carbon based supercapacitors are well described by a transmission line equivalent circuit model which contains a distribution of resistive and capacitive elements. The original treatment of a porous electrode by this description was reported by de Levie [39]. Later, Pell and Conway demonstrated that the principles found in de Levie's treatment could be applied to supercapacitor electrodes [40]. More recently, as mentioned above, other mathematical treatments have led to similar conclusions [37, 38]. The observed time dependant behavior is due to functional groups on the edges of the carbon sheets, and to regions within the material that are not equally accessible to solvent. Still, the simple RC model proved to be consistent with the other

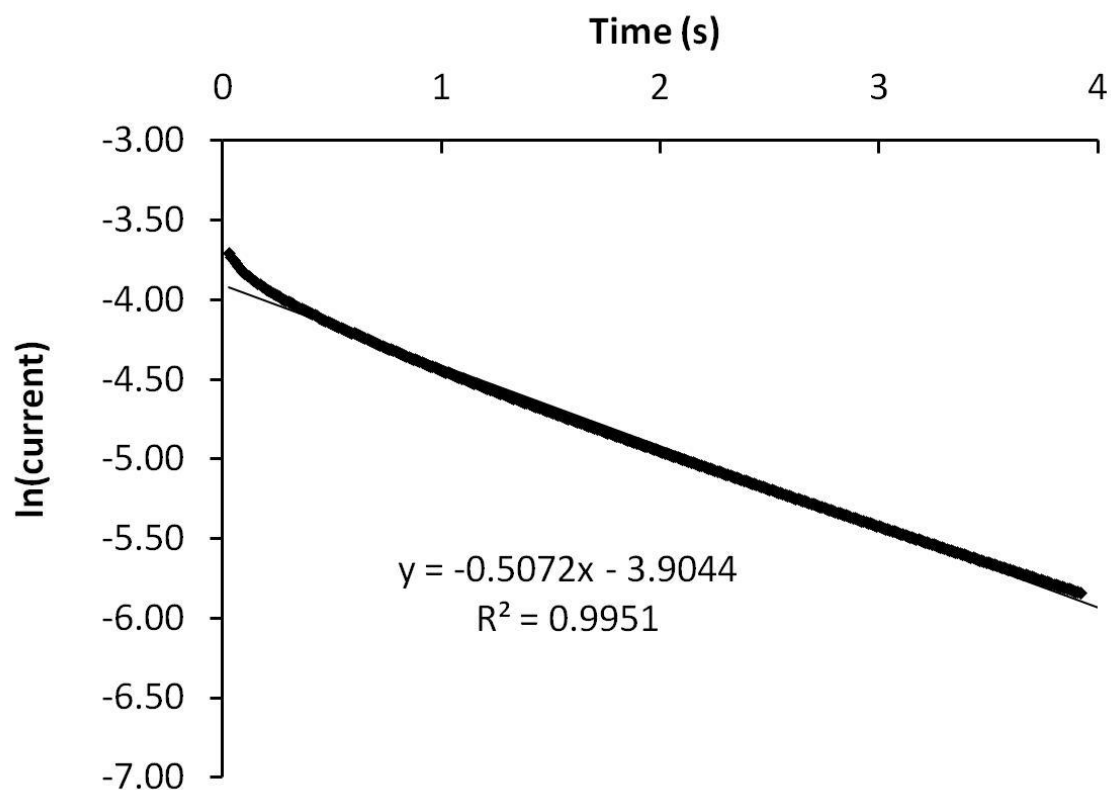


Figure 1.12. Representative plot of the chronoamperometric data for aqueous systems following a linear transform of equation (1.8). Currents plotted are between 90% and 10% of the peak value. The nominally linear response with a slight concave upward curvature indicates that the actual RC constant of the system is increasing slightly over time.

electrochemical characterizations when the currents used in the plots were between 90% and 10% of the maximum values. Applying the simple RC model results in the estimated resistances of the two-electrode devices to be $5 \pm 2 \Omega$ in aqueous KNO_3 solution and $35 \pm 2 \Omega$ in EMIBTI. Similar values were found using the chronopotentiometry based method discussed above. When aqueous electrolytes are used, it is not clear what proportion of the nominal 5Ω resistance is due to the resistance of the monolith, and what proportions are due to contact resistance and to the resistance of the electrolyte. Measurements in three-electrode configurations suggest that most of the resistance in the aqueous system is due to contact resistance and to the monoliths. The high resistance for the ionic liquid system is clearly due to the higher specific resistance of EMIBTI.

The EMIBTI system was chosen for demonstrative purposes chiefly because ionic liquids are promising candidates for electrolytes in future EDLCs. The difference between the specific capacitance in water and in EMIBTI observed in this work is typical of carbon-based supercapacitors and is indicative of the larger ion size, as well as differences in double layer structure and accessible surface area in ionic-liquid-based systems [41-44]. Even with the generally lower specific capacitance observed in ionic liquid systems, these electrolytes offer the benefits of having large electrochemical windows, very low vapor pressures, and high thermal stability, making them strong candidates as components of high-energy supercapacitors capable of operating over a wide range of temperatures. It has been estimated that there are in excess of 10^6 simple ionic liquid salts. This means that if one considers binary combinations there are 10^{12} ionic liquid electrolyte systems, and that number jumps to 10^{18} possible combinations if

ternary systems are included. As such, the properties of these electrolyte systems could be tailored to fit the specific application for which a device was being prepared [45, 46].

A consistent “engineering” challenge with these devices was how to minimize the contact resistance without changing the results of the measurements. Multiple methods were attempted to solve this problem before settling on the sandwiched electrode devices employed for this work. Using silver filled epoxy to connect the electrodes to the end of metal rods for three electrode measurements ultimately failed because the oxidation of the silver in the epoxy interfered with the signal from the monolith itself. Carbon filled epoxy eliminated the issue of contact oxidation but, as with silver epoxy, the deformation of the carbon monoliths upon solvent evaporation in the absence of HA required that the HA/carbon composite material be attached to the electrode before the HA was removed. Once attached, the HA could be removed using EDTA solution, but the epoxy was not stable in acidic solutions. These inconveniences were minor. The more problematic issue with these three electrode systems was that it was not possible to directly measure the mass of the carbon after it was attached to the electrode via epoxy. An attempt to minimize the contact resistance in the sandwich cell by sputter coating or evaporating gold onto one surface of the electrode also proved useless. The gold coating disappeared upon removal of the HA. I ultimately decided that removing the HA and sandwiching the electrodes as described in the experimental section was an expedient way to fully characterize the utility of my devices as supercapacitors.

It has been argued that, when using a three-electrode cell, reversing the polarity of the working electrode by cycling the potential through the point of zero charge may cause the value calculated for the capacitance to be artificially high [47]. It is certainly true,

and has been demonstrated by Khomenko et al., that in symmetric pseudocapacitors based on conducting polymers a two electrode cell will demonstrate a lower capacitance than a three-electrode configuration due to the lower charge storage capability of the negative electrode in most conducting polymer systems [48]. The specific capacitances measured for my carbon monoliths proved to be the same in three-electrode and two-electrode cells. Most of the measurements reported herein were obtained in a two-electrode configuration, but there was no scientific reason to do so in this case. The two-electrode cell was used chiefly for its engineering merits. Constructing a device prototype (with a capacitance of approximately 0.1 F) was accomplished with relative ease.

A more sophisticated prototype device was constructed to demonstrate that scale-up is possible with these monoliths. For this demonstration I prepared a cell similar to those previously described. For this cell I used two gold plated copper pennies that had been sanded flat on one side as current collectors. These pennies were attached to the ends of two stainless steel rods with silver filled epoxy to provide an electrical contact. Seven 6 mm x 1.5 mm monoliths were placed on the one current collector in a hexagonal arrangement. A 19 mm circle of the glass microfiber prefilter separated these monoliths from seven more monoliths which acted as active material for the second electrode. The device was encased in 19 mm diameter Tygon tubing, which is nearly identical to the diameter of a penny. The electrolyte was 2 M aqueous KNO_3 . The CV and chronopotentiometric response for this device are shown in Figure 1.13. The capacitance of this device is 0.930 F. Previous devices composed of two monoliths exhibited capacitance values of between 0.1 and 0.15 F. This device, prepared with seven times the

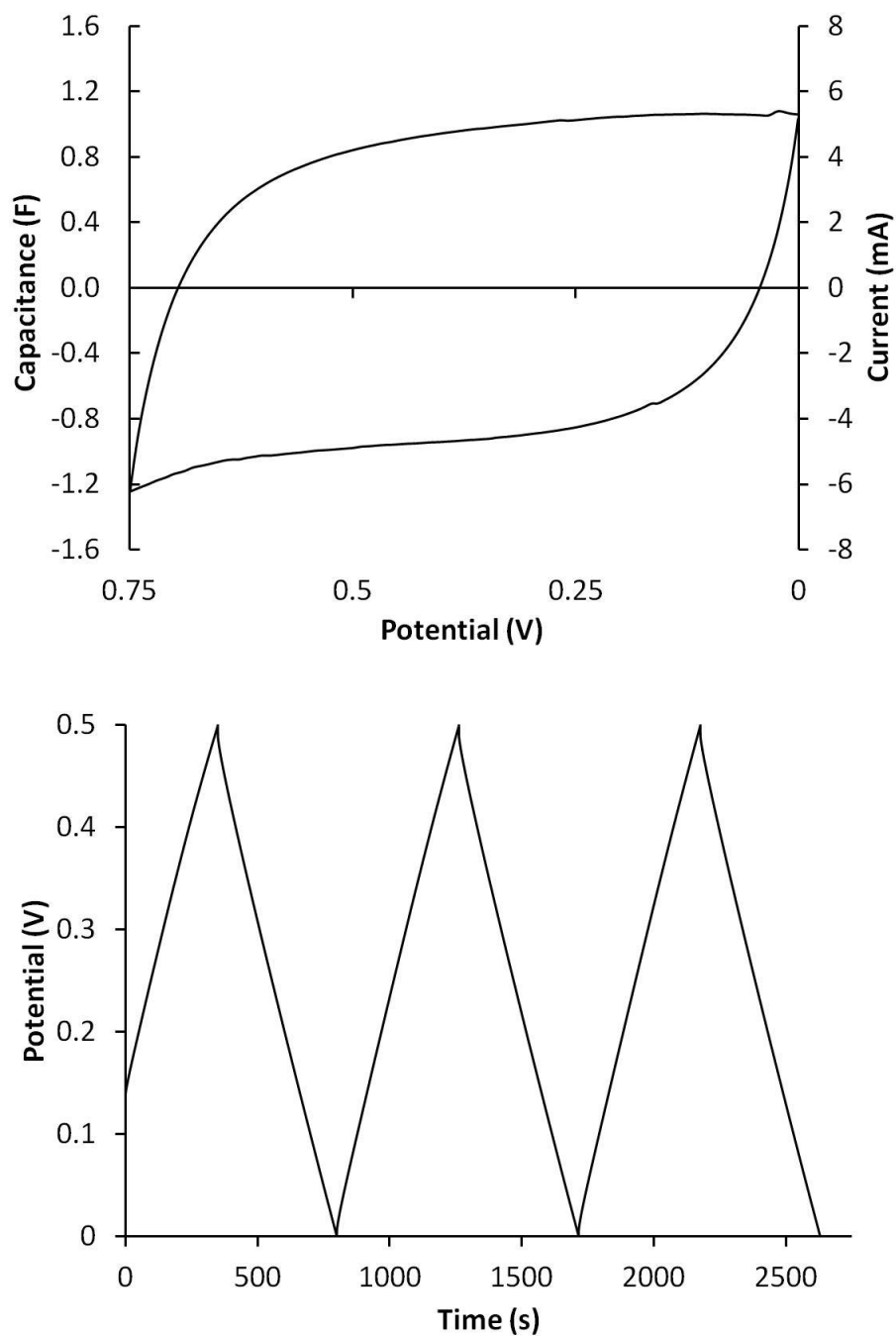


Figure 1.13. The cyclic voltammetric (top) and chronopotentiometric (bottom) responses of a larger scale EDLC device composed of 14 carbon monolith disks.

active material, proved to have a capacitance approximately seven times higher than the previous devices.

Another interesting observation based on the electrochemistry of these carbon monoliths is that the removal of the HA is not essential to achieve relatively high capacitance, as demonstrated in Figure 1.14. In this experiment a two-electrode device was assembled using the procedure discussed above, with the exception that the HA was not removed from the pyrolyzed composite material initially. Comparison of the CVs for this device before and after HA removal showed that even without extraction of the HA this device exhibited a capacitance of ca. 0.075 F. Upon removal of the HA, the capacitance increased to approximately 0.10 F. Such a result could prove to be beneficial for applications where mechanically strong, conductive, substrates with high surface area are desired but high capacitance per unit mass (due to high specific capacitance) is not critical.

Specific Surface Area and Its Relationship to Specific Capacitance: The carbon monoliths prepared for this work exhibit a specific surface area of $1383 \pm 25 \text{ m}^2/\text{g}$ (95% confidence) when measured by the BET method using nitrogen adsorption. Nitrogen adsorption/desorption isotherms, shown in Figure 1.15, of the monoliths produced in this work are a combination of the Type 1 and Type 4 classes, indicating the presence of both micro and mesopores [49]. The double-layer capacitance per unit of surface area is estimated to be approximately $10 \text{ }\mu\text{F}/\text{cm}^2$, since the measured specific capacitance in water is 134 F/g. This value is in good agreement, possibly fortuitously so, with the value of $10 \text{ }\mu\text{F}/\text{cm}^2$ estimated for basal plane graphite by Brown and Anson [50]. A noteworthy review of carbon electrodes provides some additional context for this value;

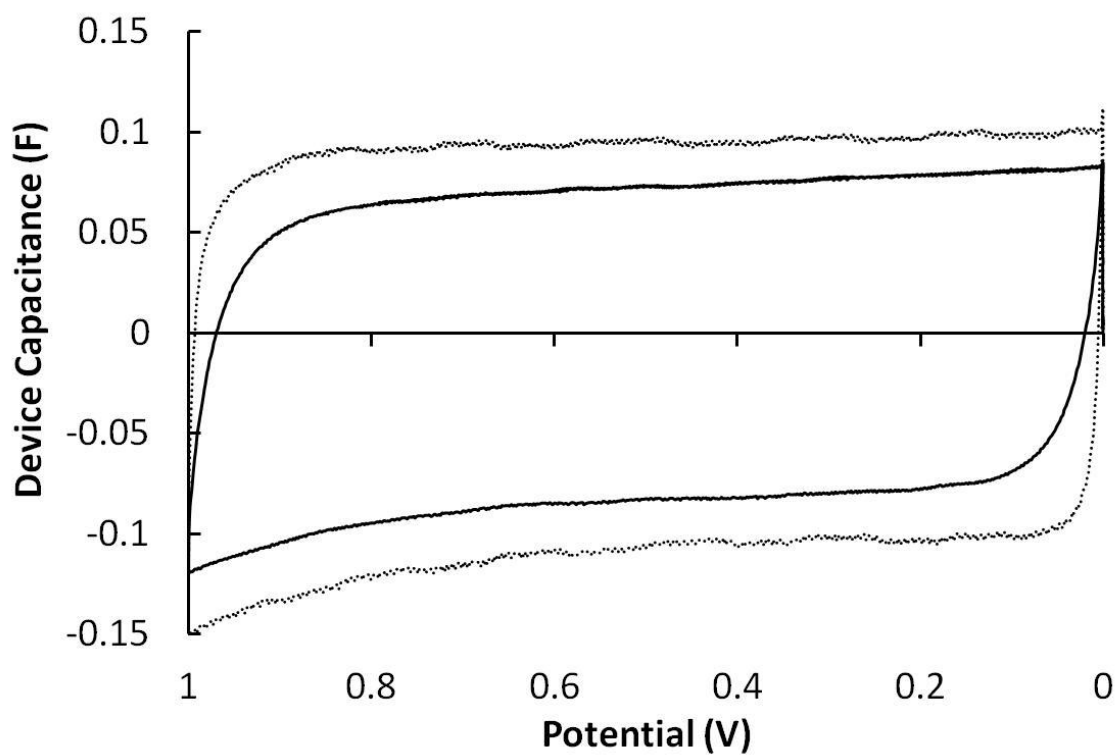


Figure 1.14. Cyclic voltammogram of a two-electrode device composed of disks of pyrolyzed bovine bone before HA removal (solid line) and after HA removal (dotted line) indicating that a large portion of the surface area of the conductive carbon is accessible to solvent and electrolyte before the HA is removed.

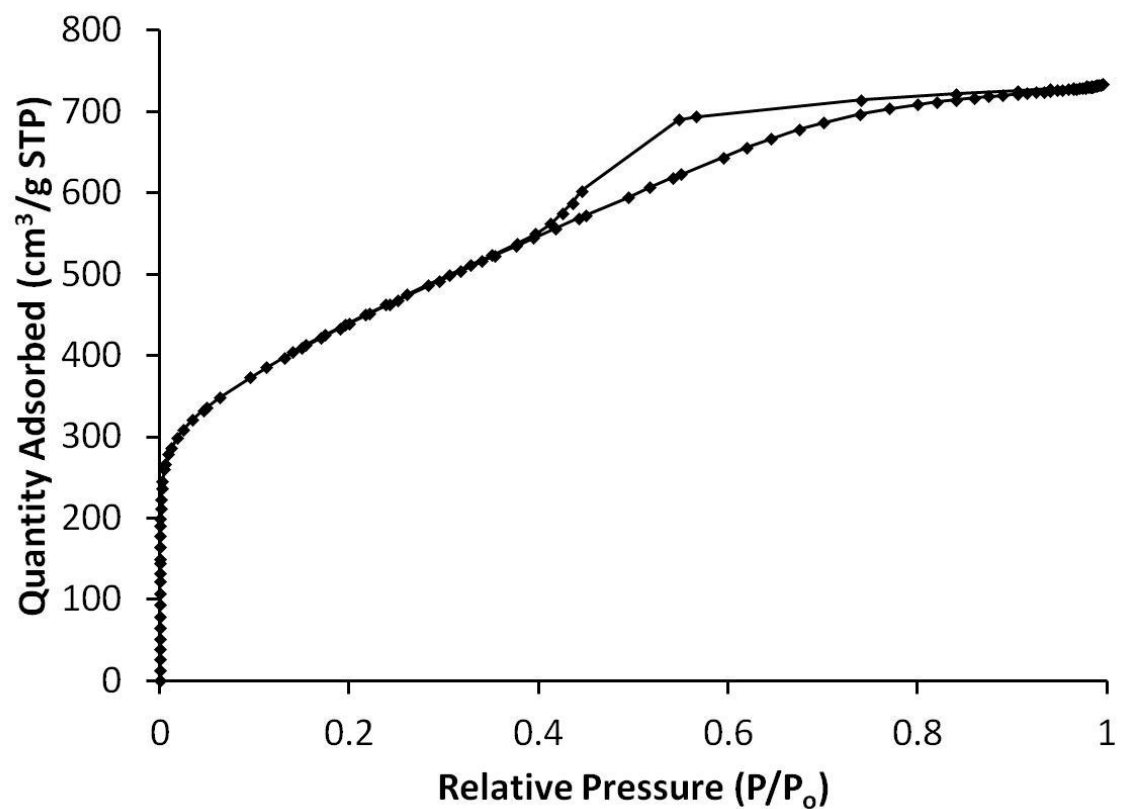


Figure 1.15. The nitrogen adsorption/desorption isotherm for a representative sample of the carbon monolith materials indicating the presence of both micropores and mesopores.

the specific capacitance of carbon is known to vary over a broad range from $1 \mu\text{F}/\text{cm}^2$ for basal plane graphite to $>50 \mu\text{F}/\text{cm}^2$ for edge plane pyrolytic graphite [51]. The capacitance of approximately $10 \mu\text{F}/\text{cm}^2$ serves as a lower limit to the actual value for the monoliths. Although the BET method provides a rapid, relatively straightforward, and commonly employed means of finding the specific surface areas for new materials, there is a consensus in the recent literature indicating that the nitrogen-based BET approach overestimates the specific surface area for high surface area carbons containing micropores. The carbon monoliths prepared as described above, exhibit specific surface areas of $647 \pm 57 \text{ m}^2/\text{g}$ (95% confidence) when determined using the density functional theory method (DFT), as shown in Figure 1.16. This value is significantly smaller than that obtained using the BET treatment. The difference observed between the BET and DFT characterizations is consistent with observations made by several other groups who have characterized microporous carbon materials. In 1992, Kaneko and Ishii demonstrated that for $\text{N}_2(\text{g})$ adsorption at carbon with pore widths less than 2 nm, physisorption increases to enhance multilayer adsorption, which is ultimately limited by pore space [52]. Ohba and Kaneko later showed that the standard isotherm for planar graphitic systems is a poor model for adsorption at well-defined geometries of carbon nanotubes [53]. In an extensive characterization of 34 different carbon microbeads and fibers, Shi demonstrated that surface morphology plays an important role in determining specific capacitance and that the specific surface areas determined by BET are much higher than those made using the DFT method [54]. More recently, Stoeckli and Centeno carefully characterized 21 different carbons and found that the BET method is accurate only for carbons with average pore width of approximately 0.8 to 1.1 nm [55]. These

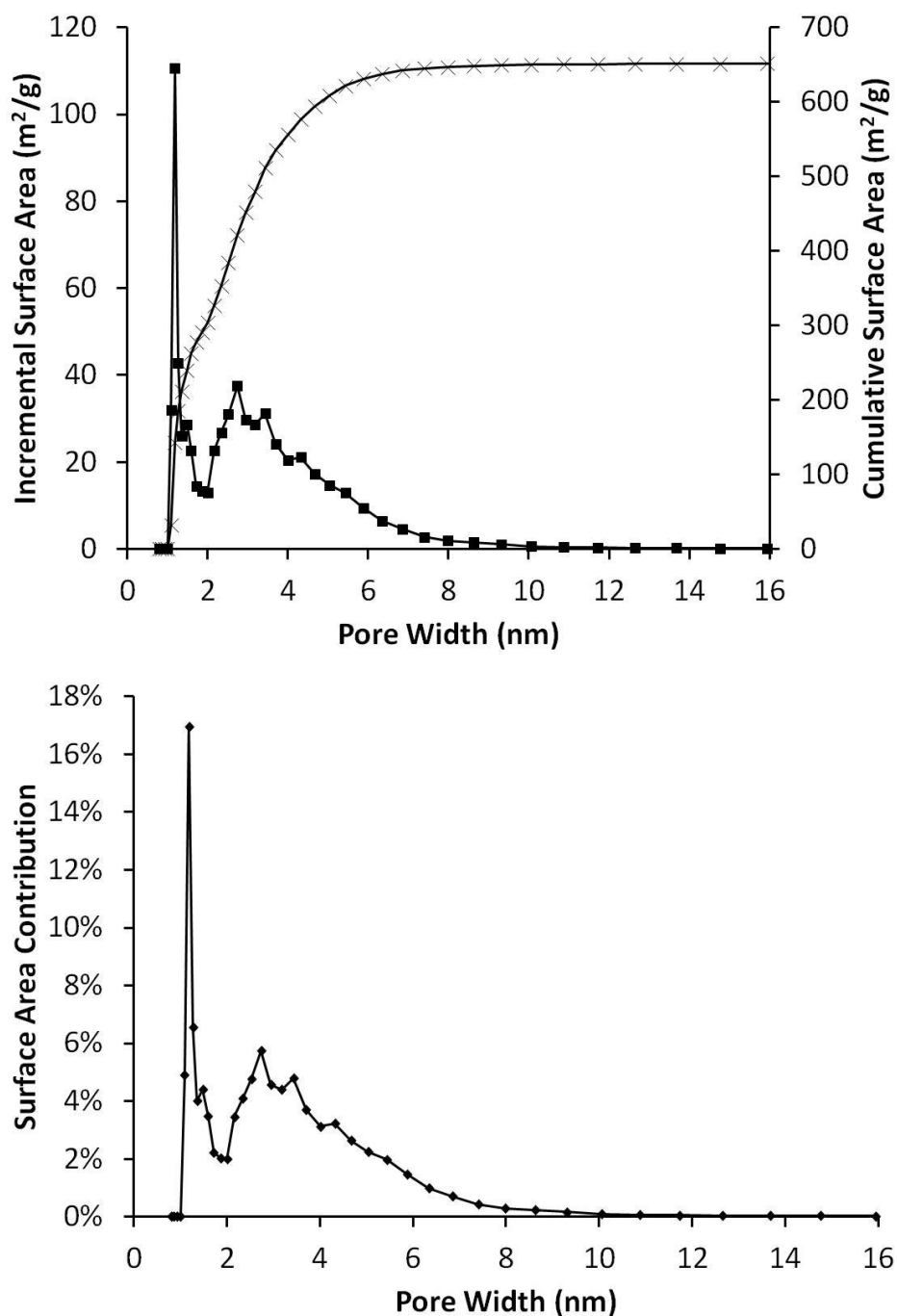


Figure 1.16. Pores size distribution (■) and total surface area (x) (top) and the percentage of total surface area contributed by the pores of a given width (bottom) as calculated via density functional theory using nitrogen adsorption data. These distributions support the conclusion that both micro and mesopores are present.

authors concluded that specific surface areas for microporous activated carbons should be determined using techniques more advanced than the simple BET method using $N_2(g)$ adsorption.

It is important also to note that the relationship between specific surface area and specific capacitance can be complicated for microporous materials. The cross sectional areas of $N_2(g)$ and solvated electrolyte ions are different. This difference, in turn, means that the surface area of the monolith accessible to the electrolyte is smaller than the surface area accessible to $N_2(g)$. Recognizing these differences in cross sectional areas, Largeot et al. examined the relationship between ion size and pore size as they relate to specific capacitance. They concluded that the ideal pore width is nearly identical to the diameter of the electrolyte ions [56]. Similar observations have been made by Barbieri et al., who also noted that while increases in specific surface area above $1200 \text{ m}^2/\text{g}$ (by DFT) have been demonstrated, they should be compensated by space limitations that prevent corresponding increases in specific capacitance [57]. They also concluded that a linear relationship between specific surface area and specific capacitance should no longer be observed when the screening length and the pore wall thickness approach the same length scale, and that specific capacitances greater than 80 F/g should be increasingly difficult to achieve by merely increasing the specific surface area.

Influence of Pyrolysis Conditions: A full characterization of these monolith materials was only carried out for the samples prepared as described in the experimental section, but some preliminary screening experiments were performed to determine if the preparation conditions led to differences in the capacitance and resistance of the resulting carbon monoliths. Three sets of samples were prepared to examine the influence of

preparation conditions. One group was heated to 800°C under vacuum. A second group was heated under the conditions listed in the experimental section, and a third was heated as listed in the experimental section but the maximum temperature was 1200°C rather than 1000°C. It should be noted that the oil used in the vacuum pump for these experiments contained a volatile contaminant, which caused the ultimate vacuum to be between 150 and 300 mTorr rather than the 20 mTorr that was generally observed. Therefore, the results discussed immediately below should only be compared to each other and not to the samples discussed elsewhere. All of the electrochemical measurements performed on these samples were done using a three-electrode cell in which the monolith material was attached to a titanium rod with conductive carbon filled epoxy. The HA was removed as before.

Table 1.1 summarizes the results of the comparison between different pyrolysis conditions. Specific capacitance values were not available, as the masses of the monoliths could not be measured due to the method by which the electrodes were fabricated. The bone was originally machined to the same dimensions in all cases and, therefore, some preliminary comparisons between the values can be made. It appears as though increasing the maximum temperature from 800°C to 1000°C leads to a decrease in both capacitance and resistance. Commercially available supercapacitors have equivalent series resistance values on the order of a few milliohms [58]. Despite the apparently higher capacitance for samples prepared at a maximum temperature of 800°C, samples prepared under these conditions were not pursued further because of their high resistance. The rate at which a capacitor will charge and discharge is inversely proportional to the resistance of the device. A high resistance will also result in a lower coulombic

Table 1.1. A comparison of the capacitive properties of carbon monoliths pyrolyzed using three different conditions. Errors are 95% confidence intervals. *1200°C contains only 2 samples and the capacitance was determined by CV only. Further experiments were not performed as the capacitance was 2 orders lower than previously seen, as discussed in the text.

Conditions	Average Capacitance (F)	Average Resistance (Ohms)
800°C	0.30 ± 0.05	34 ± 17
1000°C	0.218 ± 0.006	9.1 ± 1.4
1200°C*	0.00243	-

efficiency for a capacitor because some energy input during charging is lost upon conversion to heat; therefore minimizing the resistance is of practical importance.

It is interesting that the samples heated to 1200°C show very low capacitance when compared to those prepared under other conditions. I also observed that after 5 days of etching in EDTA solution followed by electrochemical characterizations, the electrodes were mechanically robust. This is in contrast to the normal monolith materials which are easily crushed between one's fingers. One plausible explanation for this observation can be found in the literature. In 2000, Muralithran and Ramesh described the influence of sintering temperature on the chemical and physical properties of HA. They showed that sintering temperatures of 1200°C and above caused the density of pellets pressed from HA powder to increase to a value nearly identical to that of pure HA [59]. It is likely that the HA in the carbon/HA composites I prepared changed morphology during the pyrolysis process. The increased density of the HA may have slowed the EDTA leaching process which, in turn, decreased the accessible surface area of the carbon and led to the lower observed capacitance. It is also possible that the changing morphology of the HA influenced the morphology of the carbon phase. Changes to the carbon could also result in lower observed capacitance. I did not pursue the monoliths prepared at higher temperatures because I was interested in materials with high capacitance. Further experimentation would be necessary to definitively determine the source of the lower capacitance.

Mechanical Testing: To quantify the mechanical strength of the monolith material I performed compressive testing measurements. Representative examples of the stress/strain curves for both a monolith and a carbonized bone plug still containing the

HA scaffold are shown in Figure 1.17. The shape of the curve for the monolith upon decreasing the load indicates that the material progressively deforms upon compression and is relatively inelastic. Table 1.2 summarizes the results of the 3 monoliths (without HA) that were tested. For comparison, a carbonized bone sample exhibited a compressive strength of 235 MPa, a value that is approximately 800 times larger than that of the carbon monolith once the HA was removed. The HA scaffold predictably provides a great deal of strength to the material.

Modification Attempts: A significant attraction of a material with a high specific surface area and a large void volume, such as the one I have described above, is its potential for modification. If the surface of a conductive substrate is modified with an electroactive material, a pseudocapacitor can be produced. A pseudocapacitor differs from a capacitor by its the mechanism of charge storage. In a capacitor the charge storage is based on non-Faradaic, electrostatic charge separation. In contrast, a pseudocapacitor stores charge through Faradaic electron transfer reactions with species on an electrode surface. It has been demonstrated that pseudocapacitor devices composed of electrodes modified with conducting polymers, like polyaniline, or metal oxides, like nickel hydroxide, can result in specific capacitance values an order of magnitude higher than the native double layer devices [60, 61].

The attempts to modify the carbon monoliths presented in this work were largely unsuccessful. I believe the major reasons for this lack of success were associated with engineering challenges coupled with the resistance of the monoliths. Attempts to deposit conducting polymers, such as polyaniline, polypyrrole, and poly(propylenedioxythiophene) via cyclic voltammetry resulted in highly resistive

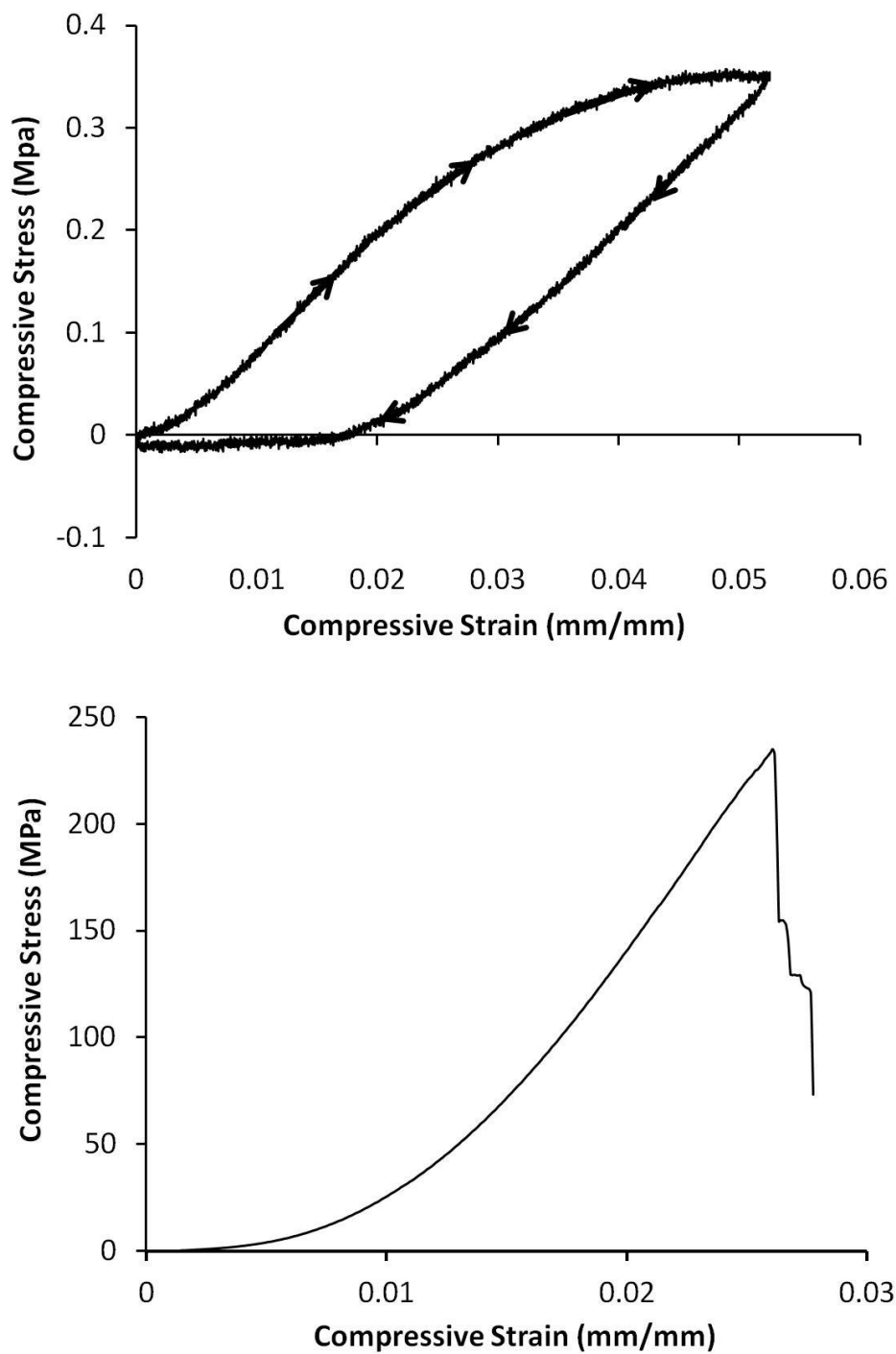


Figure 1.17. Representative stress/strain curves for a 6 mm x 12 mm carbon monolith rod (top) and a rod after pyrolysis but before the HA has been removed (bottom).

Table 1.2. Summary of the compressive testing data for carbon monolith samples.

Sample	Maximum Load (N)	Compressive Strength (MPa)
1	5.1	0.23
2	6.2	0.29
3	7.9	0.36
Average	6.4	0.29
Standard Deviation	1.4	0.07
95% Confidence Limit	±3.5	±0.16

electrodes with low charge storage capacity. A major reason for this result could be the instability of the conductive epoxy contacts in the deposition solutions used. The resistance of the monolith required the use of slow scan rates for the potential sweeps. These slow scan rates left the electrode in solution for several hours while the depositions were performed. Over this time the contacts may have weakened to produce a significant increase in resistance, if not a complete separation of the carbon material from the electrode.

Two procedures I examined showed results consistent with polymer formation inside the bulk of the carbon monolith. One of these was a homogeneous chemical polymerization of pyrrole using Fe^{3+} as an initiator. For this procedure an electrode was attached to a gold plated stainless steel rod using conductive carbon filled epoxy. The epoxy was cured at 80°C for 4 hours. The rod, with the carbon attached, was then inserted into a length of Tygon tubing leaving the surface of the carbon monolith flush the opening of the tubing. The gap between the monolith and the tubing was then sealed with the same insulating epoxy (Hardman Double Bubble) used to seal the devices prepared above. This construction prevented solvent from efficiently reaching the metal/carbon epoxy interface, which was typically where failure occurred previously. The HA was removed as described above and the remaining EDTA removed by soaking the electrode in water. The electrode was then moved into a 700 mM pyrrole, 1 M tetrabutylammonium hexafluorophosphate (TBAPF_6) solution in acetonitrile and left to soak for approximately 3 hours. Upon observing that the electrode appeared to be intact the electrode was transferred into an acetonitrile solution containing 1 M TBAPF_6 and ca. 100 mM FeCl_3 , but no pyrrole monomer. The chemical polymerization was performed in

monomer free solution to increase the propensity of the polymer to form inside the monolith. The electrode was soaked in this solution for approximately 3 hours and then transferred to an electrolyte solution containing only 1 M TBAPF₆ in acetonitrile. The resulting cyclic voltammogram is shown in Figure 1.18. Peaks in the voltammogram at approximately 0.25 and 0 V indicate that some conducting polymer was present in the electrode. Further electrochemical characterization of this composite material was not possible because of mechanical failure that occurred upon repeated cycling.

Positive preliminary results were also achieved using a second method of polymerization. For this method, an electrode was prepared the same way as described above and it was placed into a 1.0 M TBAPF₆ electrolyte solution. While in this solution, the electrode was subjected to 10 consecutive 1 mA galvanostatic pulses, which were 30 seconds in duration, to polymerize pyrrole inside the monolith. After these pulses cyclic voltammetry was used to characterize the composite in an acetonitrile solution containing 1.0 M TBAPF₆. The results of this experiment are shown in Figure 1.19. Again the results show peaks that indicate polymer has grown in the electrode and that there is a significant increase in the apparent capacitance of the pseudocapacitor.

The peak currents at approximately 0.1 V in the voltammograms shown in Figures 1.18 and 1.19 correspond to the reduction of polypyrrole [62]. In Figure 1.18 the peak current for the chemically prepared polymer decreases with each cycle. In contrast, the peak current in Figure 1.19 increases with each cycle. The reason for these contrasting results is not clear. A plausible explanation is that some monomer remained trapped in the electrochemically prepared monolith/polymer composite and that cycling the electrode resulted in further polymerization inside the monolith. Regardless of the

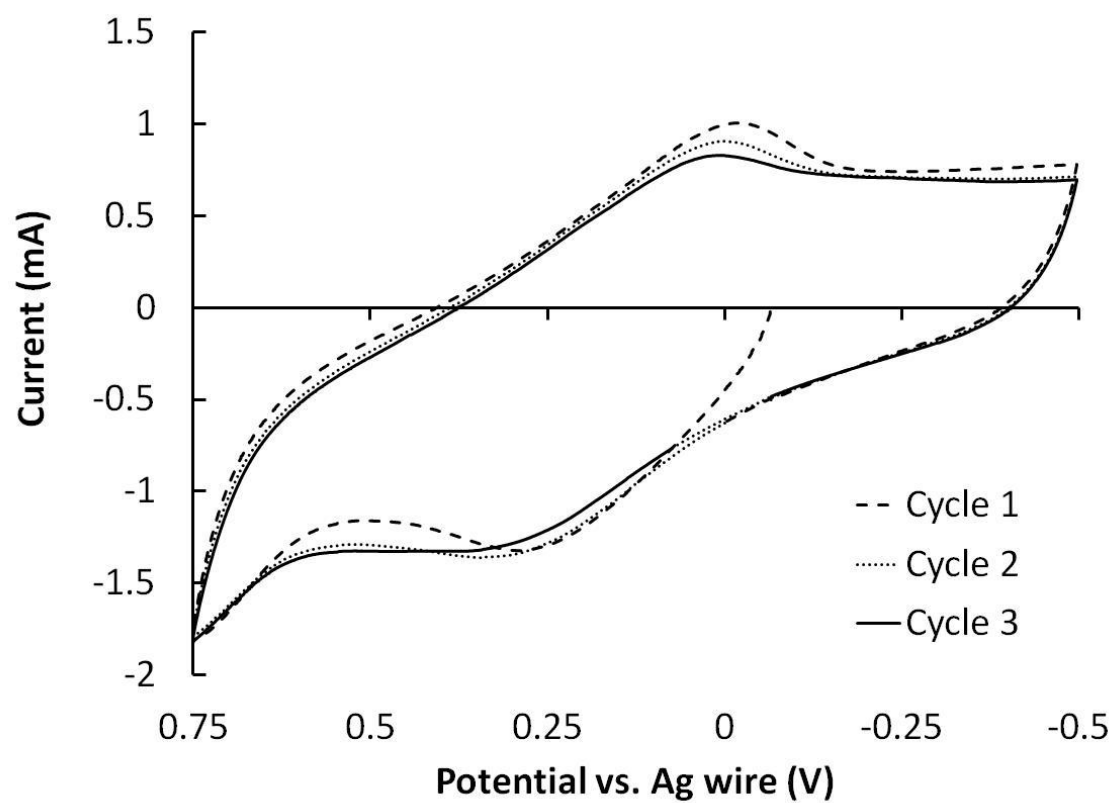


Figure 1.18. Cyclic voltammogram of a carbon monolith containing polypyrrole prepared via chemical oxidation with Fe^{3+} in a solution of 1 M TBAPF_6 at a scan rate of 1 mV/s.

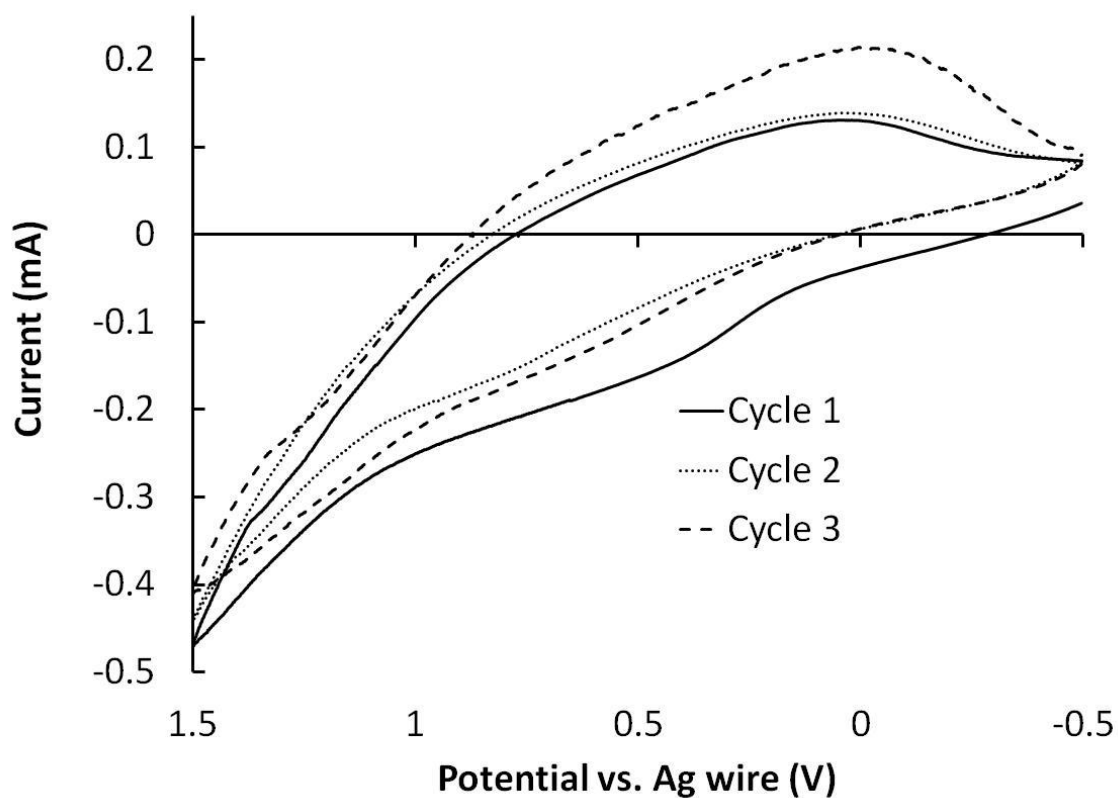


Figure 1.19. Cyclic voltammogram of a carbon monolith containing polypyrrole prepared via galvanostatic oxidation in a solution of 1 M TBAPF₆ at a scan rate of 0.5 mV/s.

reason for the difference in the signals for the two cases, I have demonstrated that modification of these monoliths with conducting polymers is possible. Further experimentation is necessary to determine the optimal conditions for this type of modification.

Conclusions: Pyrolysis of machined bovine bone leads to conductive carbon interwoven within the HA scaffold native to the original bone. This HA framework prevents the collapse of the carbon to dense forms during pyrolysis. Upon removal of the HA scaffold after pyrolysis, a monolith that preserves the macroscopic form of the original bone remains. The resulting carbon monolith contains graphene-like sheets that are loosely packed, leading to a structure that is both high in surface area and conductive. These monoliths were tested as the active material in supercapacitor devices and display a specific capacitance of 134 ± 11 F/g and 108 ± 9 F/g in aqueous KNO_3 and EMIBTI, respectively.

The fabrication of prototype devices for this work demonstrates a novel cell design for testing supercapacitor materials. The 6 mm diameter bone disks used in this work had been previously used in Professor Redepenning's research group and fortuitously allowed for the fabrication of a cell, as described in the experimental section, using readily available supplies which many laboratories have on hand [25]. Even if the necessary items must be purchased, the costs associated with this design are minimal, which makes the design well-suited for characterizing future generations of this class of electrode materials. Capacitor device prototypes of approximately 0.1 F and 0.9 F were demonstrated with relative ease.

The specific surface area of the monolith material is high. However, consistent with observations made by other groups on microporous carbons, the BET method using $N_2(g)$ appears to overestimate the specific surface area of the monoliths and the surface area accessible to electrolyte ions.

It was demonstrated that a large portion of the surface area of the conductive carbon is accessible to solvent and electrolyte even without the removal of the HA scaffold. Such materials may be useful in applications requiring electrodes with high mechanical strength and high surface area (of the conducting phase) but lower capacitance per unit mass. The mechanical strength of the carbon monoliths is relatively low, as may be expected for most materials with very high void volumes and low densities. The compressive strength of the carbonized bone before removing the HA is approximately 800 times larger than the carbon monoliths produced upon removing the HA.

A small screening study showed that the pyrolysis conditions can have a significant effect on the electrochemical characteristics of the monoliths. It is also apparent that at pyrolysis temperatures above 1200°C , structural changes to the hydroxyapatite and/or carbon lower the accessible surface area of the monolith which results in a significantly lower capacitance.

Attempts to modify the monoliths with conducting polymers were met with limited success. Two polymerization techniques, one using chemical polymerization and one using galvanostatic polymerization, led to electrochemical results consistent with the behavior of carbon/conducting polymer composite materials. In both cases the electrode design limited the ability to fully characterize the composite. Future attempts to modify

the monolith materials must start with developing an improved method of electrode fabrication.

References

- [1] Conway BE. Electrochemical supercapacitors: scientific fundamentals and technological applications: Plenum Press; 1999.
- [2] Zhang LL, Zhou R, Zhao XS. Graphene-based materials as supercapacitor electrodes. *Journal of Materials Chemistry*. 2010;20(29):5983-92.
- [3] Lewandowski A, Galinski M. Practical and theoretical limits for electrochemical double-layer capacitors. *J Power Sources*. 2007;173:822-8.
- [4] Stoller MD, Park S, Zhu Y, An J, Ruoff RS. Graphene-Based Ultracapacitors. *Nano Letters*. 2008;8(10):3498-502.
- [5] Becker H, I, inventor Low Voltage Electrolytic Capacitor. United States patent 2800616. 1957 July 23, 1957.
- [6] Bard AJ, Faulkner LR. *Electrochemical Methods: Fundamentals and Applications*: Wiley; 2000. Chapter 13: 534-580.
- [7] Grahame DC. The electrical double layer and the theory of electrocapillarity. *Chem Rev*. 1947;41:441-501.
- [8] Vivekchand SRC, Rout CS, Subrahmanyam KS, Govindaraj A, Rao CNR. Graphene-based electrochemical supercapacitors. *J Chem Sci (Bangalore, India)*. 2008;120:9-13.
- [9] Borges RS, Ribeiro H, Lavall RL, Silva GG. Temperature stable supercapacitors based on ionic liquid and mixed functionalized carbon nanomaterials. *J Solid State Electrochem*. 2012;16:3573-80.
- [10] Chen YC, Cui HL, Mullings M, Rhodes CP. Advanced electrolytes for extreme temperature supercapacitors. *Proc Power Sources Conf*. 2010;44th:589-92.
- [11] Xu Z, Li Z, Holt CMB, Tan X, Wang H, Amirkhiz BS, et al. Electrochemical Supercapacitor Electrodes from Sponge-like Graphene Nanoarchitectures with Ultrahigh Power Density. *J Phys Chem Lett*. 2012;3:2928-33.
- [12] Hung K, Masarapu C, Ko T, Wei B. Wide-temperature range operation supercapacitors from nanostructured activated carbon fabric. *J Power Sources*. 2009;193:944-9.
- [13] Lin J-H, Ko T-H, Lin Y-H, Pan C-K. Various Treated Conditions to Prepare Porous Activated Carbon Fiber for Application in Supercapacitor Electrodes. *Energy Fuels*. 2009;23:4668-77.
- [14] Pico F, Rojo JM, Sanjuan ML, Anson A, Benito AM, Callejas MA, et al. Single-walled carbon nanotubes as electrodes in supercapacitors. *J Electrochem Soc*. 2004;151:A831-A7.
- [15] Liu CG, Liu M, Li F, Cheng HM. Frequency response characteristic of single-walled carbon nanotubes as supercapacitor electrode material. *Appl Phys Lett*. 2008;92:143108/1-/3.
- [16] Pan H, Li J, Feng YP. Carbon nanotubes for supercapacitor. *Nanoscale Res Lett*. 2010;5:654-68.
- [17] Xu B, Wu F, Wang F, Chen S, Cao G-P, Yang Y-S. Single-walled carbon nanotubes as electrode materials for supercapacitors. *Chin J Chem*. 2006;24:1505-8.
- [18] Bushueva EG, Galkin PS, Okotrub AV, Bulusheva LG, Gavrillov NN, Kuznetsov VL, et al. Double layer supercapacitor properties of onion-like carbon materials. *Phys Status Solidi B*. 2008;245:2296-9.

- [19] Gao Y, Zhou YS, Qian M, He XN, Redepenning J, Goodman P, et al. Chemical activation of carbon nano-onions for high-rate supercapacitor electrodes. *Carbon*. 2013;51(0):52-8.
- [20] Barton SS, Evans MJB, Harrison BH. Pore structure and molecular sieve properties of poly(vinylidene chloride) carbons. *J Colloid Interface Sci*. 1974;49:462-8.
- [21] Korkut S, Roy-Mayhew JD, Dabbs DM, Milius DL, Aksay IA. High Surface Area Tapes Produced with Functionalized Graphene. *ACS Nano*. 2011;5(6):5214-22.
- [22] Tao Y, Endo M, Inagaki M, Kaneko K. Recent progress in the synthesis and applications of nanoporous carbon films. *Journal of Materials Chemistry*. 2011;21(2):313-23.
- [23] Purevsuren B, Avid B, Narangerel J, Gerelmaa T, Davaajav Y. Investigation on the pyrolysis products from animal bone. *J Mater Sci*. 2004;39:737-40.
- [24] Wei S, Zhang H, Huang Y, Wang W, Xia Y, Yu Z. Pig bone derived hierarchical porous carbon and its enhanced cycling performance of lithium-sulfur batteries. *Energy & Environmental Science*. 2011;4(3):736-40.
- [25] Wiegand T, Karr J, Steinkruger JD, Hiebner K, Simeitich B, Beatty M, et al. Reconstruction of Anorganic Mammalian Bone by Surface-Initiated Polymerization of L-Lactide. *Chem Mater*. 2008;20:5016-22.
- [26] Törmälä P, Romppanen M. Preparation of glassy carbon from lignins and lignin condensates. *Journal of Materials Science*. 1981;16(1):272-4.
- [27] Brunauer S, Emmett PH, Teller E. Adsorption of Gases in Multimolecular Layers. *Journal of the American Chemical Society*. 1938;60(2):309-19.
- [28] Sadezky A, Muckenhuber H, Grothe H, Niessner R, Poeschl U. Raman microspectroscopy of soot and related carbonaceous materials. Spectral analysis and structural information. *Carbon*. 2005;43:1731-42.
- [29] Czigány Z, Hultman L. Interpretation of electron diffraction patterns from amorphous and fullerene-like carbon allotropes. *Ultramicroscopy*. 2010;110(7):815-9.
- [30] Taer E, Deraman M, Talib IA, Awitdrus A, Hashmi SA, Umar AA. Preparation of a highly porous binderless activated carbon monolith from rubber wood sawdust by a multi-step activation process for application in supercapacitors. *Int J Electrochem Sci*. 2011;6:3301-15.
- [31] Li J, Wang X, Huang Q, Gamboa S, Sebastian PJ. Studies on preparation and performances of carbon aerogel electrodes for the application of supercapacitor. *J Power Sources*. 2006;158:784-8.
- [32] Li W, Probstle H, Fricke J. Electrochemical behavior of mixed CmRF based carbon aerogels as electrode materials for supercapacitors. *J Non-Cryst Solids*. 2003;325:1-5.
- [33] Chmiola J, Largeot C, Taberna P-L, Simon P, Gogotsi Y. Monolithic Carbide-Derived Carbon Films for Micro-Supercapacitors. *Science (Washington, DC, U S)*. 2010;328:480-3.
- [34] Incorporated M. Representative Test Procedure for Customer Evaluation. 2002.
- [35] Grahame DC. The electrical double layer and the theory of electro-capillarity. *Chem Rev (Washington, DC, U S)*. 1947;41:441-501.
- [36] Burke A, Miller M. Testing of electrochemical capacitors: Capacitance, resistance, energy density, and power capability. *Electrochim Acta*. 2010;55:7538-48.

- [37] Farahmandi CJ. A mathematical model of an electrochemical capacitor with porous electrodes. *Proc - Electrochem Soc.* 1997;96-25:167-79.
- [38] Srinivasan V, Weidner JW. Mathematical modeling of electrochemical capacitors. *J Electrochem Soc.* 1999;146:1650-8.
- [39] R dL. On porous electrodes in electrolyte solutions: I. Capacitance effects. *Electrochimica Acta.* 1963;8(10):751-80.
- [40] Pell WG, Conway BE. Voltammetry at a de Levie brush electrode as a model for electrochemical supercapacitor behaviour. *Journal of Electroanalytical Chemistry.* 2001;500(1-2):121-33.
- [41] Chen Y, Zhang X, Zhang D, Yu P, Ma Y. High performance supercapacitors based on reduced graphene oxide in aqueous and ionic liquid electrolytes. *Carbon.* 2011;49(2):573-80.
- [42] Fedorov MV, Kornyshev AA. Towards understanding the structure and capacitance of electrical double layer in ionic liquids. *Electrochim Acta.* 2008;53:6835-40.
- [43] Kornyshev AA. Double-Layer in Ionic Liquids: Paradigm Change? *J Phys Chem B.* 2007;111:5545-57.
- [44] Lewandowski A, Olejniczak A, Galinski M, Stepniak I. Performance of carbon-carbon supercapacitors based on organic, aqueous and ionic liquid electrolytes. *Journal of Power Sources.* 2010;195(17):5814-9.
- [45] Castner EW, Jr., Wishart JF. Spotlight on ionic liquids. *J Chem Phys.* 2010;132:120901/1-9.
- [46] Plechkova NV, Seddon KR. Applications of ionic liquids in the chemical industry. *Chemical Society Reviews.* 2008;37(1):123-50.
- [47] Stoller MD, Ruoff RS. Best practice methods for determining an electrode material's performance for ultracapacitors. *Energy & Environmental Science.* 2010;3(9):1294-301.
- [48] Khomenko V, Frackowiak E, Béguin F. Determination of the specific capacitance of conducting polymer/nanotubes composite electrodes using different cell configurations. *Electrochimica Acta.* 2005;50(12):2499-506.
- [49] Sing KSW, Everett DH, Haul RAW, Moscou L, Pierotti RA, Rouquerol J, et al. Reporting physisorption data for gas/solid systems with special reference to the determination of surface area and porosity (Recommendations 1984). *Pure Appl Chem.* 1985;57:603-19.
- [50] Brown AP, Anson FC. Cyclic and differential pulse voltammetric behavior of reactants confined to the electrode surface. *Anal Chem.* 1977;49:1589-95.
- [51] McCreery RC, Cline K. Carbon Electrodes. In: Kissinger P, Heineman WR, eds. *Laboratory Techniques in Electroanalytical Chemistry.* 2nd ed: CRC Press 1996, p. 306.
- [52] Kaneko K, Ishii C. Superhigh surface area determination of microporous solids. *Colloids Surf.* 1992;67:203-12.
- [53] Ohba T, Kaneko K. Internal Surface Area Evaluation of Carbon Nanotube with GCMC Simulation-Assisted N₂ Adsorption. *J Phys Chem B.* 2002;106:7171-6.
- [54] Shi H. Activated carbons and double layer capacitance. *Electrochim Acta.* 1996;41:1633-9.
- [55] Stoeckli F, Centeno TA. On the determination of surface areas in activated carbons. *Carbon.* 2005;43:1184-90.

- [56] Largeot C, Portet C, Chmiola J, Taberna P-L, Gogotsi Y, Simon P. Relation between the Ion Size and Pore Size for an Electric Double-Layer Capacitor. *Journal of the American Chemical Society*. 2008;130(9):2730-1.
- [57] Barbieri O, Hahn M, Herzog A, Koetz R. Capacitance limits of high surface area activated carbons for double layer capacitors. *Carbon*. 2005;43:1303-10.
- [58] Incorporated M. Boostcap Series Ultracapacitor Datasheet. [cited 2013; Available from: http://www.maxwell.com/products/ultracapacitors/docs/datasheet_bc_series_1017105.pdf]
- [59] Muralithran G, Ramesh S. The effects of sintering temperature on the properties of hydroxyapatite. *Ceramics International*. 2000;26(2):221-30.
- [60] Fu G-r, Hu Z-a, Xie L-j, Jin X-q, Xie Y-l, Wang Y-x, et al. Electrodeposition of nickel hydroxide films on nickel foil and its electrochemical performances for supercapacitor. *Int J Electrochem Sci*. 2009;4:1052-62.
- [61] Fan L-Z, Hu Y-S, Maier J, Adelhelm P, Smarsly B, Antonietti M. High electroactivity of polyaniline in supercapacitors by using a hierarchically porous carbon monolith as a support. *Adv Funct Mater*. 2007;17:3083-7.
- [62] Skotheim TA. *Handbook of conducting polymers*: M. Dekker; 1986.

Chapter Two

The Qualitative Electrochemical Analysis of Triacetone Triperoxide

Introduction

Many chemists are aware of the auto-oxidation that results in explosive peroxide formation from common ethers, such as diethyl ether and tetrahydrofuran. These explosive peroxides are a common concern in chemical laboratories. A frequently cited reference by Jackson et al. provides an extensive list of compounds that auto-oxidize to form dangerous and explosive peroxides [1]. Mirafzal and Baumgarten, prompted by incidents of explosions in teaching laboratories, found that low levels of peroxides can be found in old bottles of primary and secondary alcohols, such as 1-butanol and 2-propanol [2]. The peroxides formed in these containers through the auto-oxidation of the solvents with air, and most organic peroxides for that matter, can be shock, heat, and friction sensitive [3].

When one considers the prevalence of these auto-oxidation reactions, it is not surprising that there are a large number of reported methods for determining the presence of peroxides both qualitatively and quantitatively. The most commonly employed methods use commercially available “dip strips” or titrations [4]. Generally, the procedure for the titrations is to add a known amount of reagent to the sample being tested and then titrate the resulting oxidized product to determine the peroxide concentration. The most widely used reagent for these titrations is iodide. Upon reaction with many peroxides, iodide oxidizes to iodine. The iodine can then be titrated with thiosulfate to determine the concentration of peroxide in the original sample [5].

Despite the potential explosion hazards, organic peroxides are often put to good use. In fact, organic peroxides are used in many procedures, including polymerizations [6], epoxidation reactions [7, 8], and sulfide oxidations [9, 10], to name a few. One particular class of peroxides that has received significant recent attention is the cyclic ketone peroxides. The synthesis of this class of peroxides is straightforward, and many examples exist in the literature. All of these examples are explosive [11-14]. Of particular interest is the peroxide 3,3,6,6,9,9-hexamethyl-1,2,4,5,7,8-hexaoxacyclononane, more commonly referred to as triacetone triperoxide, or TATP. The chemical structure of TATP is shown in Figure 1.1. This compound was first reported by Wolfenstein in 1895, and reported again in a cautionary paper by Mavrodi in 1949 [15, 16]. The principle danger of TATP is its explosive velocity, which is 83% of trinitrotoluene's (TNT), coupled with its high sensitivity to explosive initiation [17].

Since its discovery, TATP has been noted as an unwanted, and potentially dangerous, byproduct in commercial processes [18, 19]. The baked goods industry, for example, uses linear acetone peroxides as bleaching agents in flour [20]. Contamination with TATP in this application is dangerous because the flour is hammer milled after addition of the peroxide, and TATP is sensitive to shock.

The use of TATP for legal civilian and military purposes has been investigated to some extent. Two important examples are its possible use in military explosives and as fuel additives [21-24]. It has been known since the 1940s that TATP is not useful as a primary explosive, or as a component of explosive primers, due to its extremely sensitive nature [22]. The high vapor pressure of TATP also results in the loss of the compound via sublimation, further limiting its utility in military applications [25].

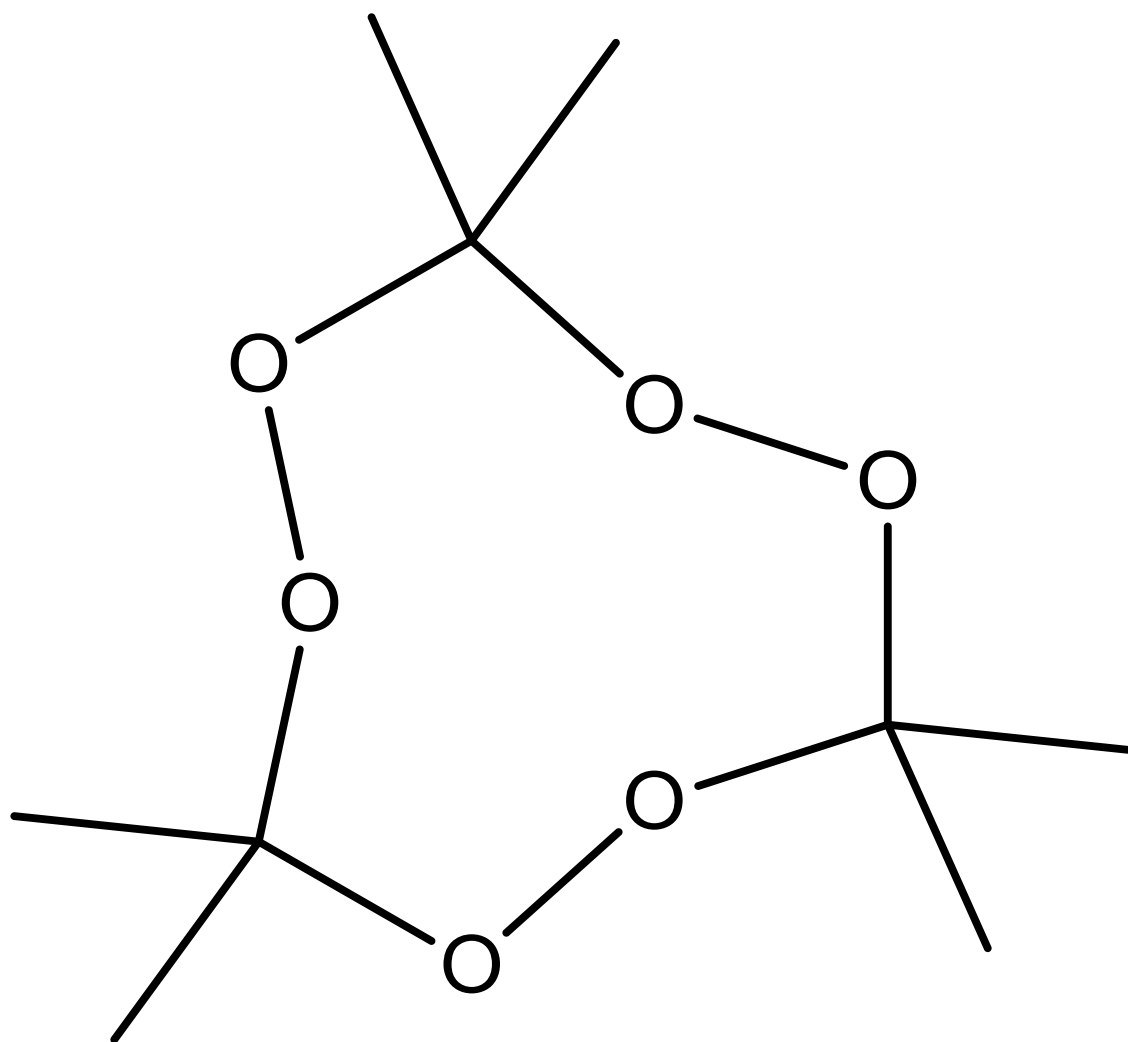


Figure 2.1. The chemical structure of 3,3,6,6,9,9-hexamethyl-1,2,4,5,7,8-hexaoxacyclononane, which is more commonly referred to as triacetone triperoxide, or TATP.

As a fuel additive, TATP was found to decrease the ignition delay in diesel fueled engines regardless of the solution composition [21, 26]. It is not clear why experiments involving these additives seem to have ended prior to World War II, but one might speculate that the use of cyclic peroxides was deemed too dangerous for many applications because of its shock sensitivity.

Regardless of the past attempts to utilize TATP for legal purposes, the peroxide's use in today's society is often nefarious, as demonstrated by Richard Reid (the "shoe bomber") in 2001 and the coordinated attacks on the London mass transit system in 2005 [27, 28]. TATP is attractive to terrorists because, like many ketone peroxides, it is an easily synthesized and powerful explosive [11-14]. TATP is particularly dangerous because the components for its synthesis are readily available and it can be difficult to detect.

Matyas et al. examined the influence of synthetic conditions on product distributions, as well as the stability of the product mixtures, for so-called TATP syntheses [29-31]. They found that many inorganic acids can be used to catalyze the formation of TATP, and the product composition was not affected by the type of acid, provided the molar ratio of catalyst to acetone was <0.5 [29]. Interestingly, they did find that the type of acid used for catalysis can influence the thermal stability of the product [31]. The researchers noted that TATP produced using a hydrochloric acid catalyst demonstrated the same thermal properties as "pure" TATP, as obtained via recrystallization. TATP synthesized using nitric, perchloric or sulfuric acid catalysts exhibited thermal properties different from those of the pure sample. They proposed that residual acid in the TATP crystals was likely responsible for this result. The authors

determined the amount of residual acid via titration of a methanol solution of the TATP product from each reaction with tetrabutylammonium hydroxide. Even inexperienced “chemists” are capable of synthesizing large quantities of TATP with relative ease, because the reaction conditions are relatively unimportant to the product composition,

One important consideration when TATP is found by law enforcement is how to efficiently destroy it. A common method for the disposal of an improvised explosive device (IED) is referred to as “blow in place”, which simply means detonating the device where it is. The “blow in place” procedure minimizes the risks associated with handling and transporting sensitive explosives. TATP is often found in densely populated areas where in place detonation may not be an option because of risks to civilians in the surrounding area. In these cases, an efficient method to destroy TATP without detonation would be preferred [32].

Despite the presence of three peroxide groups in its nine membered ring, TATP is only slowly reduced under a wide variety of conditions. This can make its chemical destruction difficult. For example, in 1949 Criegee and Schnorrenberg demonstrated that the use of the iodometric titration method discussed above to determine the peroxide content of a TATP solution was not possible because TATP does not react with iodide. The authors reported that this was due to steric effects, allowing the peroxide groups to be protected [11]. In 1999 Bellamy showed that toluene solutions of TATP are relatively safe to handle. He also demonstrated that when toluene solutions of TATP are added to boiling solutions of tin(II) chloride in methanol or ethanol, the TATP is destroyed in under 2 hours [33]. Oxley et al. expanded upon this work while searching for a “cocktail” that could be sprayed onto solid TATP in order to destroy it. They determined

that ZnSO_4 or CuCl_2 in combination with KMnO_4 , NH_2NH_2 , KI , or NaBr in a sulfuric acid solution destroyed TATP, but only after 5-8 hours. The researchers noted that the application of concentrated mineral acids (e. g., methanesulfonic acid, sulfuric acid and nitric acid) resulted in the complete destruction of 5 mg of TATP in 15 minutes, however, the application of these concentrated mineral acids to 1 g of TATP was exothermic enough to initiate detonation [32].

TATP is a nondescript white powder that generally looks like powdered sugar; therefore, it cannot be identified visually. In many cases, methods employed to detect explosives are based on the chemistry of nitrogen-containing functional groups [34]. The detection of TATP by these methods is not possible, because TATP does not contain any nitrogen atoms. Hard ionization mass spectral methods are generally not useful for the detection of TATP, because the molecular ion does not appear in the spectrum and the masses of the fragments are not specific to TATP [35]. Despite these challenges, many methods have been reported for the detection of TATP, including luminescence [36-38], soft ionization mass spectrometry [39-42], and infrared spectroscopy [43-45]. Currently, methods based on electronic nose technology appear to have the best combination of sensitivity and ease of field use, but these systems can be cost prohibitive [46]. Electrochemical sensors have also been demonstrated as useful methods for the detection of organic peroxide explosives [47-50].

Some of the benefits of simple electrochemical sensors are that they can be sensitive and inexpensive to produce. A significant challenge in the field of electrochemical sensors is selectivity. When one searches through a table of standard reduction potentials, it is worth noting that at the extremes are the following reactions [51]:



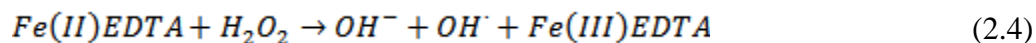
Noting this allows one to surmise that essentially every compound or element, known and unknown, will undergo redox processes within this 6.1 V range. It is unlikely that a compound or element can be identified by knowing only the potential at which it oxidizes or reduces. For example, the standard potential for both the reduction of ferrocenium to ferrocene and the reduction of Tc^{2+} to Tc is 0.400 V [51]. Ferrocenium and Tc^{2+} are two distinctly different species, but if one knows only the voltage at which they reduce and has no other knowledge of the chemistry of the system, these species would be indistinguishable from each other. As such, other chemistry must be involved in the development of electrochemical sensors to make them selective enough to be useful in the detection of specific compounds.

Most of the electrochemical sensors developed for the detection of TATP are based on blood glucose sensor systems that were originally designed to detect the hydrogen peroxide that results from the oxidation of glucose by glucose oxidase. In 1989 Gorton and Jonsson reported an electrochemical sensor for hydrogen peroxide that employed adsorbed horseradish peroxidase (HRP) on graphite electrodes as a transducer [52]. Immobilizing the enzyme onto the electrode surface alleviated the kinetically slow electron transfer between metalloproteins and electrodes, as previously reported by Frew et al., and allowed for the catalytic reduction of hydrogen peroxide at the modified electrode [53]. Gorton and Jonssen noted that the electrode lost around 40% of its activity with repeated potential cycling. They attributed this observation to protein

degradation rather than protein desorption because the decreased activity was a function of voltammetric cycle number, regardless of the cycle rate [54].

The mechanism for hydrogen peroxide reduction by HRP involves the iron porphyrin unit that is located within the active site of this enzyme [55]. Several examples have been reported that use an iron based “artificial peroxidase” as the redox catalyst. Prussian Blue (PB) modified electrodes, originally employed by Karyakin in 1994 for the detection of the hydrogen peroxide created via glucose oxidation [56], were later employed for detection of hydrogen peroxide generated by the degradation of TATP [48, 49]. In these incarnations, dissolution of solid TATP was followed by treatment with acid, UV irradiation, or laser irradiation to produce hydrogen peroxide or other hydroperoxides. These peroxides were reduced at the PB modified electrode at low potentials (0 V vs. SCE) with detection limits of 55 nM, 250 nM, and 50 nM, for acid, UV, and laser treatment, respectively [48, 49].

Another example of an electrochemical sensor with a reported ability to detect TATP is based on the catalytic reduction of hydrogen peroxide using the iron(II,III) ethylenediaminetetraacetic acid (FeEDTA) complex as an electron transfer mediator [57]. For this sensor, TATP solutions were treated with acid and then mixed with an FeEDTA solution. When the potential of an electrode that was placed into the solution was swept in the negative direction, a catalytic current resulted from the following reactions,



The magnitude of the catalytic current was dependent on the concentration of the

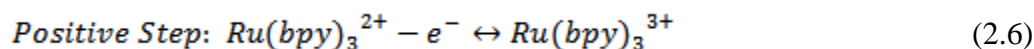
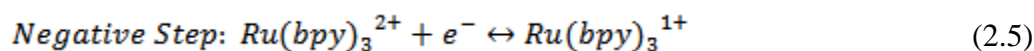
hydrogen peroxide. Using this sensor, the authors were able to achieve a limit of detection of 890 nM [57].

A set of significant challenges confronts the detection of TATP by any electrochemical scheme. These challenges include the insolubility of this molecule in water and the difficulty presented by the kinetically slow reduction of the peroxide. In the currently reported incarnations of electrochemical sensors for TATP, breaking down the TATP under harsh conditions and then detecting the resulting hydroperoxides in aqueous solution eliminates both problems. Many sensors originally developed for hydrogen peroxide detection could be used to detect TATP via its degradation products.

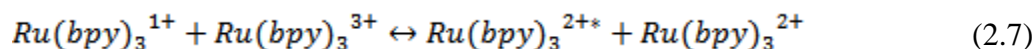
Though it has been noted many times that the direct reduction of TATP at an electrode surface occurs at very negative potentials due to slow kinetics, to the best of my knowledge the actual voltammograms do not appear in the literature [48, 49, 57, 58]. In this chapter I show the results of the direct electrochemistry of TATP in acetonitrile solutions. Analysis of the electrochemistry of the TATP alone may help direct future research into electrochemical sensors for this peroxide.

After analyzing the direct electrochemistry of TATP in nonaqueous solutions, one might conclude that a logical step toward a working sensor would be to search for compounds capable of catalytically reducing TATP at less negative potentials. Many compounds were tested for catalytic reactivity with TATP as part of the work presented in this chapter. Of the compounds that were tested, only the reduction products of tris-(2,2'-bipyridine) ruthenium(II) ($\text{Ru}(\text{bpy})_3^{2+}$), which were produced via reduction of $\text{Ru}(\text{bpy})_3^{2+}$ at an electrode surface, showed a significant catalytic response upon direct reaction with TATP.

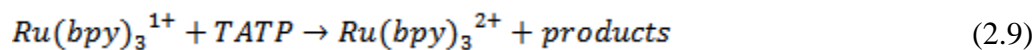
Using $\text{Ru}(\text{bpy})_3^{2+}$ as part of a scheme for detecting TATP has been demonstrated in the literature [59]. The work presented by Shaw and Calhoun makes use of the electrogenerated chemiluminescence (ECL) of $\text{Ru}(\text{bpy})_3^{\text{X}+}$. The authors' detection scheme worked by analyzing the quenching of the luminescence normally produced by a double potential step that results in the following reactions,



The combination of $\text{Ru}(\text{bpy})_3^{1+}$ with $\text{Ru}(\text{bpy})_3^{3+}$ results in this reaction sequence,



which occurs near the electrode surface. When TATP is included in the solution the general reaction



results in a quenching of the ECL, as given in equation (2.8), because it consumes the $\text{Ru}(\text{bpy})_3^{1+}$ necessary for the production of the excited state molecule, $\text{Ru}(\text{bpy})_3^{2+*}$, in equation (2.7). Using this scheme, the authors achieved a detection limit of 10 nM [59].

In this chapter I qualitatively study the direct electrochemistry of TATP at bare electrode surfaces. I also describe the search for catalytically active electron transfer mediators and show the electrochemical responses of the prospective mediator compounds in the presence and absence of TATP.

Experimental

Chemicals: Acetonitrile (extra dry, Acros Organics, Morris Plains, NJ), *N,N*-dimethylformamide (extra dry, Acros Organics, Morris Plains, NJ), dimethylsulfoxide

(anhydrous, Sigma-Aldrich, St. Louis, MO), tetrabutylammonium hexafluorophosphate (TBAPF₆, electrochemical grade, Sigma-Aldrich, St. Louis, MO), acetone (ACS reagent, Sigma-Aldrich, St. Louis, MO), 30% aqueous hydrogen peroxide (Fisher, Waltham, MA), hydrochloric acid (trace metal grade, Fluka, St. Louis, MO), 5,10,15,20-tetraphenyl-21H,23H-porphine iron(III) chloride (TPPFe, Sigma-Aldrich, St. Louis, MO), hexaammineruthenium (III) chloride (Strem Chemicals Inc., Newburyport, MA), fullerene-C₆₀ (Sigma-Aldrich, St. Louis, MO), ferrous chloride (anhydrous, Sigma-Aldrich, St. Louis, MO), Nafion (5 wt% solutions in lower aliphatic alcohols and water, Sigma-Aldrich, St. Louis, MO), stannic chloride pentahydrate (SnCl₄·5H₂O, J.T. Baker Chemical Company, Phillipsburg, NJ), ferric chloride hexahydrate (certified ACS, Fisher, Waltham, MA), and deuterated solvents for NMR analyses (Cambridge Isotopes, Andover, MA) were all purchased from their respective suppliers and used as received. Methyl viologen diiodide had been previously prepared in Professor Jody Redepenning's laboratory and was used without further purification. Porphyrin complexes including the 2,3,7,8,12,13,17,18-octafluoro-5,10,15,20-tetraphenylporphyrin (F₈TPP) complexes of cobalt and rhodium, the 2,3,7,8,12,13,17,18-octafluoro-5,10,15,20-tetrakis(pentafluorophenyl)porphyrin (F₂₈TPP) complex of rhodium, and the iron complex of 5,10,15,20-tetrakis(pentafluorophenyl)porphyrin (F₂₀TPP) were donated by the laboratory of Professor Stephen Dimagno (Department of Chemistry, University of Nebraska, Lincoln, NE) and had been prepared using their previously reported procedures [60, 61]. The iron and rhodium porphyrin complexes were obtained as the chloride salts.

TATP Synthesis: TATP was synthesized by mixing acetone that was chilled to 0°C (typically 1.1 g) with excess hydrogen peroxide (30% aqueous solution, chilled to 0°C, typically, 2.3 g). The peroxide solution contained a catalytic amount of hydrochloric acid (typically, 1 drop of concentrated HCl from a disposable pipette). The mixture was stirred at room temperature overnight. The product, which was a white solid, was collected via vacuum filtration and washed with deionized water until the pH of the wash solution was neutral. The TATP was dried by allowing the solid to remain in the vacuum filter with flowing air for approximately 1 hour before collection. The identity of the product was verified via NMR. The NMR spectrum of TATP shows only a singlet with a chemical shift of 1.41 ppm in deuterated acetonitrile [62]. It should be noted that the risk of unintentional explosive initiation increases with increasing mass of the TATP sample [63]. All syntheses were performed to provide approximately 100-200 mg of TATP. The peroxide is shock, static, and friction sensitive and was stored in vials covered with Parafilm to avoid unnecessary initiation hazards.

Electrochemical Measurements: Measurements were made using a CHI 760C potentiostat/galvanostat (Austin, TX). Glassy carbon, platinum, and gold working electrodes were polished with 50 nm alumina, rinsed with deionized water, and allowed to dry before use. A silver wire pseudo-reference electrode and platinum counter electrode were used in all electrochemical cells. The ferrocene/ferrocenium couple was used as an internal reference in some cases. The voltammetric waves associated with ferrocene interfered with the voltammetric waves corresponding to the reduction products of TATP; therefore, the internal reference was left out of many solutions. The reference will be explicitly stated wherever potentials are reported.

Bulk Electrolysis: Bulk electrolysis experiments were performed using a Princeton Applied Research 273A potentiostat/galvanostat (Oak Ridge, TN). A three compartment cell separated by fine glass frits was used for electrolysis experiments. One compartment contained a platinum foil counter electrode. The center compartment contained a silver wire pseudoreference. These two compartments were filled only with supporting electrolyte solution, 100 mM TBAPF₆ in acetonitrile. The third compartment contained the same electrolyte solution and TATP. The electrolysis was performed inside a nitrogen atmosphere glove box at -1.7 V vs. Ag wire using a 4 mm glassy carbon working electrode. The progress of the electrolysis was monitored periodically via cyclic voltammetry at the same electrode.

Digital Simulations: Digital simulations of cyclic voltammetric results were performed using Digisim version 3.03b (BASi, West Lafayette, IN). The Digisim fitting algorithm is based on the implicit finite difference method developed by Feldburg, Goldstein, Mocak, and Rudolph [64-68]. The software can adjust the parameters: standard potential (E^o), transfer coefficient (α), heterogeneous rate constant (k_o), homogeneous reaction equilibrium constant (K_{eq}), homogeneous reaction rate constant (k_f), and diffusion coefficient (D), to fit experimental cyclic voltammograms. Background currents were subtracted from all the voltammograms used for digital simulations by subtracting the voltammetric signal obtained at the same electrode in an acetonitrile solution of 100 mM TBAPF₆ that did not contain TATP.

Catalytic Reduction: The search for catalytic reducing agents for TATP was performed on a screening basis in which solution concentrations were qualitatively controlled. Generally, a solution of the potential catalytic reducing agent was made at

approximately 1 mM. The cyclic voltammogram of this solution was recorded. Then, an approximate 10-fold, or greater, excess of TATP was added to the solution and the voltammogram was recorded again. Specific information about the solutions is given in the results and discussion section.

Nafion Electrodes: Nafion coated electrodes were prepared using a 5% Nafion solution in a mixture of alcohols and water. The electrodes were prepared in two ways. Drop coating was done by using a disposable pipette to deposit 1-2 drops of the Nafion solution onto the electrode surface. The solution was spread out to cover the entire metal surface and then the electrode was allowed to dry in an oven at 40 °C for at least 5 hours before use. Spin coating was done using an analytical rotator designed for rotating electrode electrochemical experiments. For spin coating, the Nafion solution was placed onto an inverted rotating disk electrode and the film was cast by rotating at 1200 rpm for 30 seconds and dried as described above.

Tris-(2-2'bipyridine) ruthenium (II) hexafluorophosphate preparation: Tris-(2-2'bipyridine) ruthenium (II) dichloride (Sigma-Aldrich, St. Louis, MO) was converted to the hexafluorophosphate salt before use. An aqueous solution of a 10 fold excess of ammonium hexafluorophosphate (Elf Atochem, Philadelphia, PA) was added to an aqueous solution of tris-(2-2'bipyridine) ruthenium (II) dichloride. The orange precipitate was collected via vacuum filtration and washed with deionized water. The product was recrystallized from an acetone solution by slow evaporation of diethyl ether. The resulting crystals were collected via vacuum filtration, washed with diethyl ether and allowed to dry before use.

Results and Discussion

TATP Electrochemistry, Position of the Reduction Wave: A relatively large potential must be applied to an electrode surface to reduce TATP. The cyclic voltammogram of 3.9 mM TATP in acetonitrile containing 100 mM TBAPF₆ as the supporting electrolyte is shown in Figure 2.2. The reduction of TATP occurred at potentials more than 2 V negative of the $E_{1/2}$ of ferrocene in the same solution. Evidence presented in the literature may help to explain why a compound with three peroxide moieties is so resistant to reduction. In 1960 Kuta and Quackenbush polarographically determined the $E_{1/2}$ of 23 peroxide compounds. They found that, generally, as the functional groups surrounding the peroxide moiety changed from electron withdrawing to electron donating the polarographic reduction wave shifted to increasingly negative values [69]. A similar trend has been reported by others [70]. Simple electrostatic arguments validate this observation. As the electron density in the oxygen-oxygen bond increases, it becomes less favorable to add additional electrons through reduction [69]. Maciel et al., using computational methods, provided even more support for this explanation when they showed that for x-butyl hydroperoxide ($x = n, sec, tert, iso$) the bond length of the peroxide moiety decreased from 1.460 Å to 1.449 Å when the alkyl group was changed from *n*-butyl to *tert*-butyl or *sec*-butyl, indicating an increase in the electron density of the peroxide bond [71]. A similar bond shortening was calculated when the alkyl moiety was changed from *n*-propyl to *iso*-propyl [71].

It should be noted that the $E_{1/2}$ values reported by Kuta and Quackenbush mentioned above, and all $E_{1/2}$ values for irreversible electron transfer reactions, are not thermodynamic values. The $E_{1/2}$ values observed for irreversible electron transfer

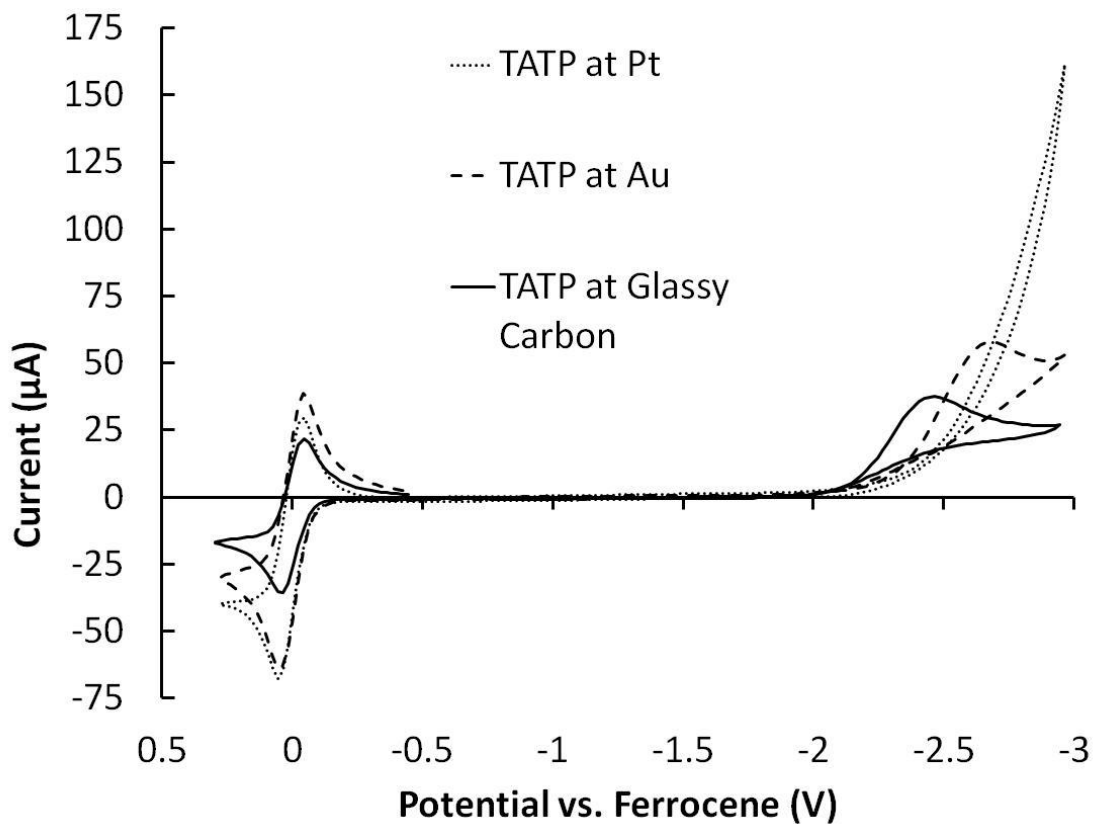


Figure 2.2. Cyclic voltammograms of 3.9 mM TATP with 100 mM TBAPF₆ in acetonitrile collected at three different electrode types, Au (2 mm), Pt (2 mm), and glassy carbon (1.6 mm) at 100 mV/s. A silver wire pseudoreference and platinum wire counter electrode were use in the cell. The potential axis has been corrected to the ferrocene internal standard.

reactions can be influenced by the kinetics of the electron transfer, as well as the kinetics of subsequent reactions [72]. The influence of following reactions was demonstrated by the report that for the small set of structurally similar hydroperoxides: hydrogen peroxide, methyl hydroperoxide, ethyl hydroperoxide, isopropyl hydroperoxide, and *tert*-butyl hydroperoxide, the $E_{1/2}$ values in aqueous solution shifted in the positive direction with values of -0.866 V, -0.791 V, -0.444 V, -0.350 V, and -0.330 V (vs. SCE), respectively [70]. Increasing adsorption of the reduction products, which are generally alcohols, as the alkyl chain length increases is the generally accepted explanation for this trend [70].

Ultimately, electrostatic arguments suggest that the electron donating isopropyl moieties in the TATP molecule may shift the $E_{1/2}$ to more negative values than the thermodynamic E° for the compound. As discussed below, the reduction products of TATP may adsorb to the electrode surface, and, as mentioned above, adsorption may result in a positive shift in $E_{1/2}$. The experiment that demonstrated a positive shift in $E_{1/2}$ for the alkyl hydroperoxide series discussed in the previous paragraph was carried out in aqueous solution [70]. The voltammetric reduction of TATP, shown in Figure 2.2, took place in nonaqueous, aprotic media so there were no solvent protons available to form alcohols in the TATP reduction experiment. Therefore, the reaction mechanism for the reduction of TATP was different than the mechanism for the reduction of the alkyl hydroperoxides and these two experiments are not directly comparable.

Further evidence that the medium affects the mechanism for the reduction of peroxides comes from the cyclic voltammograms shown in Figure 2.3. In this experiment the cyclic voltammograms of phenol (30 mM), TATP (6 mM), and phenol with TATP (52 mM and 6 mM, respectively) were recorded in an acetonitrile solution

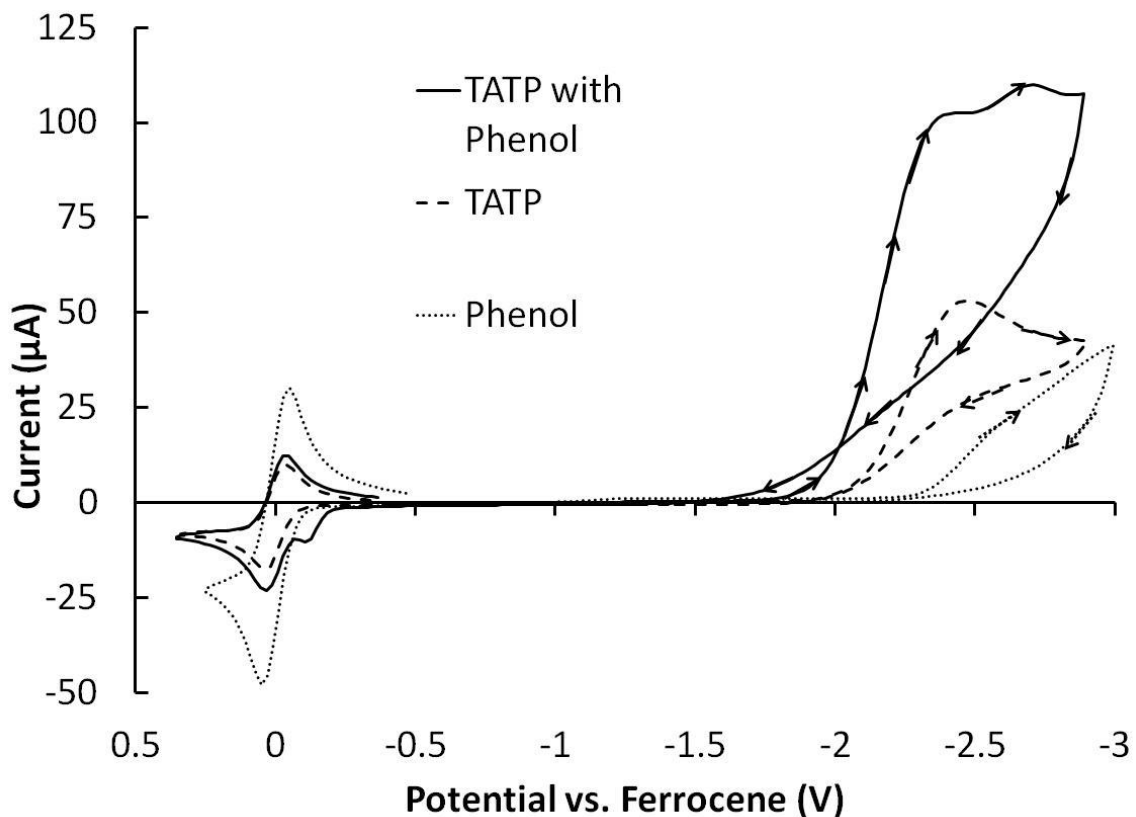


Figure 2.3. The cyclic voltammograms of TATP, phenol, and a mixture of the two chemicals. Each voltammogram was collected using a 1.6 mm glassy carbon electrode with a silver wire pseudoreference and a platinum counter electrode at a scan rate of 100 mV/s. The initial potential was -0.5 V and initial sweep direction was negative. The potential axis has been corrected to the ferrocene internal reference. The concentrations are as follows: Phenol alone, 30 mM; TATP alone, 6 mM; TATP with phenol, 6 mM and 52 mM respectively. The supporting electrolyte in all cases was 100 mM TBAPF₆ in acetonitrile.

containing 100 mM TBAPF₆ as supporting electrolyte. The reduction wave for TATP shifted in the positive direction in the presence of phenol. The change in the shape of the reduction wave for TATP, and the appearance of a small peak near the ferrocene wave in the presence of phenol, indicated that the mechanism and products of the reduction of TATP in the presence of phenol differed from the mechanism and products of the reduction of either TATP or phenol alone. One plausible explanation for the observed change in the mechanism is that the phenol provides a proton source for the TATP reduction products. Yamshchikov and Levin used phenol as a proton source in their work examining the mechanism of the polarographic reduction of some organic peroxides [73]. Another possible explanation is that, upon reduction, the peroxide reacts with phenol in a way more complex than a simple proton transfer. The change in the appearance of the voltammogram in the presence of phenol shows that a different following reaction, whether it is protonation or another process, with different kinetics, can change the mechanism for the reduction of TATP, and can cause a significant shift the observed $E_{1/2}$.

The effects of electrostatics and adsorption are not the only possible factors contributing to position of the reduction wave. Electrochemical studies using *tert*-butyl peroxides suggest that steric effects may also contribute. Salvato et al. and the team of Kuta and Quackenbush were unable to polarographically reduce di-*tert*-butyl peroxide [69, 74]. The authors attribute this result to steric effects that block the peroxide moiety from reaching the electrode surface. Vasudevan performed cyclic voltammetric experiments on di-*tert*-butyl peroxide using a glassy carbon electrode and was able to reduce the compound at approximately -2.5 V (vs. Ag wire) in organic solutions [75].

One might expect that a 9-member ring system, like TATP, would be immune to these steric effects because the ring would be constantly moving so that, at any given time, the peroxides would be accessible. According to results published by Denekamp et al. this may not be the case. In their computational study, the authors showed that two kinetically stable conformers (D_3 and C_2) of TATP exist at room temperature, and that the conformers are separated in energy by 1.85 kcal mol⁻¹. Their calculations indicate that the energy barrier between the two conformers is 26.3 kcal mol⁻¹. This barrier is high enough to prevent the “flip-flop” transition between the two conformers at room temperature. The authors also observed the presence of both conformers experimentally in the crystal structure of TATP [76]. Additional evidence for the presence of two separable conformers comes from HPLC and GC analysis of TATP, which exhibited two distinct peaks, rather than one, in their respective chromatograms [77, 78]. Haroune et al. provided further support by separating the conformers and identifying them using LC-NMR [62]. It is likely, based on reports that the ring is relatively rigid, coupled with the reports that TATP does not react with typical peroxide detection reagents like iodide, that sterics do play some role in TATP’s resistance to reduction [11].

Voltammetric Differences at Various Electrode Surfaces: Figure 2.2 shows that the reduction of TATP occurred at different potentials depending on the type of electrode used. Glassy carbon and gold electrodes provided voltammograms with a wave shaped response on the negative potential sweep. At platinum electrodes, electrolyte degradation occurred before any peak was observed. Therefore, platinum electrodes were not particularly useful for the analysis of the reduction of TATP at an electrode surface. At a gold electrode, the response after reversal of the sweep direction, from negative to

positive, showed a hysteresis near the foot of the reduction wave. The hysteresis indicated that the overpotential required to reduce the species that were present at the electrode surface on the positive potential sweep was lower than the overpotential that was required to reduce the TATP on the negative potential sweep. Glassy carbon electrodes were used for the analysis of the reduction of TATP at an electrode surface because they displayed a response that looked like the “classic” irreversible electron transfer case, as described by Bard and Faulkner [79].

The decision to use glassy carbon electrodes for the analysis of the heterogeneous reduction of TATP is consistent with other work presented in the literature that utilized glassy carbon electrodes for electrochemical studies of other organic peroxides [75]. Some researchers have noted that the use of glassy carbon electrodes for the analysis of the reduction of peroxides resulted in irreproducible currents [74]. Irreproducible voltammetry was not problematic for the work presented in this chapter, provided that the electrodes were polished between each electrochemical experiment. The previous reports that some authors observed irreproducible currents with glassy carbon electrodes further illustrates that the electrochemistry of organic peroxides cannot readily be generalized because subtle differences in compounds or conditions can affect the results of an experiment.

Cyclic Voltammetry: The heterogeneous electrochemical reduction of di-alkyl peroxides, such as di-tert-butyl peroxide, at an electrode surface in aprotic media can be described as an irreversible two-electron process [80]. As expected, the reduction of TATP at a glassy carbon electrode surface also displayed the characteristics of an irreversible electron transfer reaction. Figure 2.4 shows the voltammetric response of

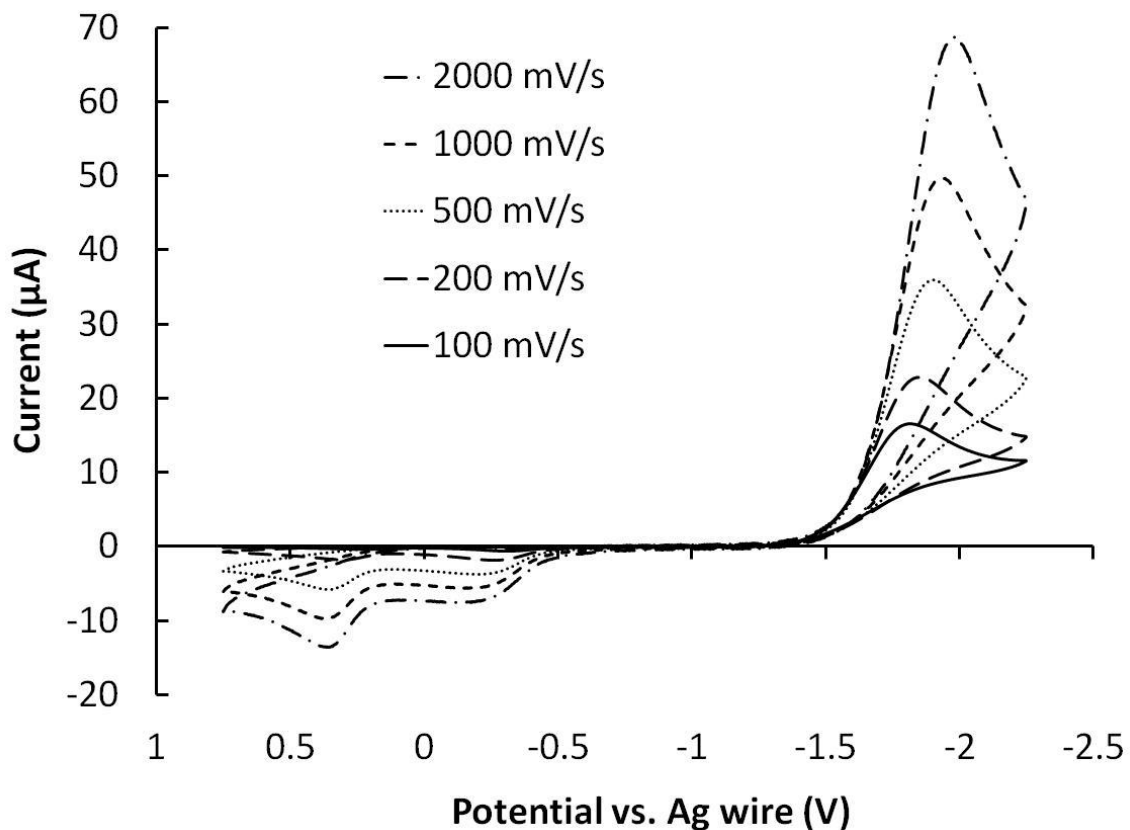


Figure 2.4. Cyclic voltammograms of a 1.96 mM TATP solution with 100 mM TBAPF₆ in acetonitrile at a 1.6 mm glassy carbon electrode, potentials vs. Ag wire. Plotted are scan rates of 100, 200, 500, 1000, 2000 mV/s. The initial potential was 0 V and the initial sweep direction was negative. The voltammograms have been corrected for background currents by subtracting the signal produced by the same electrode in a 100 mM TBAPF₆ solution. Electronic iR compensation was applied to each experiment.

TATP at a glassy carbon electrode cycled over rates ranging from 100 mV/s to 2000 mV/s. The voltammograms shown in Figure 2.4 have been corrected for background current, and electronic iR compensation was applied to each experiment. The absence of an oxidation peak upon reversal of the direction of the potential sweep, from negative to positive, is one indication that the electron transfer reaction is irreversible. In addition, the peak potential (E_p) shifts cathodically with increasing scan rate, as predicted for an irreversible charge transfer system [79]. Using the theory developed by Nicholson and Shain [72], one can calculate some information about the reduction of TATP at a glassy carbon electrode from the data shown in Figure 2.4. The E° for an irreversible electron transfer reaction at an electrode surface is rarely known [72]. However, Nicholson and Shain derived the following relationship,

$$\left| E_p - E_{1/2} \right| = \frac{1.857 RT}{\alpha n F} \quad (2.10)$$

where E_p , $E_{1/2}$, R , T , α , n , and F are the peak potential, half peak potential, gas constant, temperature, transfer coefficient, number of electrons, and Faraday's constant, respectively, which can be used to determine the value of αn for an irreversible electron transfer process [72]. The application of equation (2.10) on the data in Figure 2.4 resulted in an average value of $\alpha n = 0.246 \pm 0.008$ at the 95% confidence level. Nicholson and Shain also reported that for an irreversible electron transfer system the voltammetric peak potential should shift by $30/\alpha n$ mV for every ten-fold increase in the scan rate [72]. A plot of the peak potential vs. $\log_{10}(\text{scan rate})$, as shown in Figure 2.5, resulted in a linear correlation. By assuming the slope of the best fit line calculated for this data was equivalent to $30/\alpha n$, I obtained a value of $\alpha n = 0.241$, which is consistent

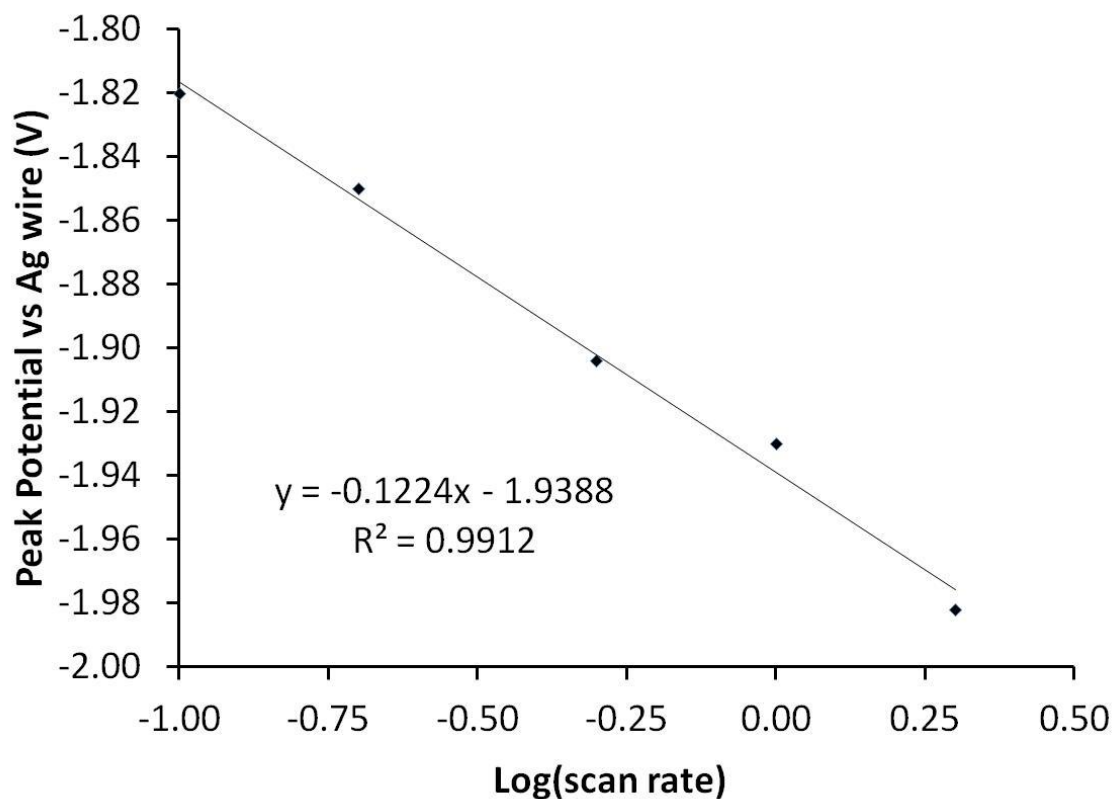


Figure 2.5. The peak potential theoretically varies by $30/\alpha n$ with each 10 fold increase in the scan rate for an irreversible electron transfer at an electrode surface. Using the slope of the plot of peak potential vs. $\log(\text{scan rate})$ allowed for the calculation of αn for the reduction of TATP. Based on this theory, $\alpha n = 0.241$.

with the previous calculation and provided a starting point for further analysis, which is discussed below.

Several additional observations about the reduction of TATP at electrode surfaces can be made based on cyclic voltammetry experiments. The reduction of TATP is irreversible at a 1 mm diameter glassy carbon electrode at any scan rate that produced meaningful data. The data collected at faster scan rates using a 1 mm diameter electrodes was not meaningful because the influences of iR drop significantly distorted the voltammograms, even when electronic iR compensation was employed. The reduction of TATP is also irreversible at up to 10,000 V/s when a 10 μm diameter gold electrode is used, but, as discussed above, the reduction of TATP takes place via a different mechanism at gold electrodes. Therefore, the results obtained using gold electrodes are not directly comparable to those obtained using glassy carbon electrodes. Another observation, based on the voltammogram shown in Figure 2.6, is that the products of the reduction of TATP results in two oxidation waves that are observed on the positive potential sweep subsequent to the TATP reduction. One of these oxidation waves appears at approximately -0.3 V (vs. Ag wire) and the other at approximately 0.3 V (vs. Ag wire). The reduction wave that is observed at approximately -0.75 V (vs. Ag wire) on the second negative potential sweep of the voltammogram shown in Figure 2.6 only appears if the electrode is swept in the negative direction again immediately following the first voltammetric cycle. The identities of the species responsible for the voltammetric waves at -0.3 V, 0.3 V, and -0.75 V are not currently known. The voltammograms shown in Figure 2.7 suggests that an adsorption process occurs when TATP is reduced at a glassy carbon electrode surface. Alternatively, it is possible that

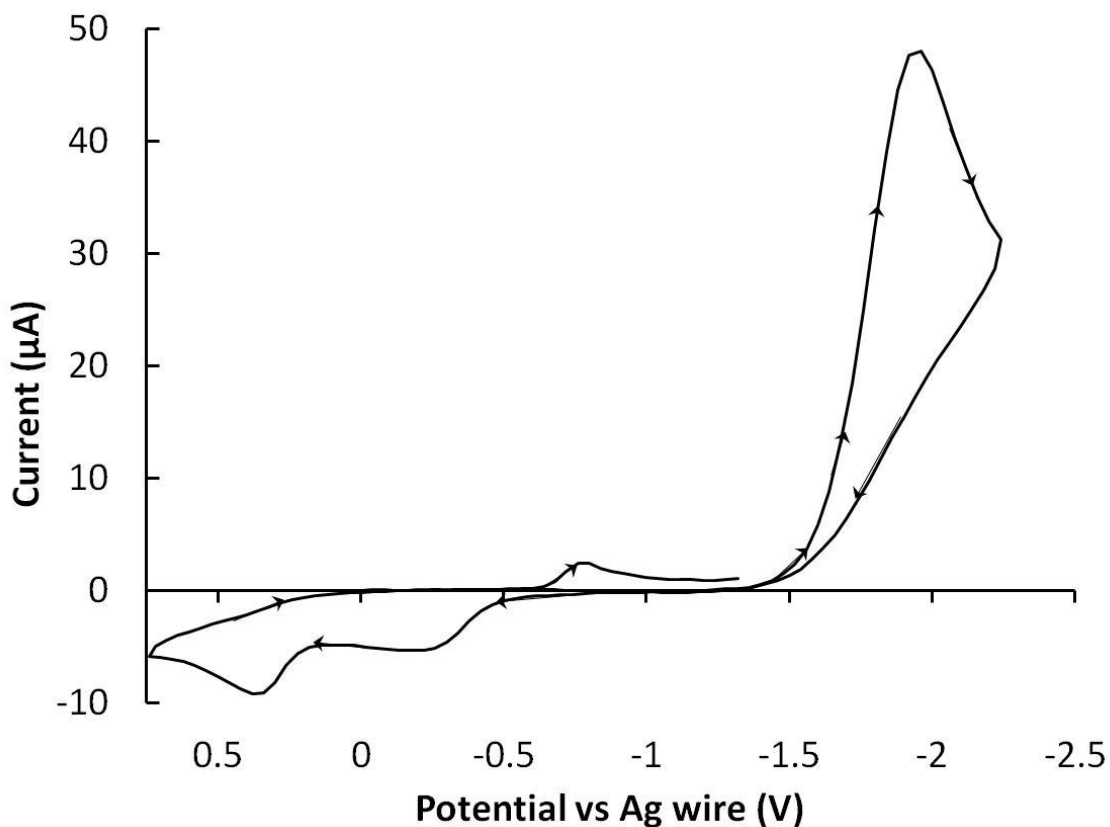


Figure 2.6. Cyclic voltammogram of a 1.96 mM TATP solution with 100 mM TBAPF₆ in acetonitrile at a 1.6 mm glassy carbon electrode at a scan rate of 1 V/s. The initial potential was -1 V and the initial sweep direction was negative. The peak at ca. -0.75 V appears only on the second sweep in the negative direction. The voltammogram has been corrected for background currents by subtracting the signal produced by the same electrode in a 100 mM TBAPF₆ solution. Electronic IR compensation was applied to the experiment.

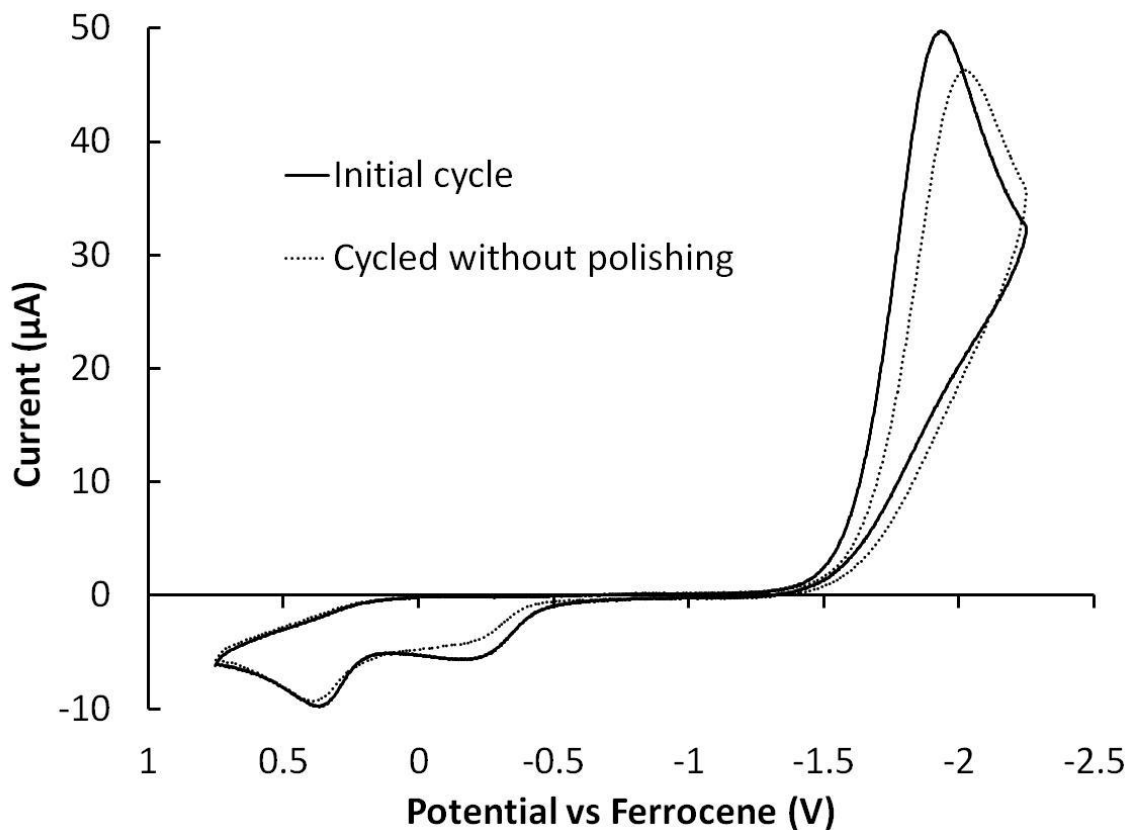


Figure 2.7. Cyclic voltammograms of TATP in acetonitrile with 100 mM TBAPF₆ at a glassy carbon electrode at a scan rate of 1 V/s. The initial potential was -0.5 V and the initial sweep direction was negative. The initial cycle was collected at a freshly polished electrode; the subsequent voltammogram was collected at the same electrode without polishing.

the electrode surface is changed in some other manner (by the reduced but still highly oxidized products) to produce heterogeneous electron transfer kinetics that are no longer as facile. When a glassy carbon electrode is cycled once through the TATP reduction wave, the solution stirred, and the electrode cycled through the reduction wave again, the wave shape remains roughly consistent, but the peak height decreased and shifted slightly in the cathodic direction indicating the adsorption of a passivating layer, or that the reaction products have been swept away so that they cannot react with the electrode surface.

Bulk Electrolysis: Yamshchikov and Levin reported that the reduction of some organic peroxides at an electrode surface takes place via a single electron transfer ($n=1$) process in aprotic solvents [70, 73]. Based on this report, and the number of peroxide moieties in TATP, one could surmise that the number of electrons transferred to TATP upon reduction at an electrode surface could be anywhere from 1 to 6. As such, a measurement of the value of n , which is not available from the voltammetric experiments described above, became important. Bulk electrolysis was employed for this determination.

The results for one bulk electrolysis are shown in Figure 2.8. The working electrode compartment originally contained 3.5 mg of TATP. Using Faraday's law, one can calculate that for this quantity of TATP (1.57×10^{-5} moles), 1.5 coulombs of charge should pass per electron transferred. The plot of charge passed in the electrolysis cell over the duration of the experiment, shown in Figure 2.8 (top), reveals that the charge approaches 3 coulombs, indicating that under these conditions TATP undergoes a two-electron reduction.

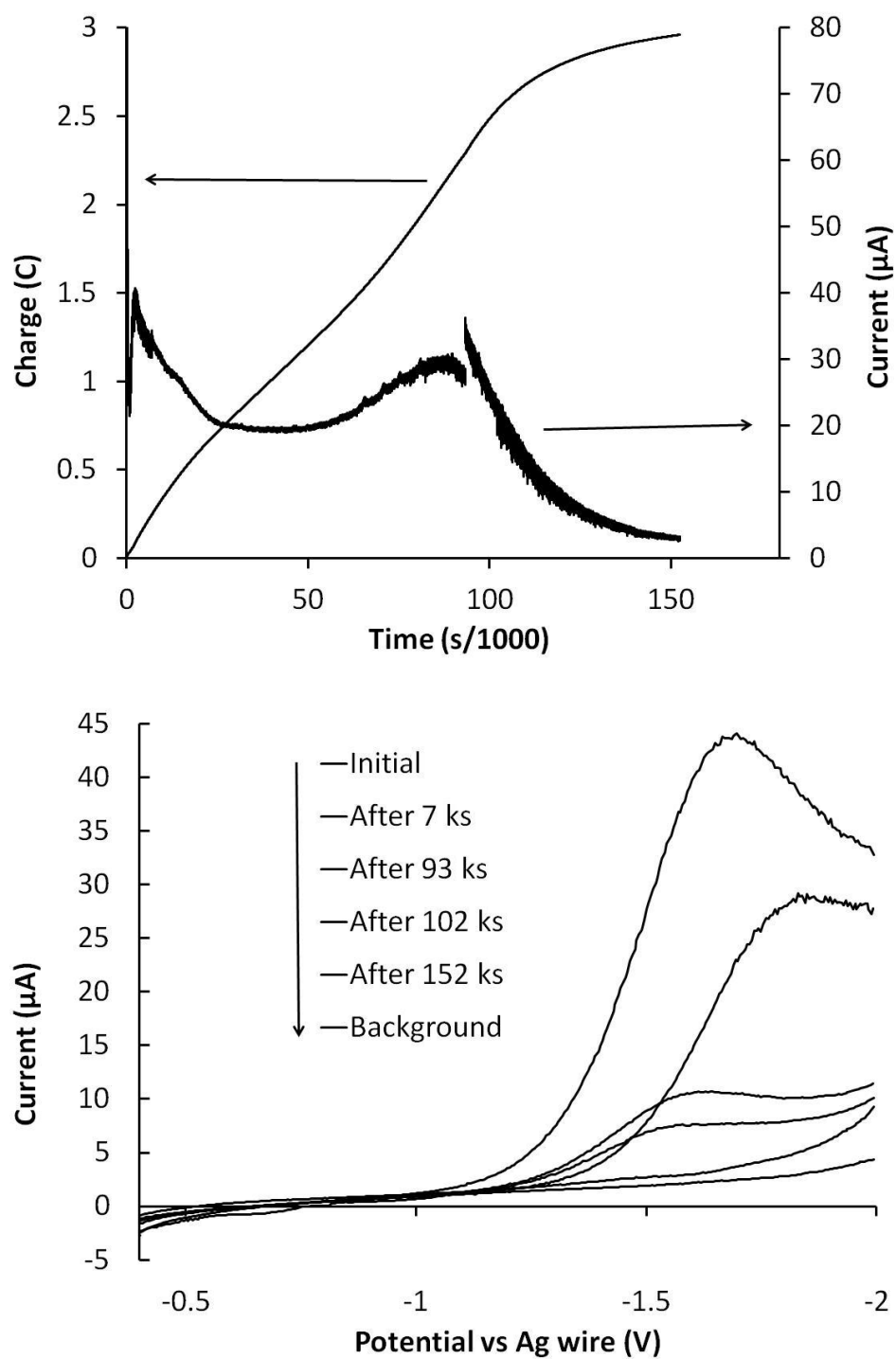


Figure 2.8. Bulk electrolysis current and charge (top) and progressive linear sweep voltammogram (bottom). The voltammetric peak current decreased with increasing electrolysis time.

To monitor the progress of the electrolysis, I periodically recorded cyclic voltammograms. Figure 2.8 (bottom) shows that the voltammetric current decreases with electrolysis time until it reaches a value near the background. The decrease in the voltammetric current and the decay of the electrolysis current from ca. 80 μA to 3 μA provides further verification that the electrolysis performed under these conditions had reached completion.

The duration of the preceding bulk electrolysis was quite long making it possible that some small fraction of the TATP originally in the solution diffused through the glass frit separator and into the reference electrode compartment of the cell. However, the products of the reduction of TATP caused the solution in the working electrode compartment to turn distinctly yellow. The solution in the reference electrode compartment did not become discolored leading me to the conclusion that loss of TATP by diffusion through the separator was insignificant, and that my value of $n=2$ was reliable.

Digital Simulation: I wanted independent verification of reduction stoichiometry determined by bulk electrolysis. Digital simulations were performed to provide this verification. Evidence in the literature shows that the heterogeneous reduction of alkyl peroxides at electrode surfaces often occurs via an irreversible electron transfer followed by some form of chemical dissociation [75, 80, 81]. I attempted to model the cyclic voltammetric response for the reduction of TATP in acetonitrile solutions with the digital simulation software Digisim, using an electron transfer followed by a chemical reaction (EC) mechanism.

I began by examining the voltammogram obtained at a scan rate of 200 mV/s. Previous analysis of the voltammetric peak potentials, described above, resulted in an average value for the transfer coefficient (α) of 0.245/n. This value provided a starting point for α in the simulations. When the software was allowed to adjust α , the value did not change significantly, which helped to validate the previous result. When the diffusion coefficients of the chemical species were allowed to adjust during the simulations the resulting values were physically unreasonable. The voltammetric peak current for an irreversible charge transfer system is proportional to the square root of the diffusion coefficient of the redox active species [79]. The square root dependence means that a diffusion coefficient must change by a relatively large amount to have a significant impact on the magnitude of currents in the calculated voltammograms. The diffusion coefficients used in the simulations were fixed at $2 \times 10^{-5} \text{ cm}^2/\text{s}$. This value was chosen because the diffusion coefficients of small molecules in acetonitrile solutions have been shown to be approximately $2 \times 10^{-5} \text{ cm}^2/\text{s}$ by several authors, and as mentioned above, small deviations from this value would have little impact on the simulated voltammograms [82-84]. The initial values for the heterogeneous rate constant (k_o), the homogeneous reaction equilibrium constant (K_{eq}), and the homogeneous rate constant for the forward reaction (k_f) were selected based on the qualitative characteristics of the voltammograms. A small heterogeneous rate constant manifests itself as a large overpotential for electron transfer [79]. A low initial value for k_o ($1 \times 10^{-4} \text{ cm/s}$) was used in the simulations of the voltammetric response for TATP reduction because the reduction wave appears at relatively negative potentials. K_{eq} and k_f were initially set to large values (1×10^5 , and $1 \times 10^5 \text{ s}^{-1}$, respectively) because no voltammetric peak was

observed upon reversing the potential sweep to the positive direction. The rate constants (k_o , k_f) and the equilibrium constant (K_{eq}) were allowed to adjust until a local minimum was achieved for the data at 200 mV/s. The rate constants and the equilibrium constant that resulted from the simulation of the voltammogram collected at 200 mV/s were then used to model the voltammograms collected at 100, 500 and 1000 mV/s. The parameters calculated from the 200 mV/s data provided reasonable fits for the data collected at each of the other scan rates, as displayed in Figure 2.9.

The E^o for the half reaction involving the voltammetric reduction of TATP is not known, nor can I reasonably determine it from my experimental results. E^o used in the model can be fixed at different values and by adjusting the heterogeneous rate constant, an equivalent fit can be achieved. Table 2.1 summarizes the variation in k_o as the value of E^o was adjusted from -1.1 V to -1.6 V while all other parameters were held constant. It was not possible to perform the simulations using E^o values more positive than -1.1 V because the modeling software calculates the equilibrium concentrations of the reactants before the simulation, and when I input E^o values more positive than -1.1 V, the equilibrium concentration of TATP, calculated by the software, was significantly lower than the analytical concentration. The variation in k_o as E^o was adjusted to different values demonstrates that the values calculated for the rate constants are not quantitatively meaningful. Qualitatively, regardless of the exact k_o used in the model, the voltammetric response is well described by an electron transfer followed by a fast chemical reaction. The k_o for the ferrocene/ferrocenium couple has been reported to be 6×10^{-2} cm/s [85]. The k_o calculated for the reduction of TATP using $E_o = -1.6$ V (i.e., 1.09×10^{-3} cm/s) is an

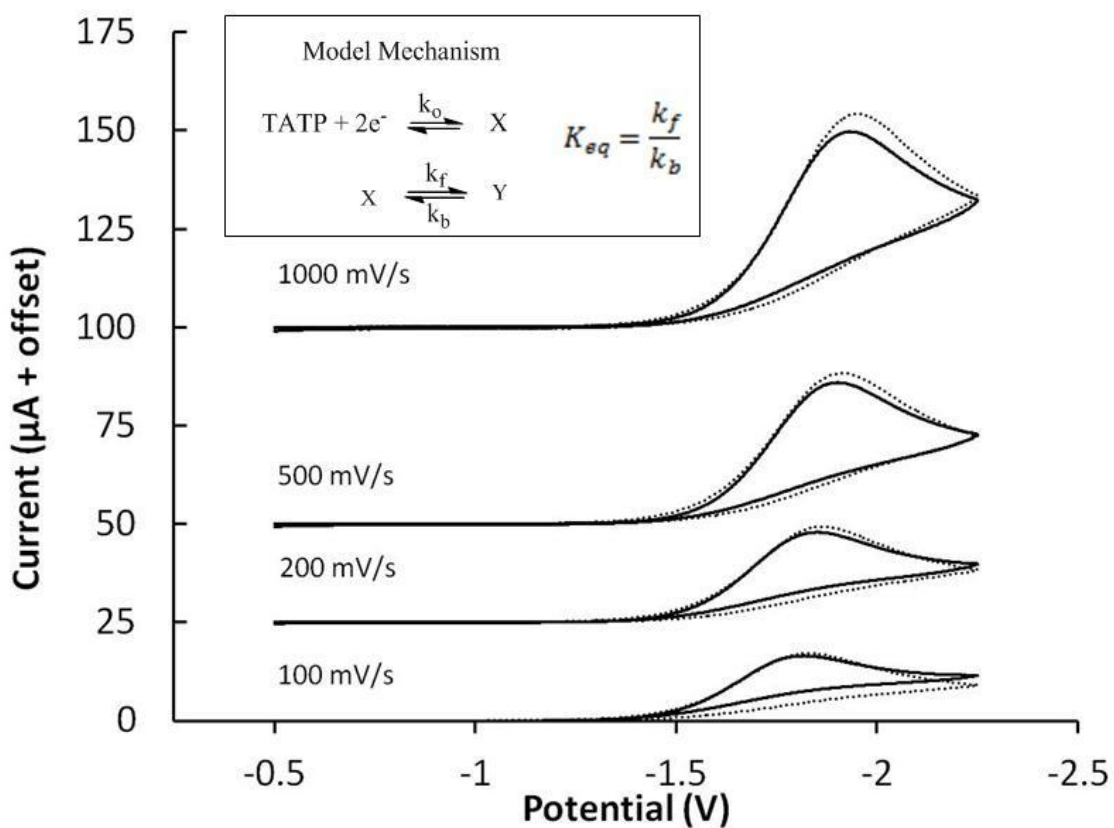


Figure 2.9. Results of digital simulations using Digisim. The experimental voltammograms are solid lines. The fitting results are overlaid as dotted lines. The values of the fitting parameters were $E^o = -1.4$ V, $\alpha = 0.122$, $k_o = 1.64 \times 10^{-4}$ cm/s, $K_{eq} = 1.0 \times 10^{16}$, $k_f = 2.0 \times 10^{20}$ s $^{-1}$.

Table 2.1. Average digital simulation best fit heterogeneous rate constants (k_o) for scan rates 100, 200, 500, 1000 mV/s while adjusting the E_o and holding all other parameters constant.

Fixed E_o (V)	Average Rate Constant (k_o) (cm/s x 10^3)	Standard Deviation (cm/s x 10^3)
-1.1	0.0094	0.0001
-1.2	0.0243	0.0002
-1.3	0.0628	0.0005
-1.4	0.162	0.002
-1.5	0.420	0.004
-1.6	1.09	0.01

order of magnitude lower than the value reported for ferrocene. One would expect that the E^o for TATP is likely more positive than -1.6 V because of the three peroxide groups in the molecule, and, by extension, that k_o is likely smaller than 1.09×10^{-3} cm/s. A qualitative conclusion one can draw from the simulations is that, assuming E^o is more positive than -1.6 V, the electron transfer is slow when compared to ferrocene. The fits shown in Figure 2.9 were not perfect matches to the experimental data. As shown in Figure 2.7 and discussed above, the reduction of TATP at a glassy carbon electrode in acetonitrile solutions produces some changes to the electrode surface. The simulation software is not capable of accounting for these changes, and one can hypothesize that these effects are the reason that the simulations do not fit experimental results more precisely. Despite the minor imperfections, the simulations are a good fit to the experimental data and match the logical conclusions one might make upon visual inspection of the voltammetric wave shapes.

The results of the digital simulations can be used to support some general conclusions about the reduction of TATP at a glassy carbon electrode surface. First, two electrons are transferred in the reduction of TATP. No reasonable fit of the voltammetric data could be achieved with $n = 1, 3, 4, 5,$ or 6 electrons, regardless of how the other parameters were adjusted. The value $n = 2$, as determined from the simulations, verified the result obtained from the bulk electrolysis experiment discussed above. Additionally, the value $\alpha = 0.122$, calculated from the simulations, closely matches the value calculated above using peak potentials of the voltammograms. Based on the results of the simulations, the reduction of TATP at a glassy carbon electrode is well described by a relatively slow two-electron transfer followed by a very fast chemical reaction, which,

based on evidence presented in the literature, is likely the dissociation of a peroxide [75, 80, 81].

Catalytic Reduction, Introduction: I attempted to identify compounds that would catalytically reduce TATP through homogeneous electron transfer mediation at potentials less negative than those observed for the direct reduction of TATP at a bare electrode. A compound capable of mediating this catalytic reduction could be the basis for an electrochemical sensor that is selective for TATP. Additionally, or alternatively, an efficient catalytic reducing agent could be employed to electrochemically destroy TATP.

I used cyclic voltammetry to screen potential catalytic reducing agents, and looked for two qualitative diagnostic criteria in the voltammograms. One criterion was a positive shift in the reduction wave for TATP, corresponding to a reduction of the mediating species. The other criterion was the indication of a catalytic mechanism. The voltammetric response for a catalytic reaction sequence, like the one shown in equations (2.3) and (2.4), would appear as some form of increased current in the presence of TATP and a reversible or quasireversible wave in the absence of TATP [79]. Most of the species I examined were of little utility in this regard, but the screening process did lead to the identification and preliminary characterization of several interesting candidates. Examples of compounds that were tested, even those that showed no catalytic activity, are discussed below.

Porphyrins: As discussed in the introduction, electrochemical peroxide sensors have been developed that use horse radish peroxidase as a transducer [52, 53, 86]. The enzyme has an iron porphyrin unit in the active site [55]. As such, I decided to test

several porphyrin derivative complexes containing three different metal ions, Co, Fe, and Rh, for catalytic activity with TATP.

Figure 2.10 shows the voltammogram for [2,3,7,8,12,13,17,18-octafluoro-5,10,15,20-tetraphenyl]porphyrinato]cobalt (F_8TPPCo) in the presence and absence of TATP. Two quasireversible waves are present in the voltammogram of F_8TPPCo . The first wave, at approximately -1 V (vs. ferrocene), corresponds to a metal center reduction of the F_8TPPCo/F_8TPPCo^- redox couple. The second wave, at approximately -2 V (vs. ferrocene), corresponds to the reduction of the macrocyclic π -system and the F_8TPPCo^-/F_8TPPCo^{2-} redox couple [87]. In the presence of TATP the wave corresponding to the F_8TPPCo/F_8TPPCo^- couple was distorted but the current did not increase significantly. A significant increase in the current did occur in the presence of TATP at potentials associated with the F_8TPPCo^-/F_8TPPCo^{2-} . The mediated electron transfer is complicated because it occurs close to the potential at which TATP reduces at the bare electrode surface, and the waves overlap. This process occurred at potentials so negative that it was of little catalytic utility, and I did not investigate it further.

Figure 2.11 (top) shows the voltammogram for [5,10,15,20-tetraphenylporphyrinato]iron(III)⁺ ($TPPFe^+$) in the presence and absence of TATP. The two quasireversible voltammetric waves are the result of metal center reductions corresponding to the $TPPFe^+/TPPFe$ redox couple at approximately 0 V (vs. Ag wire), and the $TPPFe/TPPFe^-$ couple at approximately -0.9 V vs. Ag wire [87]. Scanning the potential further in the negative direction did not reveal any additional redox activity. No change in the response occurred when TATP was added to the solution.

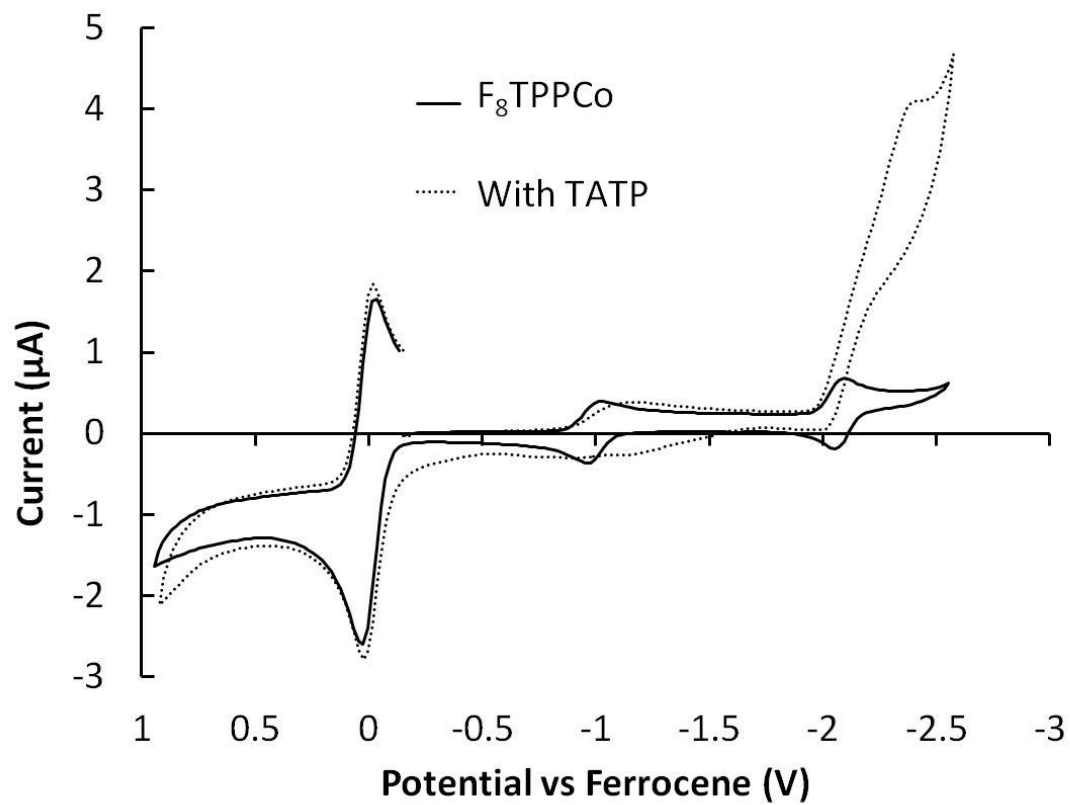


Figure 2.10. Cyclic voltammograms of F₈TPPCo with 100 mM TBAPF₆ at 100 mV/s in DMF at a gold working electrode both before and after the addition of TATP.

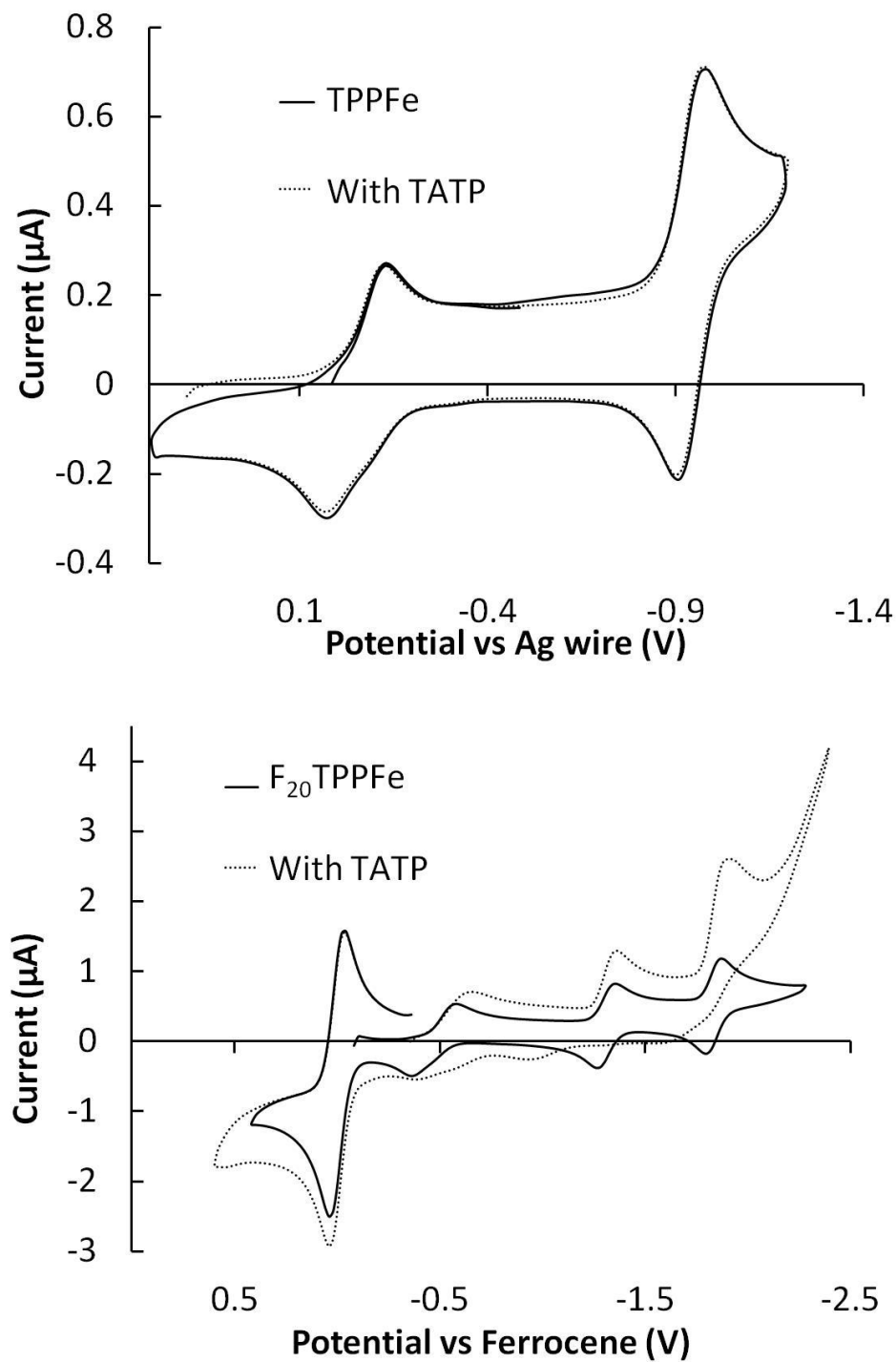


Figure 2.11. Cyclic voltammograms of TPPFe (top), and $\text{F}_{20}\text{TPPFe}$ (bottom). The voltammograms were collected in DMF solution with 100 mM TBAPF_6 as supporting electrolyte. The potential axis for $\text{F}_{20}\text{TPPFe}$ was corrected to the ferrocene internal reference. Both voltammograms were collected using Pt working electrodes at 100 mV/s.

Figure 2.11 (bottom) shows the voltammogram for 5,10,15,20-tetrakis(pentafluorophenyl)porphyrinato]iron(III)⁺ (F₂₀TPPFe⁺). Three reductions are observed in the electrochemical window of the DMF/TBAPF₆ electrolyte system used in the experiment. The voltammetric waves correspond to the F₂₀TPPFe⁺/F₂₀TPPFe couple (ca. -0.5 V vs. ferrocene), the F₂₀TPPFe/F₂₀TPPFe⁻ couple (ca. -1.3 V vs. ferrocene), and the F₂₀TPPFe⁻/F₂₀TPPFe²⁻ couple (ca. -1.8 V vs. ferrocene) [87]. The waves that appear at -0.5 V and -1.3 V (vs. ferrocene) are the result of metal center reductions. The electron withdrawing fluorine substitution shifts the reduction of the π-system far enough in the positive direction, when compared to the parent TPPFe⁺ complex, that it is accessible in the electrochemical window [87]. All three reduction waves of F₂₀TPPFe⁺ appear to show limited increases in current in the presence of TATP. The most significant increase in the current occurs with the reduction of the π-system at approximately -1.8 V (vs. ferrocene).

Figure 2.12 shows the voltammograms for the rhodium complexes of F₈TPP (top) and F₂₈TPP (bottom). The electrochemical behavior of fluorinated rhodium porphyrin complexes is highly dependent on the presence of axial ligands and the solvent in which the experiments are performed [88]. The voltammograms shown in Figure 2.12 were recorded in solutions containing the chloride salts of the F_xTPPRh⁺ complexes in THF solutions. The first reduction for each compound, which is observed at approximately -0.6 V and -0.3 V (vs. Ag wire) for the F₈TTP and F₂₈TPP complexes, respectively, appear irreversible for both compounds. This reduction corresponds to the F_xTPPRh⁺/F_xTPPRh redox couple [88]. The second reduction for each compound, which

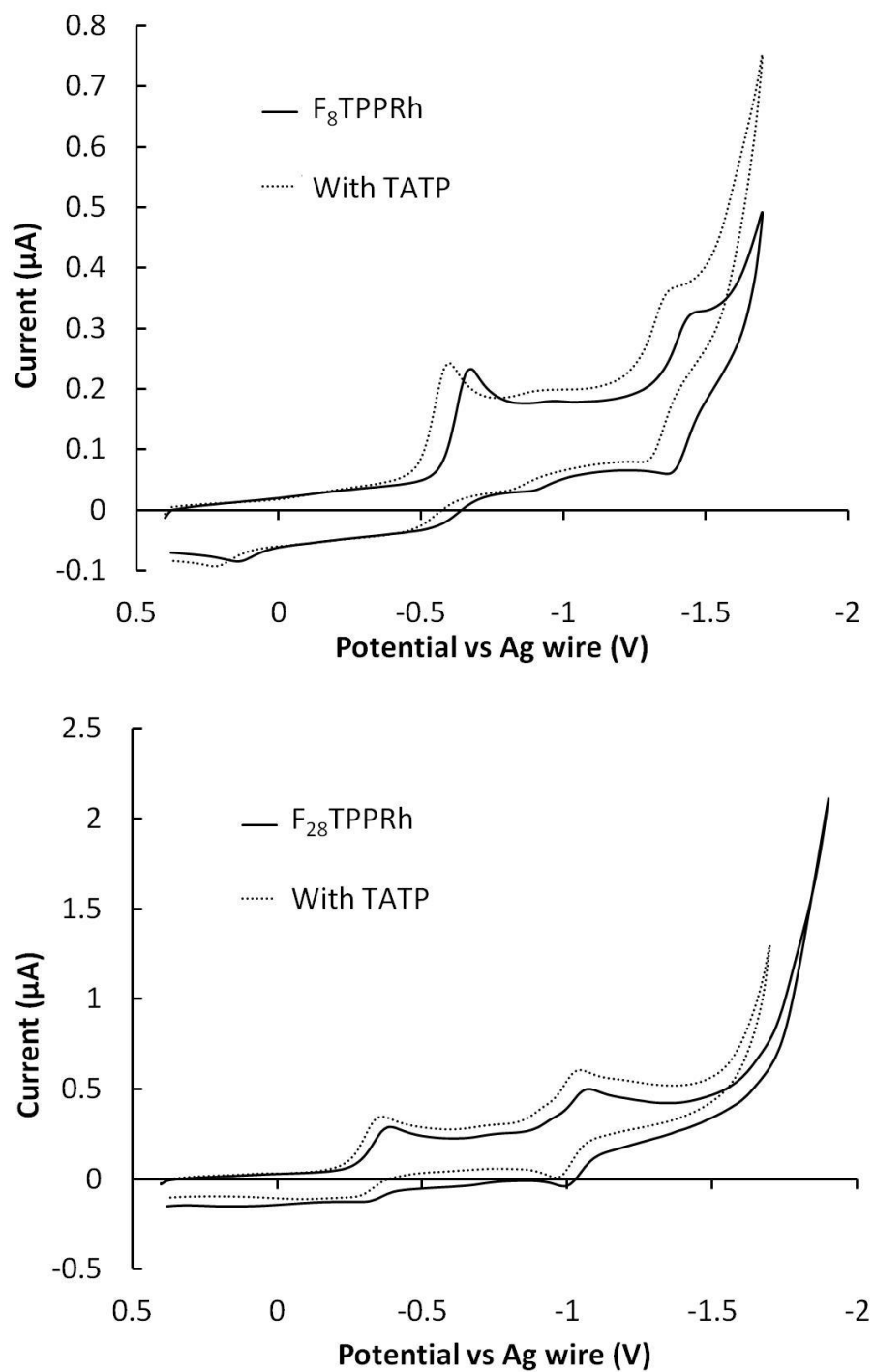


Figure 2.12. Cyclic voltammograms of $F_8\text{TPPRh}$ (top) and $F_{28}\text{TPPRh}$ (bottom) both before and after the addition of TATP in THF with 100 mM TBAPF_6 collected at a Pt working electrode with Ag wire pseudoreference at 100 mV/s.

is observed at -1.3 V and -1.0 V (vs. Ag wire) for the F_8TTP and $F_{28}TPP$ complexes, respectively, appears quasireversible for both compounds and corresponds to the F_xTPPRh/F_xTPPRh^- redox couple. It has been reported that the neutral oxidation state (F_xTPPRh) of fluorinated rhodium porphyrin complexes will undergo disproportionation in the presence of chloride ions [88]. It is likely that the chloride ions in this system were the reason for the irreversible characteristics that were observed. No catalytic response was observed in the presence of TATP for either the complex, so these compounds were not explored in greater detail.

Of the porphyrin compounds that I tested, $F_{20}TPPFe$ appears to be the most promising based on the increase in current observed with the π -system reduction in the presence of TATP, as shown in Figure 2.11. These compounds were not readily available for further investigation and their preparation is relatively complex and expensive [60, 61]. Therefore, I chose to explore other options for practical reasons.

Ferrous ion: Ferrous ion (Fe^{2+}) generated via the reduction of Fe^{3+} at an electrode surface was tested as a potential electron transfer mediator because it was observed that acetonitrile and DMSO solutions containing TATP and anhydrous $FeCl_2$ turned yellow over the course of several days under oxygen free conditions. The yellow color suggested that Fe^{3+} was generated by the reaction of the Fe^{2+} with TATP. I observed that the Fe^{3+}/Fe^{2+} couple is not voltammetrically reversible in acetonitrile solutions so the electrochemical analysis was performed in DMSO. The couple produces an essentially reversible voltammetric wave at approximately 0.1 V (vs. Ag wire), as shown in Figure 2.13. The presence of TATP does not result in an increase in the peak current when Fe^{2+}

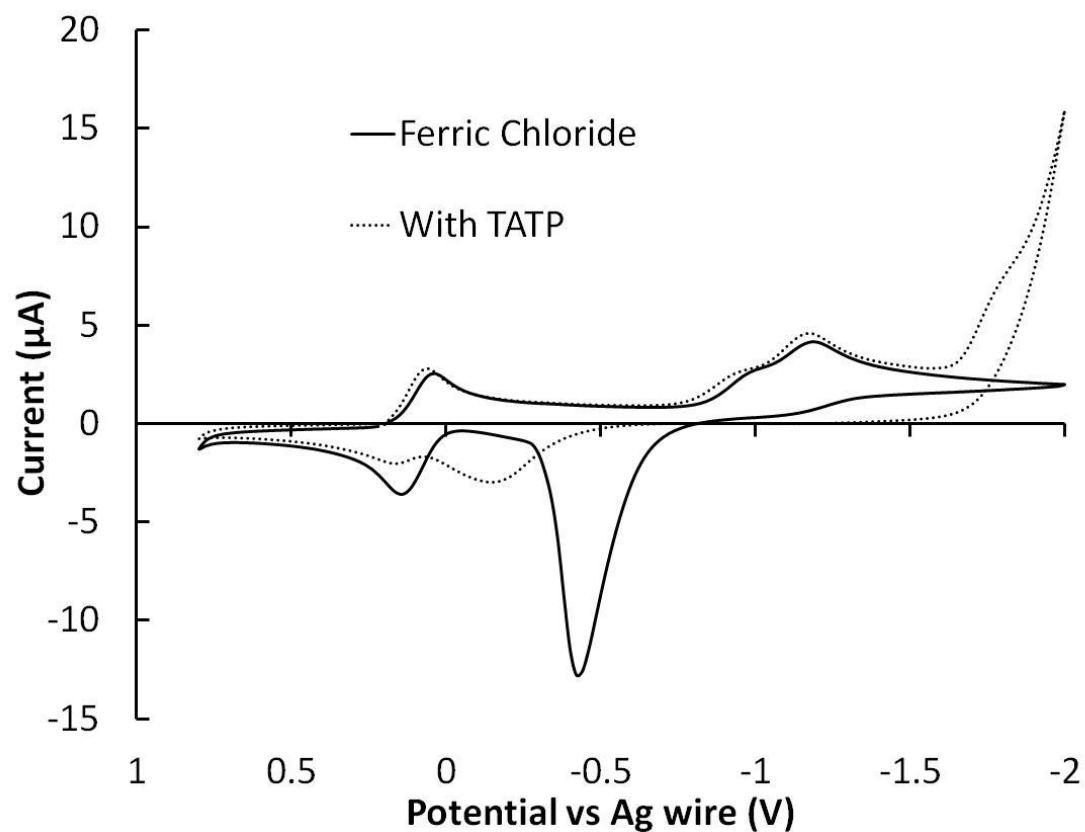


Figure 2.13. Cyclic voltammograms of FeCl_2 in DMSO before and after the addition of TATP. The solution contained 100 mM TBAPF_6 as supporting electrolyte and were collected at a Pt working electrode at 100 mV/s. The initial potential was 0.5 V and the initial sweep direction was negative.

is generated at the electrode surface, which indicates that on the timescale of the cyclic voltammetry experiment the reduction of TATP by Fe^{2+} does not occur.

Iron electrodeposition occurs at approximately -1 V (vs. Ag wire) and is followed by the direct reduction of TATP at the electrode surface. Reversal of the potential sweep to the positive direction in the presence of TATP reveals that the size of the peak associated with the oxidation of Fe^0 , which appears at -0.5 V (vs. Ag wire), is significantly diminished. A similar effect, caused by the presence of electrodeposited iron on an inert electrode surface, was demonstrated previously by Baron et al. in systems containing tert-butyl hydroperoxide in DMF [89].

Miscellaneous compounds: A compilation of the voltammograms of other compounds recorded in the presence and absence of TATP is shown in Figure 2.14. Cobaltocene (top left), methyl viologen (top right), C_{60} (middle right), and hexaammineruthenium (III) (bottom right) were tested because each compound has been reported to be useful in oxygen or peroxide reduction schemes [90-95]. Dissolved hydrogen (H_2) (bottom left) was tested because it was hypothesized that lowering the effective pH near the electrode by oxidizing H_2 to H^+ at the surface would result in the decomposition of TATP. Samarium (III) triflate was tested because complexes of Sm^{2+} have been demonstrated to be relatively powerful reducing agents [96-98]. I attempted to reduce TATP by electrochemically generating Sm^{2+} from a solution of samarium (III) triflate (middle left). None of these schemes displays catalytic reactivity with TATP, as demonstrated by the respective voltammograms shown in Figure 2.14.

Samarium (III) triflate appears to distort the voltammetric signal produced by ferrocene in DMSO solution, as shown in Figure 2.14 (middle left). The addition of

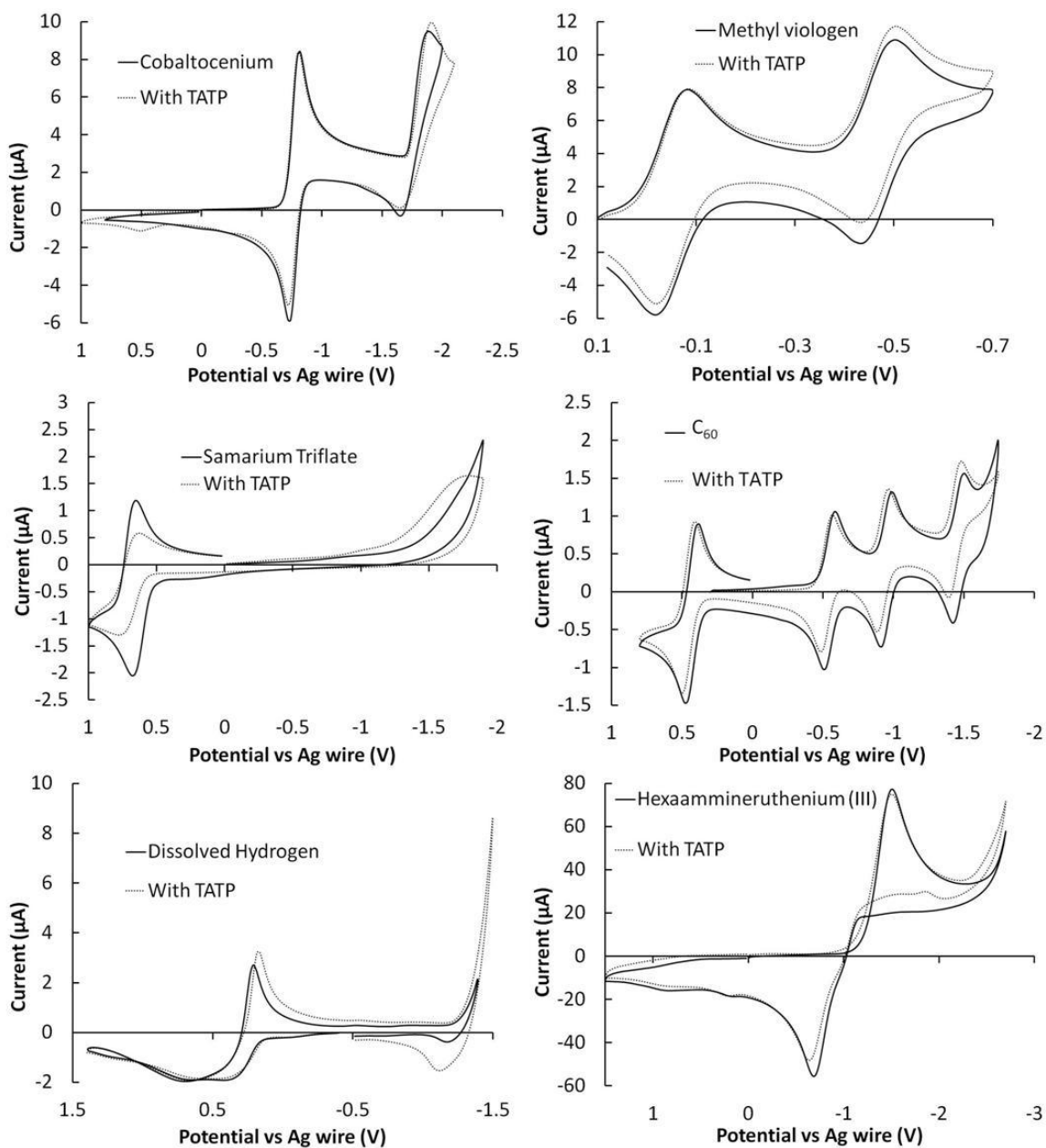


Figure 2.14. Cyclic voltammograms before and after the addition of TATP for cobaltocenium hexafluorophosphate in acetonitrile (top left), methyl viologen diiodide in acetonitrile (top right), samarium triflate in DMSO (middle left), fullerene in dichloromethane (middle right), hydrogen dissolved in an acetonitrile solution (bottom left), and hexaammineruthenium (III) trichloride in acetonitrile (bottom right). All solutions contained 100 mM TBAPF₆ as supporting electrolyte and the voltammograms were collected at a gold electrode at a scan rate of 100 mV/s. The initial sweep direction was positive for dissolved hydrogen and negative for all other experiments.

TATP to the samarium triflate solution resulted in further distortion the ferrocene signal and caused a peak to appear at approximately -1.8 V vs. Ag wire. The source of the distortion of the ferrocene peak is unknown. The peak that appears at -1.8 V is likely the direct reduction of TATP at the electrode surface, but the peak is distorted when compared to those observed in Figure 2.4. Sm^{3+} is a Lewis acid [99]. Lewis acids can react with peroxides and cause peroxide fragmentation [100]. The distortion in the voltammogram led me to speculate that some interaction, or possibly a reaction, had occurred between Sm^{3+} and TATP. Analysis of the NMR spectrum of a DMSO solution of samarium (III) triflate and TATP exhibited no difference from the NMR spectrum of TATP alone. The NMR result indicates that no reaction occurs between Sm^{3+} and TATP, and no further analysis was performed on the interaction between the species.

Nafion film electrodes: Nafion is a sulfonated polytetrafluoroethylene based ionomer originally made in the 1960's at Dupont [101]. As discussed in the introduction, in 1999 Bellamy showed that TATP was destroyed when refluxed with Sn^{2+} ions in certain solvents [33]. I originally sought to employ the reaction of Sn^{2+} with TATP by incorporating Sn^{4+} ions into a Nafion film on an electrode surface and then electrochemically reducing the Sn^{4+} to generate the active Sn^{2+} species.

In the initial experiment a Nafion film was cast on a gold electrode surface by drop coating, as described in the experimental section, and the electrode was submerged in a 10 mM aqueous $\text{SnCl}_4 \cdot 5\text{H}_2\text{O}$ solution. The peaks in the cyclic voltammetric response, shown in Figure 2.15 (top), at approximately 0.4 V (vs. Ag wire) display the general characteristics of a surface wave [79]. The voltammetric peak current for the reduction of a species that is adsorbed onto an electrode surface varies linearly with the

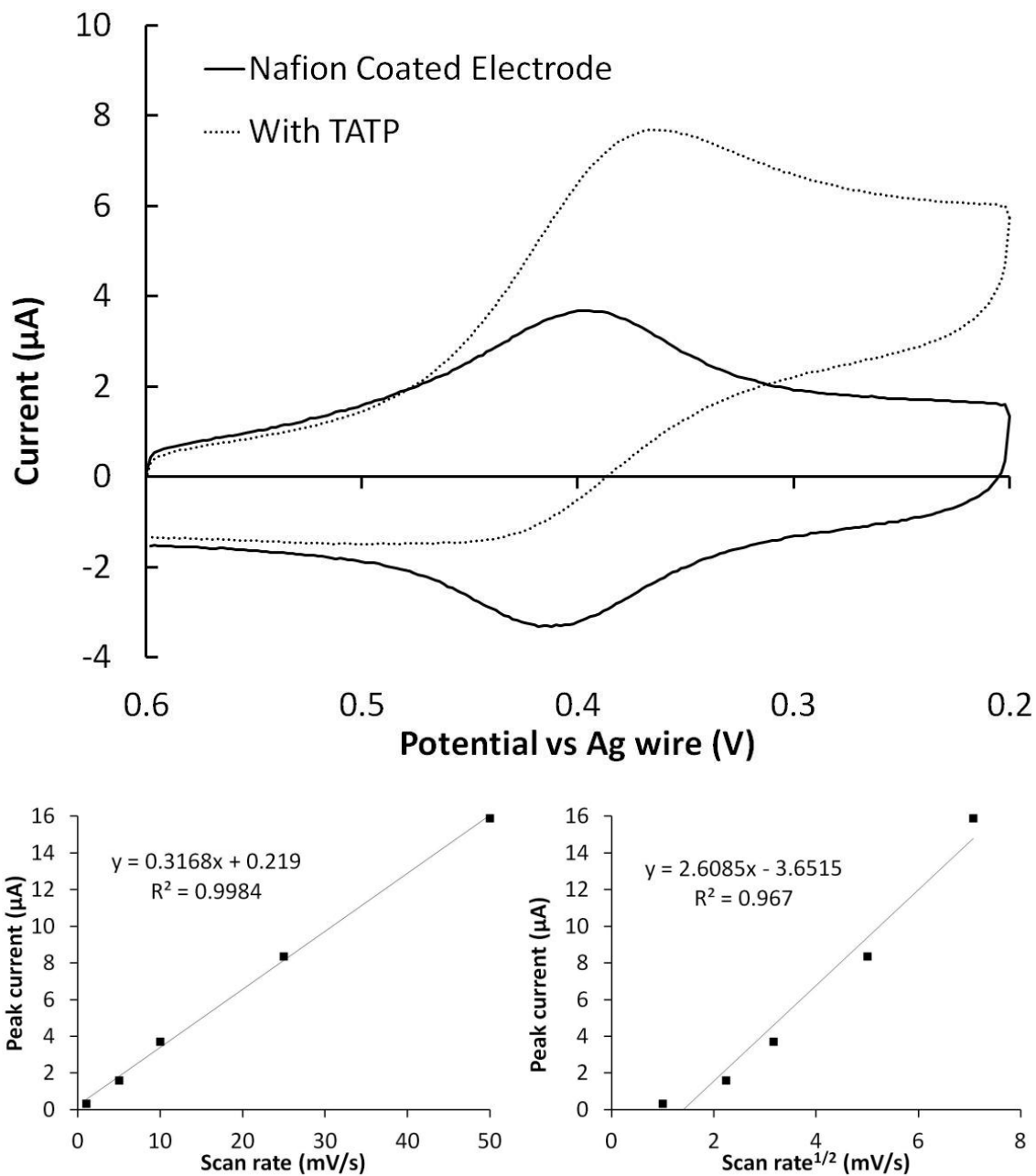


Figure 2.15. The cyclic voltammetric response of a Nafion coated electrode in aqueous SnCl_4 solution at 10 mV/s before and after the addition of acid treated TATP (top). The linear correlation between the peak current vs. scan rate (bottom left) rather than the peak current vs. scan rate^{1/2} (bottom right) demonstrated that the voltammetric response was the result of a surface based process.

scan rate. In contrast, the voltammetric peak current for the reduction of a solution phase species varies linearly with the square root of the scan rate [79]. The linear correlation between the scan rate and the peak current, displayed in Figure 2.15 (bottom-left) supports the conclusion that the voltammetric process is associated with some species incorporated in the Nafion surface layer. At the time I conducted these experiments, I believed that the peak was due to the reduction of Sn^{4+} that was immobilized in the Nafion film, because Sn^{4+} was the only electroactive species that had been added to the solution. The voltammetric response of this electrode in the presence of TATP was tested by adding approximately 15 mg of solid TATP to the solution. TATP is poorly soluble in water so the solution was stirred for approximately 1 hour before I repeated the cyclic voltammetry experiment. The results are shown in Figure 2.15 (top). A clear increase in the current occurs in the presence of the peroxide. Again, at this time I thought that the response was due to electrogenerated Sn^{2+} reacting with TATP.

The 10 mM $\text{SnCl}_4 \cdot 5\text{H}_2\text{O}$ solution had a pH of approximately 1.5 due to hydrolysis of Sn^{4+} ions [99]. As a control, a new film was cast on an electrode and the electrode was placed into a hydrochloric acid solution at pH 1.5. A similar response, both in the presence and absence of TATP, was observed with the freshly prepared film in the HCl solution. This result suggests that a contaminant was present in both the $\text{SnCl}_4 \cdot 5\text{H}_2\text{O}$ solution and in the HCl solution that was used for the control experiment. The only reasonable common contaminant that was listed on the bottle for each chemical was iron. The $\text{Fe}^{3+}/\text{Fe}^{2+}$ couple in a HCl solution at pH 1.5 exhibited a reversible voltammetric response at approximately 0.4 V vs. SCE at a gold electrode surface. The observed potential for this couple at a bare gold electrode was similar to the observed potential for

the surface wave that appeared when the Nafion coated electrode was used. The addition of FeCl_3 to a HCl solution, in which a Nafion coated electrode was submerged, resulted in an increase in the voltammetric peak currents, as demonstrated in Figure 2.16. This result suggests the additional loading of electroactive species. Nafion films have been shown to incorporate Fe^{3+} and Fe^{2+} ions, and when such films are cast on electrode surfaces, the $\text{Fe}^{3+}/\text{Fe}^{2+}$ couple exhibits a voltammetric response similar to those displayed in Figures 2.15 and 2.16 in the absence of peroxide. Nafion coated electrodes have even been used as sensors for iron ions in environmental water samples [102, 103]. Maletzky et al. showed that hydrogen peroxide reacts with Fe^{2+} immobilized in Nafion membranes. The authors produced hydroxyl radicals, via the Photo-Fenton method, by submerging a Nafion membrane containing Fe^{2+} ions in an aqueous solution of hydrogen peroxide and the irradiating the membrane with UV light [104]. Previous reports describing the reactivity of the iron/Nafion membranes with peroxides suggest that iron was a likely contaminant in my system.

As mentioned above, the signal increase observed in the presence of TATP in aqueous $\text{SnCl}_4 \cdot 5\text{H}_2\text{O}$ solutions, shown in Figure 2.15, was also observed in HCl solutions at pH 1.5. The signal increase was not observed when solutions above pH 2.25 were used. This result suggests that the reaction that occurs at the Nafion film electrode does not involve the reduction of TATP directly, but rather the reaction involves the degradation products that are formed when TATP is treated with acid. This observation is in accord with other TATP sensor systems reported in the literature, which show no reaction with TATP directly and require degradation of the TATP before analysis [57].

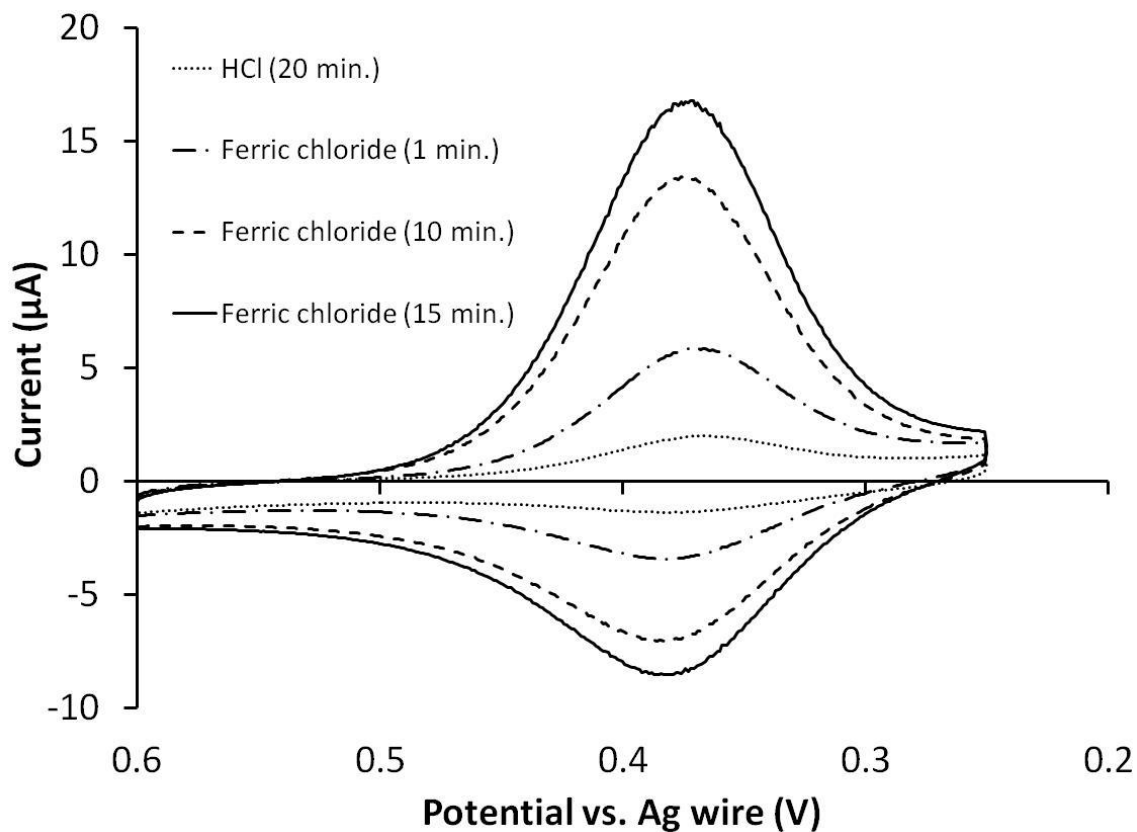


Figure 2.16. Cyclic voltammograms of a Nafion coated electrode that had been submerged in a HCl solution for 20 minutes before the addition FeCl_3 to the solution. The concentration of FeCl_3 after the addition was approximately 10 ppm. The relatively rapid increase the peak current indicates the additional uptake of electroactive material.

Additional experimentation demonstrated that the source of the contaminant was actually the Nafion solution, not the $\text{SnCl}_4 \cdot 5\text{H}_2\text{O}$ or the HCl used in the previous experiments. When thinner Nafion films, prepared via spin coating, were submerged in a stirred solution of trace metal grade HCl the peaks associated with the contaminant disappeared. This observation led me to the hypothesis that the contaminant was in the Nafion and that, if given enough time, the species would diffuse out of the film. This hypothesis was tested by placing an electrode with a spin coated Nafion membrane into a solution of trace metal grade HCl and monitoring the cyclic voltammetric response over time. The results of the experiment are shown in Figure 2.17. Initially, the voltammetric peaks are relatively small and the peak separation is relatively large, which indicates that the film is resistive. The second CV, recorded approximately two minutes later, is similar to the voltammogram shown in Figure 2.15. After approximately 1 hour the peak current at the stationary electrode settled at a value of around $2 \mu\text{A}$. Rotating the electrode resulted in further decreases in current until the peak essentially disappeared. The disappearance of the voltammetric peak indicates that the electroactive contaminant diffused out of the membrane and led me to the conclusion that the contaminant was already in the Nafion film before the electrode was submerged into the solution.

The original goal of this project was to identify compounds capable of reacting directly with TATP. The Nafion systems described above show no evidence for the mediated reduction of TATP, but my work does suggest the presence of a more complex mechanism in which unidentified species mediate the reduction of TATP degradation products produced in highly acidic solutions. Further study of similar Nafion modified

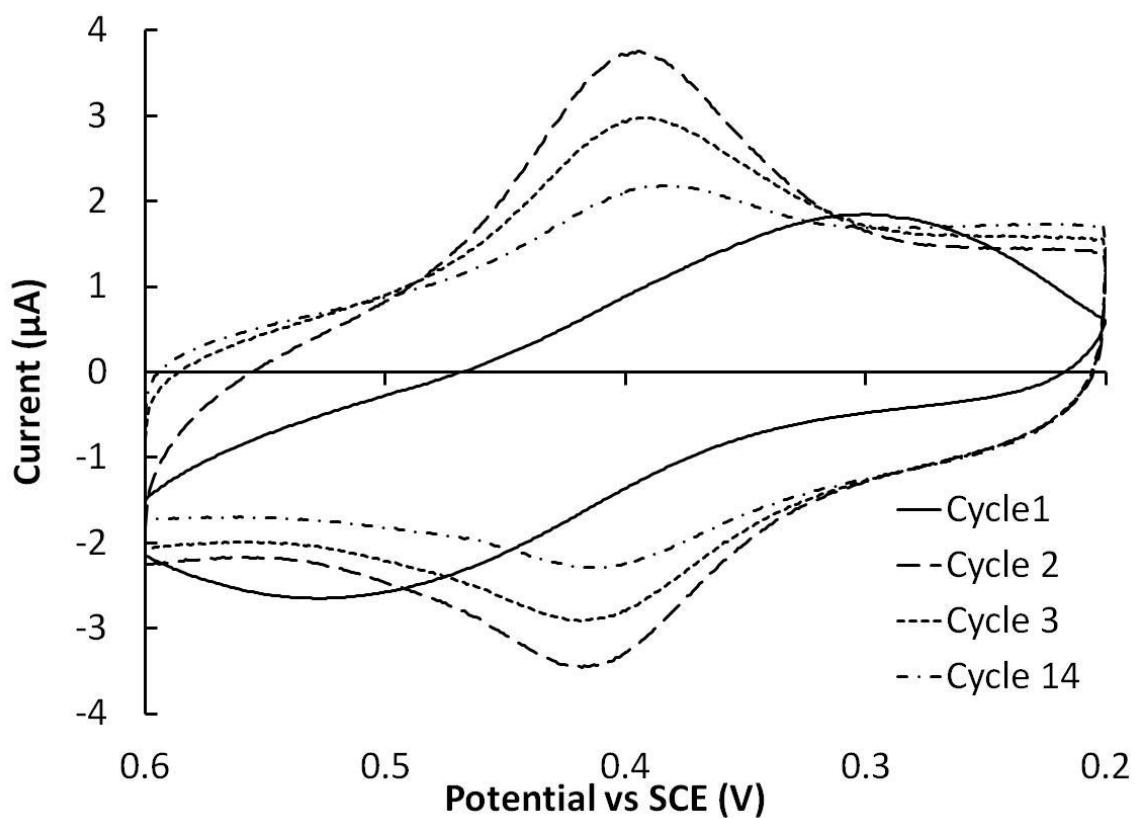


Figure 2.17. A gold electrode spin coated with Nafion membrane showed voltammetric peak currents that initially increased as the Nafion wet. The peak current then decreased with time as the redox active species responsible for the peak diffused out of the membrane. Stirring the solution increased the rate at which this decrease occurred.

electrode systems may be useful for other applications such as hydrogen peroxide sensors or wastewater treatment [37, 104, 105].

Ruthenium Tris Bipyridine: One compound that was tested showed a significant catalytic reaction with TATP, tris(bipyridine)ruthenium(II) ($\text{Ru}(\text{bpy})_3^{2+}$). As shown in Figure 2.18, the reduction of $\text{Ru}(\text{bpy})_3^{2+}$ in the presence of TATP exhibits a significant increase in current at each of the three reductions that are present in the voltammogram of $\text{Ru}(\text{bpy})_3^{2+}$ alone. These reductions are known to be three separate one-electron reductions of the ligands. The formal potentials differ because of coupling through the metal center [106]. At more negative potentials the direct reduction of TATP at the electrode surface also contributes to the observed current and complicates the system.

The increased current at each of the three reduction waves of $\text{Ru}(\text{bpy})_3^{2+}$, shown in the voltammogram in Figure 2.18, indicates that TATP reacts with each of the reduction products of $\text{Ru}(\text{bpy})_3^{2+}$ (i.e., $\text{Ru}(\text{bpy})_3^{1+}$, $\text{Ru}(\text{bpy})_3^0$, and $\text{Ru}(\text{bpy})_3^{1-}$). One might expect that the multiply reduced $\text{Ru}(\text{bpy})_3^0$, and $\text{Ru}(\text{bpy})_3^{1-}$ complexes may be better electron transfer mediators for TATP reduction because these complexes could potentially transfer multiple electrons, as opposed to the singly reduced $\text{Ru}(\text{bpy})_3^{1+}$, which likely only transfers one electron. The voltammogram is extremely complex beyond the first reduction of $\text{Ru}(\text{bpy})_3^{2+}$ in the presence of TATP, and extensive analysis would be required to analyze the processes involving $\text{Ru}(\text{bpy})_3^0$, and $\text{Ru}(\text{bpy})_3^{1-}$, which occur beyond the first reduction wave.

The reaction between TATP and the first reduction product of $\text{Ru}(\text{bpy})_3^{2+}$, $\text{Ru}(\text{bpy})_3^{1+}$, resulted in an approximate 4.5-fold increase in the voltammetric peak current at a scan rate of 100 mV/s. The voltammetric wave associated with this reaction is

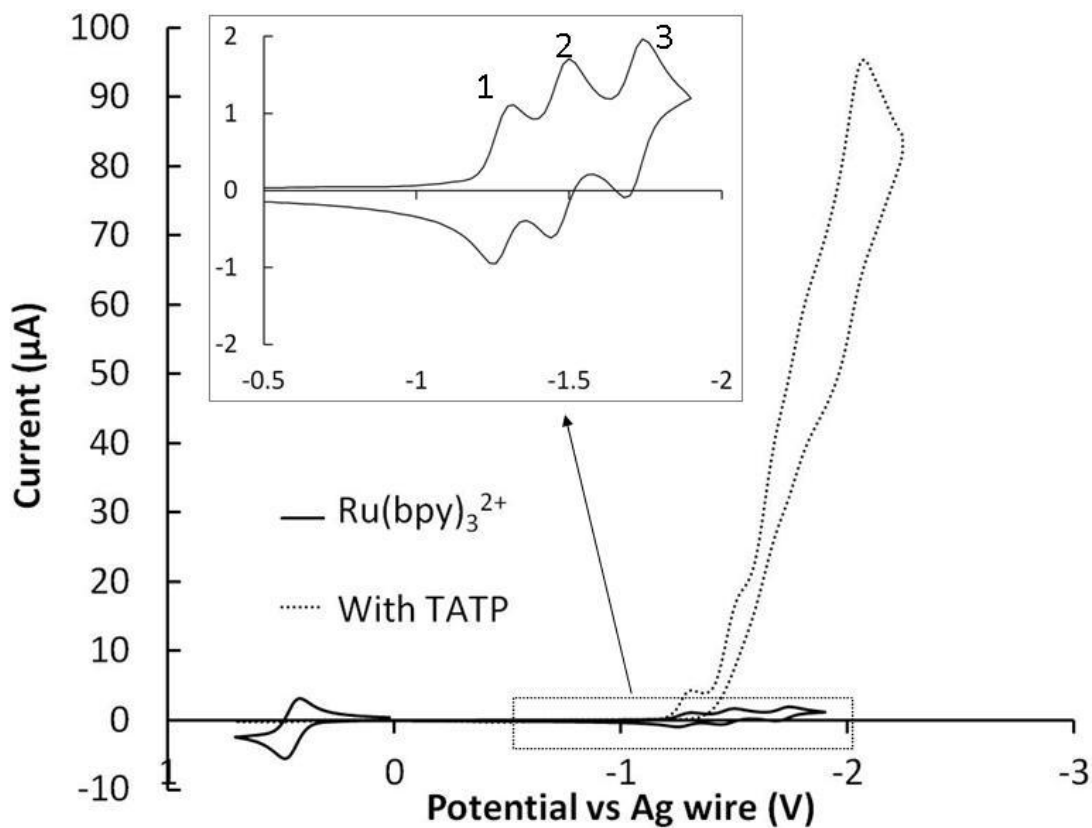


Figure 2.18. Cyclic voltammogram of $430 \mu\text{M Ru}(\text{bpy})_3^{2+}$ in acetonitrile with 100 mM TBAPF_6 as supporting electrolyte at 100 mV/s . The overlay is the same $\text{Ru}(\text{bpy})_3^{2+}$ solution with 28 mM TATP . The inset shows the three voltammetric waves corresponding to the redox couples $\text{Ru}(\text{bpy})_3^{2+}/\text{Ru}(\text{bpy})_3^{1+}$ (labeled 1), $\text{Ru}(\text{bpy})_3^{1+}/\text{Ru}(\text{bpy})_3^0$ (labeled 2), and $\text{Ru}(\text{bpy})_3^0/\text{Ru}(\text{bpy})_3^{1-}$ (labeled 3). The wave at $+0.4 \text{ V}$ corresponds to the ferrocene/ferrocenium couple that was present in the $430 \mu\text{M Ru}(\text{bpy})_3^{2+}$ solution.

reasonably well separated from the other waves that occur in the voltammogram shown in Figure 2.18. The reaction of $\text{Ru}(\text{bpy})_3^{1+}$ with TATP has been noted in the literature by Shaw and Calhoun, though their publication came after this work was initially performed [59]. For this work I focused on the first reduction product of $\text{Ru}(\text{bpy})_3^{2+}$ because it shows catalytic reactivity with TATP and the mediated electron transfer shifts the potential necessary for the reduction of TATP by 550 mV in the positive direction. The $E_{1/2}$ values for this system are summarized in Table 2.2.

I used a catalytic mediated electron transfer mechanism (EC') to model this system [79, 107-109]. The EC' model provides a straightforward method for analyzing the kinetics of the homogeneous catalytic reaction between $\text{Ru}(\text{bpy})_3^{1+}$ and TATP. In a chronoamperometric analysis of an EC' system one can calculate the homogeneous rate constant for the following reaction based upon the equation

$$\frac{i}{i_d} = \sqrt{\lambda} \left[\text{erf}(\sqrt{\lambda}) \sqrt{\pi} + \frac{e^{-\lambda}}{\sqrt{\lambda}} \right] \quad (2.11)$$

where

$$\lambda = k' C_{sub}^* t \quad (2.12)$$

i is the current measured in the presence of the substrate (here TATP), i_d is the diffusion limited current in the absence of the substrate, k' is the rate constant for the homogeneous catalytic reaction, C_{sub}^* is the concentration of the substrate, and t is time [79]. When λ is small, for instance when the concentration of the substrate is small or the rate constant for the homogeneous reaction is small, i/i_d approaches 1, and the waveshape approaches that of a reversible voltammogram for which there is no evidence of a coupled catalytic step.

Table 2.2. Listed are the $E_{1/2}$ values for the reduction wave of TATP, the first reduction wave of $\text{Ru}(\text{bpy})_3^{2+}$, and the reduction wave corresponding to the first reduction of $\text{Ru}(\text{bpy})_3^{2+}$ in the presence of TATP. All potentials are reported vs. ferrocene in acetonitrile solution at 100 mV/s at a glassy carbon electrode. The potential of the TATP reduction is shifted by 550 mV when $\text{Ru}(\text{bpy})_3^{2+}$ is used as an electron transfer mediator.

Compound	<i>E</i> _{1/2} vs. Ferrocene at 100 mV/s (V)
TATP	-2.25
$\text{Ru}(\text{bpy})_3^{2+} / \text{Ru}(\text{bpy})_3^{1+}$	-1.70
$\text{Ru}(\text{bpy})_3^{2+} / \text{Ru}(\text{bpy})_3^{1+}$ (With TATP)	-1.70

When λ is large, $\text{erf}(\sqrt{\lambda}) \rightarrow 1$ and $e^{-\lambda}/\sqrt{\lambda} \rightarrow 0$, which simplifies equation (2.11) to

$$\frac{i}{i_d} = \sqrt{\pi\lambda} \quad (2.13)$$

In the limit of Equation 2.13 a plot of the current ratio (i/i_d) vs. \sqrt{t} produces a straight line with $\text{slope} = \sqrt{k'C_{sub}^*\pi}$ [79].

A plot of (i/i_d) vs. \sqrt{t} for the $\text{Ru}(\text{bpy})_3^{2+}/\text{TATP}$ system is shown in Figure 2.19. Despite the noise at longer times the data are well fit by a straight line with an intercept of zero, a result that is consistent with the expectation from equation (2.13). From this plot the rate constant for the following reaction was calculated to be $1800 \pm 100 \text{ M}^{-1} \text{ s}^{-1}$ at the 95% confidence level. I also repeated the calculation after smoothing the noise by applying a 7-point moving boxcar average to the measured currents. After smoothing the data, the correlation coefficient improved from 0.906 to 0.985 and the resulting rate constant was $1740 \pm 40 \text{ M}^{-1} \text{ s}^{-1}$ at the 95% confidence level.

As mentioned briefly above, the three reduction waves of $\text{Ru}(\text{bpy})_3^{2+}$ in the voltammogram shown in Figure 2.18 are ligand reductions. Each reduction results in an electron localized in the π^* molecular orbital for one of the three bipyridine ligands [106]. A $d \rightarrow \pi^*$ transition occurs when $\text{Ru}(\text{bpy})_3^{2+}$ is irradiated with visible light, and a $\pi \rightarrow \pi^*$ transition occurs upon irradiation with ultraviolet light [110]. The photon induced $d \rightarrow \pi^*$, and $\pi \rightarrow \pi^*$ transitions prompted an attempt to see if TATP could be photochemically destroyed using the $\text{Ru}(\text{bpy})_3^{2+*}$ excited state to transfer an electron to TATP. To test this hypothesis I measured the fluorescence that was produced as $\text{Ru}(\text{bpy})_3^{2+*}$ relaxed to $\text{Ru}(\text{bpy})_3^{2+}$ in the presence and absence of TATP in acetonitrile

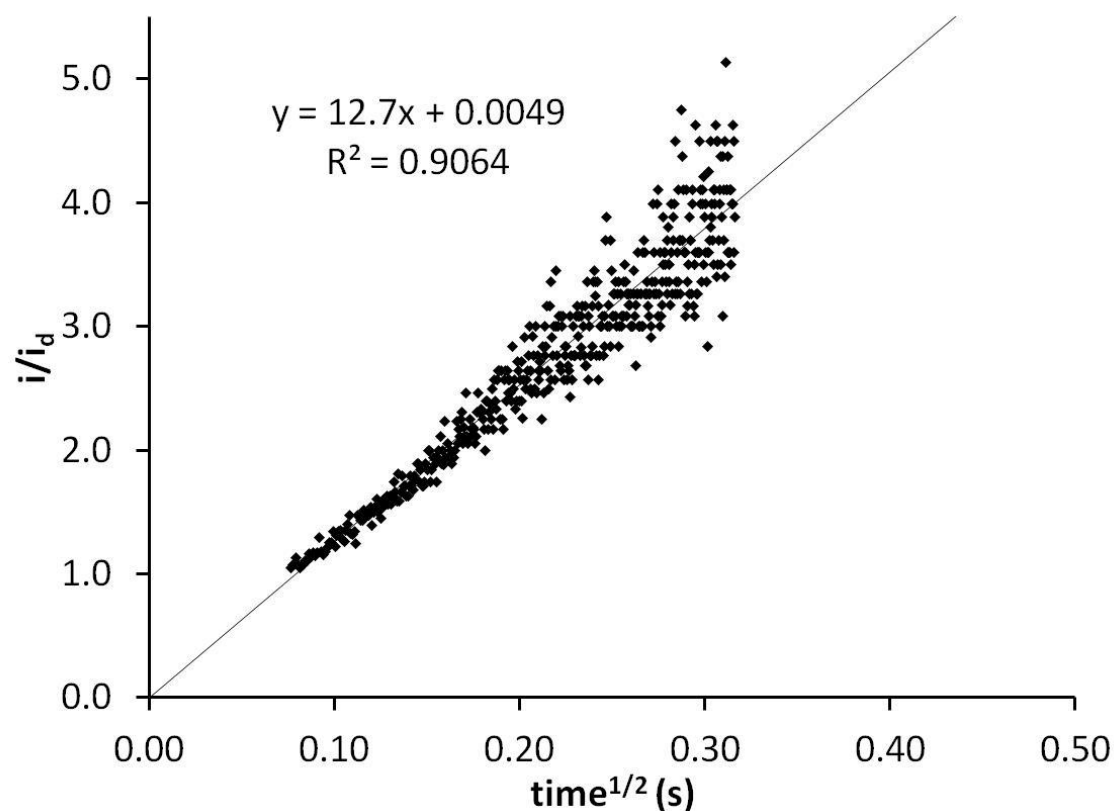


Figure 2.19. A plot of the ratio of the catalytic current/diffusion limited current (i/i_d) vs. $\text{time}^{1/2}$. From the slope of this line a homogeneous rate constant of $1800 \pm 100 \text{ M}^{-1} \text{ s}^{-1}$ for the reaction between TATP and $\text{Ru}(\text{bpy})_3^{1+}$ was calculated. The diffusion limited current was recorded in $430 \mu\text{M}$ $\text{Ru}(\text{bpy})_3^{2+}$ in acetonitrile with 100 mM TBAPF_6 as supporting electrolyte at a 1 mm glassy carbon electrode. The catalytic current was recorded in the same $\text{Ru}(\text{bpy})_3^{2+}$ with 28 mM TATP added. The potential step was applied from -0.96 V to -1.35 V , corresponding to a potential just past the first reduction wave of $\text{Ru}(\text{bpy})_3^{2+}$.

solutions. The fluorescence measurements in the presence of TATP were made using 1.4×10^{-4} M $\text{Ru}(\text{bpy})_3^{2+}$ solutions with various excesses of TATP. The excess amounts of TATP varied from 10 to 80 times the molar concentration of $\text{Ru}(\text{bpy})_3^{2+}$. The wavelengths of maximum absorbance and emission were determined experimentally to be 470 nm and 600 nm, respectively, and these wavelengths match those reported previously for $\text{Ru}(\text{bpy})_3^{2+}$ [111]. This experiment did not show any quenching of the fluorescence when TATP was present in the solution, which led to the conclusion that no reaction was occurring between the $\text{Ru}(\text{bpy})_3^{2+*}$ and TATP. To verify the result, I mixed TATP with $\text{Ru}(\text{bpy})_3^{2+}$ in an equimolar ratio in deuterated acetonitrile under oxygen free conditions in a sealed NMR tube. The NMR spectrum was recorded initially and the reaction mixture was exposed to sunlight for approximately 10 hours. No change in the spectrum was observed and this was taken as confirmation that there was no detectable reaction between $\text{Ru}(\text{bpy})_3^{2+*}$ and TATP.

Conclusions: A qualitative assessment of the reduction of TATP at a glassy carbon electrode surface was performed. Cyclic voltammetric analysis shows that TATP reduces at -2.25 V vs. a ferrocene/ferrocenium internal reference in acetonitrile solutions. The reduction of TATP is well described by a kinetically slow electron transfer followed by a kinetically fast chemical transformation. Based on information presented in the literature, the chemical transformation is likely the dissociation of a peroxide bond [75, 80, 81]. Dependence of the voltammetric peak current on potential scan rate indicates that the transfer coefficient, α , for the heterogeneous reduction of TATP is $0.245/n$. Digital simulation of the voltammetric data and bulk electrolysis shows that this reduction takes place via a two-electron mechanism. Taken together, my experimental

results for the reduction of TATP are consistent with a large body of scientific literature involving the electrochemistry of organic peroxides.

An electrode coated with a Nafion membrane containing a presently unidentified contaminant catalyzed the reduction of TATP degradation products in aqueous acidic solutions. A distinct increase in the voltammetric peak current was observed upon reduction of the contaminant in the presence of the TATP treated with an aqueous HCl solution at pH 1.2. No increase in the peak current was observed when the TATP was treated with solutions of pH 2.25 or greater. The Nafion solution purchased from Sigma-Aldrich appears to be the source of the contaminant. When a Nafion coated electrode was submerged in an aqueous HCl solution and FeCl_3 was added, a rapid uptake of electroactive material, Fe^{3+} , was observed. The voltammetric wave for the $\text{Fe}^{3+}/\text{Fe}^{2+}$ couple appeared at the same potential as the wave for the contaminant. The qualitative experiments described in this chapter suggest that the contaminant is likely iron, and because of the examples presented in the literature that show that iron/Nafion membranes can catalyze the reduction of hydrogen peroxide, further analysis of iron/Nafion coated electrodes would be a good starting point for future investigations [104, 112].

Utilizing mediated electron transfer to reduce TATP is not trivial. This chapter demonstrates that many reduced species show little or no reaction with TATP. Mediated electron transfer reactions occurred between TATP and each of the electrochemical reduction products of $\text{Ru}(\text{bpy})_3^{2+}$ that were tested ($\text{Ru}(\text{bpy})_3^{1+}$, $\text{Ru}(\text{bpy})_3^0$, and $\text{Ru}(\text{bpy})_3^{-1}$). Electrochemically generated $\text{Ru}(\text{bpy})_3^{1+}$ reacts catalytically with TATP, and further analysis of this reaction showed the mediated electron transfer reaction shifts the reduction of the peroxide in the positive direction by +550 mV to -1.70 V vs. ferrocene in

acetonitrile solutions. This +550 mV shift in potential for mediated reduction of TATP is a significant improvement over the highly negative potential for direct reduction of TATP at an electrode surface. The mediated electron transfer reaction that was demonstrated in this chapter may serve as a guide to future research into the electrochemical detection or destruction of TATP.

References

- [1] Jackson HL, McCormack WB, Rondestvedt CS, Smeltz KC, Viele IE. Control of peroxidizable compounds. *J Chem Educ.* 1970;47:A175-A88.
- [2] Mirafzal GA, Baumgarten HE. Control of peroxidizable compounds: an addendum. *J Chem Educ.* 1988;65:A226-A9.
- [3] Evans AG. Explosion hazards of autoxidized solvents. *J Roy Inst Chem.* 1956;80:386-9.
- [4] Kelly RJ. Review of safety guidelines for peroxidizable organic chemicals. *Chem Health Saf.* 1996;3:28-36.
- [5] Johnson RM, Siddiqi IW. *The Determination of Organic Peroxides (Monographs in Organic Functional Group Analysis, Vol. 4): Pergamon; 1970.*
- [6] Antonovskii VL. Initiating and crosslinking ability of organic peroxides: Chemical kinetic methods for the determination. *Kinet Catal.* 2003;44:54-73.
- [7] Swern D. Organic peroxy acids as oxidizing agents. *Epoxidation. Interscience;* p. 355-533.
- [8] Colonna S, Perdicchia D. Epoxidation of enones by nucleophilic oxidation. *Georg Thieme Verlag;* p. 123-53.
- [9] Baeckvall J-E. Selective oxidation of amines and sulfides. *Wiley-VCH Verlag GmbH & Co. KGaA;* p. 277-313.
- [10] Hwu JR, Chen B-L, Neelamkavil SF. Bis(trimethylsilyl) peroxide. *John Wiley & Sons Ltd.;* p. 79-81.
- [11] Criegee R, Schnorrenberg W, Becke J. Constitution of ketone peroxides. *Ann der Chimie.* 1949;565:7-21.
- [12] Milas NA, Golubovic A. Studies in organic peroxides. XXVI. Organic peroxides derived from acetone and hydrogen peroxide. *J Am Chem Soc.* 1959;81:6461-2.
- [13] Dilthey W, Inckel M, Stephan H. Enium. XXXV. Oxidation of ketones with perhydrol. *J Prakt Chem (Leipzig).* 1940;154:219-37.
- [14] Kharasch MS, Sosnovsky G. Structure of peroxides from cyclohexanone and hydrogen peroxide. *J Org Chem.* 1958;23:1322-6.
- [15] Wolffenstein R. Action of hydrogen peroxide on acetone and mesityl oxide. *Ber.* 1895;28(.):2265-9.
- [16] Mavrodi GE, inventor Organic peroxide explosive patent GB620498. 1949.
- [17] Dobson LR. Ultrasonic Activation of Triacetone Triperoxide. University of Nebraska-Lincoln, MS, 2010.
- [18] Brewer AD. Peroxide/acetone mixture hazard. *Chem Br.* 1975;11:335.
- [19] Noponen A. Violent explosion [of trimeric acetone peroxide]. *Chem Eng News.* 1977;55:5.
- [20] Renner HO, inventor Baked goods patent US3084048. 1963.
- [21] Broeze JJ, Hinze JO. Experiments with doped fuels for high-speed Diesel engines. *J Inst Pet.* 1939;25:657-77.
- [22] Ficheroulle H, Kovache A. Explosive primers. *Meml Poudres.* 1949;31:7-27.

- [23] Moser FR, inventor Shell Development Co. . assignee. Organic peroxide compositions suitable for use with Diesel engine fuels, etc patent US2133733. 1938.
- [24] Moser FR, inventor Shell Development Co. . assignee. Motor fuel patent US2107059. 1938.
- [25] Oxley JC, Smith JL, Shinde K, Moran J. Determination of the Vapor Density of Triacetone Triperoxide (TATP) Using a Gas Chromatography Headspace Technique. *Propellants, Explosives, Pyrotechnics*. 2005;30(2):127-30.
- [26] Thiemann AE. Additives for Diesel fuels. *ATZ, Automobiltech Z*. 1942;45:454-7.
- [27] Maichalske TE, N.; Sigman, M.; Trehwella, J. Basic Research Needs for Countering Terrorism. 2002 [cited 2012 August 8]; Available from: http://science.energy.gov/~media/bes/pdf/reports/files/nct_rpt_print.pdf
- [28] IntelCenter. Londone Tube Bus Attack. 2005 [cited 2012 August 8]; Available from: <http://www.intelcenter.com/LTBA-PUB-v1-5.pdf>
- [29] Matyas R, Pachman J. Study of TATP: Influence of Reaction Conditions on Product Composition. *Propellants Explos Pyrotech*. 2010;35(1):31-7.
- [30] Pachman J, Matyas R. Study of TATP: Stability of TATP solutions. *Forensic SciInt*. 2011;207(1-3):212-4.
- [31] Matyas R, Pachman J. Thermal stability of triacetone triperoxide. *Sci Technol Energ Mater*. 2007;68:111-6.
- [32] Oxley JC, Smith JL, Huang J, Luo W. Destruction of peroxide explosives. *J Forensic Sci*. 2009;54:1029-33.
- [33] Bellamy AJ. Triacetone triperoxide: its chemical destruction. *J Forensic Sci*. 1999;44:603-8.
- [34] Singh S, Singh M. Explosives detection systems (EDS) for aviation security. *Signal Processing*. 2003;83(1):31-55.
- [35] Sigman ME, Clark CD, Fidler R, Geiger CL, Clausen CA. Analysis of triacetone triperoxide by gas chromatography/mass spectrometry and gas chromatography/tandem mass spectrometry by electron and chemical ionization. *Rapid Communications in Mass Spectrometry*. 2006;20(19):2851-7.
- [36] Apblett AW, Kiran BP, Malka S, Materer NF, Piquette A. Nanotechnology for neutralization of terrorist explosives. *Ceram Trans*. 2006;172:29-35.
- [37] Germain ME, Knapp MJ. Turn-on Fluorescence Detection of H₂O₂ and TATP. *Inorg Chem (Washington, DC, U S)*. 2008;47:9748-50.
- [38] Sanchez JC, Trogler WC. Polymerization of a boronate-functionalized fluorophore by double transesterification: applications to fluorescence detection of hydrogen peroxide vapor. *J Mater Chem*. 2008;18:5134-41.
- [39] Cotte-Rodriguez I, Hernandez-Soto H, Chen H, Cooks RG. In Situ Trace Detection of Peroxide Explosives by Desorption Electrospray Ionization and Desorption Atmospheric Pressure Chemical Ionization. *Anal Chem (Washington, DC, U S)*. 2008;80:1512-9.
- [40] Rasanen R-M, Nousiainen M, Perakorpi K, Sillanpaa M, Polari L, Anttalainen O, et al. Determination of gas phase triacetone triperoxide with aspiration ion mobility

spectrometry and gas chromatography-mass spectrometry. *Anal Chim Acta*. 2008;623:59-65.

[41] Stambouli A, El BA, Bouayoun T, Bellimam MA. Headspace-GC/MS detection of TATP traces in post-explosion debris. *Forensic Sci Int*. 2004;146:S191-S4.

[42] Oxley JC, Smith JL, Kirschenbaum LJ, Marimganti S, Vadlamannati S. Detection of explosives in hair using ion mobility spectrometry. *J Forensic Sci*. 2008;53:690-3.

[43] Dunayevskiy I, Tsekoun A, Prasanna M, Go R, Patel CKN. High-sensitivity detection of triacetone triperoxide (TATP) and its precursor acetone. *Appl Opt*. 2007;46:6397-404.

[44] Bauer C, Sharma AK, Willer U, Burgmeier J, Braunschweig B, Schade W, et al. Potentials and limits of mid-infrared laser spectroscopy for the detection of explosives. *Appl Phys B: Lasers Opt*. 2008;92:327-33.

[45] Pena AJ, Pacheco-Londono L, Figueroa J, Rivera-Montalvo LA, Roman-Velazquez FR, Hernandez-Rivera SP. Characterization and differentiation of high energy cyclic organic peroxides by GC/FT-IR, GC-MS, FT-IR, and Raman microscopy. *Proc SPIE-Int Soc Opt Eng*. 2005;5778:347-58.

[46] Staples E. *Electronic Noses & Sensors for the Detection of Explosives*: Kluwer Academic Publishers; 2004.

[47] Laine DF, Roske CW, Cheng IF. Electrochemical detection of triacetone triperoxide employing the electrocatalytic reaction of iron(II/III)-ethylenediaminetetraacetate and hydrogen peroxide. *Anal Chim Acta*. 2008;608:56-60.

[48] Lu D, Cagan A, Munoz RAA, Tangkuaram T, Wang J. Highly sensitive electrochemical detection of trace liquid peroxide explosives at a Prussian-blue 'artificial-peroxidase' modified electrode. *Analyst (Cambridge, U K)*. 2006;131:1279-81.

[49] Munoz RAA, Lu D, Cagan A, Wang J. 'One-step' simplified electrochemical sensing of TATP based on its acid treatment. *Analyst (Cambridge, U K)*. 2007;132:560-5.

[50] Bohrer FI, Colesniuc CN, Park J, Schuller IK, Kummel AC, Trogler WC. Selective Detection of Vapor Phase Hydrogen Peroxide with Phthalocyanine Chemiresistors. *J Am Chem Soc*. 2008;130:3712-3.

[51] Weast RC. *Handbook of Chemistry and Physics: Crc : a Ready Reference Book of Chemical and Physical Data*: Taylor & Francis Group; 1985.

[52] Joensson G, Gorton L. An electrochemical sensor for hydrogen peroxide based on peroxidase adsorbed on a spectrographic graphite electrode. *Electroanalysis (N Y)*. 1989;1:465-8.

[53] Frew JE, Harmer MA, Hill HAO, Libor SI. A method for estimation of hydrogen peroxide based on mediated electron transfer reactions of peroxidases at electrodes. *J Electroanal Chem Interfacial Electrochem*. 1986;201:1-10.

[54] Jonsson G, Gorton L, Pettersson L. Mediated electron transfer from glucose oxidase at a ferrocene-modified graphite electrode. *Electroanalysis (N Y)*. 1989;1:49-55.

[55] Veitch NC. Horseradish peroxidase: a modern view of a classic enzyme. *Phytochemistry*. 2004;65(3):249-59.

- [56] Karyakin AA, Gitelmacher OV, Karyakina EE. A High-Sensitive Glucose Amperometric Biosensor Based on Prussian Blue Modified Electrodes. *Analytical Letters*. 1994;27(15):2861-9.
- [57] Laine DF, Roske CW, Cheng IF. Electrochemical detection of triacetone triperoxide employing the electrocatalytic reaction of iron(II/III)-ethylenediaminetetraacetate and hydrogen peroxide. *Analytica Chimica Acta*. 2008;608(1):56-60.
- [58] Bernard MLJ. Polarographic study of organic peroxides. *Ann Chim (Paris)*. 1955;10:315-52.
- [59] Shaw A, Calhoun RL. Electrogenerated chemiluminescence with ruthenium trisbipyridine and TATP. *ECS Trans*. 2012;41:49-56.
- [60] Woller EK, DiMugno SG. 2,3,7,8,12,13,17,18-Octafluoro-5,10,15,20-tetraarylporphyrins and Their Zinc Complexes: First Spectroscopic, Electrochemical, and Structural Characterization of a Perfluorinated Tetraarylmetalloporphyrin. *J Org Chem*. 1997;62:1588-93.
- [61] DiMugno SG, inventor University of Nebraska-Lincoln, USA . assignee. Synthesis of octafluoro-meso-tetraarylporphyrins and their metal complexes for use as catalysts patent US6124452A. 2000.
- [62] Haroune N, Crowson A, Campbell B. Characterisation of triacetone triperoxide (TATP) conformers using LC-NMR. *Science & Justice*. 2011;51(2):50-6.
- [63] Contini AE, Bellamy AJ, Ahad LN. Taming the Beast: Measurement of the Enthalpies of Combustion and Formation of Triacetone Triperoxide (TATP) and Diacetone Diperoxide (DADP) by Oxygen Bomb Calorimetry. *Propellants Explos Pyrotech*. 2012;37(3):320-8.
- [64] Feldberg SW, Goldstein CI, Rudolph M. A stability criterion for accurate simulation of electrochemical diffusion-kinetic phenomena at the rotating disk electrode and implications for simulation of diffusion-migration and other problems. *J Electroanal Chem*. 1996;413:25-36.
- [65] Feldberg SW, Goldstein CI. Examination of the behavior of the fully implicit finite-difference algorithm with the Richtmyer modification: behavior with an exponentially expanding time grid. *J Electroanal Chem*. 1995;397:1-10.
- [66] Mocak J, Feldberg SW. The Richtmyer modification of the fully implicit finite difference algorithm for simulations of electrochemical problems. *J Electroanal Chem*. 1994;378:31-7.
- [67] Rudolph M. Digital simulations with the fast implicit finite difference (FIFD) algorithm. Part II. An improved treatment of electrochemical mechanisms with second-order reactions. *J Electroanal Chem*. 1992;338:85-98.
- [68] Rudolph M. A fast implicit finite difference algorithm for the digital simulation of electrochemical processes. *J Electroanal Chem Interfacial Electrochem*. 1991;314:13-22.
- [69] Kuta EJ, Quackenbush FW. A polarographic study of organic peroxides. *Anal Chem*. 1960;32:1069-72.
- [70] Lund H, Editor. *Encyclopedia of Electrochemistry of the Elements: Organic Section, Vol. 11: Hydrocarbons, Hydroxy Compounds*: Dekker; 1978.

- [71] Maciel GS, Bitencourt ACP, Ragni M, Aquilanti V. Alkyl peroxides: effect of substituent groups on the torsional mode around the O-O bond. *Int J Quantum Chem.* 2007;107:2697-707.
- [72] Nicholson RS, Shain I. Theory of stationary electrode polarography. Single scan and cyclic methods applied to reversible, irreversible, and kinetic systems. *Anal Chem.* 1964;36:706-23.
- [73] Yamshchikov AV, Levin ES. Mechanism of the reduction of the peroxide group on a mercury electrode. *Elektrokhimiya.* 1970;6:588-90.
- [74] Salvato B, Jambon C, Vittori O, Rochefort O. Differential pulse polarography of some organic peroxides. *Electroanalysis.* 1995;7:88-91.
- [75] Vasudevan D. Cyclic voltammetric studies on the electroreduction of peroxides in aprotic media. *Bull Electrochem.* 2000;16:277-9.
- [76] Denekamp C, Gottlieb L, Tamiri T, Tsoglin A, Shilav R, Kapon M. Two Separable Conformers of TATP and Analogues Exist at Room Temperature. *Org Lett.* 2005;7:2461-4.
- [77] Muller D, Levy A, Shelef R, Abramovich-Bar S, Sonenfeld D, Tamiri T. Improved method for the detection of TATP after explosion. *J Forensic Sci.* 2004;49:935-8.
- [78] Schulte-Ladbeck R, Kolla P, Karst U. Trace Analysis of Peroxide-Based Explosives. *Analytical Chemistry.* 2003;75(4):731-5.
- [79] Bard AJ, Faulkner LR. *Electrochemical Methods: Fundamentals and Applications*: Wiley; 2000.
- [80] Workentin MS, Maran F, Wayner DDM. Reduction of Di-tert-Butyl Peroxide: Evidence for Nonadiabatic Dissociative Electron Transfer. *Journal of the American Chemical Society.* 1995;117(7):2120-1.
- [81] Donkers RL, Maran F, Wayner DDM, Workentin MS. Kinetics of the Reduction of Dialkyl Peroxides. New Insights into the Dynamics of Dissociative Electron Transfer. *Journal of the American Chemical Society.* 1999;121(31):7239-48.
- [82] Martin RD, Unwin PR. Scanning electrochemical microscopy: theory and experiment for the positive feedback mode with unequal diffusion coefficients of the redox mediator couple. *J Electroanal Chem.* 1997;439:123-36.
- [83] Wang Y, Rogers EI, Compton RG. The measurement of the diffusion coefficients of ferrocene and ferrocenium and their temperature dependence in acetonitrile using double potential step microdisk electrode chronoamperometry. *Journal of Electroanalytical Chemistry.* 2010;648(1):15-9.
- [84] Kishioka S-y, Ohsaka T, Tokuda K. Electrochemical studies of acid-promoted disproportionation of nitroxyl radical. *Electrochimica Acta.* 2003;48(11):1589-94.
- [85] Haymond S, Babcock GT, Swain GM. Electron Transfer Kinetics of Ferrocene at Microcrystalline Boron-Doped Diamond Electrodes: Effect of Solvent and Electrolyte. *Electroanalysis.* 2003;15(4):249-53.
- [86] Csoeregi E, Gorton L, Marko-Varga G. Amperometric microbiosensors for detection of hydrogen peroxide and glucose based on peroxidase-modified carbon fibers. *Electroanalysis.* 1994;6:925-33.

- [87] Sun H, Smirnov VV, DiMugno SG. Slow electron transfer rates for fluorinated cobalt porphyrins: electronic and conformational factors modulating metalloporphyrin ET. *Inorg Chem.* 2003;42:6032-40.
- [88] Sun H, Xue F, Nelson AP, Redepenning J, DiMugno SG. Reversible Electrochemical Generation of a Rhodium(II) Porphyrin: Thwarting Disproportionation with Weakly Coordinating Anions. *Inorg Chem.* 2003;42:4507-9.
- [89] Baron R, Darchen A, Hauchard D. Electrocatalytic reduction of tert-butyl hydroperoxide at iron electrodes. *Electrochim Acta.* 2004;49:4841-7.
- [90] Kristine FJ, Johnson CR, O'Donnell S, Shepherd RE. Reduction of hydrogen peroxide by ruthenium(II) ammine complexes: the surprisingly identical mechanism for hexaammineruthenium(2+), pentaammine(aquo)ruthenium(2+), and pentaammine(1-methylimidazole)ruthenium(2+). *Inorganic Chemistry.* 1980;19(8):2280-4.
- [91] Pladziewicz JR, Broomhead JA, Taube H. Reduction of oxygen by hexaammineruthenium(II) and by tris(ethylenediamine)ruthenium(II). *Inorganic Chemistry.* 1973;12(3):639-43.
- [92] Ghica ME, Brett CMA. A glucose biosensor using methyl viologen redox mediator on carbon film electrodes. *Analytica Chimica Acta.* 2005;532(2):145-51.
- [93] Hu S. Electrocatalytic reduction of molecular oxygen on a sodium montmorillonite-methyl viologen carbon paste chemically modified electrode. *Journal of Electroanalytical Chemistry.* 1999;463(2):253-7.
- [94] Kuzume A, Herrero E, Feliu JM, Ahlberg E, Nichols RJ, Schiffrin DJ. Electrochemical reactivity in nanoscale domains: O₂ reduction on a fullerene modified gold surface. *Physical Chemistry Chemical Physics.* 2005;7(6):1293-9.
- [95] Rapicault S, Paday F, Degrand C. Redox-catalytic reduction of dioxygen by cobaltocene at a carbon paste electrode: Application to trace analysis. *Journal of Organometallic Chemistry.* 1996;525(1-2):139-44.
- [96] Fukuzawa S-i, Yahara Y, Kamiyama A, Hara M, Kikuchi S. Stereoselective Pinacol Coupling of Chiral Formylferrocene Using Divalent Samarium Triflate: Preparation of a New Chiral Bisferrocenyl Oxazoline Ligand and Its Application to Asymmetric Diels-Alder Reactions. *Organic Letters.* 2005;7(26):5809-12.
- [97] Fukuzawa S-i, Mutoh K, Tsuchimoto T, Hiyama T. Samarium(II) Triflate as a New Reagent for the Grignard-Type Carbonyl Addition Reaction. *The Journal of Organic Chemistry.* 1996;61(16):5400-5.
- [98] Procter DJ, Robert A. Flowers I, Skrydstrup T. *Organic Synthesis Using Samarium Diodide: A Practical Guide*: Rsc; 2010.
- [99] Housecroft CE, Sharpe AG. *Inorganic Chemistry*: Prentice Hall; 2005.
- [100] Dussault PH, Lee H-J, Liu X. Selectivity in Lewis acid-mediated fragmentations of peroxides and ozonides: application to the synthesis of alkenes, homoallyl ethers, and 1,2-dioxolanes. *Journal of the Chemical Society, Perkin Transactions 1.* 2000;0(17):3006-13.
- [101] Connolly DJ, Gresham WF, inventors; du Pont de Nemours, E. I., and Co. . assignee. Sulfo derivatives of perfluorovinyl ether monomers patent GB1034197. 1966.

- [102] Ugo P, Cavaliere F, Rudello D, Moretto LM, Argese E. Nafion coated electrodes as voltammetric sensors for iron analysis in sediments and pore waters: an example from the lagoon of Venice. *Sensors*. 2001;1:102-13.
- [103] Ugo P, Moretto LM, Rudello D, Birriel E, Chevalet J. Trace iron determination by cyclic and multiple square-wave voltammetry at Nafion coated electrodes. Application to pore-water analysis. *Electroanalysis*. 2001;13:661-8.
- [104] Maletzky P, Bauer R, Lahnsteiner J, Pouresmael B. Immobilization of iron ions on Nafion and its applicability to the Photo-Fenton method. *Chemosphere*. 1999;38:2315-25.
- [105] Karyakin AA, Karyakina EE, Gorton L. Amperometric biosensor for glutamate using Prussian Blue-based "artificial peroxidase" as a transducer for hydrogen peroxide. *Analytical Chemistry*. 2000;72(7):1720-3.
- [106] Elliott CM, Freitag RA, Blaney DD. Electrochemistry, spectroelectrochemistry, and photochemistry of a series of new covalently linked tris(2,2'-bipyridine)ruthenium(II)/diquat complexes. *Journal of the American Chemical Society*. 1985;107(16):4647-55.
- [107] Miller SL. Polarographic currents from a combination of diffusion and reaction. *J Am Chem Soc*. 1952;74:4130-4.
- [108] Brdicka R, Wiesner K. Polarographic determination of the rate of the reaction between ferrohem and hydrogen peroxide. *Collect Czech Chem Commun*. 1947;12:39-63.
- [109] Delahay P, Stiehl GL. Theory of catalytic polarographic currents. *Journal of the American Chemical Society*. 1952;74(14):3500-5.
- [110] Lytle FE, Hercules DM. Luminescence of tris(2,2'-bipyridine)ruthenium(II) dichloride. *Journal of the American Chemical Society*. 1969;91(2):253-7.
- [111] Bhasikuttan AC, Suzuki M, Nakashima S, Okada T. Ultrafast Fluorescence Detection in Tris(2,2'-bipyridine)ruthenium(II) Complex in Solution: Relaxation Dynamics Involving Higher Excited States. *Journal of the American Chemical Society*. 2002;124(28):8398-405.
- [112] Sabhi S, Kiwi J. Degradation of 2,4-dichlorophenol by immobilized iron catalysts. *Water Research*. 2001;35(8):1994-2002.

Chapter Three

Bridged Nanojunctions via the Electrochemical Polymerization of Aniline and Pyrrole

Introduction

Conducting polymers are a class of conjugated organic molecules that have the electronic properties usually associated with semiconductors. In most cases the neutral state of the polymer is insulating. Upon oxidation (p-doping) the polymers become electrical conductors due to the formation of polarons. A polaron is a charge carrier (an electron or hole) and the accompanying structural deformation caused by the localized charge [1]. Polarons can also be formed through the reduction of the polymer (n-doping), although stable n-doped conducting polymers, like poly(3, 4-ethylenedioxythiophene), are rare [2]. Polarons formed upon oxidation of a polymer film allow for charge transport within a single chain of the polymer. Transport between chains occurs through a hopping mechanism [3]. The electronic properties of the conducting polymer are influenced by its structural uniformity and by the number of charge carriers. Two of the most commonly studied conducting polymers are polyaniline and polypyrrole, which have been used in applications ranging from corrosion protection [4-9] to photovoltaics [10-12]. A great deal of interest has also been given to the use of conducting polymers, like polyaniline and polypyrrole, in sensors, because of the sensitivity of their electronic properties to changes in the chemical environment [3, 13-22].

Variation of the synthetic method used to produce a conducting polymer is one way to control the structural uniformity, and influence the electronic properties of the polymer. Many different methods for preparing conducting polymers can be found in the scientific literature, but the vast majority can be categorized as either homogeneous or

heterogeneous oxidations, the latter generally occurring at electrode surfaces. Homogeneous oxidations are typically performed by dissolving the monomer into solution and then adding an oxidant, such as Fe^{3+} [23]. This usually results in the precipitation of the insoluble polymer that can be used for a specific application or studied further. Heterogeneous electrochemical polymerizations generally involve the electrochemical oxidation of a monomer directly at an electrode surface. In general, the polymerization takes place via coupling of radical cations formed at the electrode surface. In appropriate solvents, the coupled species precipitate onto the electrode leaving behind a stable film [24-26]. Soluble conducting polymers can be generated by adding polar functional groups to the monomer or by incorporating water soluble support polymers, like poly(4-styrenesulfonate) [27-30]. In this thesis all of the conducting polymers examined were prepared via heterogeneous electrochemical deposition onto electrode surfaces.

The specific methods and conditions used to electrochemically polymerize a monomer at an electrode surface influence the morphology and conductivity of the resulting films. For example, Vork and Janessen found that polypyrrole films electrochemically deposited from acetonitrile solutions were dense and uniform, while those formed from aqueous solutions had a tube-like structure [31]. A contradictory account was reported by Carquigny et al. who found that films electrochemically deposited from acetonitrile were thin and non-uniform, while those formed from water or 1% water in acetonitrile were uniform and dense [32]. Kim et al. found that polyaniline grown potentiodynamically using cyclic voltammetry (CV) at 20 V/s in an aqueous sulfuric acid solution produced films that were dense and uniform, in contrast to films

grown at 50 mV/s, which were amorphous and rough [33]. Dinh et al. reported that the electrochemical polymerization of aniline by cycling at lower potentials (0-1 V vs. a reversible hydrogen electrode) in aqueous solution resulted in films that were denser and more conductive than those formed by cycling to higher potentials (1.7 V) [34]. Upon oxidation of a conducting polymer, the film must incorporate anions to maintain electroneutrality. Diaz et al. found that the choice of counterion incorporated into the polymer film influences the stability of the polymer, as well as its electronic properties [35].

The eventual goal of the work presented in this chapter was to develop a sensor device based on conducting polymers. The vast amount of research already performed on the synthesis of conducting polymers, some of which is contradictory, makes it difficult to predict exactly what polymerization conditions to use for new research projects. Ultimately, it becomes necessary to start somewhere and worry about optimization as the need arises in the specific system being studied. In the case described in this thesis, the system sought was an electrochemical sensor for strong oxidants, in particular oxidants that might be used as explosives.

One of the primary goals of most analytical techniques or sensors is a low limit of detection. In 1995 Fan and Bard used scanning electrochemical microscopy (SECM) to demonstrate the detection of a single molecule in solution [36]. In the arrangement developed by the authors, a SECM tip was placed approximately 10 nm above a conductive substrate. In this configuration they were able to trap a single electroactive molecule in the gap and measure the current produced as it “bounced” back and forth between the oxidizing tip and the reducing substrate. Based on the simple diffusion

model, $x = \sqrt{2Dt}$ where x is the distance traveled, D is the diffusion coefficient and t is the time, they were able to predict the current produced by a single trapped molecule at a given tip-substrate distance. For example, if the tip was 10 nm from the substrate, as it was in their experiment, a molecule with a diffusion coefficient of $1 \times 10^{-5} \text{ cm}^2/\text{s}$ can traverse the gap between the electrodes 2×10^7 times per second. If an electron transfer event occurs each time the molecule approaches either the tip or the substrate, 2×10^7 electrons are transferred each second. Multiplying the number of electrons by Faraday's constant and dividing by Avogadro's number leads to the conclusion that a current of approximately 3 pA should be observed. The authors observed that the experimental results matched this diffusion based model.

The premise for the work presented in this chapter is that the principle of single molecule detection through a current amplification caused by trapping an electron "shuttle" in a small area can be extended to other systems. The basic design used in this work was one in which two gold electrodes were separated by a gap of approximately 50-200 nm. The gap was bridged by heterogeneous electrochemical polymerization of either polypyrrole or polyaniline, although a variety of other conducting polymers could be used in principle. For the device to work as a sensor, a bias would be applied across the gap while the polymer is in its neutral/insulating state. When an analyte strikes the polymer film and oxidizes, it a polaron would form. In this configuration the polaron would be confined to the polymer film on the electrodes, and, due to the bias, it would move from anode to cathode. Upon reaching the cathode and becoming reduced, a new oxidized site must be generated to conserve charge balance within the film. This cycle would then repeat and result in a relatively large current response to a single oxidation

event. In principle, this amplification could be used to detect single molecules of gas phase analytes. The overall goal of the work presented in this chapter was to create a device that could take advantage of this amplification and extend it to the detection of triacetone triperoxide (TATP). More specifically, the work focuses on examining polymerization methods in an attempt to create junctions applicable to such a system.

Experimental

Preparation of the Substrate: Silicon wafers (Silicon Quest International, Inc., Santa Clara, CA) were cleaned with isopropyl alcohol then water and dried with flowing nitrogen. Negative tone photoresist (ma-N 1410, Micro Resist Technology, Berlin, Germany) was applied via spin coating at 3000 rpm for 30 s in a dark room to protect the samples from light. The spin coating procedure, according to the manufacturer, resulted in a 1 μm film thickness. From this point in the procedure, the samples were protected from light during transport outside the darkroom. The samples were then heated on a hotplate at 100°C for 90 s. An appropriate mask was placed above the sample then the sample was irradiated using a UV lamp at 200 watts for 20 s. After being exposed, the wafers were placed in developer solution (ma-D 533S, Micro Resist Technology, Berlin, Germany) for approximately 30 s and then washed with water. The developing stage was monitored via a filtered light microscope to guarantee that the edges of the pattern were well defined. If the edges were not well defined, the sample was placed back into the developer solution for 10 s increments until well defined edges were achieved.

After the lithographic procedure was completed, approximately 5 nm of chromium and then approximately 50 nm of gold were sputter coated onto the substrates using the 3M magnetron sputtering system located in the University of Nebraska

Department of Physics and Astronomy (Lincoln, NE). After the metal deposition, the remaining resist was removed using acetone. A SEM micrograph of the resulting patterned electrodes is shown in Figure 3.1 (top).

The next step was to use Focused Ion Beam (FIB) milling to introduce a nanoscale gap. FIB milling uses a focused beam of gallium ions, which is produced by an ion column similar to those used in scanning electron microscopes, to ablate the surface of a sample. This technique can be used to incorporate arbitrary and sometimes complex patterns into substrates [37-39]. Adjusting the parameters of the ion beam, like the accelerating voltage, beam current, and the angle of incidence allows one to control the ablation of the sample [39]. Ben Wymore performed the FIB milling of the samples used in this chapter. For this work, the accelerating voltage of the ion beam was set to 30 keV, the beam current was set to 11 pA, and the angle of incidence was normal to the surface of the sample. The patterned metal electrodes were cut using the gallium ion beam to create two electrodes separated by a nanoscale gap. Generally, these gaps were 50-200 nm wide. A typical gap is shown in Figure 3.1 (bottom).

Electrochemical Polymerization Cell: The electrochemical cell design was based on one used previously by others in Professor Redepenning's research group [37, 38]. Electrical connections to the patterned, sputter coated, electrodes were made via ultrasonic welding of gold wire. After the electrodes were connected to external leads, a

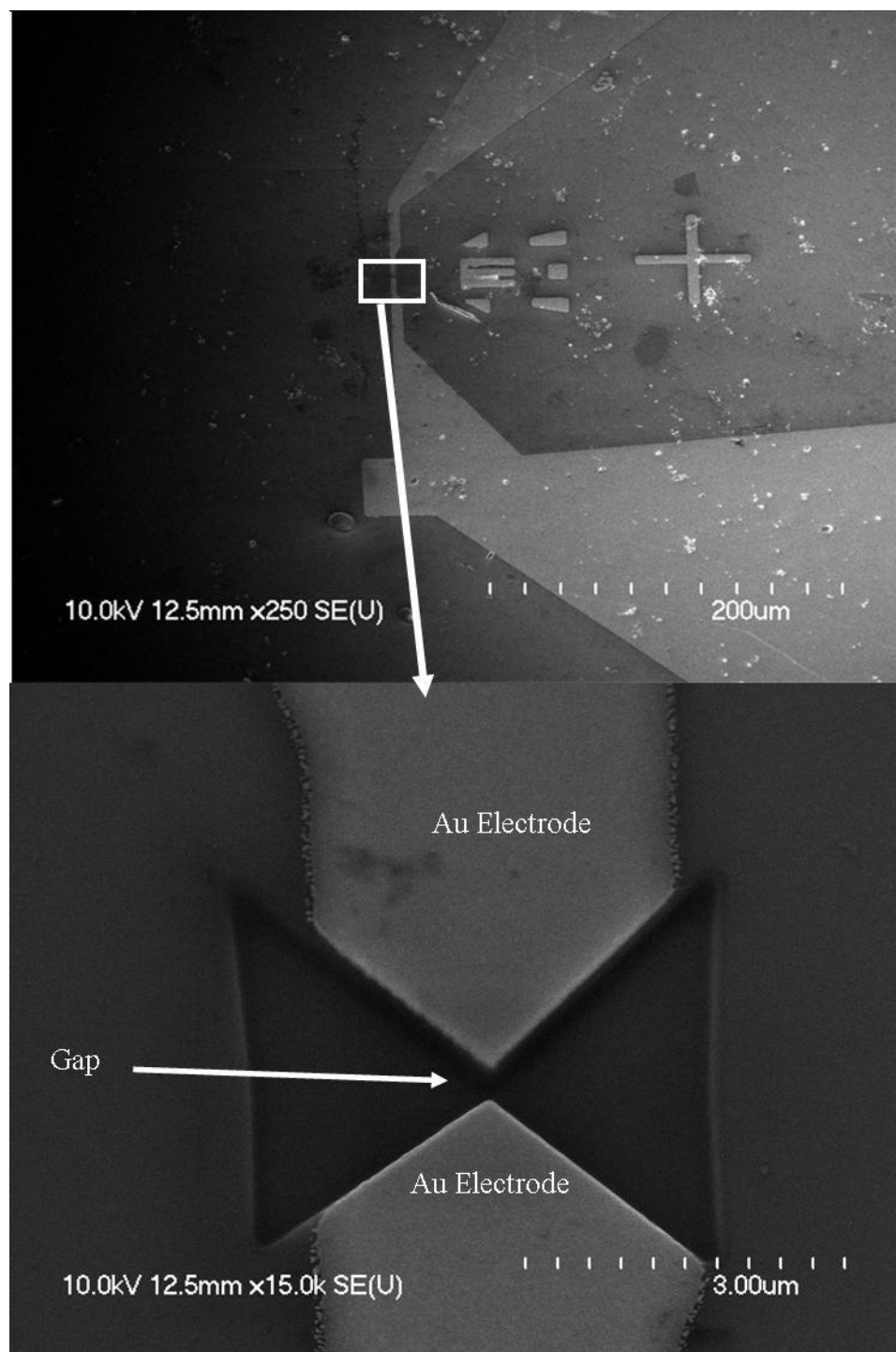


Figure 3.1. SEM micrograph of the patterned electrodes used for electrodeposition of conducting polymers (top), and an example of the junction area cut between the two electrodes using FIB milling (bottom).

silicone gasket was placed on top of the silicon chip and a solvent reservoir was attached to the top of the cell. The reservoir contained a platinum wire to act as a counter electrode. The reservoir was filled with an electrolyte or polymer deposition solution, and a silver wire was dipped into the solution to act as a pseudo-reference electrode. A photograph of the components of this cell is shown in Figure 3.2.

Electrochemical Polymerization Procedure: The polymerization bath for aniline was generally a 1 M aqueous sulfuric acid (Fisher, Waltham, MA) solution containing approximately 20 mM aniline monomer (Sigma-Aldrich, St. Louis, MO). Polypyrrole was generally deposited from solutions in acetonitrile (Acros, extra dry, New Jersey, USA) containing 100 mM tetrabutylammonium hexafluorophosphate (TBAPF₆, Sigma-Aldrich, St. Louis, MO) and approximately 10 mM pyrrole (Sigma-Aldrich, St. Louis, MO). The specific polymerization bath and conditions for the nanojunction devices discussed below are listed in Table 3.1.

Aniline and pyrrole both degrade over time in air and take on a yellow or brown color associated with unspecified oxidized species. These species were removed chromatographically by passing the monomer through a column of alumina (Fisher, chromatography grade, 80-200 mesh, Fair Lawn, NJ) that had been activated at 500°C for 18 hours prior to use. The chromatography was performed in a nitrogen atmosphere glove box by plugging the bottom of a disposable pipette with glass wool, partially filling the pipette with alumina, and placing the “as received” monomer onto the column directly without any additional solvent. The polar contaminants adsorbed on the polar stationary phase to produce clear and colorless liquids, which were then used for the polymerization baths.

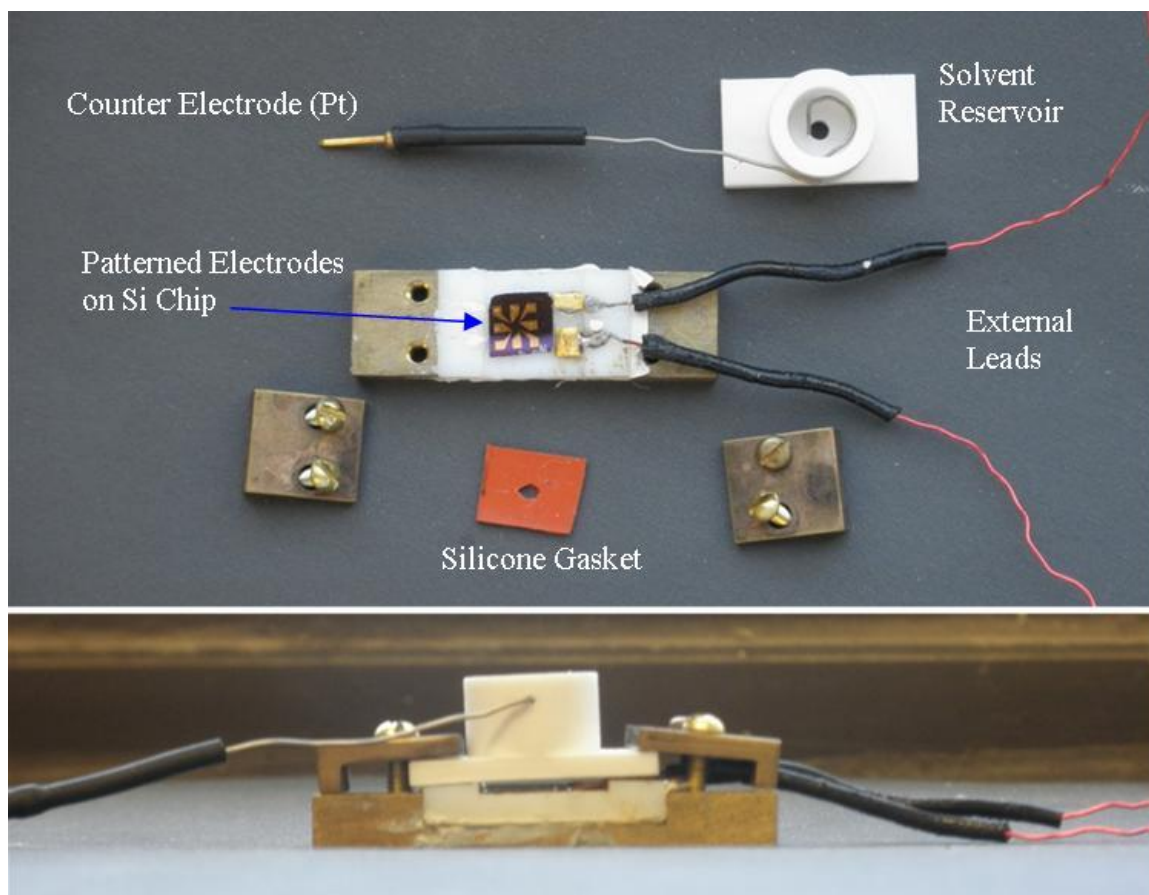


Figure 3.2. Photograph of the components of the electrochemical cell used for polymer deposition (top) and a side view of the assembled cell (bottom).

Table 3.1. The polymerization bath compositions and the working electrode (WE) potentials used for the nanojunctions discussed in this chapter.

Junction ID	Monomer concentration (M)	WE 1 Maximum Potential (V)	WE 1 Minimum Potential (V)	Scan rate (V/s)	WE 2 Conditions
Polyaniline					
1	0.022	0.7	-0.4	0.1	Fixed at -0.35 V
2	0.022	0.7	-0.45	0.1	Fixed at -0.45 V
3	0.025	0.7	-0.4	0.1	1 polymerization cycle Scanned with WE 1
4	0.025	0.7	-0.45	0.1	Scanned with WE 1 for 40 cycles Uncontrolled for final 3 cycles
5	0.029	0.7	-0.4	20	Scanned with WE 1
6	0.032	0.7	-0.4	20	Fixed at -0.3 V
7	0.025	0.7	-0.6	20	Fixed at -0.3 V
Polypyrrole					
1	0.015	1.5	-0.2	0.1	Fixed at 0 V
2	0.007	1.1	-0.2	0.1	Fixed at 0 V
3	0.01	0.95	-0.4	0.1	2 polymerization cycles Fixed at -0.3 V
4	0.007	0.9	-0.8	0.1	Uncontrolled

After the cell was assembled, a monomer free electrolyte solution was added to the solvent reservoir and the electrodes were cycled until a stable, reproducible, charging current was observed. This cycling was done to make sure that the electrode surface was clear of contaminants before polymer deposition.

The polymerizations were performed via cyclic voltammetry using a bipotentiostat (CHI 760C, Austin, TX). One of the working electrodes (WE 1) was cycled between a potential at which the monomer was oxidized and polymerization occurred, and a potential at which the deposited polymer film was neutral/insulating and no growth occurred. The potential of the other electrode (WE 2) was fixed at a single value, cycled along with WE 1, or left uncontrolled, depending on the specific experiment. Examples of the various deposition methods are discussed in the experimental results.

Characterization: Much of the characterization was done by interpreting scanning electron microscopy (SEM) images of the junctions after the electropolymerizations. The images in Figure 3.26 were collected by Dr. Andrei Sokolov of the University of Nebraska Department of Physics and Astronomy (Lincoln, NE); all other images were obtained by me using a Hitachi S4700 Field-Emission SEM (University of Nebraska, Lincoln, NE). Length measurements from the SEM images were made using the free software ImageJ developed by the National Institutes of Health (Bethesda, MD). Some polymer junctions were also subjected to conductivity testing via DC (cyclic voltammetry, and potentiostatic experiments) and AC (AC impedance) methods. All conductivity testing was performed using the same CHI 760C bipotentiostat.

Results and Discussion

Polyaniline: The goal of this project, as mentioned in the introduction, was to develop a vapor phase sensor for TATP. It is well known that aniline reacts, sometimes violently, with peroxides [40]. Considering this reactivity, and the fact that polyaniline is a commonly used conducting polymer, I attempted to use polyaniline to bridge the gap between the patterned electrodes. There were two additional enticements for the choice of polyaniline. One was that it had been demonstrated that control of the morphology of polyaniline could be achieved by relatively simple means, like controlling the potential sweep rate during heterogeneous electrochemical polymerization, changing the pH of the deposition solutions, or using different anions as dopants [33, 41, 42]. The other lure was the demonstration by He et al. of discrete conductance switching from the insulating to conducting states of polyaniline nanowires bridging small gaps between electrodes [43].

An example of a typical heterogeneous electrochemical polymerization of aniline on a gold disk electrode is shown in Figure 3.3. Yang and Bard analyzed the mechanism for the polymerization of aniline in sulfuric acid solutions and were able to identify the peaks in the voltammogram shown in Figure 3.3 [44]. The magnitude of the current in the voltammogram increases with increasing cycle number due to the growth of the electroactive polymer film. The lower voltammogram in Figure 3.3 is the last voltammetric cycle of the polymerization. The peaks at 0.02 V and 0.52 V on the positive sweep correspond to the polaron and bipolaron oxidations of the polymer film. The peaks on the negative sweep at 0.46 V and -0.14 V are the reduction of the bipolaron and polaron states, respectively. The peaks in the intermediate region correspond to the

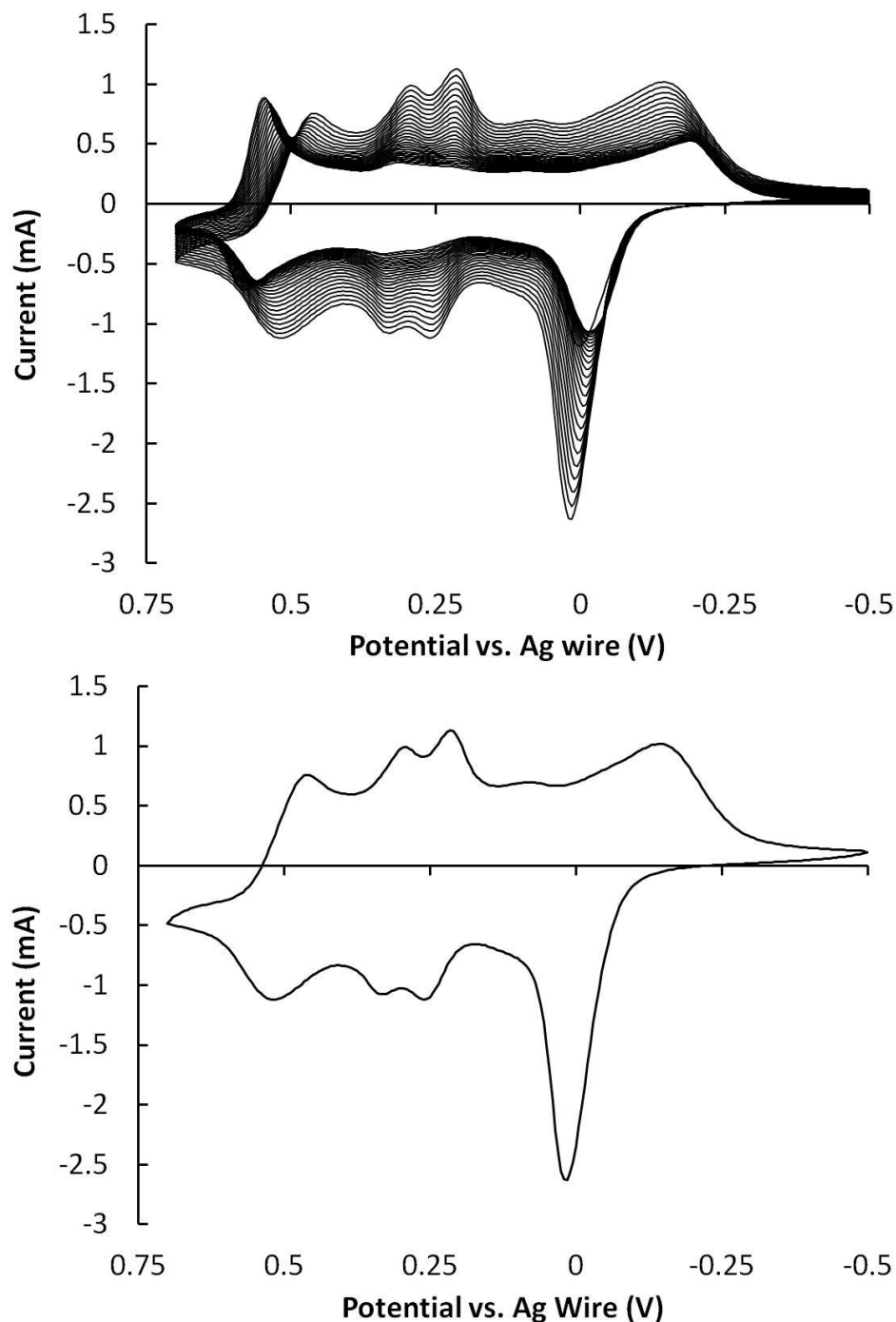


Figure 3.3. A typical cyclic voltammogram showing the electrochemical polymerization of aniline at a gold electrode from a 20 mM solution of aniline in 1 M sulfuric acid at a scan rate of 100 mV/s (top). The final cycle of the polymerization displaying the peaks associated with the various oxidation states of the polymer (bottom). On the forward sweep from -0.5 V to -0.1 V, the film is in the leucoemeraldine state; between -0.1 V and 0.4 V, the polymer is in the emeraldine state; and at potentials more positive than 0.4 V, the film is in the pernigraniline state.

byproducts benzoquinone/hydroquinone (ca. 0.25 V) and p-aminophenol/benzoquinoneimine (ca. 0.3 V) [44].

Polyaniline is electrochromic [45, 46]. The neutral, polaron, and bipolaron states are named leucoemeraldine, emeraldine, and pernigraniline, respectively, based on the colors associated with their oxidation states [45]. The polymer changes from a clear yellow to a blue-green color as it switches from the neutral/insulating state to the polaron oxidized/conductive state. Oxidation of the polymer to the bipolaron state causes the color to turn black. This electrochromic property can be used to visually determine if a polymer film has been formed on the electrode surface and to determine which oxidation state the film is in. This property has also been used to create prototypes of adjustable light filtering windows [47, 48].

Polyaniline Nanojunction 1: A polymerization of aniline onto a nanojunction was attempted using a solution containing 22 mM aniline in 1 M aqueous H_2SO_4 . For this experiment, WE 1 was cycled at a scan rate of 100 mV/s. The polymerization resulted in an identifiable connection between the electrodes in the junction. Figure 3.4 displays the voltammogram recorded during the polymerization (top) and the voltammogram that indicated an electrical connection occurred between WE 1 and WE 2 (bottom). The spike in the current at WE 2, which was held at a fixed potential of -0.35 V (vs. reference), provided evidence that a connection between the working electrodes had formed. The connection between the working electrodes occurred when WE 1 was at a potential of 0.1 V (vs. reference). It is interesting that the connection between the nanojunction electrodes did not occur at potentials where the aniline monomer typically oxidizes, in

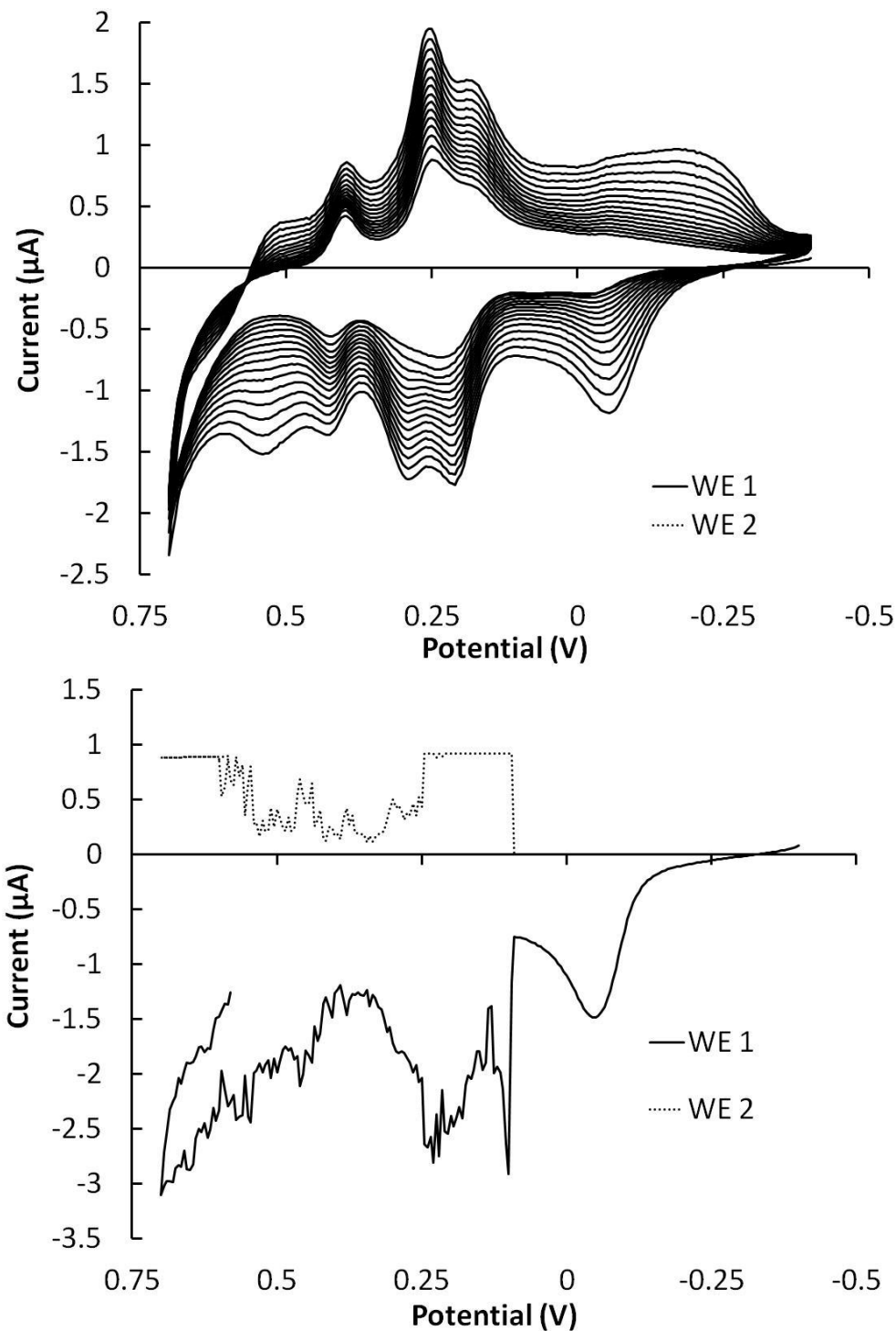


Figure 3.4. The cyclic voltammogram of the polymerization of polyaniline onto nanojunction 1 (top). The WE 2 current in the top voltammogram traces the x-axis. The connection between the electrodes occurs upon oxidation of the film, as evidenced by the current step seen at both WE 1 and WE 2 (bottom). The current at WE 2 went off scale at 1 μA .

this case at approximately 0.7 V (vs. reference). Here the connection occurred upon oxidation of the polymer film to the polaron state.

Two factors help to justify this observation. First, the polymerization of aniline takes on an autocatalytic mechanism after the initial formation of a polyaniline film [49-51]. The second factor is that the polymer film swells upon oxidation. This swelling occurs because anions and solvent are incorporated into the polymer to maintain electroneutrality, as has been studied previously by Lizarraga et al. [52].

To estimate the resistance of the connection between the working electrodes in the device, I bathed the junction in a monomer free electrolyte solution (1M H₂SO₄) and performed a differential scan cyclic voltammetry experiment. During the experiment, a potential sweep was applied to both working electrodes vs. a silver wire while a constant potential difference of 10 mV was maintained between WE 1 and WE 2. The results of this experiment are shown in Figure 3.5. The current is plotted vs. time rather than potential to better display the current passing between the working electrodes.

One would expect the response of WE 1 during the differential scan voltammetry experiment to be similar to the response of the same electrode during the polymerization because the experiments were qualitatively similar (i.e., a potential sweep was applied to an electrode coated with polyaniline). For the differential scan voltammetry experiments performed in this work, one can usually attribute deviations from the typical voltammogram obtained during polymerization (Figure 3.4, top) to currents passing between the two working electrodes in response to a potential difference. For example, when a connection formed between the two working electrodes during the polymerization

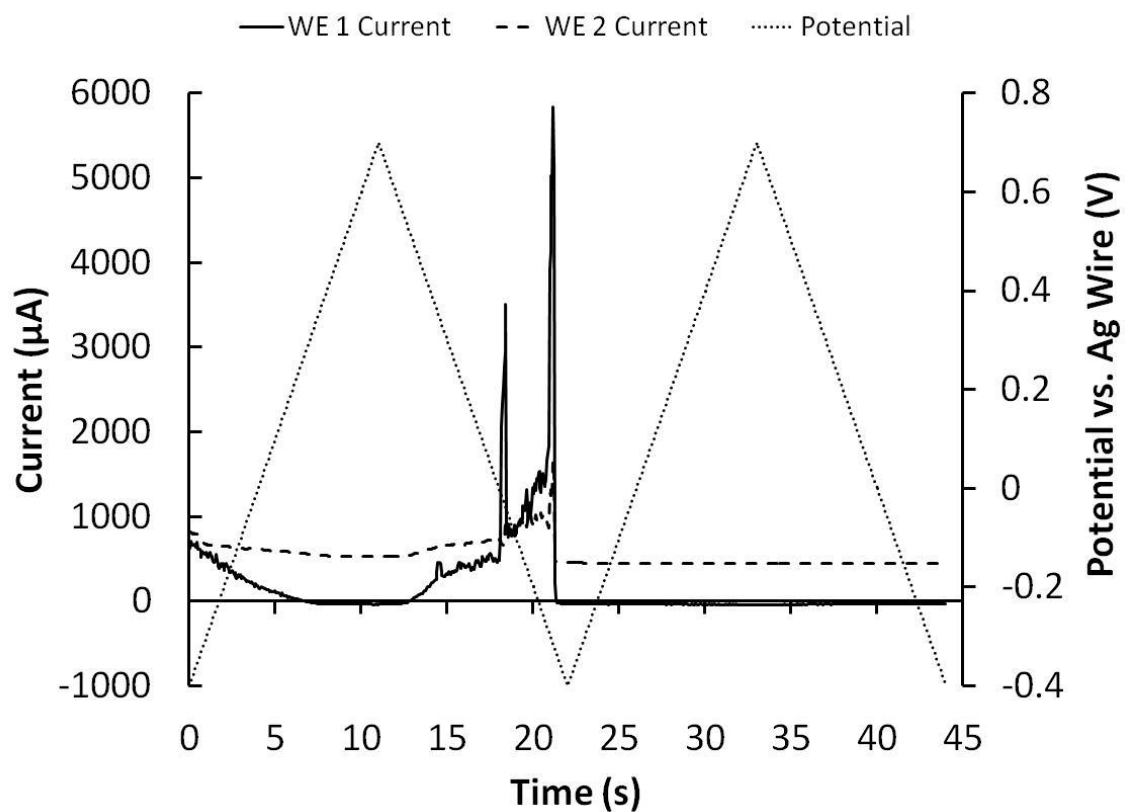


Figure 3.5. The differential scan cyclic voltammogram of polyaniline nanojunction 1 plotted as a function of time. Both electrodes were swept vs. a silver wire while a constant potential difference of 10 mV was maintained between WE 1 and WE 2. Plotted are the current at WE 1 (solid line), the current at WE 2 (dashed line), and the potential of WE 1 vs. the silver wire (dotted line).

(Figure 3.4, bottom) a current step occurred due to the potential difference between WE 1 and WE 2.

The currents recorded during the differential scan voltammetry experiment were significantly larger than those observed during polymerization. During the first potential sweep of the differential scan voltammetry experiment (Figure 3.5, from 0-22 s), the current at WE 1 began at nearly 600 μA , dropped to approximately -30 μA near the switching potential, and then gradually rose before spiking to almost 6 mA. The current at WE 2 remained at roughly 600 μA through most of the first voltammetric cycle, then rose to approximately 1 mA near the end of the cycle. The cause of the responses recorded during the first cycle of the differential scan voltammetry experiment are not clear, though based on the responses recorded during the second cycle I suspect a short circuit was present somewhere in the system.

Constant currents of approximately -30 μA and 500 μA for WE 1 and WE 2, respectively, were recorded during the second voltammetric cycle, as shown in Figure 3.5 (from 22-44 s). The magnitude of the maximum current recorded during the polymerization was approximately 2 μA , as shown in Figure 3.4. The relatively low currents associated with the redox processes of the polymer film led me to conclude that the majority of the current measured during the second cycle of the differential scan voltammetry experiment was passing between the working electrodes. A current of 500 μA passing through the junction seemed improbable if the connection between the working electrodes were composed of conducting polymer. A current of 500 μA with a potential difference of 10 mV corresponds to a resistance of 20 Ω . If one estimates that the size of the contact between the working electrodes in the junction was 100 nm in

length with a cross sectional area of 50 nm^2 , the resulting conductivity of the connection was $2 \times 10^6 \text{ Sm}^{-1}$, as calculated using equation (3.1)

$$\sigma = \frac{l}{RA} \quad (3.1)$$

where σ is conductivity, l is length, R is resistance, and A is the cross sectional area. This value is similar to those measured for metals like platinum [53]. In contrast, the conductivity of polyaniline has been reported to range from approximately 0.1 Sm^{-1} to 6000 Sm^{-1} [54, 55]. I tried to verify the resistance measured during the differential scan voltammetry experiment by measuring the resistance of the junction using a digital ohmmeter after the device had been removed from the electrochemical cell. The resistance of the junction exceeded the maximum value measureable by the ohmmeter, which indicated that the electrodes in the junction were no longer connected. Previously I had observed that over-tightening the screws holding the solvent reservoir onto the electrochemical cell sometimes resulted in short circuits. These short circuits produced voltammetric results similar to the one shown in Figure 3.5. I also observed that the electrical connections that resulted from the over-tightened reservoir screws would not be present after the devices were removed from the electrochemical cell. Based on my previous experiences and the conductivity estimates discussed above, I concluded that a short circuit, caused by over-tightening the reservoir screws, was the reason for the high current observed in the second cycle of the differential scan voltammetry experiment. Because the connection between the electrodes in the junction had been destroyed, I proceeded to another sample. Regardless of the source of the relatively large current measured by differential scan cyclic voltammetry, the results of this attempt to grow

polyaniline were promising because of the connection that occurred between the two working electrodes during the polymer deposition experiment.

Polyaniline Nanojunction 2: The successful connection of the previous junction prompted an attempt to repeat the polymerization using the same conditions but with one small modification. One potential sweep was applied to WE 2 to deposit a small amount of polymer. I hypothesized that the polymer might connect more strongly with polymer than with the bare metal, and this would result in a robust connection that would allow me to obtain SEM images of the intact junction.

An initial connection for this junction occurred during the 17th voltammetric cycle. An additional voltammetric cycle was performed to strengthen the connection in the junction and lower the resistance. The results of this additional cycle are shown in Figure 3.6. The approximately equal and opposite current spikes observed in the data shown in Figure 3.6 demonstrate that an electrical connection was present between the electrodes. The initial current spike upon connection for this junction reached around 7×10^{-8} A. After the additional cycle, the current was as high as approximately 8×10^{-7} A.

SEM images of the junction are shown in Figure 3.7. The distance between the electrodes was 180 nm. The thickness of the polymer on the right electrode (WE 1), when measured away from the tip of electrode, was 130 nm. The micrograph supports the conclusion that a connection existed between the electrodes. The polymer on WE 1 (right) appeared to be relatively uniform in the area of the junction. The polymer on WE 2 was thin and nodular in appearance. Moving the junction from the polymerization cell to the electron microscope and back resulted in a break in the connection and therefore no further measurements were performed.

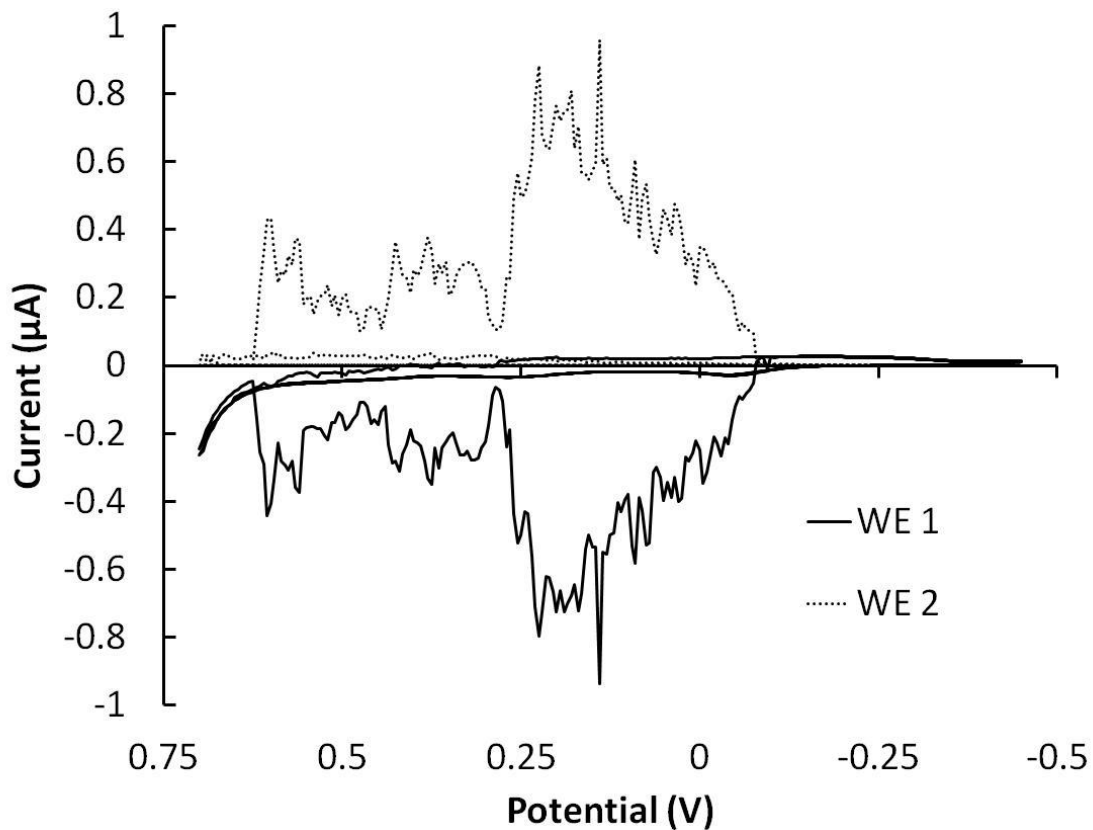


Figure 3.6. Cyclic voltammogram of polyaniline nanojunction 2 during polymer deposition. The mirrored currents show that a connection was formed between the electrodes in the junction. WE 1 was swept at 100 mV/ s. WE 2 was fixed at -0.45 V (vs. reference).

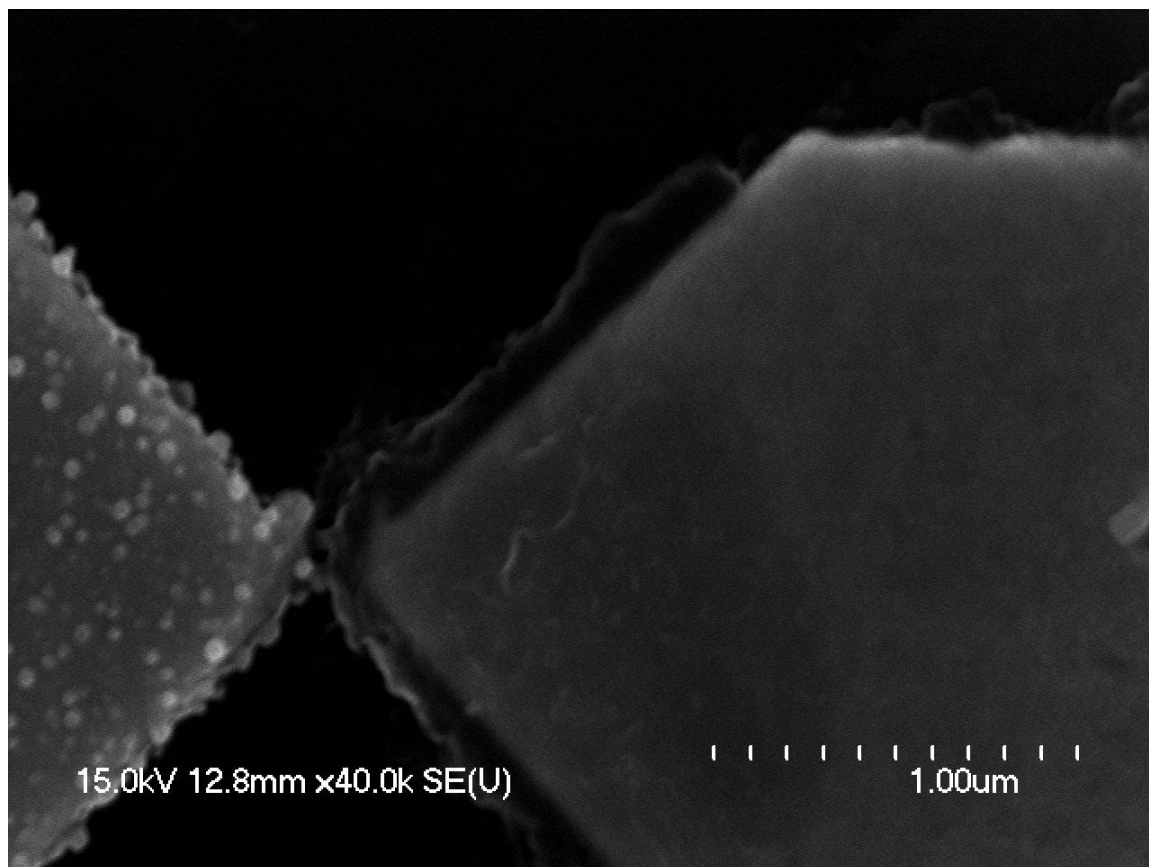


Figure 3.7: SEM micrograph of the junction area of polyaniline nanojunction 2. WE 1 is on the right. Polyaniline was present on both electrodes. The polymer on WE 1 had a relatively smooth texture. The polymer on WE 2 had some modules on the surface.

Polyaniline Nanojunction 3: Transporting the devices described in this chapter without destroying the fragile polymer junction area was a frequent challenge. I attempted to grow a relatively large amount of polymer in some junctions to form connections that were more robust. One such junction was prepared by polymerizing on both electrodes simultaneously for 40 cycles from bath similar to those used previously. I assumed that 40 cycles of polymerization at each electrode would produce such a large amount of polymer that the electrodes would be completely covered, and that this procedure would result in a robust connection between the electrodes. I chose 40 cycles because of the previous observation that approximately 20 cycles on one electrode was sufficient to bridge the gap between the two electrodes in the junction. The final two cycles of this polymerization are shown in Figure 3.8. The shape of the voltammetric response indicates a film of polyaniline was successfully deposited on each electrode.

Figure 3.9 shows the SEM micrograph of the junction. The films on the electrodes looked relatively uniform and smooth, just like the previous example, (Figure 3.7) which was produced under the same polymerization conditions. The SEM image in Figure 3.9 shows that there was a relatively large amount of polymer on both electrodes, and it appears that the polymer grew near the junction area, particularly on WE 2 (right). This image might lead one to conclude that a connection existed between the electrodes.

To test whether a connection was truly present, I performed a differential scan cyclic voltammetry experiment. During the voltammetric potential sweep, a constant 60 mV potential difference was maintained between the two working electrodes. If there were a connection between the electrodes, one would expect that the 60 mV potential difference in this experiment would produce voltammograms that were offset due to the

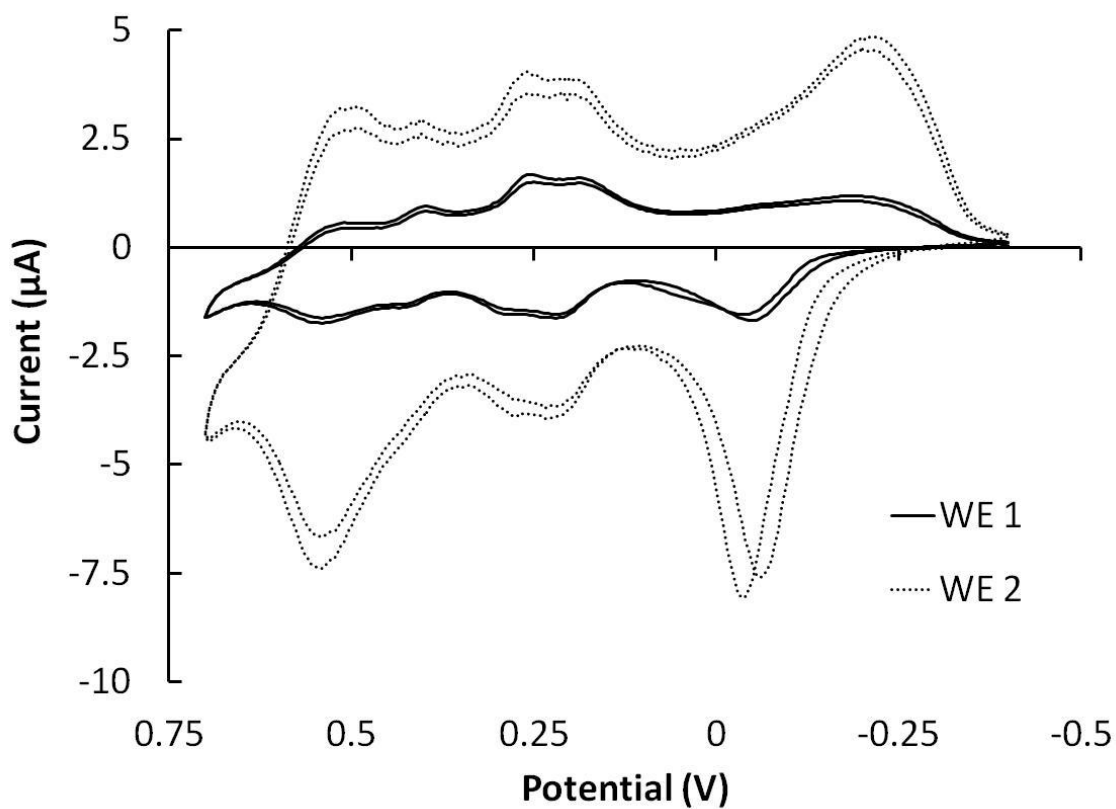


Figure 3.8. The voltammogram of the final two voltammetric cycles during polymerization for polyaniline nanojunction 3. Both electrodes were cycled through the full potential range 40 times at 100 mV/s to deposit a large amount of polymer on each.

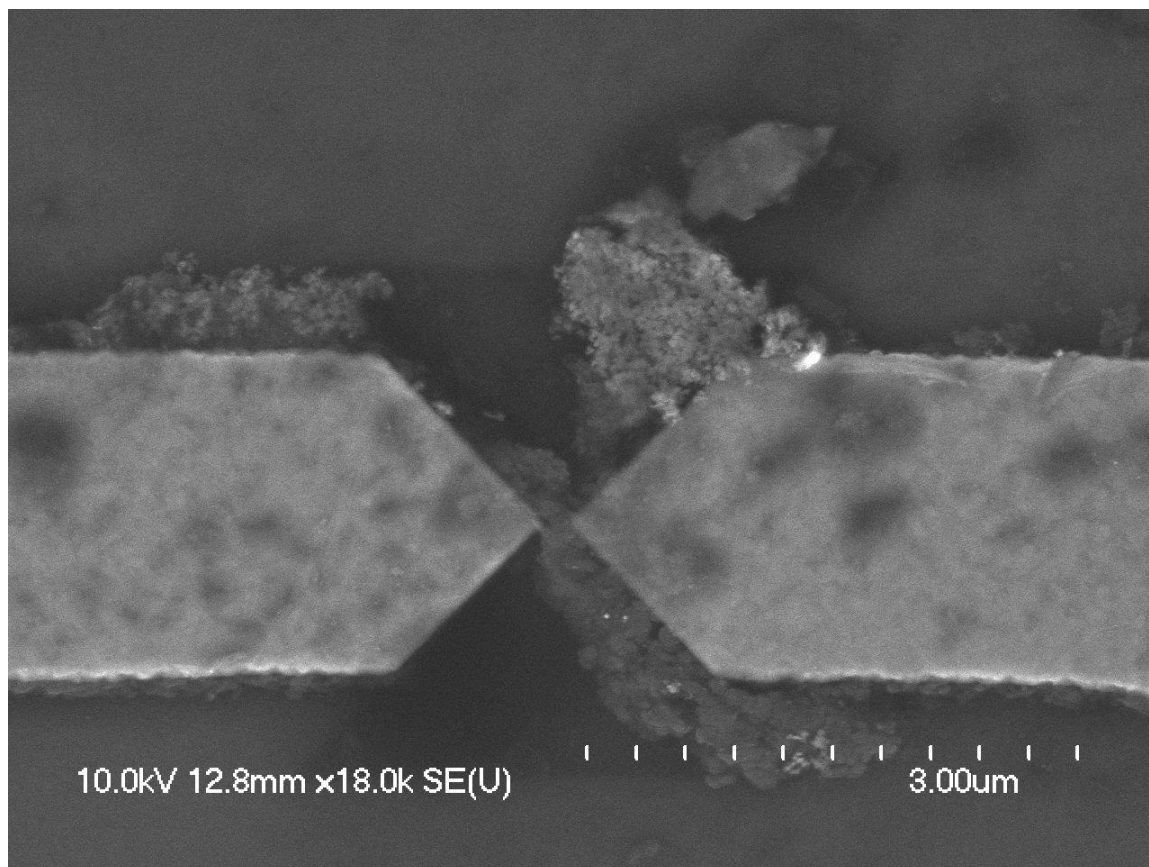


Figure 3.9. SEM micrograph of polyaniline nanojunction 3, showing polymer on both electrodes. WE 1 is on the left.

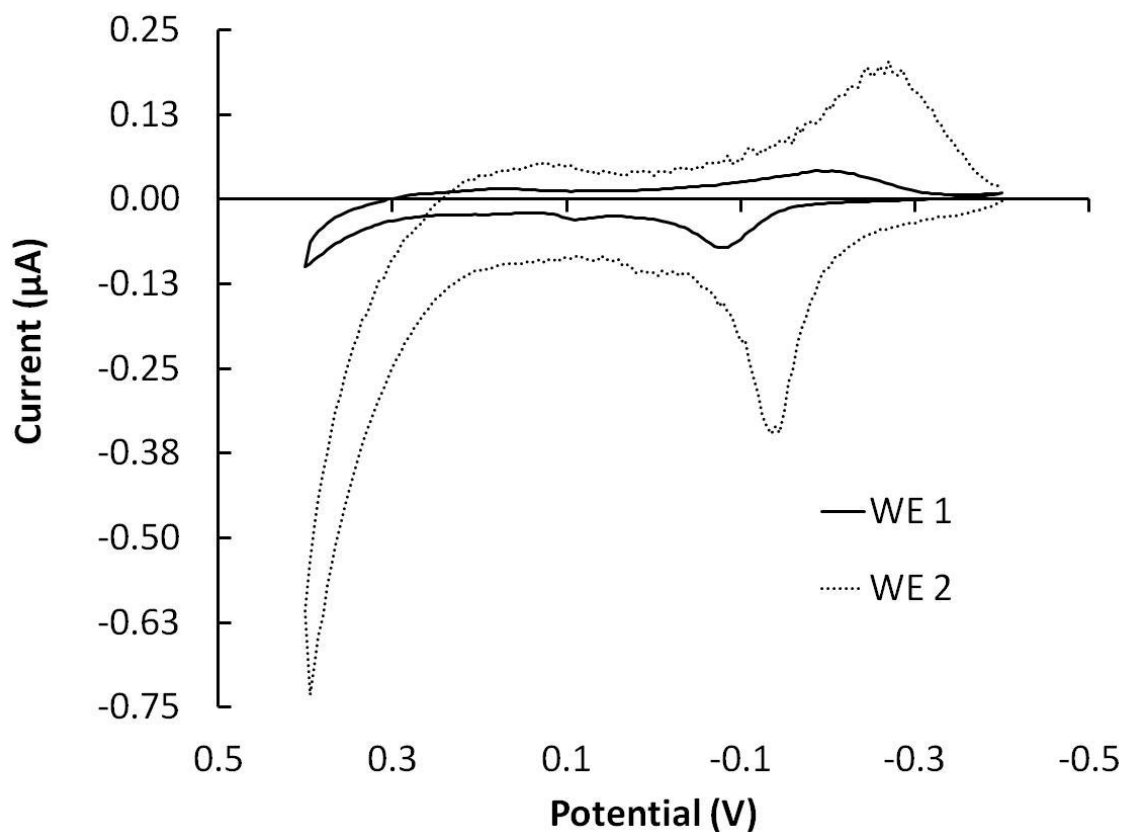


Figure 3.10. The differential scan cyclic voltammogram of polyaniline nanojunction 3. A 60 mV differential was maintained between WE 1 and WE 2 during the potential sweep. The shape of the voltammograms indicates that a polymer film is on both electrodes, but the voltammograms do not appear to show a connection between the electrodes.

current flowing between the working electrodes. Figure 3.10 shows that the voltammogram for each electrode in monomer free 1 M H₂SO₄ solution displayed the typical characteristics of an electrode coated with a polyaniline film, but there appeared to be no current offset even though the voltammograms showed the expected potential offset. Despite evidence to the contrary in the SEM images, a logical conclusion of these observations is that this junction remained "open" (i.e., that the polyaniline had not successfully traversed the gap).

Polyaniline Nanojunction 4: A large amount of polymer that connected the two working electrodes in a junction was deposited using a 25 mM aniline solution with 1 M aqueous H₂SO₄ as supporting electrolyte. The potentiodynamic electrochemical polymerization was performed at a scan rate of 100 mV/s. Polymer was deposited on both electrodes for 43 cycles, followed by 3 cycles on only WE 1. I stopped the polymerization when I observed an increase in the noise during the final three cycles to investigate the source of the noise. Figure 3.11 shows the voltammogram of the final three cycles of the polymerization.

As is seen in Figure 3.12, cycling the working electrodes at 10 mV/s while maintaining a fixed potential difference of 10 mV between WE 1 and WE 2 resulted in voltammograms exhibiting a current caused by the 10 mV potential difference. A similar result was seen by He et al. in their conducting polymer junctions after deposition of a relatively large amount of polymer [56]. The SEM micrograph (Figure 3.13) shows that a significantly larger amount of polymer was deposited on these electrodes compared to the junctions discussed previously.

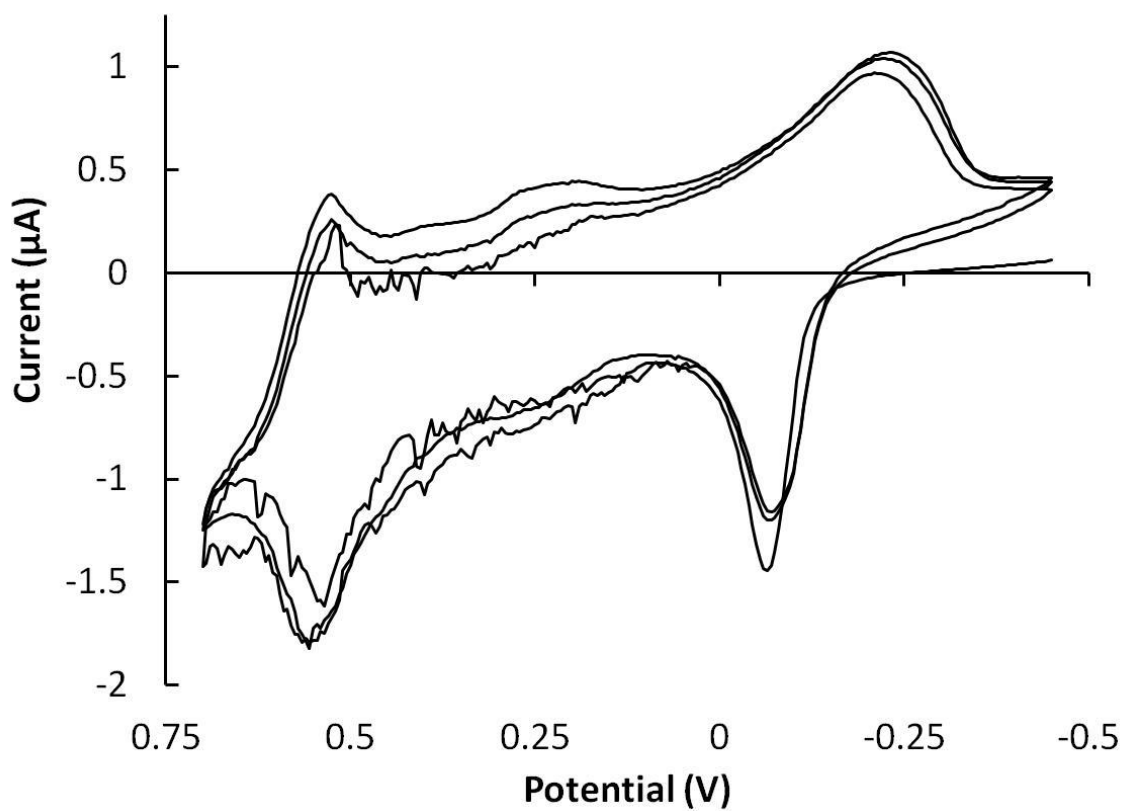


Figure 3.11. Cyclic voltammogram of the final three polymerization cycles for polyaniline nanojunction 4.

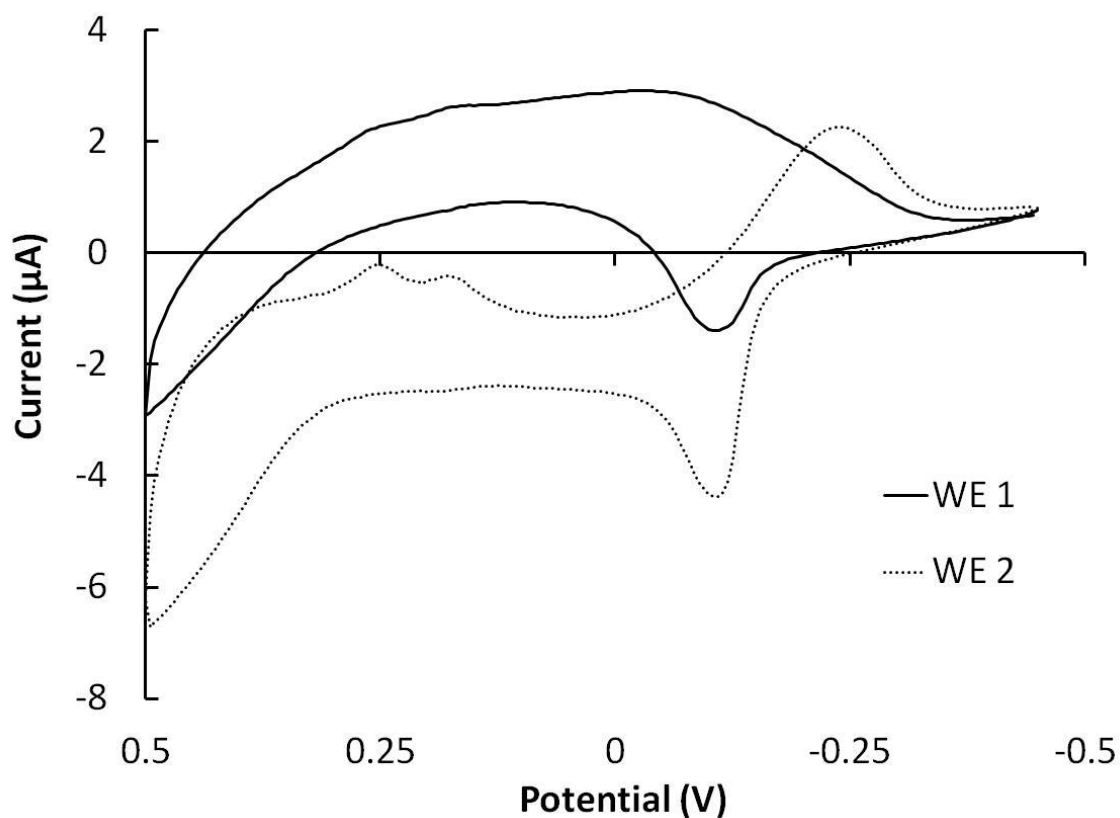


Figure 3.12. The result of a differential scan cyclic voltammogram performed on polyaniline nanojunction 4. A constant potential difference of 10 mV was maintained between WE 1 and WE 2 while both electrodes were swept at 10 mV/s. The curved response is indicative of a connection between the electrodes.

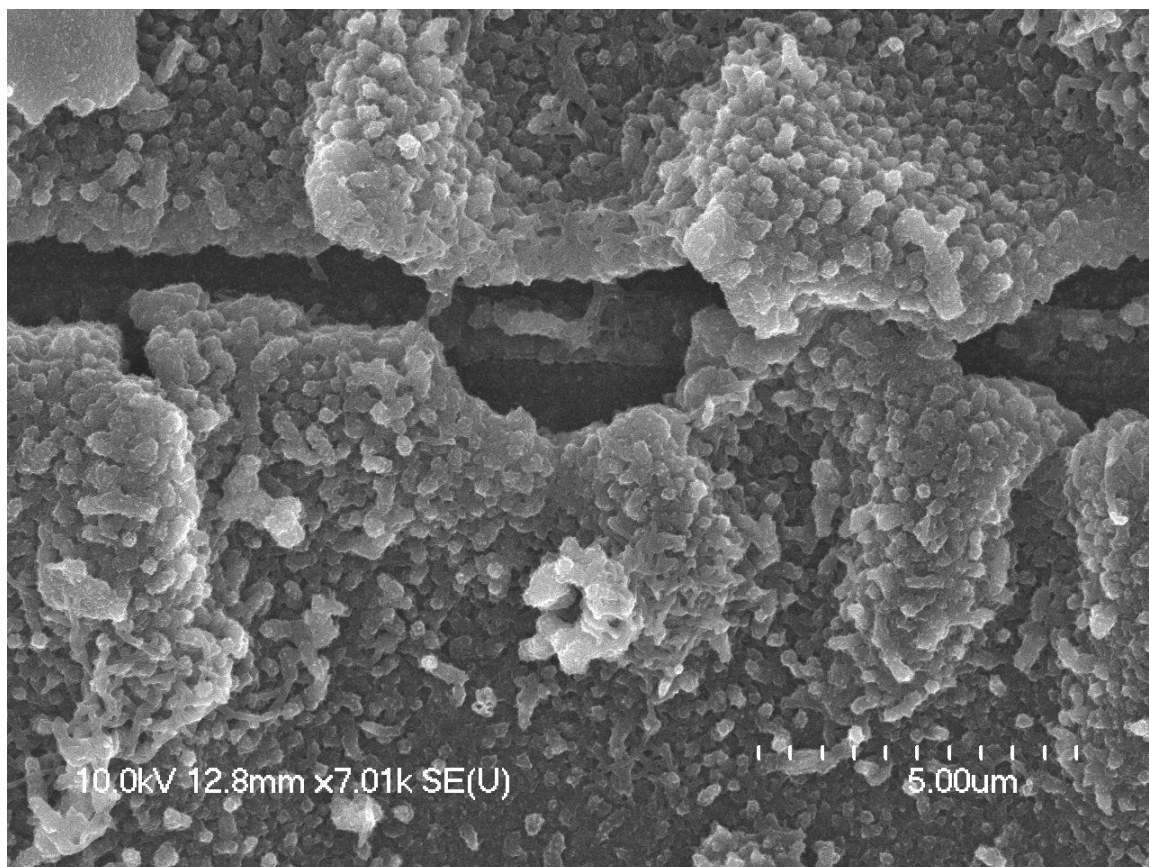


Figure 3.13. SEM micrograph of polyaniline junction 4. The large amount of polymer on the electrodes buried the junction area underneath.

Overall, the utility of this junction for further analysis was limited by the fact that the amount of polymer was so large that the junction was no longer visible in the SEM micrograph. The real successes of this experiment were that the deposition conditions resulted in a connection between the electrodes and that the junction exhibited electronic properties qualitatively similar to those reported elsewhere [56].

Polyaniline Nanojunction 5: As noted above, the scan rate used during polymerization can affect the morphology of the resulting polymer films. Yang et al. noted that using scan rates of 20 V/s resulted in polyaniline films that were more uniform than those produced at slower scan rates [33, 44]. I applied faster scan rates to the polymerizations in my work to see what effect the adjustment of the scan rate would have on both the electrical connection and the morphology of the polymer junctions.

An interesting case occurred the first time this procedure was attempted, and this case illustrates one of the problems I occasionally encountered with polymerizations across nanoscale gaps. Figure 3.14 shows three SEM micrographs. The first (Figure 3.14, top-left) was obtained after 7713 voltammetric cycles on both electrodes at 20 V/s. A relatively thick (225 nm) film of polymer was formed on each electrode, but the polymer was only deposited in the area away from the junction. The top-right image in Figure 3.14 shows the same junction after an additional 8000 voltammetric cycles. The bottom image shows the junction again, after another 9250 voltammetric cycles. Both the top-right and bottom images show that a large amount of additional polymer was deposited, but only in the areas away from the junction. It is unclear why the polymer did not grow in the junction area of this particular sample initially. A reasonable hypothesis is that a small bubble may have been blocking the area. Additional polymer

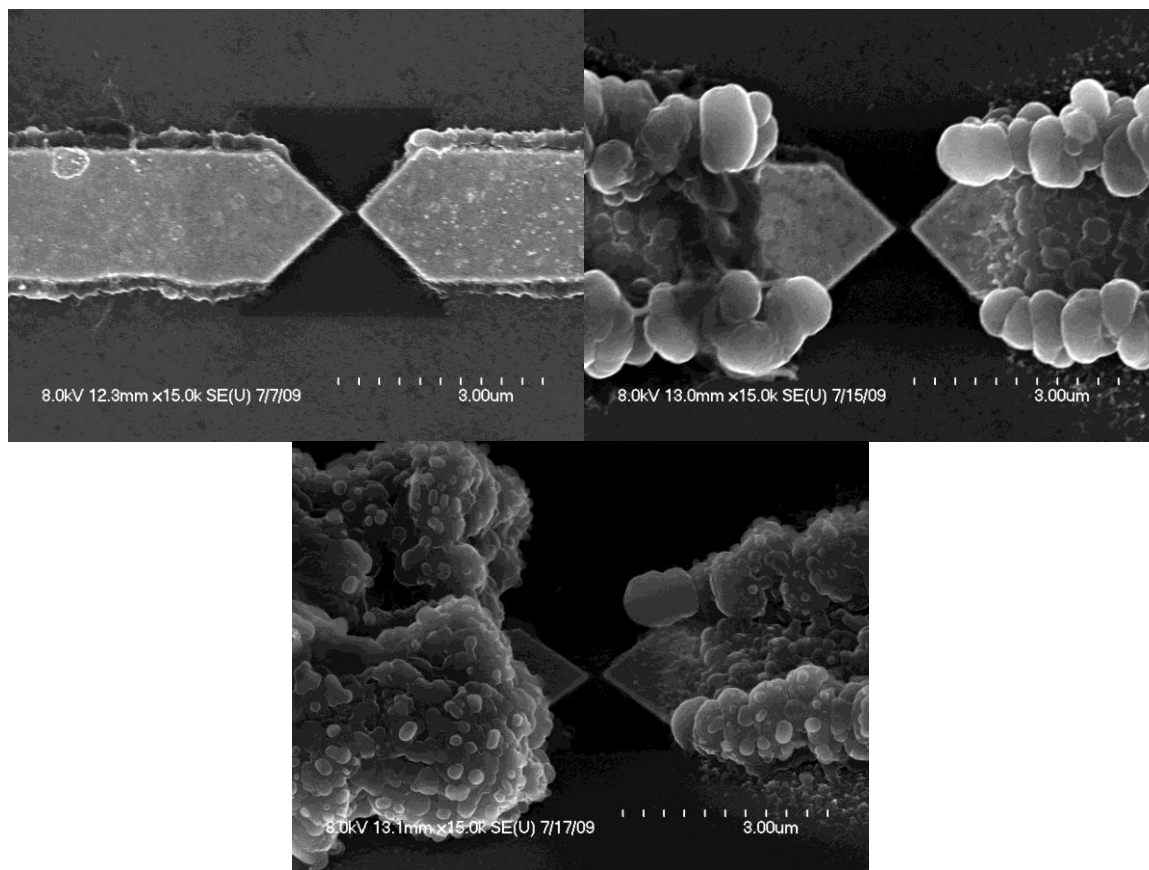


Figure 3.14. SEM images of polyaniline nanojunction 5 after the initial polymerization (top left), as well as a second (top right), and third (bottom) polymerization. Large amounts of polymer formed all over the electrode but not in the junction area.

growth on the areas where polymer had already been deposited is expected, because it has been shown that after the formation of an initial polymer film the overpotential required to continue the polymerization decreases [57].

Polyaniline Nanojunction 6: The 225 nm thick polymer film formed at 20 V/s during the initial polymerization in the previous example was relatively uniform. This uniform film led me to use faster scan rates during polymerization on other junctions.

In this example, a 20 V/s scan rate was applied to WE 1 while WE 2 was fixed at -0.3 V (vs. reference) during the deposition. A connection was achieved after 2250 cycles. I analyzed the connection using cyclic voltammetry in a monomer free 1 M H₂SO₄ (aq) solution at a scan rate of 100 mV/s. The potential of WE 2 was fixed at -0.3 V (vs. reference) during the CV. The result of this experiment is shown in Figure 3.15. In the 2250th cycle, the current at WE 2 jumped from 1×10^{-8} A to 2×10^{-7} A as the potential of WE 1 approached 0.4 V (vs. reference), and the current remained elevated until the potential of WE 1 had swept back to approximately 0 V (vs. reference), at which point the current dropped back down to approximately 1×10^{-9} A. This result indicated that a connection was present between the electrodes. It also demonstrated that the current flowing between the working electrodes when the polymer was in the oxidized state was relatively high when compared to the current flowing between the electrodes when the polymer was in the neutral state. The SEM micrograph in Figure 3.16 shows that a bundle of polymer fibers was present directly in the junction area.

This device was used as a test case to find out if polyaniline junctions would be responsive to interaction with TATP. For this test, I bathed the junction in a solution of 100 mM TBAPF₆ in acetonitrile. As mentioned above, changing the electrolyte can

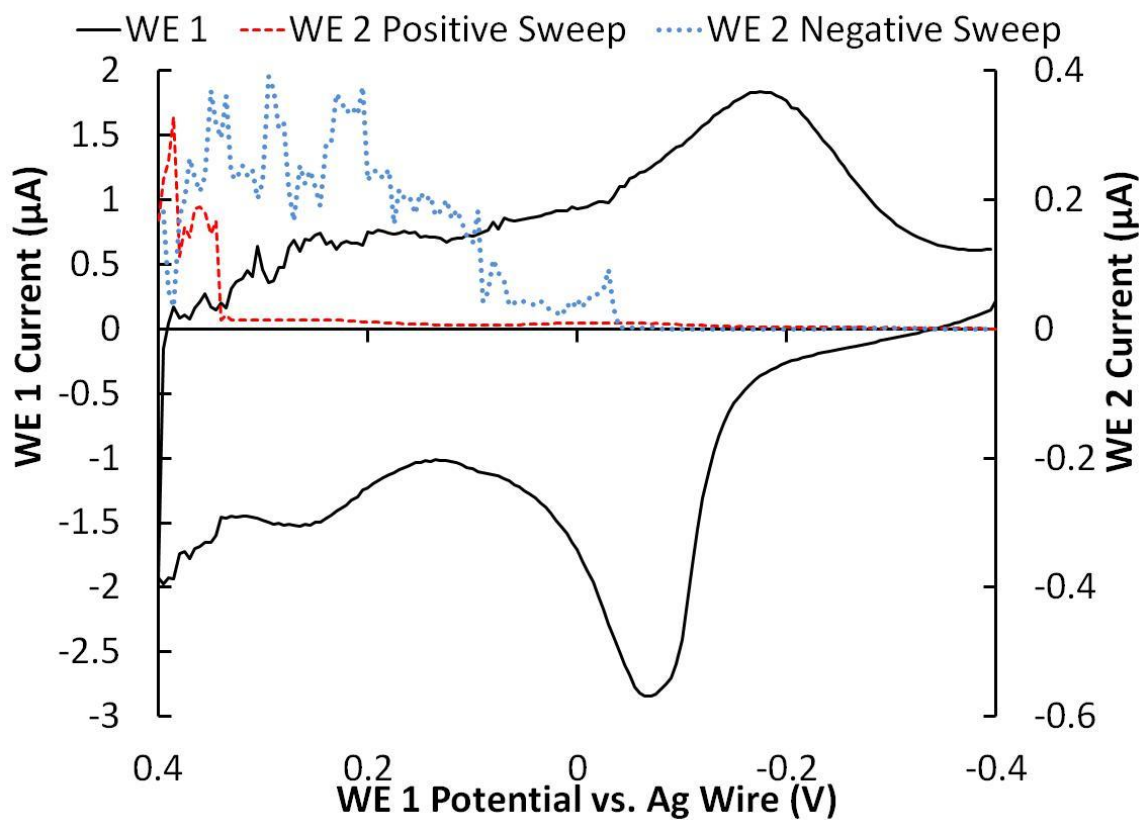


Figure 3.15. A cyclic voltammogram in clean 1 M H_2SO_4 of polyaniline nanojunction 6. WE 1 was cycled at 100 mV/s, while WE 2 was held fixed at -0.3 V (vs. reference). The current trace at WE 2 indicates that a connection was present between the working electrodes.

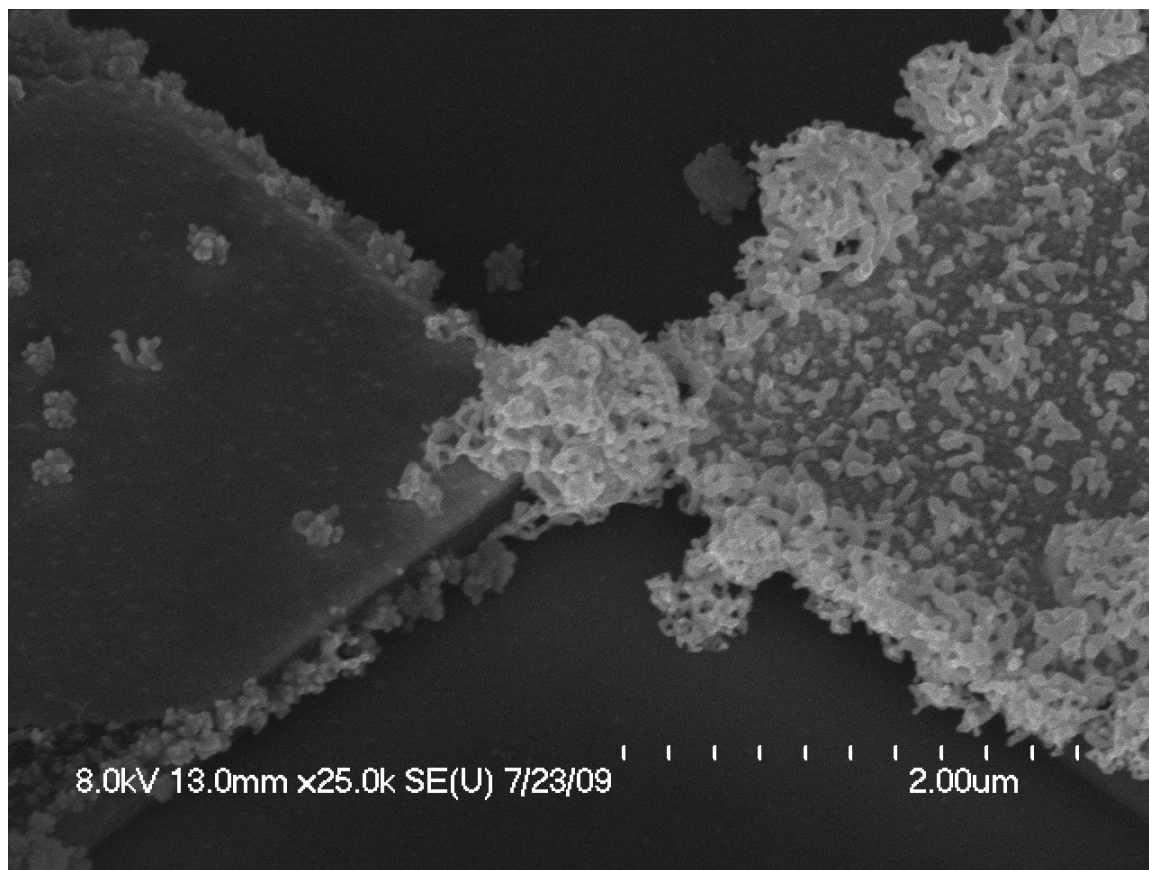


Figure 3.16. SEM micrograph of polyaniline nanojunction 6 showing fibrous polymer in the junction area. WE 1 is on the right.

change the conductivity of a conducting polymer. I cycled the potential of both WE 1 and WE 2 in the TBAPF₆ solution until a consistent response was observed. I did this to minimize the effect of changing the electrolyte, and to verify that the polymer still became conductive upon oxidation. The voltammetric response of the film in the TBAPF₆ solution is shown in Figure 3.17. The response in the TBAPF₆ solution was different than it was in the sulfuric acid solution, but the film still became more conductive upon oxidation. The potential of the working electrodes was positioned at -0.4 V (vs. reference) to switch the film to the neutral/insulating leucoemeraldine state. The oxidation state was verified by observing that the film was a clear yellow color. The impedance of the junction was monitored by shorting the potentiostat's counter and reference electrode leads to one side of the junction and attaching the working electrode lead of the potentiostat to the other side of the junction. The impedance was monitored over time by applying a 5 mV amplitude AC signal across the junction at 100 Hz. Figure 3.18 shows that the impedance of the junction drifted slightly over time, but was generally consistent. Figure 3.18 also shows that the addition of TATP had little effect on the impedance. The result was discouraging and indicated that a control experiment should be performed using a different analyte to verify that the polymer film could be oxidized by a solution phase chemical oxidant. The control experiment was not performed on this junction because the electrical connection between the electrodes was destroyed by the accidental application of a large potential across the junction. I repeated the TATP experiment and performed the control experiment on another sample, as discussed below.

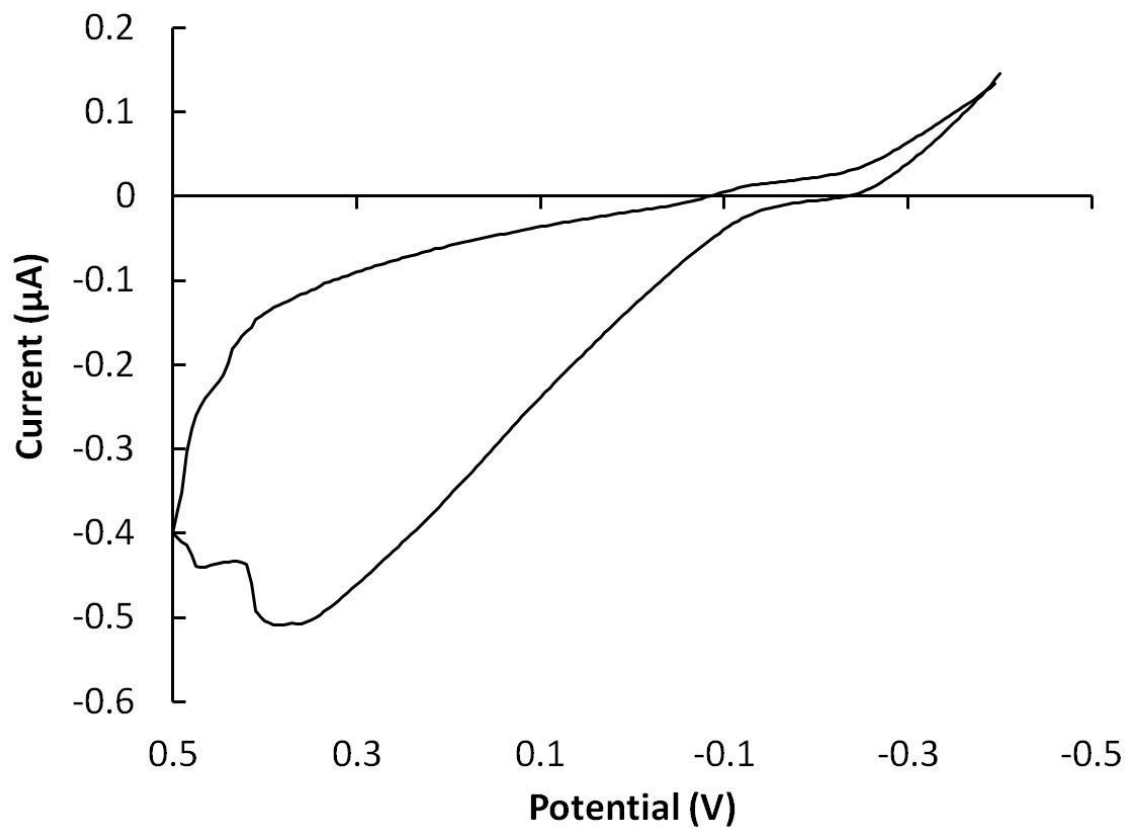


Figure 3.17. The cyclic voltammogram of polyaniline nanojunction 6 recorded at 100 mV/s after moving the device from aqueous sulfuric acid to 100 mM TBAPF₆ in acetonitrile.

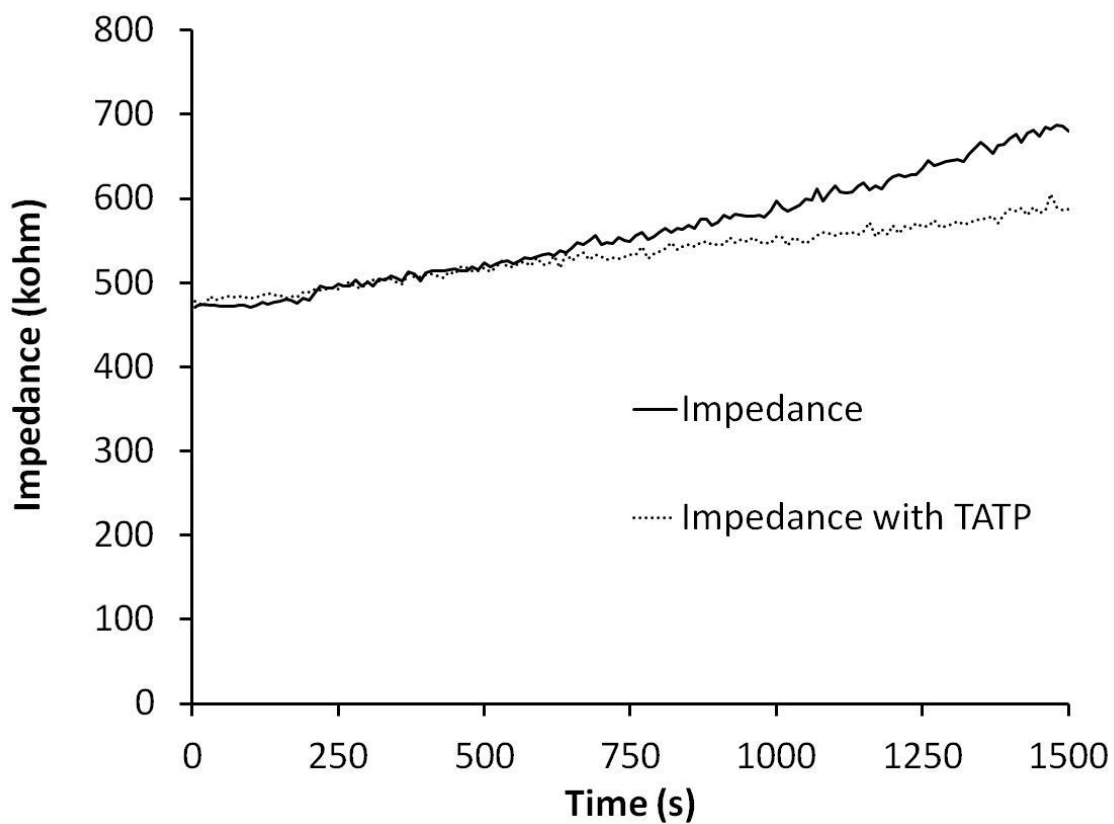


Figure 3.18. The impedance response of polyaniline nanojunction 6 bathed in 100 mM TBAPF₆/acetonitrile in its reduced state before and after TATP was added to the solution. The response does not differ greatly, indicating that the TATP did not significantly affect the junction resistance.

Polyaniline Nanojunction 7: The fibrous morphology of the polymer in the previous example prompted the preparation of another junction using similar conditions, but with a slight modification to see if a smoother polymer film would be produced. For this device, I fixed the potential of WE 2 at -0.3 V (vs. reference), just as it was in the previous example, but I set the negative limit of the potential sweeps of WE 1 to -0.6 V (vs. reference), rather than -0.4 V (vs. reference). It appears, based on the SEM micrograph in Figure 3.19, that the procedural change resulted in a more globular polymer morphology on this electrode when compared to the previous example (Figure 3.16).

The mirrored currents in the cyclic voltammetric experiment shown in Figure 3.20 (WE 2 fixed at -0.3 V) demonstrate that a connection was present between the working electrodes. The resistance of this connection was much lower than the previous example (polyaniline nanojunction 6). For polyaniline nanojunction 7, the resistance of the junction, when the polymer was in the oxidized state, was on the order of $10^5 \Omega$, as based on the cyclic voltammogram shown in Figure 3.20.

The response of the impedance of this junction to the addition of chemical oxidants dissolved in solution was tested using the same procedure as in the previous example. Initially, TATP was added to verify the previous result. Again, the addition of TATP did not result in a change in the impedance. The solution in the reservoir was replaced with fresh TBAPF₆ solution to remove the TATP, and then I began to monitor the impedance of the junction over time. Approximately 200 s into the impedance experiment, a drop of cold 3% hydrogen peroxide solution (aq) was added to the solvent

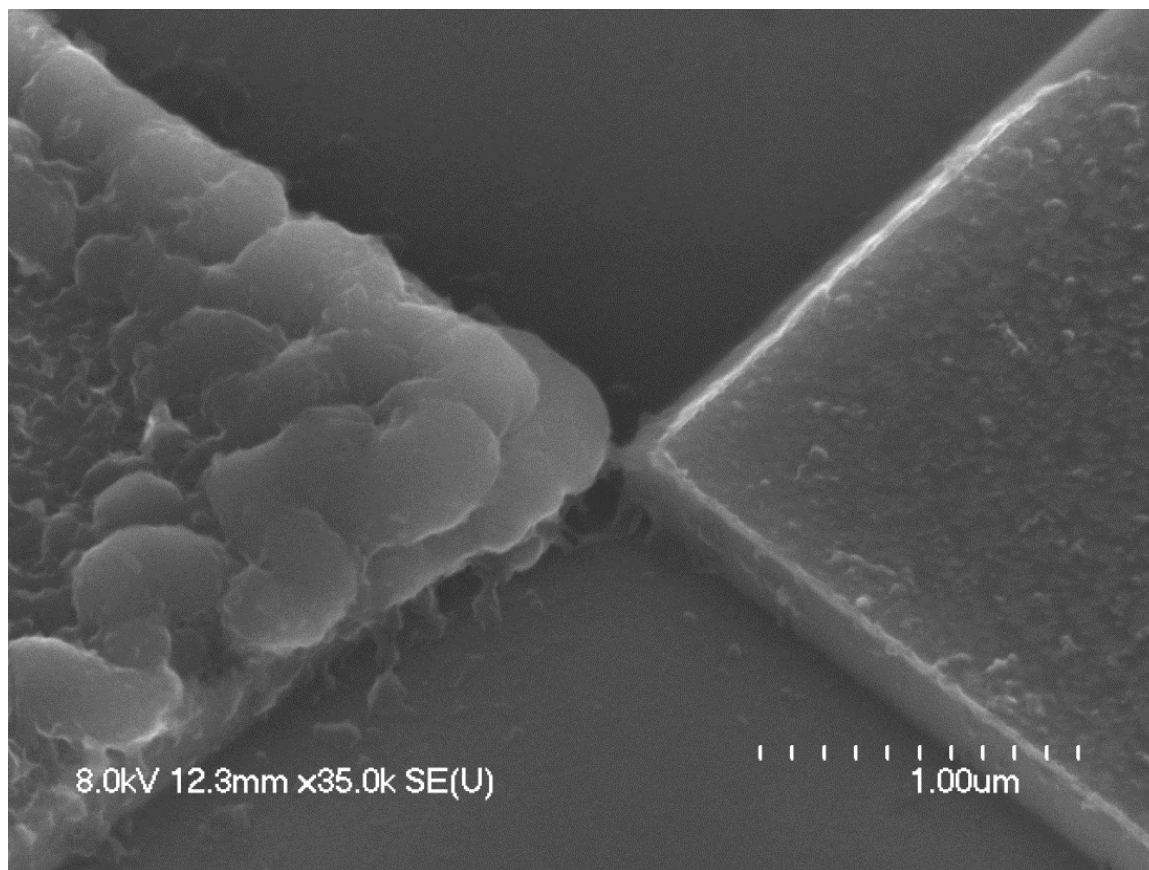


Figure 3.19. SEM micrograph of polyaniline nanojunction 7 showing a connection between the electrodes. WE 1 is on the left.

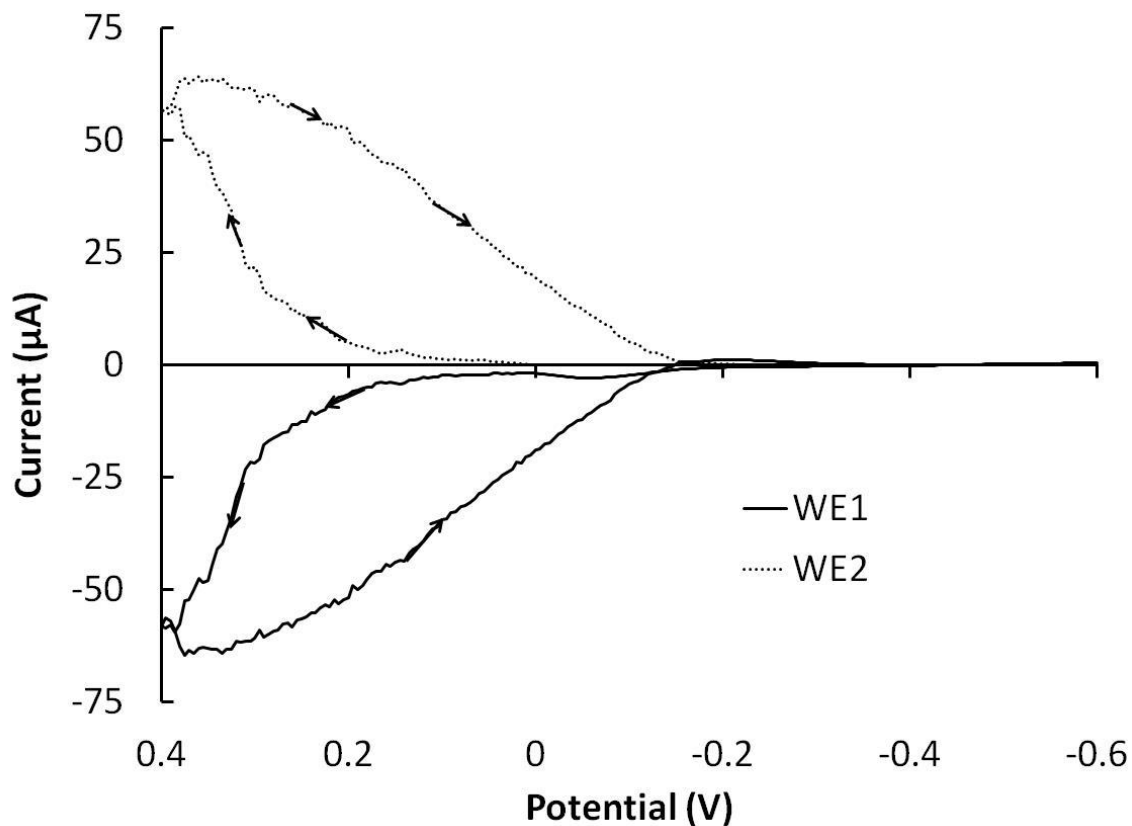


Figure 3.20. The cyclic voltammogram of polyaniline nanojunction 7 in 1 M H_2SO_4 during which the potential of WE 2 remained fixed at -0.3 V. The large mirrored current at more positive potential and lower current at more negative potentials indicate a connection between the working electrodes composed of conducting polymer.

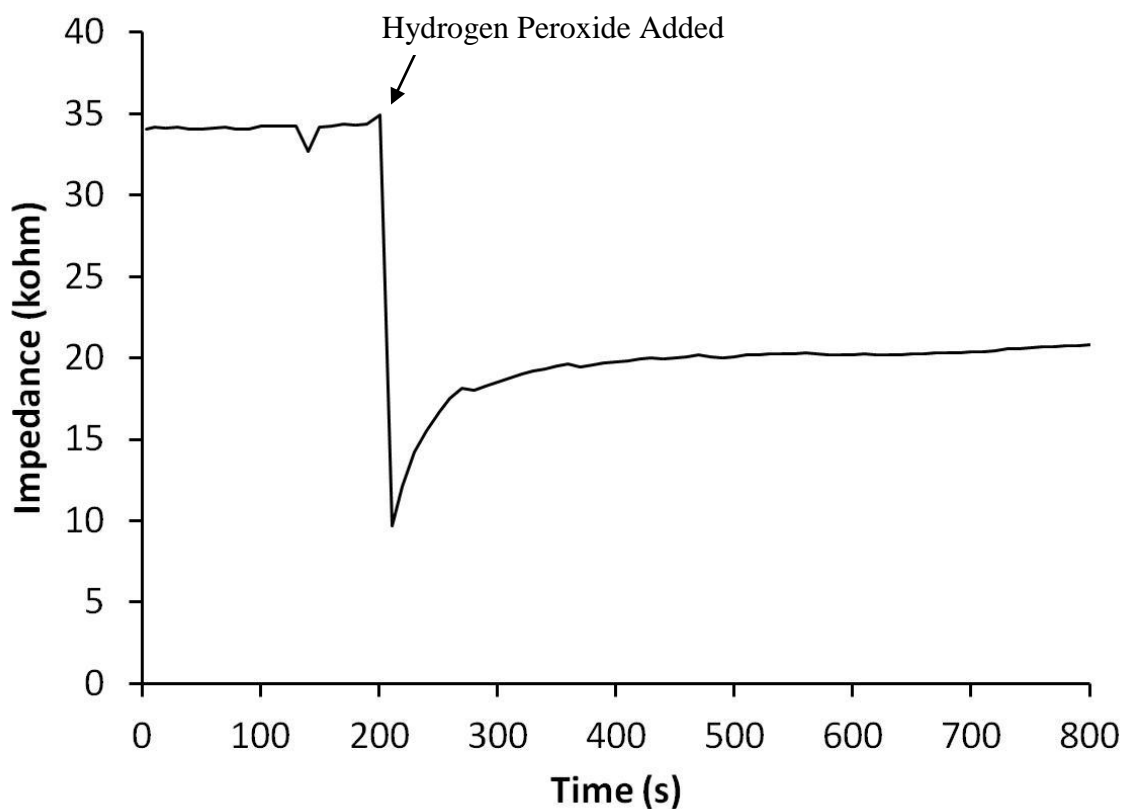


Figure 3.21. The impedance response of polyaniline nanojunction 7 bathed in 100 mM TBAPF₆ in acetonitrile. Hydrogen peroxide was added to the solution at approximately 200 seconds. A clear decrease in the impedance occurred indicating that the polymer film was oxidized by the peroxide.

reservoir. The concentration of peroxide in the cell was approximately 20 mM. Figure 3.21 shows that a large decrease in the impedance of the junction resulted immediately after the addition of the peroxide. The initial drop in the impedance was followed by a gradual increase. After about 80 s, the impedance settled at approximately 60% of the initial value.

After the previous experiment with hydrogen peroxide, I performed a control experiment. The electrolyte solution in the solvent reservoir was changed to remove the peroxide, and the polymer film was switched to the leucoemeraldine state by stepping the potential to -0.5 V (vs. reference). Then I began monitoring the impedance of the junction with time under the same conditions as before. During this experiment, I added a drop of cold water to the cell. The addition of the water resulted in an approximate 20% decrease in the impedance. The impedance of the junction then returned to its initial value over approximately 80 s.

The stabilization time after the addition of pure water was similar to the stabilization time after the addition of the cold aqueous hydrogen peroxide solution. Based on this result, I concluded that the immediate decrease in the impedance in both experiments was due to temperature fluctuation and/or changes in the solvation of the polymer film, and that the stable 40% decrease in impedance after the addition of the peroxide was due to the oxidation of the polymer film. These results demonstrated that junctions bridged by polyaniline could be used in sensor devices, because oxidation of the polymer film led to a distinct change in the conductivity of the junction.

Polypyrrole: Polyaniline was successfully used to form the bridging layer in nanojunctions of the type described in this chapter. I also tested polypyrrole as a bridging

species. As mentioned in the introduction, the scientific literature contains a voluminous amount of research regarding the influence of polymerization conditions on the properties of conducting polymers. As such, I began my experiments with polypyrrole using a simple polymerization bath that was loosely based on the work by Lange and Mirsky [1]. In their original work, an acetonitrile solution containing 100 mM TBAPF₆, 100 mM pyrrole, and 1% water was used to grow polymer films that were approximately 1 μm thick. I reduced the concentration of pyrrole in this bath, because the interest in this project was growing polymer films to bridge 50-200 nm gaps between patterned electrodes on silicon substrates. I also initially omitted the water in the interest of the simplicity. A typical cyclic voltammogram for the heterogeneous electrochemical polymerization of pyrrole on a gold disk electrode from an anhydrous acetonitrile solution containing 100 mM TBAPF₆ and approximately 20 mM pyrrole is shown in Figure 3.22.

The shape of the voltammogram shows that at potentials more negative than approximately 0.3 V the polymer film was in the neutral/insulating state and little current flowed in the cell. On the positive sweep, when the potential reached approximately 0.5 V, the polymer film oxidized. At approximately 1.3 V, the current began to rapidly change, and a much higher oxidation current was observed. This rapid change in current was the result of the oxidation of the pyrrole monomer. The magnitude of the current at 1.5 V increased with each successive cycle. The increase in the maximum oxidation current with increasing cycle number was observed in many conducting polymers and indicated that the overpotential required to oxidize the monomer decreased after a polymer film has been deposited on the electrode surface [24]. A relatively high current

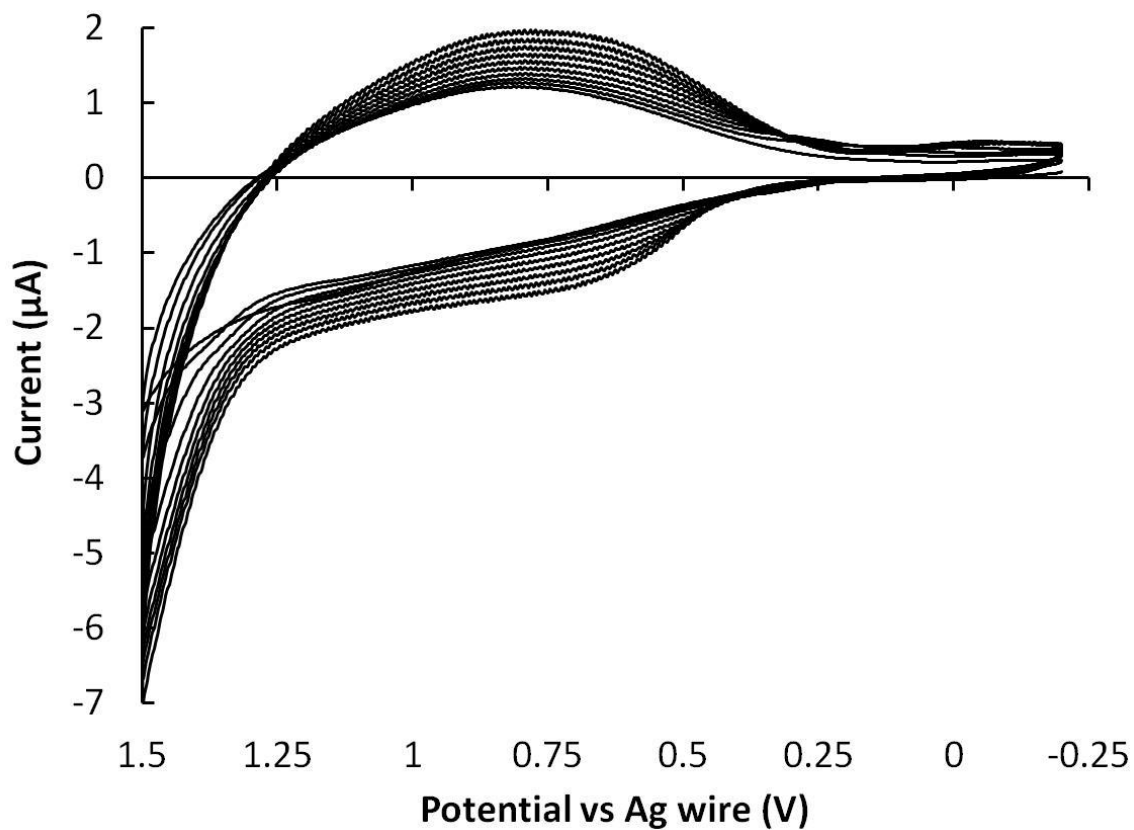


Figure 3.22. Cyclic voltammetry associated with a typical polymerization of pyrrole from a 15 mM pyrrole solution with 100 mM TBAPF₆ in acetonitrile on a gold disk electrode.

continued to pass on the negative potential sweep, until approximately 0.3 V when the polymer film reduced back to the neutral state. The current in the conductive state increased with the cycle number. This increasing current indicated that the thickness of the polymer film was increasing with each cycle.

Polypyrrole Nanojunction 1: An acetonitrile solution containing 15 mM pyrrole and 100 mM TBAPF₆ was used to polymerize pyrrole onto a nanojunction, and the polymerization resulted in a successful connection between the electrodes. The cyclic voltammogram of the growth of the polymer on WE 1 and the current at WE 2 (fixed at 0 V vs. reference) are shown in Figure 3.23. The general shape of the voltammogram for WE 1 is the same as that shown in Figure 3.22. A spike in the current at WE 2 occurred when the conducting polymer bridged the gap between the working electrodes. The connection took 22 cycles. The cycling was stopped shortly after this connection was made so that the smallest possible polymer connection could be characterized.

After the polymerization was stopped, I removed the monomer solution and replaced it with a solution of the same electrolyte (100 mM TBAPF₆ in acetonitrile) containing no monomer. Cycling the electrodes in this electrolyte solution resulted in the voltammogram (WE 1) and current trace (WE 2, fixed at 0 V vs. reference) shown in Figure 3.24 (top). When the potential of WE 1 was below about 0.3 V (vs. reference) very little current flowed at WE 2 because the polymer was in the neutral/insulating state. When the potential of WE 1 was swept to values that were more positive, the current at WE 2 appeared to vary linearly with the potential difference between the working electrodes. This linear relationship indicated that the junction was behaving like an ohmic resistor, governed by Ohm's law, $V=iR$, where V is voltage, i is the current, and R

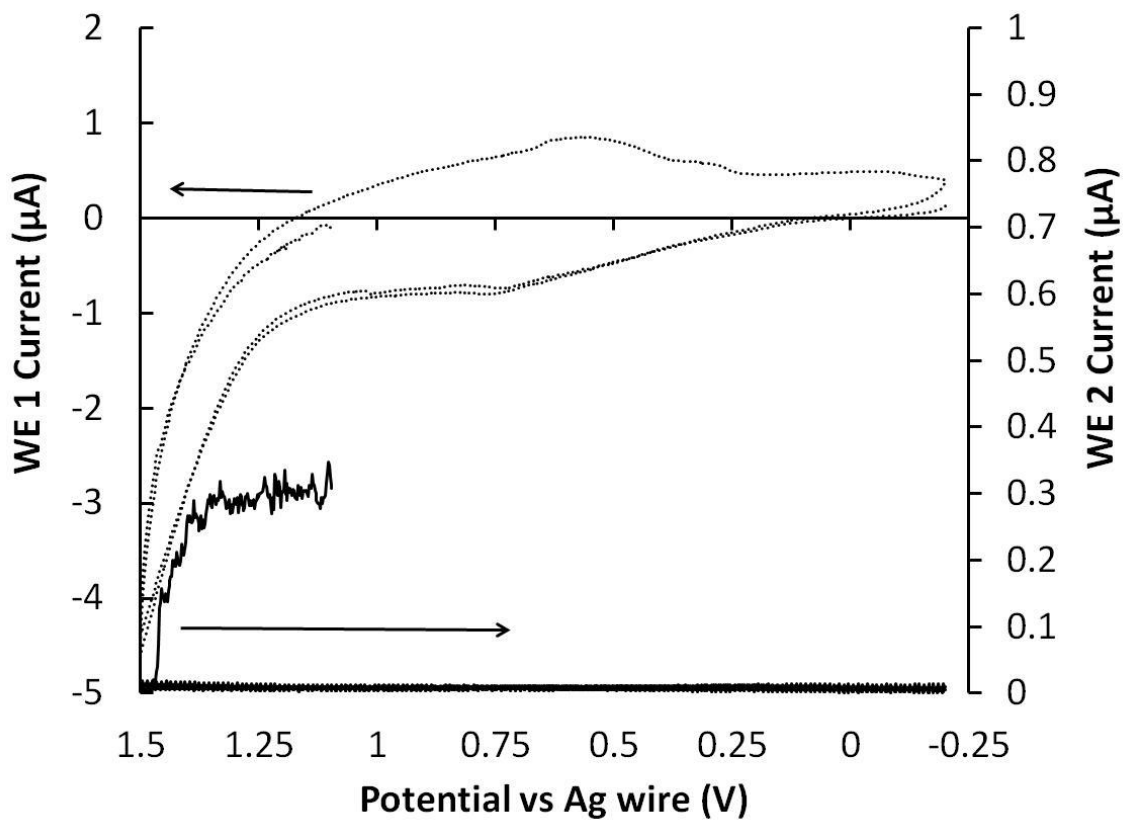


Figure 3.23. The voltammogram of the polymerization of pyrrole onto nanojunction 1 from a 15 mM solution of pyrrole in 100 mM TBAPF₆/acetonitrile. The connection between electrodes was indicated by the current spike at WE 2. The potential of WE 2 was fixed at 0 V (vs. reference).

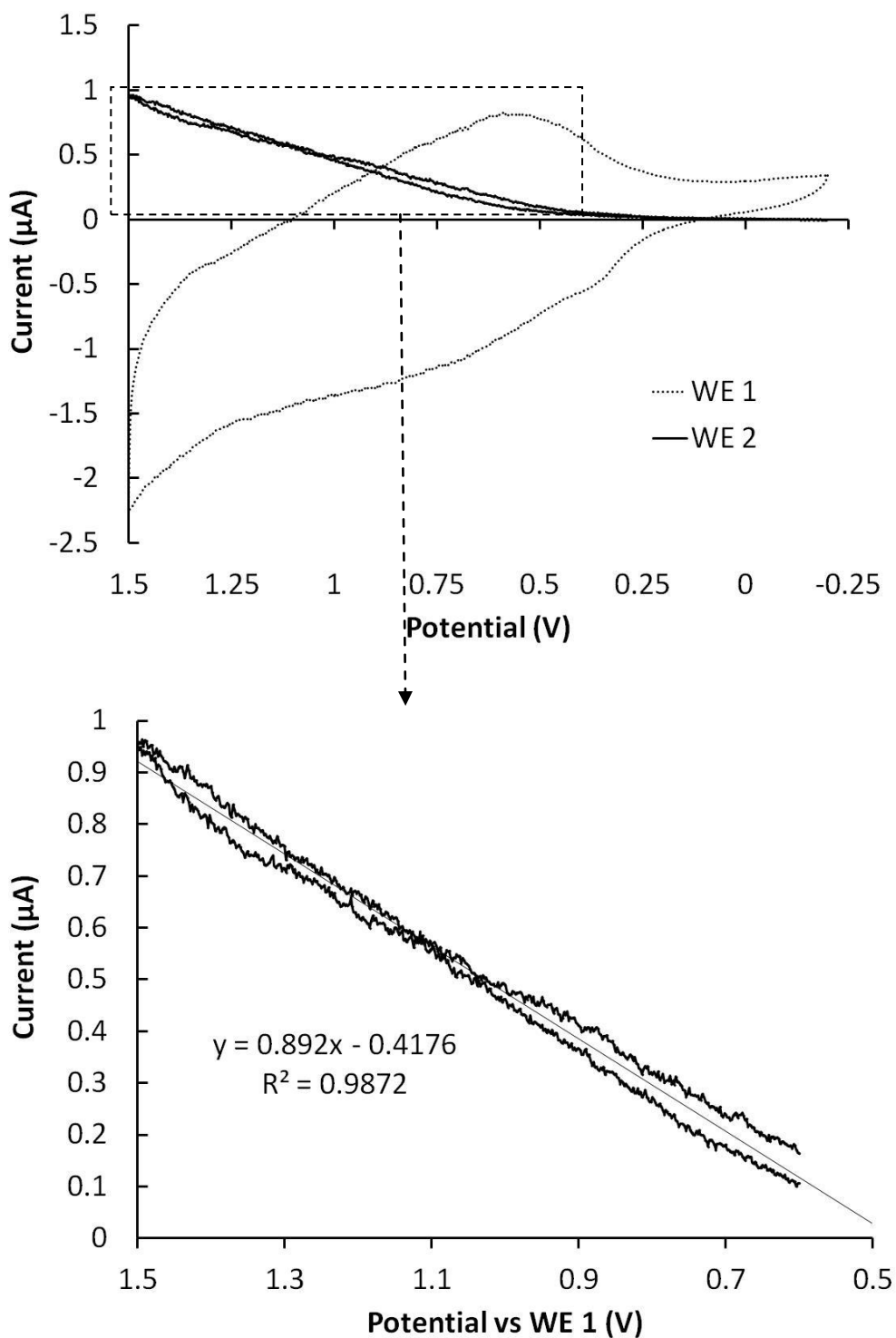


Figure 3.24: The cyclic voltammogram of polypyrrole nanojunction 1 in 100 mM TBAPF₆/acetonitrile (top). The potential of WE 2 was fixed at 0 V (vs. reference). The current at WE 2 as a function of potential vs. WE 1 was used to calculate the resistance of the junction (bottom).

is the resistance. I used the slope of the best-fit line of the current-potential curve, shown in Figure 3.24 (bottom), to calculate the resistance of the junction. The resistance, as calculated by this method, was $1.12 \times 10^6 \Omega$.

The junction was not characterized in any other fashion because the polymer connection between the electrodes broke when I tried to remove the device from the electrochemical cell. The results obtained from this junction were encouraging because a distinct connection between the working electrodes formed during the polymerization.

Polypyrrole Nanojunction 2: The growth on the previous junction took only 22 cycles to connect the two electrodes. I lowered the concentration of the monomer from 15 mM to 7 mM in an attempt to slow the growth rate. The junction used in this example required 86 total cycles to bridge the gap between the electrodes. The results of the polymerization are shown in Figure 3.25. As soon as I observed the connection, I stopped the voltammogram in an attempt to preserve the smallest possible connection.

I obtained SEM images to gain perspective on the scale of the connection. A collection of micrographs is shown in Figure 3.26. WE 1 is on the left in all the images in the figure. The gap between the gold electrodes in this junction was 200 nm, when measured from the tip of one gold electrode to the tip of the other. The polypyrrole film appears to be relatively uniform and smooth. From the image in the lower left, it is possible for one to see the thickness of the polymer film. The polymer thickness on WE 1 was 150 nm, when measured away from the electrode tip.

As mentioned above, 86 total voltammetric cycles were performed on this junction before a connection was observed. Two of these cycles were performed on WE 2 to verify that the leads to the electrode were still intact. WE 2 appears to have a thin,

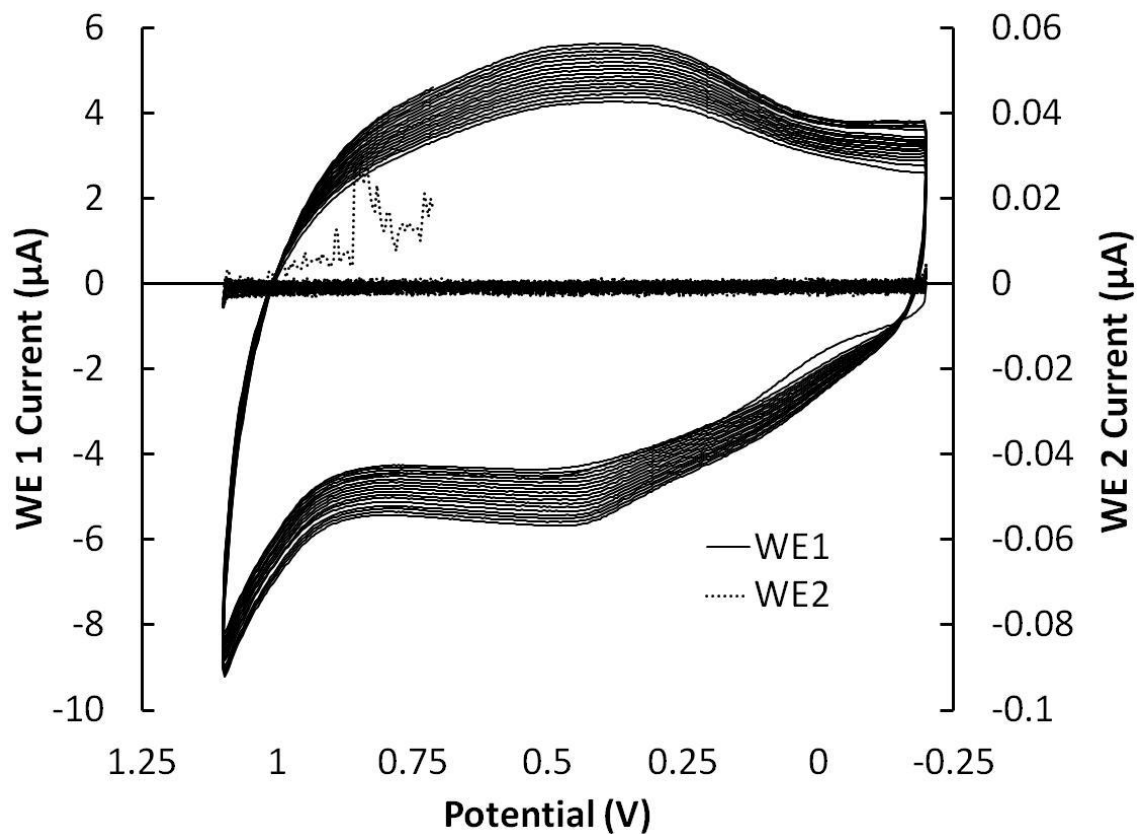


Figure 3.25. The polymerization cyclic voltammogram (WE 1) and current trace (WE 2). The spike in the current at WE 2 indicated a connection had formed between the two electrodes in polypyrrole nanojunction 2.

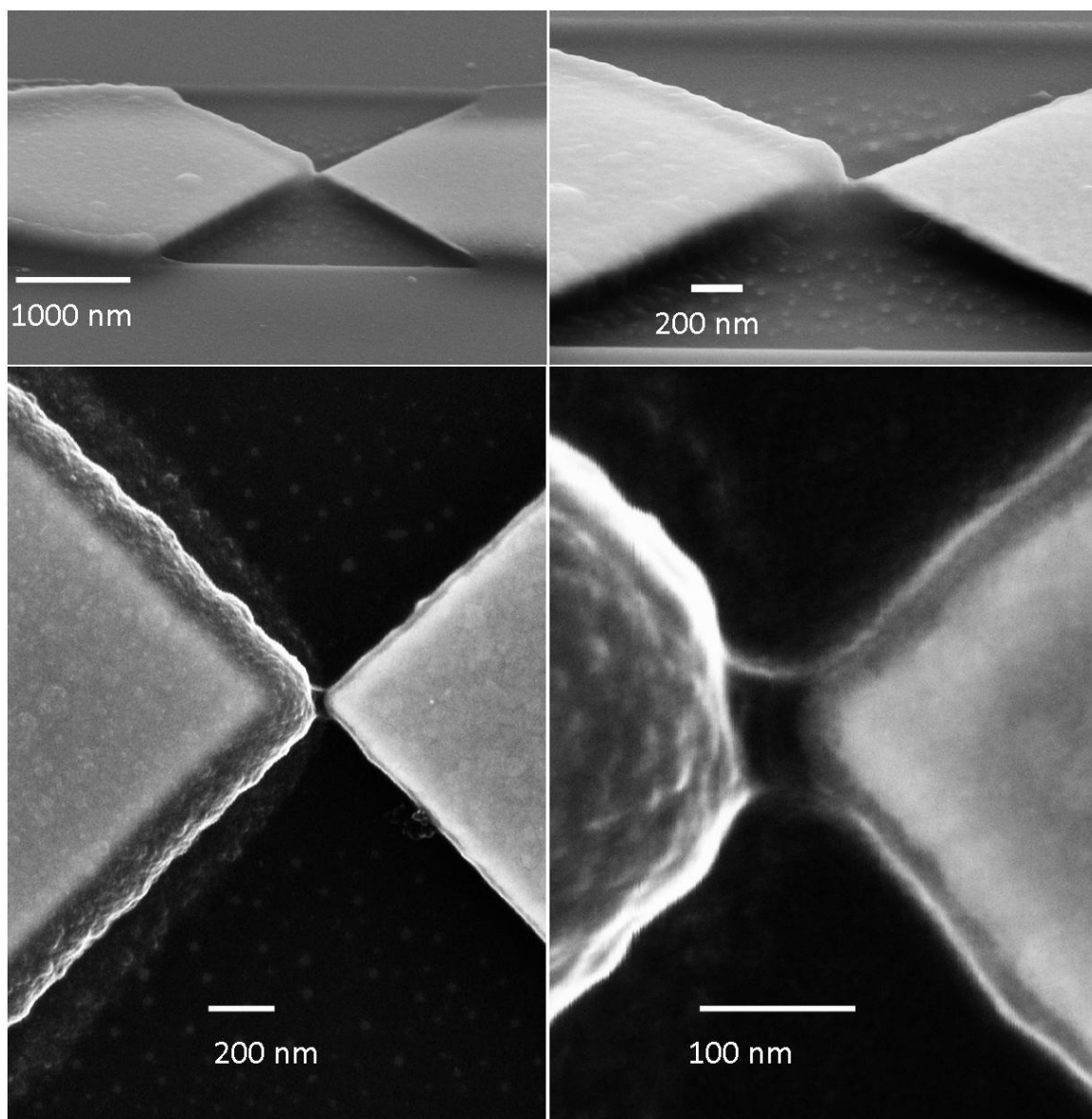


Figure 3.26. SEM images at various magnifications of polypyrrole nanojunction 2 showing a uniform layer of polymer on the left electrode (WE 1) and an apparent connection between the two electrodes.

but still visible, layer on the surface. The thickness of this layer is 20 nm. If one assumes that the thin layer appearing on WE 2 is polymer with a thickness of 20 nm, the polymerization on this electrode took place at a rate of approximately 10 nm/cycle. A deposition rate of 10 nm/cycle on WE 2 is rapid when compared to the deposition rate for WE 1. The 150 nm thick polymer film on WE 1 was deposited over 84 voltammetric cycles, which corresponds to a rate of 1.8 nm/cycle. The observed decrease in the deposition rate is in accord with a report by Fan and Maier, in which they determined that the deposition of polypyrrole takes place at a faster rate early on and that the deposition rate decreases with increasing voltammetric cycle number [58]. Based solely on the SEM images, it is not possible to identify the substance on WE 2 as polypyrrole, but if the substance is polypyrrole, the observed difference in the apparent growth rate is consistent with the previous report.

I used cyclic voltammetry to verify the presence of a conducting polymer on both electrodes. The device was returned to the electrochemical cell, bathed in 100 mM TBAPF₆ and the potential of both working electrodes was swept from -0.2 V to 1.1 V vs. Ag wire. The results of this experiment are shown in Figure 3.27. The peak at approximately 0.35 V on the positive potential sweep has previously been assigned to the oxidation of polypyrrole. The similarity in the shapes of the voltammograms indicates that the molecular structures of the polymers present on the electrodes are quite similar, despite the polymers being quite different in thickness [59, 60].

The images in the lower left and lower right of Figure 3.26 appear to show a faint filament connecting the two electrodes. Upon returning the junction to the electrochemical cell, I did not observe any evidence of an electrical connection. The

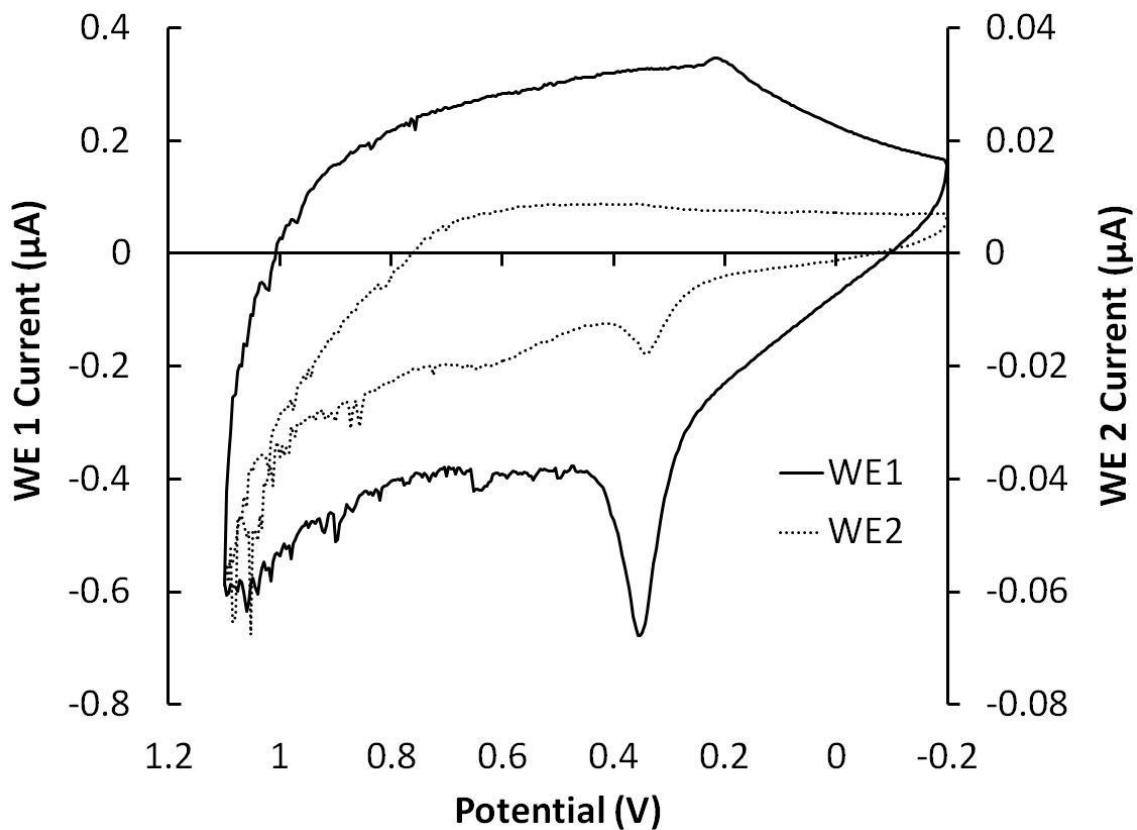


Figure 3.27. The differential scan cyclic voltammogram of polypyrrole nanojunction 2, during which a constant potential difference of 10 mV was maintained between the working electrodes, showing that a polymer film was on both electrodes.

open circuit strongly suggests that the filament broke while the device was in transit between the electron microscope and the electrochemical cell used later to attempt to characterize it.

It is possible to estimate the resistance of the original electrical connection based on the current step observed in Figure 3.25. The current at WE 2 when the deposition was stopped was 1.8×10^{-8} A. The potential difference between the electrodes at this point was 0.713 V. Therefore, the resistance was $4.0 \times 10^7 \Omega$. If one assumes that the bulk polymer acted as if it were a continuation of the metal electrode, and that the filament observed in the SEM images in Figure 3.26 was the source of the resistance of the connection, the conductivity of the polymer can be estimated using equation (3.1). The filament connecting the two electrodes was approximately 20 nm wide and 50 nm long. The thickness was more difficult to measure, but for the purposes of assessment, I estimated it to be approximately 50 nm. The conductivity of the small polypyrrole connection, using the conventional units, was 0.013 S/cm. Conductivity values for polypyrrole as high as 300 S/cm, and as low as 0.001 S/cm have been reported-[61, 62].

Some useful observations can be made based on the results obtained from this junction. The deposition rate can be reasonably well controlled by adjusting the solution concentration, and the polymerization conditions used for this junction resulted in a uniform polymer film on the surface of the electrode.

Polypyrrole Nanojunction 3: The polypyrrole connection between the electrodes in the previous two examples ultimately failed. I believed that the junctions might have been destroyed by static discharges. I hypothesized that increasing the conductivity of the polymer would allow the polymer junction to carry larger currents and perhaps

survive a static discharge. It has been reported that acetonitrile solutions containing 1% water produce polypyrrole films with higher conductivity than those produced from anhydrous solutions [57, 62]. As such, I attempted polymerizations with 1% water added to the polymerization baths.

The polymerization baths with water included were largely unsuccessful in producing polymer films that bridged the gap between the electrodes in the junctions. In fact, only one successfully closed gap was achieved from a 1% water bath, and it is unclear if the material that closed the gap was polymer or some other contaminant. A current spike during polymer deposition, like those seen in the examples above, was not observed for this junction. Figure 3.28 shows the results of two consecutive, identical, cyclic voltammetry experiments. In these experiments, the potential of WE 1 was swept and the potential of WE 2 was fixed at -0.3 V (vs. reference). The first experiment, Figure 3.28 (top), showed no indication of connection between the working electrodes, based on the lack of current at WE 2. The second experiment, Figure 3.28 (bottom), displayed a linear relationship between the applied potential and the recorded current at WE 2, indicating that a connection was present. I was skeptical that polypyrrole was the source of the connection between the working electrodes, because I did not observe a current spike, corresponding to a connection event, during the voltammetry used to deposit the polymer. I decided to obtain SEM images of this junction to see if I could identify the source of the connection between the electrodes. An SEM image of this junction is shown in Figure 3.29.

The image shows a large dark region across the junction area. The visible electrode area on the right of the image (WE 1) has some relatively bright globular

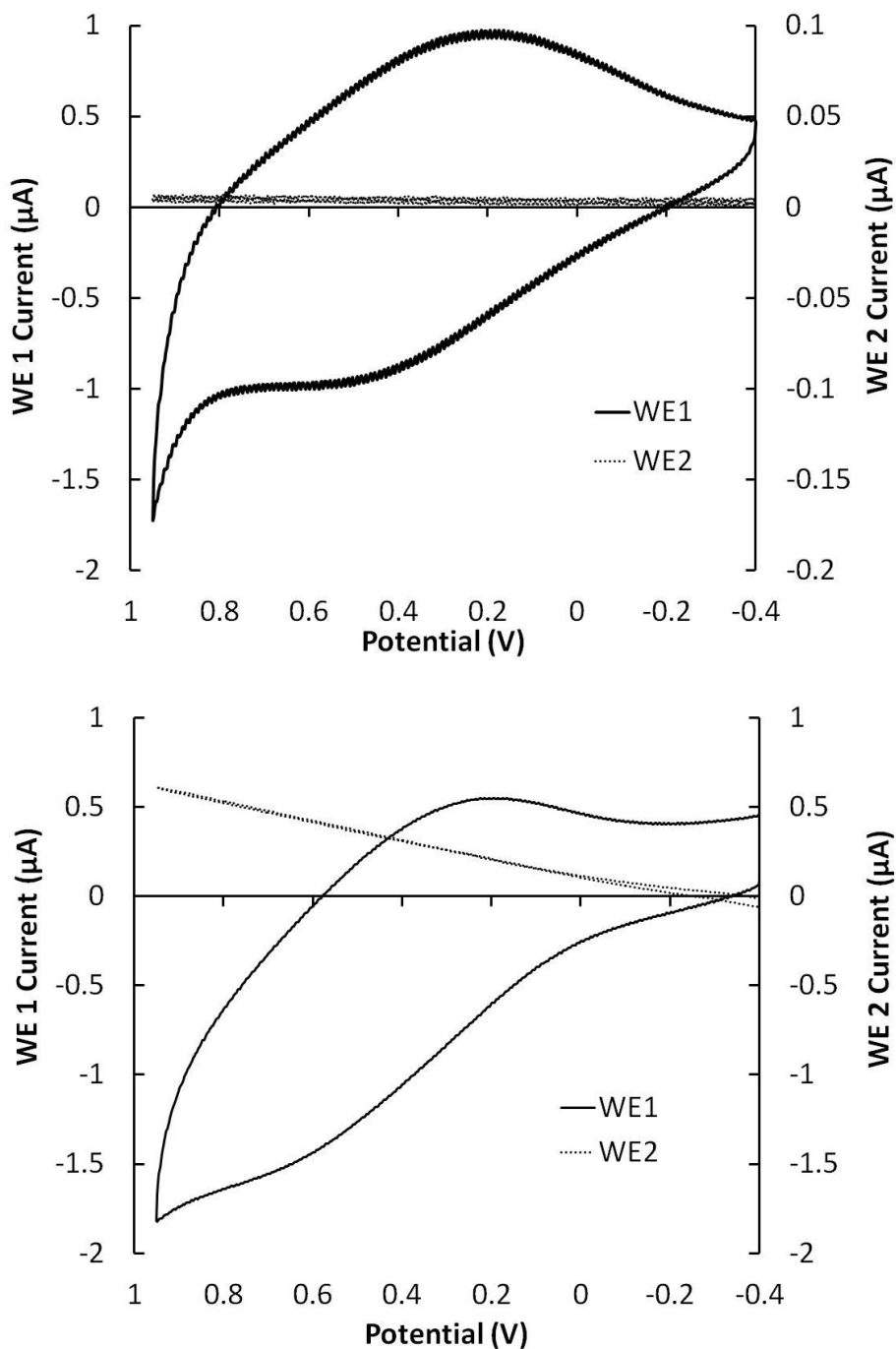


Figure 3.28. During polymerization on polypyrrole nanojunction 3 two consecutive experiments were performed during which the potential of WE 1 was cycled and the potential of WE 2 was held fixed at -0.3 V (vs. reference). The voltammogram from the first experiment (top) showed no connection between the two working electrodes, based on the low current observed at WE 2. The voltammogram from the second experiment (bottom) did show a connection.

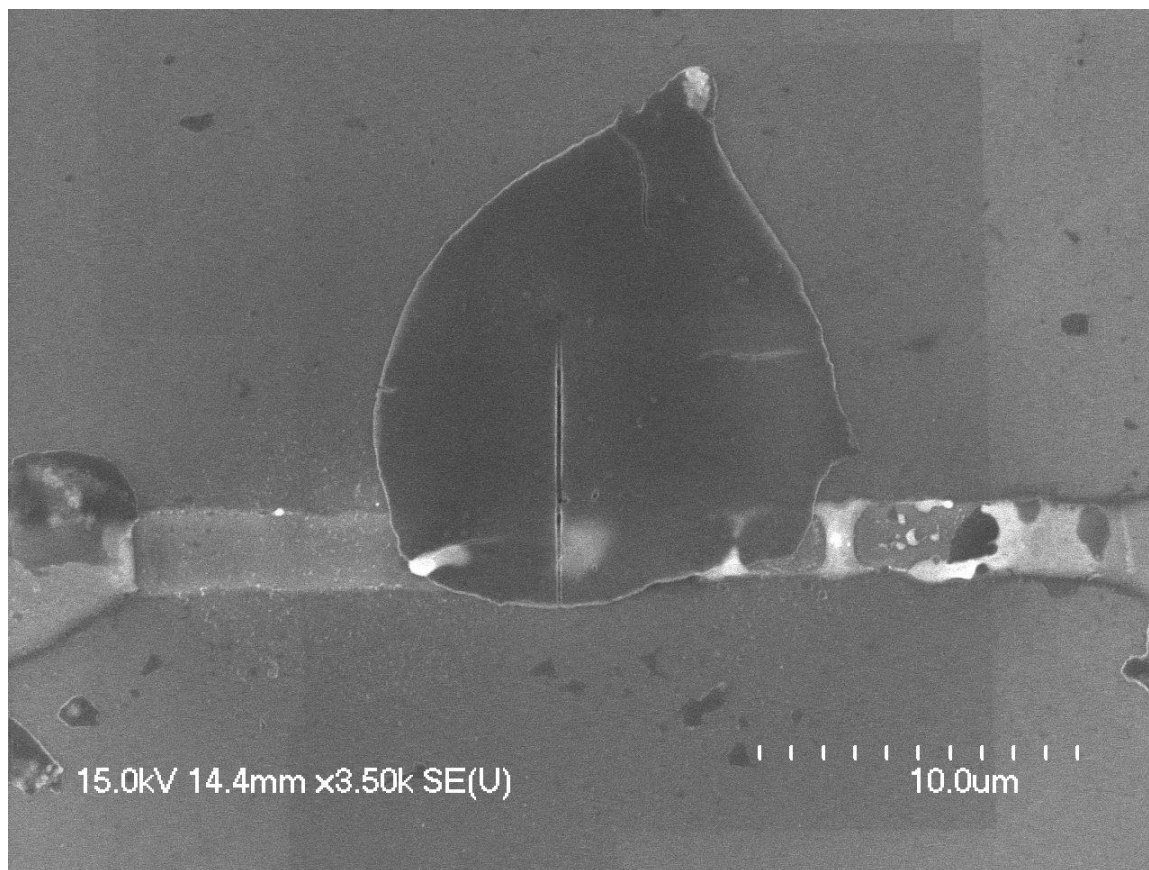


Figure 3.29. SEM micrograph of polypyrrole nanojunction 3. The image shows a large dark region covering the junction area and bright beaded regions on WE 1 (right).

formations on it. It is possible that these globular locations were conducting polymer. It is also possible that the globular structures were gold that had beaded after a current surge caused it to melt. The cyclic voltammetric data, discussed above, indicated that polypyrrole was present on WE 1 during the deposition. However, no definitive conclusions about this junction can be made from this image. As was the case for many of the junctions described above, the connection across this junction also failed upon returning the device to the electrochemical cell for subsequent characterizations.

I chose to abandon the use of deposition solutions containing water because such solutions failed to produce any junctions that were clearly connected with conducting polymer.

Polypyrrole Nanojunction 4: A more complete analysis of the resistance of a conducting polymer junction was necessary to evaluate the utility of polypyrrole as a bridging material for this system. For this analysis, I attempted to prepare a conducting polypyrrole junction using an anhydrous solution of 7 mM pyrrole with 100 mM TBAPF₆ in acetonitrile. The potential of WE 1 was cycled to form a polymer film. The potential of WE 2 was not controlled in this experiment. The progress of the polymerization was monitored by examining changes in the voltammetric current at the working electrode. When a connection between the two patterned electrodes (WE 1 and WE 2) occurred, the total surface area of the working electrode under potential control increased (from the area of WE 1 and its connections, to the sum of the areas of WE 1 and WE 2 with their connections), and as a result, the current increased. This connection event is clearly evident in Figure 3.30. I verified the presence of the connection via SEM. The image in Figure 3.31 shows that both electrodes were covered by a substantial amount of polymer

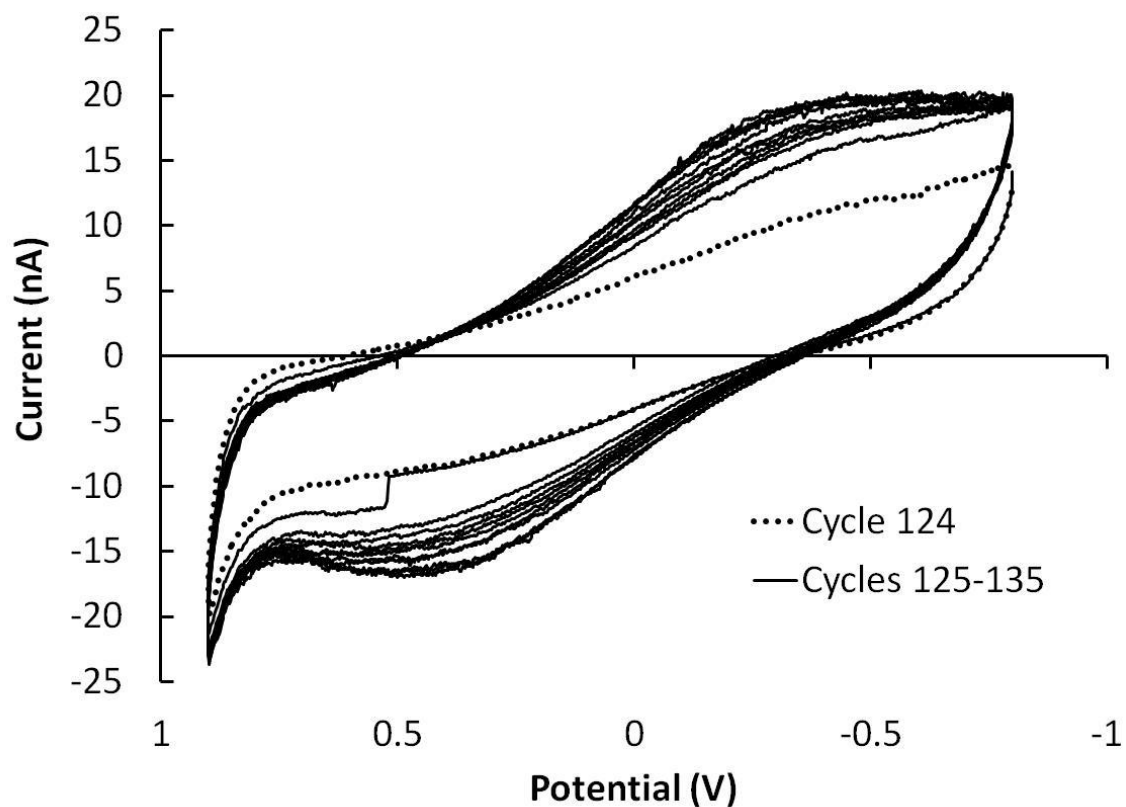


Figure 3.30. The polymerization cyclic voltammogram for polypyrrole nanojunction 4. The final twelve voltammetric cycles are plotted. The connection between the electrodes in the junction was indicated by the relatively large increase in current during cycle 125. The higher current is due to the increase surface area of the electrode. The potential of WE 2 was not controlled during this experiment.

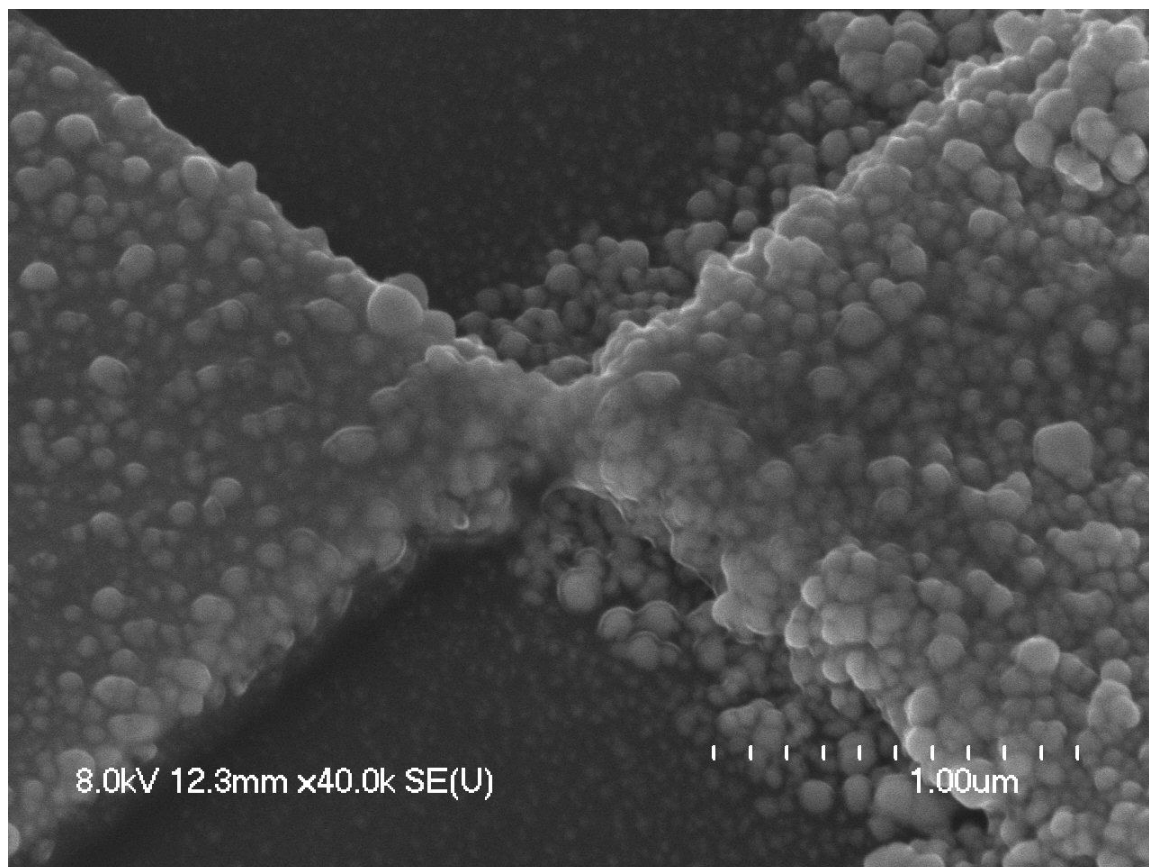


Figure 3.31. SEM micrograph of polypyrrole nanojunction 4 showing polymer on both electrodes. WE 1 is on the right.

and that the polymer bridged the gap between the electrodes. The surface of the polymer film is covered with nodules that are approximately 100-200 nm in diameter.

The device was returned to the electrochemical cell to measure the change in the resistance of the junction when the polymer was switched from the neutral to the oxidized state. The resistance was measured in two ways. For one method, a constant potential difference of 10 mV was maintained between the working electrodes. Then the potential of both electrodes was stepped to various potentials with respect to the silver wire reference, and the current was recorded. For example, one point in the graph shown in Figure 3.32 was recorded when the potential of WE 1 was positioned at -0.5 V vs. reference. For this point WE 2 was positioned at -0.49 V vs. reference, or 10 mV positive of WE 1. The currents plotted in Figure 3.32 are the average current flowing between the working electrodes over the last 20 s of a 60 s potential step. Using the average value over the last 20 s of the step averaged the noise and eliminated contributions from electrochemical double layer charging. As shown in Figure 3.32, when the potential of the electrodes is negative enough for the polymer to be predominately reduced and poorly conducting, the current is lower than the case when the potential of the electrodes is more positive and the polymer is predominately oxidized and conductive. The loosely sigmoid shape of this current response as a function of potential is expected for such a material as it gradually changes between insulating and conducting states.

The second method used to assess the resistance of the polymer junction was performed by applying a potential difference between the working electrodes that varied in magnitude from 10 to 50 mV. These potential differences were applied while the

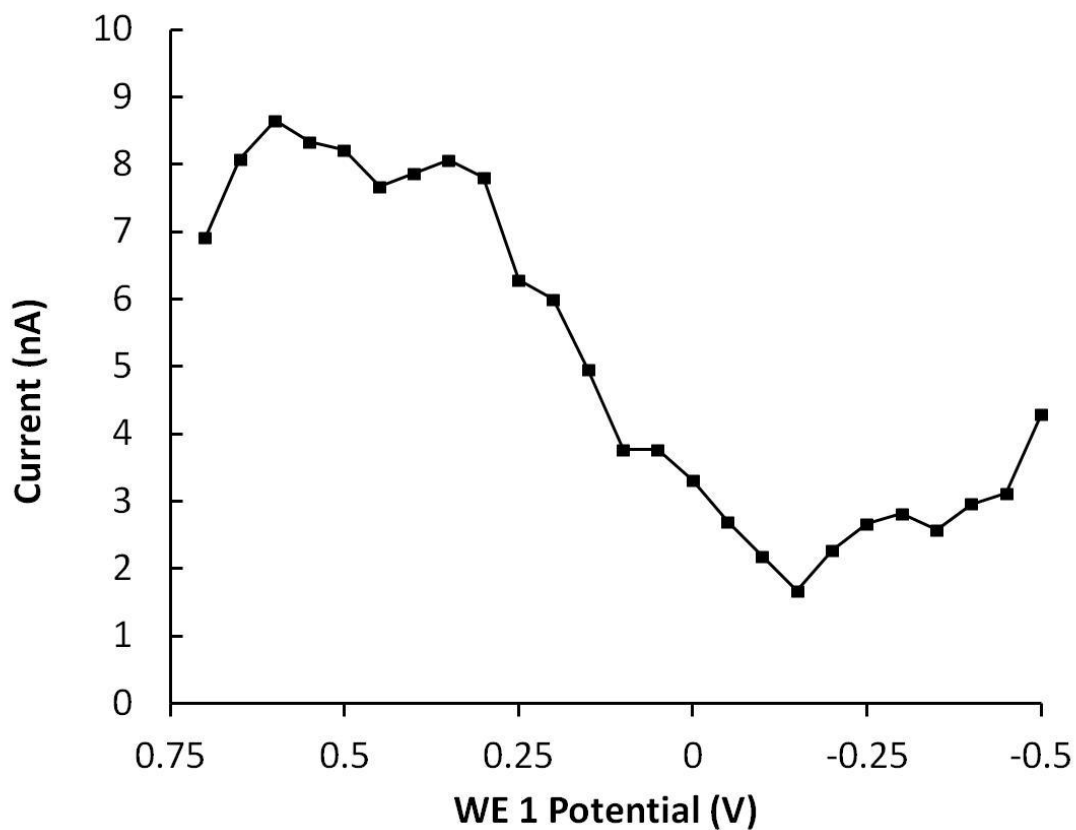


Figure 3.32. A constant potential difference of 10 mV was maintained between WE 1 and WE 2. The current between WE 1 and WE 2 is plotted as a function of the potential of WE 1 (vs. reference). The increase in current at more positive potentials indicates that the polymer switched from the neutral/insulating state to the oxidized/conductive state.

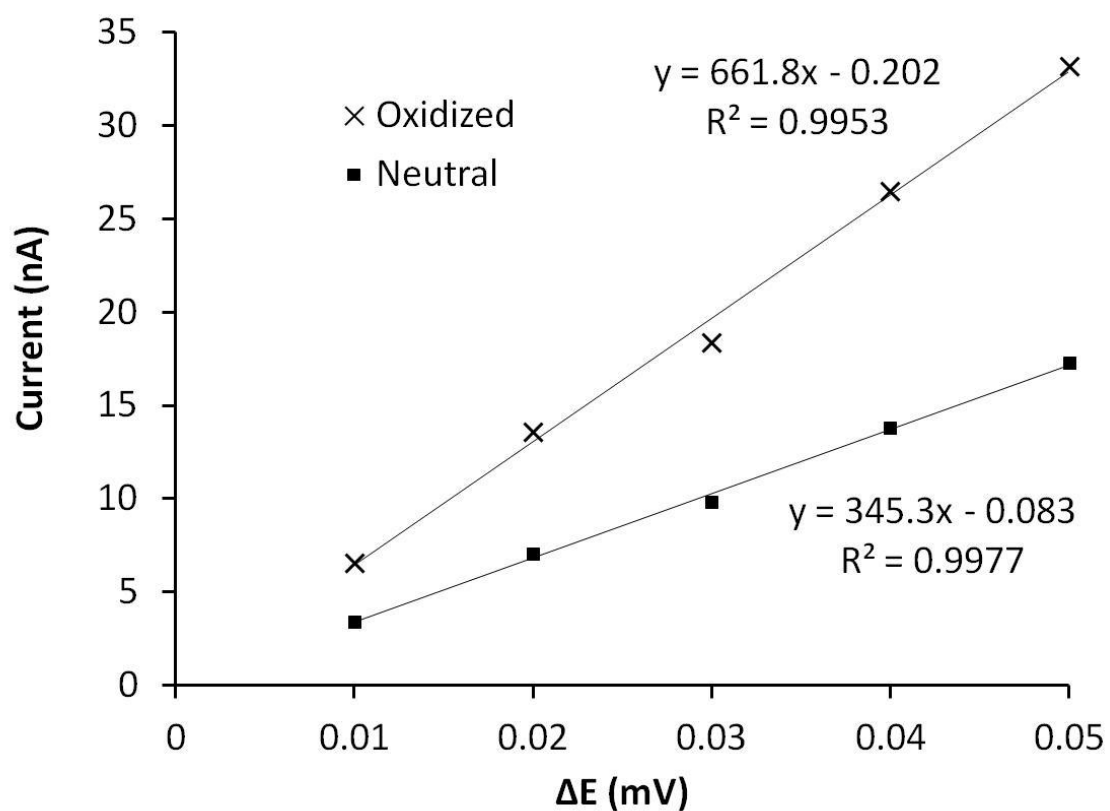


Figure 3.33. The current between WE 1 and WE 2 at potential differences ranging from 10 mV to 50 mV. The resistance of the junction decreases when the polymer is switched from the neutral to the oxidized state.

polymer was in the insulating state and again when the polymer was in the conductive state. The results of this experiment are shown in Figure 3.33. The linear character of the data for both the neutral and oxidized forms of the polymer show that the junction is behaving like an ohmic resistor. As such, the resistance was calculated from the slope of the best fit lines shown in Figure 3.33. For this conducting polymer junction the resistance of the polypyrrole in the neutral state was $2.90\text{ M}\Omega$ and the resistance in the oxidized state was $1.51\text{ M}\Omega$. While the resistance is high in both states, there is a clear difference between the two. The distinct difference in the resistance of the polypyrrole junction when the polymer switches oxidation states demonstrates that polypyrrole may also work in sensor devices based on this design.

Conclusions: Polyaniline and polypyrrole were used to bridge gaps between gold electrodes on the 100 nm scale using heterogeneous electrochemical polymerization. For both polyaniline and polypyrrole, a distinct change in junction conductivity was observed when the polymers were switched from the neutral/insulating state to the oxidized/conductive state. The deposition rate and the morphology of the polymers can be controlled by varying the monomer concentration in the deposition solution, the scan rate of the deposition, and the potential limits of the voltammetric deposition cycles.

The conducting polymer junctions described in this chapter were often irreparably damaged, probably by static discharge or nonspecific mechanical events. As such, the junctions must be protected from unnecessary hazards. I observed that storing the polymer devices in plastic containers wrapped in aluminum foil increased the “survival rate” of the junctions. It is also worth noting that fewer conducting polymer junctions were lost when the depositions were performed in late spring or summer. The reason for

the observed increase in the “survival rate” during these seasons might be coincidental. However, it is speculated that increased humidity during the spring and summer months decreased the buildup of static charge on surfaces, and helped prevent static discharge through the conducting polymer junctions.

Deposition solutions composed of 1 M aqueous sulfuric acid and approximately 30 mM aniline, in combination with potentiodynamic heterogeneous electrochemical polymerization, resulted in relatively uniform polyaniline films bridging the gap between the patterned electrodes. The polymer formed under these conditions showed a clear response to the application of hydrogen peroxide. The addition of the peroxide to the neutral/insulating polymer in the junction oxidized the polymer film and lowered the resistance between the electrodes by about 40%.

Nonaqueous polymerization solutions containing 7 mM pyrrole and 100 mM TBAPF₆ in acetonitrile consistently resulted in junctions bridged by conducting polymer. Potentiodynamic heterogeneous electrochemical polymerization of pyrrole from these solutions resulted in relatively uniform polymer films. These films contained some nodular structures upon longer polymerization times. The resistance of the polypyrrole junction changed by approximately 50% upon electrochemical oxidation.

The original goal of this project was to develop a sensor capable of detecting low concentrations of gas phase oxidants. Conducting polymer junctions, similar to those discussed in this chapter, have been demonstrated as sensors for ammonia in human breath [20]. Based on the work presented by Aguilar et al., the area of the electrodes exposed to the polymerization solutions must be reduced to produce smaller polymer connections capable of responding to low concentrations of analyte [20]. Creating

smaller gaps between the electrodes and minimizing the size of the polymer contacts are the future challenges associated with this project.

The work in this chapter has demonstrated several relatively straightforward methods of producing polymer films of varying morphologies. These polymer films can be used to bridge nanoscale gaps between patterned electrodes. The polymerization methods discussed in this chapter might act as a guide for the fabrication of future sensor devices.

References

- [1] Lange U, Mirsky VM. Separated analysis of bulk and contact resistance of conducting polymers: Comparison of simultaneous two- and four-point measurements with impedance measurements. *J Electroanal Chem.* 2008;622:246-51.
- [2] Ahonen HJ, Lukkari J, Kankare J. n- and p-Doped Poly(3,4-ethylenedioxythiophene): Two Electronically Conducting States of the Polymer. *Macromolecules.* 2000;33(18):6787-93.
- [3] Potje-Kamloth K, ed. *Gas sensing with conducting polymers*: Wiley-VCH Verlag GmbH & Co. KGaA 2010.
- [4] Silva DPB, Neves RS, Motheo AJ. Corrosion protection of aluminum alloys by methoxy-silanes (SAM)/polyaniline double films. *ECS Trans.* 2012;43:57-64.
- [5] Johansen HD, Brett CMA, Motheo AJ. Corrosion protection of aluminum alloy by cerium conversion and conducting polymer duplex coatings. *Corros Sci.* 2012;63:342-50.
- [6] El-Shazly AH, Al-Turaif HA. Developing of polyaniline coating on rotating steel cylinder for improving its corrosion resistance. *Int J Electrochem Sci.* 2012;7:5388-99.
- [7] Deshpande PP, Vagge ST, Jagtap SP, Khairnar RS, More MA. Conducting polyaniline based paints on low carbon steel for corrosion protection. *Prot Met Phys Chem Surf.* 2012;48:356-60.
- [8] Gonzalez MB, Saidman SB. Corrosion protection properties of polypyrrole electropolymerized onto steel in the presence of salicylate. *Prog Org Coat.* 2012;75:178-83.
- [9] Annibaldi V, Rooney AD, Breslin CB. Corrosion protection of copper using polypyrrole electrosynthesised from a salicylate solution. *Corros Sci.* 2012;59:179-85.
- [10] Hasler R, Sanahuja V, inventors; Sandoz-Erfindungen Verwaltungsgesellschaft M.B.H., Austria; Sandoz-Patent-GmbH; Sandoz Ltd. . assignee. Photovoltaic cell patent WO9320569A1. 1993.
- [11] Bourdo SE, Saini V, Piron J, Al-Brahim I, Boyer C, Rioux J, et al. Photovoltaic Device Performance of Single-Walled Carbon Nanotube and Polyaniline Films on n-Si: Device Structure Analysis. *ACS Appl Mater Interfaces.* 2012;4:363-8.
- [12] Bejbouji H, Vignau L, Wantz G, Miane JL, Olinga T, Harmouchi M, et al. Photovoltaic devices based on polyaniline as Hole Injection Layer. *Phys Chem News.* 2010;53:1-4.
- [13] Bai H, Shi G. Gas sensors based on conducting polymers. *Sensors.* 2007;7:267-307.
- [14] Lange U, Roznyatovskaya NV, Mirsky VM. Conducting polymers in chemical sensors and arrays. *Anal Chim Acta.* 2008;614:1-26.
- [15] Janata J, Josowicz M. Conducting polymers in electronic chemical sensors. *Nat Mater.* 2003;2:19-24.
- [16] Yakhmi JV, Saxena V, Aswal DK. *Conducting polymer sensors, actuators and field-effect transistors.* Elsevier Ltd.; p. 61-110.
- [17] Bailey RA, Persaud KC. *Sensing volatile chemicals using conducting polymer arrays.* Springer-Verlag; p. 149-81.
- [18] Maksymiuk K. Chemical reactivity of polypyrrole and its relevance to polypyrrole based electrochemical sensors. *Electroanalysis.* 2006;18:1537-51.

- [19] Diaz AA, Forzani ES, Leright M, Tsow F, Cagan A, Iglesias RA, et al. A hybrid nanosensor for TNT vapor detection. *Nano Lett.* 2010;10:380-4.
- [20] Aguilar AD, Forzani ES, Nagahara LA, Amlani I, Tsui R, Tao NJ. A breath ammonia sensor based on conducting polymer nanojunctions. *IEEE Sens J.* 2008;8:269-73.
- [21] Forzani ES, Li X, Tao N. Hybrid Amperometric and Conductometric Chemical Sensor Based on Conducting Polymer Nanojunctions. *Anal Chem (Washington, DC, U S).* 2007;79:5217-24.
- [22] Lin C-Y, Chen J-G, Hu C-W, Tunney JJ, Ho K-C. Using a PEDOT:PSS modified electrode for detecting nitric oxide gas. *Sensors and Actuators B: Chemical.* 2009;140(2):402-6.
- [23] Myers RE. Chemical oxidative polymerization as a synthetic route to electrically conducting polypyrroles. *J Electron Mater.* 1986;15:61-9.
- [24] Waltman RJ, Bargon J. Electrically conducting polymers: a review of the electropolymerization reaction, of the effects of chemical structure on polymer film properties, and of applications towards technology. *Canadian Journal of Chemistry.* 1986;64(1):76-95.
- [25] Sabouraud G, Sadki S, Brodie N. The mechanisms of pyrrole electropolymerization. *Chem Soc Rev.* 2000;29:283-93.
- [26] Rau JR, Chen SC, Liu PH. Mechanistic studies of the electrosynthesis of polypyrroles. *J Electroanal Chem Interfacial Electrochem.* 1991;307:269-74.
- [27] Choi M-R, Han T-H, Lim K-G, Woo S-H, Huh D-H, Lee T-W. Soluble Self-Doped Conducting Polymer Compositions with Tunable Work Function as Hole Injection/Extraction Layers in Organic Optoelectronics. *Angew Chem, Int Ed.* 2011;50:6274-7, S/1-S/9.
- [28] Sankaran B, Vaia RA, Tan L-S. Thiophene-based branched conjugated polymers. *Polym Prepr (Am Chem Soc, Div Polym Chem).* 2001;42:602-3.
- [29] Ray DK, Himanshu AK, Sinha TP. Study of impedance spectroscopy conducting polymer prepared with the use of water soluble support polymer. *Indian J Pure Appl Phys.* 2005;43:787-93.
- [30] Himanshu AK, Ray DK, Sinha TP. Ac conductivity of conducting polymer prepared with the use of water soluble support polymer. *Indian J Phys.* 2005;79:1049-52.
- [31] Vork FTA, Janssen LJJ. Structural effects in polypyrrole synthesis. *Electrochim Acta.* 1988;33:1513-17.
- [32] Carquigny S, Segut O, Lakard B, Lallemand F, Fievet P. Effect of electrolyte solvent on the morphology of polypyrrole films: Application to the use of polypyrrole in pH sensors. *Synth Met.* 2008;158:453-61.
- [33] Kim YT, Yang H, Bard AJ. Electrochemical control of polyaniline morphology as studied by scanning tunneling microscopy. *J Electrochem Soc.* 1991;138:L71-L4.
- [34] Dinh HN, Vanysek P, Birss VI. The effect of film thickness and growth method on polyaniline film properties. *J Electrochem Soc.* 1999;146:3324-34.
- [35] Salmon M, Diaz AF, Logan AJ, Krounbi M, Bargon J. Chemical modification of conducting polypyrrole films. *Mol Cryst Liq Cryst.* 1982;83:1297-308.
- [36] Fan FR, Bard AJ. Electrochemical detection of single molecules. *Science (New York, NY).* 1995;267(5199):871-4.

- [37] Zhang C. *Electrochemical Depositions Directed Towards the Development of Magneto-electronic Devices*. University of Nebraska-Lincoln, PhD, 2007.
- [38] Rajasekaran R. *Preparation and Characterization of Materials for Tunneling and Ballistic Nanojunctions*. University of Nebraska-Lincoln, PhD, 2008.
- [39] Reyntjens S, Puers R. A review of focused ion beam applications in microsystem technology. *J Micromech Microeng.* 2001;11:287-300.
- [40] Pohanish RP, Greene SA. *Wiley Guide to Chemical Incompatibilities*: Wiley; 2005.
- [41] Ding Z, Yang D, Currier RP, Obrey SJ, Zhao Y. Polyaniline Morphology and Detectable Intermediate Aggregates. *Macromol Chem Phys.* 2010;211:627-34.
- [42] Choi S-J, Park S-M. Electrochemistry of conductive polymers XXVI. Effects of electrolytes and growth methods on polyaniline morphology. *J Electrochem Soc.* 2002;149:E26-E34.
- [43] He HX, Li XL, Tao NJ, Nagahara LA, Amlani I, Tsui R. Discrete conductance switching in conducting polymer wires. *Phys Rev B: Condens Matter Mater Phys.* 2003;68:045302/1-6.
- [44] Yang H, Bard AJ. The application of fast scan cyclic voltammetry. Mechanistic study of the initial stage of electropolymerization of aniline in aqueous solutions. *J Electroanal Chem.* 1992;339:423-49.
- [45] Foot PJS, Simon R. Electrochromic properties of conducting polyanilines. *J Phys D: Appl Phys.* 1989;22:1598-603.
- [46] Dao LH, Nguyen MT. Design and optical modulation of electrochromic windows. *Proc Intersoc Energy Convers Eng Conf.* 1989;24:1737-41.
- [47] Jelle BP, Hagen G. Performance of an electrochromic window based on polyaniline, prussian blue and tungsten oxide. *Solar Energy Materials and Solar Cells.* 1999;58(3):277-86.
- [48] Jelle BP, Hagen G, Hesjevik SM, Ødegård R. Transmission through an electrochromic window based on polyaniline, tungsten oxide and a solid polymer electrolyte. *Materials Science and Engineering: B.* 1992;13(3):239-41.
- [49] Stilwell DE, Park SM. Electrochemistry of conductive polymers. II. Electrochemical studies on growth properties of polyaniline. *J Electrochem Soc.* 1988;135:2254-62.
- [50] Stilwell DE, Park SM. Electrochemistry of conductive polymers. IV. Electrochemical studies on polyaniline degradation - product identification and coulometric studies. *J Electrochem Soc.* 1988;135:2497-502.
- [51] Zotti G, Cattarin S, Comisso N. Cyclic potential sweep electropolymerization of aniline. The role of anions in the polymerization mechanism. *J Electroanal Chem Interfacial Electrochem.* 1988;239:387-96.
- [52] Lizarraga L, María Andrade E, Victor Molina F. Swelling and volume changes of polyaniline upon redox switching. *Journal of Electroanalytical Chemistry.* 2004;561(0):127-35.
- [53] Serway RA, Jewett JW. *Principles of Physics: A Calculus-Based Text*: Brooks/Cole; 2006.
- [54] Boara G, Sparpaglione M. Synthesis of polyanilines with high electrical conductivity. *Synthetic Metals.* 1995;72(2):135-40.

- [55] Taka T. Humidity dependency of electrical conductivity of doped polyaniline. *Synthetic Metals*. 1993;57(2-3):5014-9.
- [56] He H, Zhu J, Tao NJ, Nagahara LA, Amlani I, Tsui R. A conducting polymer nanojunction switch. *J Am Chem Soc*. 2001;123:7730-1.
- [57] Skotheim TA. *Handbook of conducting polymers*: M. Dekker; 1986.
- [58] Fan L-Z, Maier J. High-performance polypyrrole electrode materials for redox supercapacitors. *Electrochem Commun*. 2006;8:937-40.
- [59] Feldberg SW. Reinterpretation of polypyrrole electrochemistry. Consideration of capacitive currents in redox switching of conducting polymers. *Journal of the American Chemical Society*. 1984;106(17):4671-4.
- [60] Bull RA, Fan FRF, Bard AJ. Polymer Films on Electrodes: VII . Electrochemical Behavior at Polypyrrole-Coated Platinum and Tantalum Electrodes. *Journal of The Electrochemical Society*. 1982;129(5):1009-15.
- [61] Kim JH, Sung HK, Kim JH, Yoon CO, Lee K, Lee H. Electrochemical synthesis of metallic polypyrrole films. *J Korean Phys Soc*. 1997;31:91-4.
- [62] Lee HJ, Park S-M. Electrochemistry of Conductive Polymers 37. Nanoscale Monitoring of Electrical Properties during Electrochemical Growth of Polypyrrole and Its Aging. *J Phys Chem B*. 2005;109:13247-54.